1986

Detection Of Carbon Dioxide By Laser Resonance Absorption Spectroscopy

Craig William Schneider

CANADIAN THESES

THÈSES CANADIENNES

NOTICE

The quality of this microfiche is heavily dependent upon the quality of the original thesis submitted for microfilming. Every effort has been made to ensure the highest quality of reproduction possible.

If pages are missing, contact the university which granted the degree.

Some pages may have indistinct print especially if the original pages were typed with a poor typewriter ribbon or if the university sent us an inferior photocopy.

Previously copyrighted materials (journal articles, published tests, etc.) are not filmed.

Reproduction in full or in part of this film is governed by the Canadian Copyright Act, R.S.C. 1970, c. C-30.

AVIS

La qualité de cette microfiche dépend grandement de la qualité de la thèse soumise au microfilmage. Nous avons tout fait pour assurer une qualité supérieure de reproduction.

S'il manque des pages, veuillez communiquer avec l'université qui a conféré le grade.

La qualité d'impression de certaines pages peut laisser à désirer, surtout si les pages originales ont été dactylographiées à l'aide d'un ruban usé ou si l'université nous a fait parvenir une photocopie de qualité inférieure.

Les documents qui font déjà l'objet d'un droit d'auteur (articles de revue, examens publiés, etc.) ne sont pas microfilmés.

La reproduction, même partielle, de ce microfilm est soumise à la Loi canadienne sur le droit d'auteur, SRC 1970, c. C-30.

THIS DISSERTATION HAS BEEN MICROFILMED EXACTLY AS RECEIVED

LA THÈSE A ÉTÉ MICROFILMÉE TELLE QUE NOUS L'AVONS REÇUE

NL-339 (r. 86/06)

Canada

Detection of Carbon Dioxide by Laser Resonance Absorption Spectroscopy

by
Craig William Schneider

Faculty of Engineering Science

Submitted in partial fulfillment
of the requirements for the degree of
Doctor of Philosophy

Faculty of Graduate Studies
The University of Western Ontario
London, Ontario
February, 1986

ISBN 0-315-29501-5

Abstract

An analysis and description of a single detector laser resonance absorption spectrometer for the quantitative spectroscopic determination of carbon dioxide at 4.2 μm is presented. The work consisted of the design and construction of a 4.2 μm helium neon laser not available commercially, the construction of an optical spectrometer and signal processing unit and the determination of the carbon dioxide spectroscopic parameters required for calibration of the system.

The Fletcher Powell Method is used to locate the optimum laser frequency and broadening cross sections from absorption data for both pure carbon dioxide and nitrogen broadened carbon dioxide tests. Pure carbon dioxide absorption in a pressure range of 0.0016 atm (1.25 Torr) to 0.33 atm (250 Torr) is described well by a Lorentzian bandshape model with a self broadening cross section of 2.99 $\pm$ 0.30 GHz/atm at laser frequencies of 71.0730 $\pm$ 0.0008 THz (2370.74 $\pm$ 0.03 cm^{-1}) and 71.0847 $\pm$ 0.0008 THz (2371.13 $\pm$ 0.03 cm^{-1}). Nitrogen broadened carbon dioxide in the total pressure range of 0.13 atm (100 Torr) to 1.18 atm (900 Torr) is characterized by the same model with the laser frequency at 71.0835 $\pm$ 0.0012 THz (2371.09 $\pm$ 0.04 cm^{-1}) and the nitrogen broadening cross section of 2.40 $\pm$ 0.24 GHz/atm. The extinction coefficient for low concentrations of carbon dioxide in a 1 atm total pressure nitrogen environment has been determined as 9.90 $\pm$ 1.49 cm^{-1} atm^{-1}.

Acknowledgements

The author would like to thank his supervisor, Dr. Z. Kucerovsky, for his guidance and supervision throughout this work. A special thanks is also in order to Prof. E. Brannen of the Department of Physics at the University of Western Ontario.

He is indebted to Laurie Harnick of the U.W.O. glassblowing shop for her cooperation during the construction of the laser tube. He would also like to thank Mr. Heinz Walter for his assistance in the fabrication of the optical system.

This project could not be completed without the appearance of Mr. A. C. Simmons of Maverik Systems, Toronto. Many thanks Alan for the optimization software package.

The author wishes to extend special thanks to his wife, Margaret, for her help, encouragement and patience during the course of this work.

Dedication

This thesis is dedicated to two very special people in my life
my wife
Margaret
and
my son
Alan Donald.

Table of Contents

List of Tables

List of Figures

Chapter One
Introduction

Quantitative analysis of gaseous molecular species by laser resonance absorption spectroscopy is well established as a spectroscopic technique. ([1], [2]). In the most commonly applied form, the method relies on the frequency coincidence between a molecular absorption band and fixed frequency laser probe radiation. The success of the technique depends on accurate knowledge of both the laser frequency relative to the absorption peak and the characteristics of the absorption band in the probing environment.

A general system study and description of a prototype resonance absorption spectrometer has been published previously by the author [1] to which the interested reader is referred. The objective of this thesis is to provide both an analysis of carbon dioxide line broadening effects in the near infrared region of the electromagnetic spectrum and subsequent determinations of the required spectroscopic parameters by resonance absorption spectroscopy for quantitative gas measurements. Probe radiation from a low gain helium-neon laser operating in the 4.2 μm carbon dioxide band region is suitable for this application. This laser is not available commercially and was constructed by the author specifically for this project.

The organization of this thesis is in accordance with the system study objectives. Chapter 2 details the effects of environment on the carbon dioxide ν_3 absorption band and models the system to provide design guidelines for the spectrometer.

Chapter 3 describes the design strategy for the helium-neon laser source.

Specific details and experimental characterizations of the laser follow in Chapter 4.

Chapter 5 concerns the design and construction of the spectrometer. This chapter also includes the details and results of carbon dioxide absorption tests in both nitrogen and pure carbon dioxide environments.

Conclusions and recommendations are presented in Chapter 6.

Chapter Two
Problem Formulation

The vibrational spectroscopy of carbon dioxide has been the topic of many papers ([3]-[10]) and will not be analyzed here beyond the necessary background to clarify terminology.

Carbon dioxide is well established structurally as a linear molecule with $D_{\infty h}$ symmetry [11]. Vibrational motion is characterized by three normal modes; ν_1, ν_2 and ν_3, as shown in Figure 2-1. The convention used in this work assigns energy levels as $(\nu_1 \nu_2^{l} \nu_3)$ where l refers to quantized angular momentum along the figure axis that can occur as a result of phase differences between the ν_2 bending modes.

The ν_3 fundamental mode absorption $00^00 \rightarrow 00^01$ is active in the infrared and closely matches the frequency of a He-Ne laser system operating with the $3s_2 \rightarrow 3p_1$ transition[1].

The purpose of the following sections is to detail the theoretical considerations of utilizing this laser line to quantitatively determine carbon dioxide gas.

2.1. The Assymmetric Stretching Band of Carbon Dioxide

The ν_3 absorption band is classified as a $\Sigma_g^+ \rightarrow \Sigma_u^+$ type according to the symmetry notation proposed originally by Mulliken [12]. The individual rotational levels of the upper and lower vibrational states are shown in Figure

[1]Laser transition spectroscopic notation is outlined in Chapter 3.

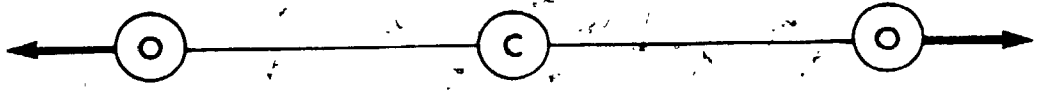

(a) Symmetric Stretch

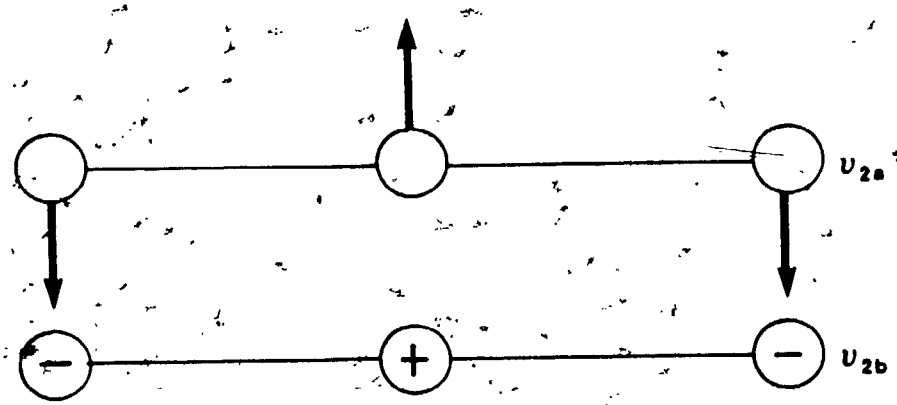

(b) Bending

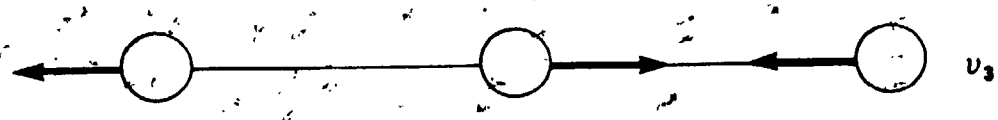

(c) Antisymmetric Stretch

Figure 2-1: Normal Vibrations of Carbon Dioxide

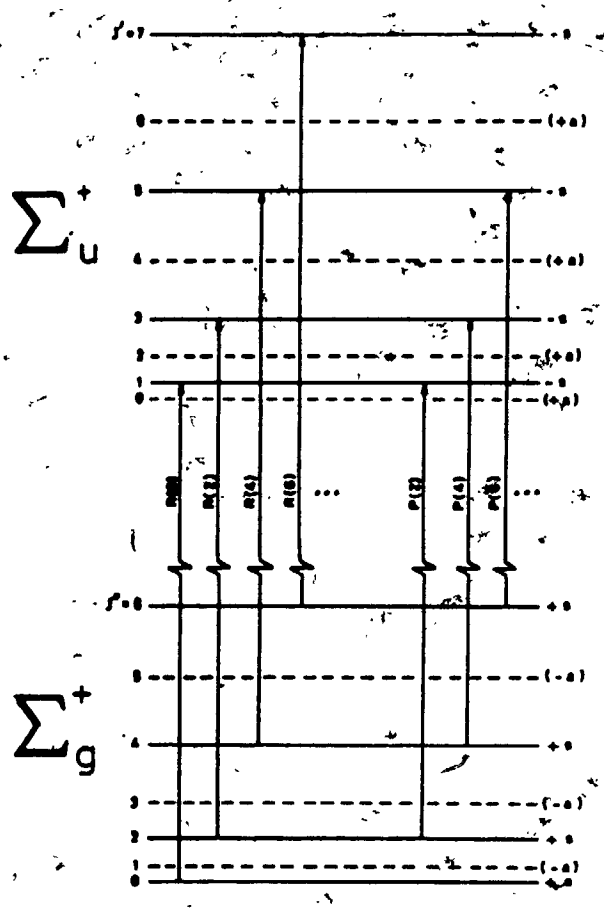

KEY

s: symmetric with respect to nuclei inversion
a: antisymmetric with respect to nuclei inversion
+: symmmetric with respect to nuclei and electron inversion
-: antisymmetric with respect to nuclei and electron inversion

SELECTION RULES

s <——> s a <——> a s <—|—> a

\+ <—|—> + - <—|—> - + <——> -

Figure 2-2: Allowed Transitions for the ν_3 CO_2 Absorption Band

2-2 with total molecular wave function symmetry indicated at the right hand side. Selection rules that apply in this case are rigorous and hold for any type of transition [13]. Given this restriction, every second level is missing from the upper and lower states as noted by dotted lines in the figure. (For a detailed discussion of missing alternate lines in the vibrational spectra of $D_{\infty h}$ molecules, see Reference [4].)

The ν_3 band structure as originally resolved into rotational components by Cameron and Nielson [3] is shown in Figure 2-3. The peak assignments are in standard fashion with the R(J″) and P(J″) branches defined by ΔJ equals +1 and -1 respectively. The two branch progressions are illustrated in Figure 2-2. A table of ν_3 band transition frequencies as determined by Plyler et al. [8] is found in Appendix A.

The bands R(28), R(30), R(32) and R(34) at 71.0247 THz (2369.13 cm^{-1}), 71.0616 THz (2370.36 cm^{-1}), 71.0952 THz (2371.48 cm^{-1}) and 71.1303 THz (2372.65 cm^{-1}) respectively[2] will overlap the He-Ne $3s_2 \rightarrow 3p_1$ laser transition frequency under certain line broadening conditions. The balance of this chapter will deal exclusively with theory applicable to these three transitions.

2.2. Theoretical Considerations

The effectiveness of a single molecular line as an absorber of fixed frequency laser radiation is determined by the extinction coefficient, $k(\nu)$. This parameter is dependent on the absorption line position relative to the laser emmision line, absorption line spectral intensity, width and bandshape. These

---

[2] Frequencies will be listed in this work in accordance with the SI system of units. Spectroscopic units in more common usage will follow as bracketed quantities.

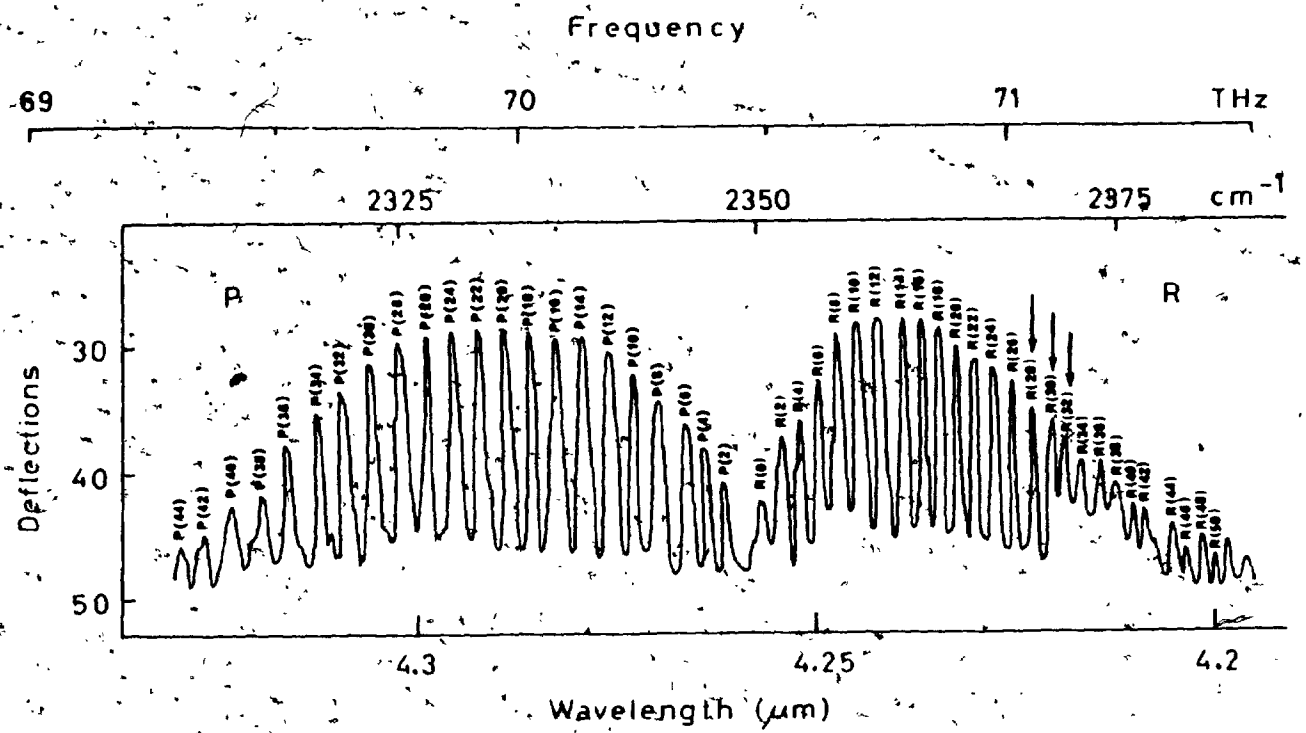

Figure 2-3: ν_3 Absorption Spectrum of Carbon Dioxide

considerations have been reviewed by the author [1] and will be briefly presented here to formulate this specific problem.

2.2.1. Preliminaries

Transmission, $T(\nu)$, will be defined following the notation of Benedict et. al. [14] via the Beer-Lambert Law, such that

$$T(\nu) = \frac{I_\nu}{I_\nu^o} \qquad (2-1a)$$

$$= \exp(-k(\nu)L) \qquad (2-1b)$$

where I_ν^o = incident light intensity at frequency ν

I_ν = intensity of light at frequency ν after absorption by the sample

$k(\nu)$ = extinction coefficient (cm^{-1})

L = geometrical pathlength (cm)

Dependence of the absorption line shape and width on system pressure will, in general, lead to a nonlinear relationship between $k(\nu)$ and absorber number density. Two extreme cases will linearize the relationship, i) total system pressure low enough to remove molecular collision processes as appreciable line broadening mechanisms, and ii) dilute absorber gas concentrations in a non-absorbing (foreign) gas matrix at constant total pressure.

As a measure of total absorption line strength, integrated absorption, S, is defined as

$$S = \int_0^\infty k(\nu)d\nu \quad \cdot \quad (\text{THz/cm}) \tag{2-2}$$

Under experimental conditions relevant to this work, integrated intensity may be related to number density by

$$S = S^d \cdot N_a \tag{2-3a}$$

$$= S^o \cdot p_a (1+0.005p_a) \frac{T_{ref}}{T_{amb}} \tag{2-3b}$$

where S^d = line strength (THz cm^{-1} Amagat^{-1})

S^o = line strength (THz cm^{-1} atm^{-1})

p_a = absorber gas pressure (atm)

T_{ref} = reference temperature ($^\circ$K)

T_{amb} = ambient temperature ($^\circ$K)

N_a = absorber molecule density (Amagat)

Equation (2-3) uses the appropriate Van der Waal's constants [15] to relate number density[3] and pressure for carbon dioxide. In this work, i) absorber pressures will be restricted to below 1 atmosphere and ii) reference temperature will be assigned as ambient (295 $^\circ$K), i.e.

$$S^d \cdot N_a \approx S^o \cdot p_a \tag{2-3c}$$

[3] Amagat is defined as the gas density at STP such that 1 Amagat equals $n_o m_o$ where n_o is Loschmidt's number and m_o is the mass of one molecule [14].

and the line strength parameter S^o will be used in place of S^d throughout the body of the text.

Parameters associated with individual vibrational rotational transitions will be denoted by the subscripts $v'',J'' \rightarrow v',J''$ where v'' and v' are the lower and upper vibrational quantum numbers respectively. For overlapping lines with individual lines strengths $S^o_{v'',J'' \rightarrow v',J'}$ in the absense of collisional mode coupling[4], the vibrational band strength, $S^o_{v'' \rightarrow v'}$ for a specific $v'' \rightarrow v'$ transition may be expressed simply as,

$$S^o_{v'' \rightarrow v'} = \sum_{J''} \sum_{J'} S^o_{v'',J'' \rightarrow v',J'} \qquad (2-4)$$

Conversely, in many systems $S^o_{v'' \rightarrow v'}$ is known and individual values of $S^o_{v'',J'' \rightarrow v',J'}$ may be calculated with knowledge of the individual rotational partition functions, transition frequencies and, vibrational and rotational transition matrix elements [17]. (Gray [16] outlines this calculation for carbon dioxide.) In this case, line strength may be represented as

$$S^o_{v'',J'' \rightarrow v',J'} = a_{v'',J'' \rightarrow v',J'} \; S^o_{v'' \rightarrow v'} \qquad (2-5)$$

where $a_{v'',J'' \rightarrow v',J'}$ = relative line intensity coefficient

given that $\sum_{J''} \sum_{J'} a_{v'',J'' \rightarrow v',J'} = 1$

---

[4] This point is further clarified on page 18.

Given the definition of integrated absorption by Equation (2-2) and the approximation (2-3c), the extinction coefficient for an isolated vibrational rotational line, $k(\nu)_{v'',J'' \rightarrow v',J'}$ may be expressed as

$$k(\nu)_{v'',J'' \rightarrow v',J'} = S^{o}_{v'',J'' \rightarrow v',J'} \cdot p_a \cdot f(\nu-\nu_o) \qquad (2-6)$$

where $f(\nu-\nu_o)$ = normalized bandshape function

such that $\int_{-\infty}^{\infty} f(\nu-\nu_o)d(\nu-\nu_o) = 1$

and ν_o = centre frequency of the specific line

The actual form of $f(\nu-\nu_o)$ depends on the molecular environment under consideration. A rigorous examination of this function should include the actions of radiative damping, Doppler shifting, wall-molecule and molecule-molecule collisions, motional narrowing and molecule-laser beam interaction geometry. These effects combine to loosely distinguish the environment types as naturally, Doppler and pressure broadened.

2.2.2. Radiative Damping

One consequence of energy radiating from a freely oscillating dipole is that the amplitude of oscillation must decay over time. Fourier Transformation of this motion in the time domain leads to a spectral response that may be described by a Lorentzian distribution of frequency components about the centre frequency ν_o. This bandshape is characterized by a radiative or "natural" halfwidth at the half power points (HWHM), γ_n. The natural line halfwidth in the infrared is typically in the order of 10 KHz (3×10^{-7} cm^{-1}) to 500 KHz (2×10^{-5} cm^{-1}) and will not contribute significantly to the shape function for the range of temperatures and pressures examined in this work.

2.2.3. Doppler Broadening

At room temperature and total system pressures below approximately 10^{-2} atmospheres (7.6 Torr), the motion of the molecules relative to an observation point Doppler shifts the individual naturally broadened Lorentzian bandshapes with respect to the resonant frequency. The resulting bandshape may generally be described by

$$f_d(\gamma_d, \nu-\nu_o) = \frac{\ln 2}{\pi \gamma_d} \exp(-\ln 2 (\nu-\nu_o)^2/\gamma_d^2) \qquad (2-7)$$

where γ_d = Doppler broadened HWHM (Hz)

$$= \left\{\frac{2 \ln 2 \, k \, T_{amb}}{mc^2}\right\}^{1/2} \nu_o$$

given that k = Boltzmann constant (1.38×10^{-23} J/molecule °K)

T_{amb} = ambient temperature (°K)

m = mass of absorbing molecule (kg)

c = speed of light (3.00×10^8 m/sec)

This function provides an accurate description of absorption within the Doppler halfwidth. In the far wings, however, some caution should be exercised due to increased contributions by the wings of the Lorentzian components ([18]-[19]). Doppler broadened halfwiths in the infrared are typically 20 MHz (7×10^{-4} cm^{-1}) to 1 GHz (3×10^{-2} cm^{-1}).

2.2.4. Collision Effects

At increased pressures the frequency and type of molecular interactions generally become the dominant factor affecting the lineshape function. For simplicity, two types of system will be considered in this work, i) absorption by a pure gas at pressure and number density p_a and N_a respectively, and ii) a binary mixture at total pressure P_T and number density N_T of absorbing molecules (p_a, N_a) and non absorbing molecules (p_f, N_f).

A complete mechanistic description of pressure (collision) broadening can be very complex and has been the subject of many papers in the last seventy-five years[5]. The usual solution to specific problems is to delineate an environment of interest by restricting temperature and pressure ranges. This environment is treated with the simplifying assumption that one or two of the many existing mechanisms will model the collision process to a good approximation.

Some caution should be exercised in the formulation of lineshape functions for the particular experiments in this work. Molecular collisions may lead to absorption line broadening or narrowing, frequency shifting and shape distortion that ultimately will determine the single frequency absorption

---

[5] A chronology of collision broadening would find roots in the work of Michelson [20] and Lorentz (strong collisions) and Debye (weak collisions). Advances in the development of the classically based theory include the description of bandshape by a convolution of Gaussian and Lorentzian functions by Voigt , the introduction of the correlation function to model pressure broadening in the time domain by Lenz and Weisskopt with further clarification by van Trigt [21], the observation and interpretation of motional narrowing by Dicke [23] and intermolecular potential calculations and the semiclassical treatment of molecular reorientation effects during collisions by Gordon ([24]-[26]). Quantum mechanical developments include the introduction of scattering matrix techniques by Anderson [22] and further development by Tsao and Cournutte [34] and the use of Liouville space formalism to model foreign gas broadening by Fano [27]. Excellent reviews with original literature references by Breene [28], Hindmarsh and Farr [29] and Ben-Reuven [30] are suggested to the interested reader.

coefficient for the laser probe radiation. Speculation on the changing nature of the individual components that determine this overall absorption coefficient can be dangerous if the lineshapes are not determined by more direct means than those considered here[6]. For this reason the lineshape model will be a simplistic one with experimentally determined quantities used in place of those calculated theoretically whenever possible. This approximation will serve the purpose of providing a framework to establish design criteria for the spectrometer as outlined in Chapter 5.

2.2.4.1. Strength of Collision

Classical treatment of molecular collisions is done most simply with the phase shift approximation [29]. This theory considers the system as an ensemble of freely oscillating dipoles fixed in space and described in the absense of radiative damping by a periodic time function of the form[7] $f(t) = Re\{\exp(i\omega_o t)\}$. A collision is defined as the approach of two molecules with a corresponding energy level shift as the molecules interact. This action frequency modulates the radiating dipole and reduces the coherence time to approximately the time between collisions [31]. If the collision frequency is low with respect to the dipole radiation frequency, and if internal energy is not transferred between collision partners by non radiative transitions, the effect may be interpreted as a changing of the dipole radiation phase with no change in amplitude. This situation is conveniently described by the use of temporal correlation functions that may be Fourier transformed via the autocorrelation

---

[6] Ben-Reuven [30] points to several examples of failure to recognize competing effects and subsequent claims of exceptional line shift observation in the microwave region.

[7] $Re\{\ \}$, means "the real part of". This representation is used for algebraic convenience in place of the equivalent $f(t) = \cos(\omega_o t)$ form.

theorem [32] to yield the intensity profile of the time function[8] (impact approximation). The normalized intensity profile is the lineshape function that is required for solution of Equation (2-6). For the case of pure absorbing gas volumes, the function may be expressed in terms of radian frequency as a shifted Lorentzian distribution[9],

$$f_c(\omega)=\frac{1}{\pi}\frac{N_a \bar{v}\sigma_{b_a}}{(\omega-\omega_o-N_a\bar{v}\sigma_{s_a})^2+(N_a\bar{v}\sigma_{b_a})^2} \qquad (2-8)$$

where σ_{b_a} = self broadening cross section

$$= 2\pi\int_0^\infty (1-\cos\eta(b))\,b\,db$$

σ_{s_a} = self shift cross section

$$= 2\pi\int_0^\infty \sin\eta(b)\,b\,db$$

$\bar{v}$ = mean molecular relative velocity

N_a = absorber molecule density

given that $\eta(b)$ = total phase shift due to all collisions

b = impact parameter

The impact parameter is defined as the distance of closest approach during collision as shown in Figure 2-4. This geometry implies that for impact

---

[8] This calculation is fully detailed in References [29], [30], [33] and [34]. In this thesis, the exact formulation will not be used to calculate absolute values but rather to distinguish between collision processes contributing to absorption line broadening and frequency shifting.

[9] All terms in the original derivation with $\omega+\omega_o$ in the denominator have been assumed negligible for the spectral region of interest and have been ignored.

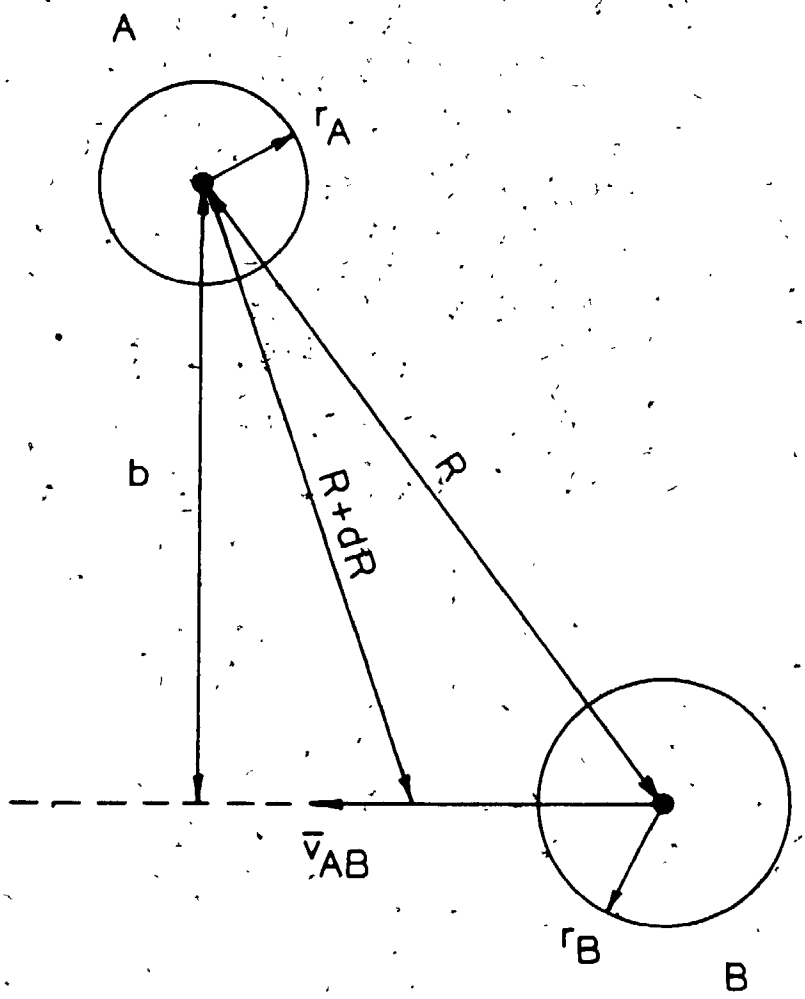

Figure 2-4: Impact Parameter Geometry

parameters less than a certain minimum value (b_{min}), the physical sizes of A and B cause a distinct trajectory deflection for molecule B. The phase interruption for the absorbing molecule is strong in this case and completely randomizing with an equal probability of any phase occurring after collision. Alternately, at large values of b, it is expected that partial phase disruptions may occur such that the "no memory" effect tacitly stated for strong collisions no longer applies. This situation leads to small phase shifts or, in the extreme, the weak collisions of Debye.

The phase disruption for a specific collision depends on the energy level shifts that occur, and hence, requires formulation of the intermolecular potential energy function V(R) or V(b). Solution of the integral equations for σ_{b_a} and σ_{s_a} with V(R) of the form $1/R^n$ indicates[10] that strong collisions determine σ_{b_a} whereas weaker effects are responsible for σ_{s_a}. Given the small phase shifts associated with weak collisions, it is necessary that a large number occur to produce an appreciable frequency shift [36].

Formulation of the molecular potential energy curves as a function of radial distances alone neglects the possibility of rotational phase disruptions and molecular reorientation effects. Gordon [25] points to these actions as being responsible for P(J″+1) ⟷ R(J″) interbranch intensity exchange (reorientation[11]) and P(J″) → P(J″±1) or R(J″) → R(J″±1) intensity transfer (rotational phase disruption).

---

[10] A simple example would be the Leonard-Jones Equation $V(R) = C_{12}/R^{12} - C_6/R^6$

[11] This interpretation of the reorientation effect is that collisional rotation of J through some angle corresponds to a transition between degenerate rotational states that are distinguishable with respect to a quantization axis [37].

Carbon dioxide does not exhibit a permanent dipole moment, hence, transitions between m or J states as implied by Gordon's theory require a temporary change of vibrational quantum number during collisional approach. The large vibrational energy gap indicates a very low probability of this transition and these effects will be assumed negligible for carbon dioxide ν_3 transitions. The validity of this assumption may be examined by comparison with experimentally observed pressure induced frequency shifts in the infrared at low pressures ($\sim$ 1 atmosphere) for hydrogen chloride molecules ([38]-[41]). The shifts are very small and are typically a maximum of 10% of the apparent line halfwidth [41]. The polar nature of hydrogen chloride allows for m state transitions during temporary J transitions and therefore, it is expected that these weak collisions will have a much larger effect than those between carbon dioxide molecules. In this work, experimental pressures will be restricted to below 1.25 atmospheres (950 Torr) so that the line shift cross section, σ_{s_a}, may be assumed to be negligible as noted above[12]. This approximation is a restatement of the impact theory in that line broadening is assumed to be governed directly by the collision frequency and that intermolecular forces have little effect. In the absense of line mixing effects, the assumption that extinction coefficients associated with individual lines may be calculated independently and summed to produce the overall extinction coefficient is reasonable (Equation 2-4).

---

[12]Gordon's method does, however, provide a qualitative rationale for the observed decrease of broadening cross section with increasing rotational energies in the infrared [15]. A $P \leftarrow \rightarrow R$ intensity exchange alters the internal energy states of the absorbing molecule and requires that the energy difference be taken up in some fashion by the collision partners. For a collision partner such as nitrogen, this must be as translational energy. As transition J numbers increase, the energy differences between specific $P \leftarrow \rightarrow R$ exchange lines also increase and render the energy transfer and broadening processes less efficient.

Equation (2-8) may be rewritten for pure carbon dioxide volumes as

$$f_c(\gamma_c, \nu-\nu_o) = \frac{1}{\pi} \frac{\gamma_c}{(\nu-\nu_o)^2+\gamma_c^2} \chi(\nu-\nu_o) \qquad (2-9)$$

where γ_c = collision halfwidth

$= p_a \sigma_{b_a}'$ (Hz)

σ_{b_a}' = modified self broadening cross section (Hz/atm)

$\chi(\nu-\nu_o)$ = distortion correction factor (see page 20)

In this formulation, the mean molecular velocity has been incorporated into the broadening cross section, and hence, the lineshape function is specified for a single temperature only.

The impact theory is presented in this thesis to distinguish between the effects of strong and weak collisions and is strictly only applicable to the strong collision case. Theories such as the quantum mechanical approach by Anderson [22] and semiclassical approach by Gordon provide better generalized descriptions of pressure broadening effects. Both these formulations lead to Equation (2-8) as the strong collision extreme is approached and the problem remains to solve for the collision halfwidth in terms of the impact parameter. A large number of publications using Anderson's method have appeared in which experimental and theoretical IR collision halfwidths have been favourably compared. It has been noted, however, that this is usually accomplished with limited data and a certain degree of arbitrariness in the selection of b_{min} [35]. Gordon's method encounters similiar problems for the

specification of matrix elements for the interline exchange. For this reason, the calculation will not be considered further. Experimentally determined halfwidth values will be used to estimate the overall extinction coefficient at the laser frequency.

The Lorentz lineshape loses validity at distant frequencies from the line centre. It has been suggested that asymmetry in the far wings results from intermolecular forces playing a larger role than within the central region of the line [14]. Experimentally determined lineshapes may be corrected for distortion effects by introduction of the empirical correction factor $\chi(\nu-\nu_o)$ [15]. Pronounced assymmetry is not expected for vibrational-rotational lineshapes [14], and this factor is assumed to be close to unity within a few GHz (cm^{-1}) of the line centre [43].

Equation (2-9) is formulated for pure absorbing gas volumes. Binary mixtures of absorbing and nonabsorbing gases may be treated by the introduction of a self broadening coefficient, B, and definition of an equivalent pressure P_e such that [44],

$$P_e = B p_a + p_b \qquad (2-10a)$$

and

$$B = \frac{\sigma'_{b_a}}{\sigma'_{b_f}} \qquad (2-10b)$$

where σ'_{b_f} = foreign gas broadening cross section

The value of B is an empirical quantity that must be determined experimentally for a specific gas mixture. Substitution of P_e and σ'_{b_f} for p_a and σ'_{b_a} in Equation (2-9) will lead to the required expression for binary gas mixtures.

2.2.4.2. Motional Narrowing

As pressures increase from the Doppler region as outlined in Section 2.2.3, absorption lines may both narrow and alter in shape if i) the radiation wavelength is long compared to the molecular mean free path, and ii) collision broadening effects as described in Section 2.2.4.1 remain small with respect to those of Doppler shifting (Dicke narrowing [23]). Dicke first observed this effect in the complete absence of collisional broadening, however, a more common situation requires the consideration of the combined effects of motional narrowing and collision broadening. Gersten and Foley [49] treat this problem and present a simple mathematical model for these combined effects.

Collision narrowing has been observed for water vapour transitions in the region of 60 THz (2000 cm^{-1}) [45]. In these cases, narrowing effects are evident only for transitions involving states with high rotational energies and associated small collision broadening cross sections ($\sim$ 450 MHz/atm). This study [45] found that nitrogen as the buffer gas only narrowed the lines a maximum of 7% relative to the expected halfwidth in the absence of Dicke narrowing. The carbon dioxide ν_3 R branch transitions under consideration in this work have experimentally determined collision broadening cross sections in the order of 2 GHz/atmosphere ([15], [35] and [43]). It is therefore assumed that collision broadening will mask any appreciable Dicke narrowing effects.

2.2.5, Combined Doppler and Collision Broadening

In the absense of appreciable Dicke narrowing effects, a general relationship to describe lineshapes over a wide range of temperatures and pressures is given by the Voigt integral [1]; a Doppler broadened distribution of Lorentzian line profiles[13]. The normalized shape factor may be expressed in this instance as, [46]

$$f_v(w,u) = \frac{w}{\pi}\int_{-\infty}^{\infty} \frac{\exp(-y^2)\,dy}{(u-y)^2 + w^2} \qquad (2-11)$$

where w = normalized collision HWHM Doppler HWHM ratio

$= (\gamma_c/\gamma_d)(\ln 2)^{1/2}$

u = line separation normalized to Doppler HWHM

$= ((\nu-\nu_o)/\gamma_d)(\ln 2)^{1/2}$

y = integration parameter normalized to Doppler HWHM

$= (x/\gamma_d)(\ln 2)^{1/2}$

The integration parameter x may be expressed as $\nu - \nu_o$ such that integration from $\pm\infty$ includes all possible molecular velocities [47]. Evaluation of Equation (2-11) may be done numerically, graphically or by use of the appropriate mathematical expansion for the region of interest [14]. An alternate technique is feasible if, prior to Voigt curve solution; the collision broadening cross section σ_b' and laser line - absorption line frequency separation are determined by numerically fitting higher pressure data to

---

[13] Doppler - Lorentzian curve convolution.

Equation (2-9). These values and the Doppler HWHM as determined by Equation (2-7a) may then be used as a good approximation to specify the extinction coefficient at the laser frequency from the appropriate family of Voigt profiles [46].

2.2.6. Miscellaneous Effects

Time of flight broadening will occur in laser spectroscopy if the interaction time between molecules and laser beam is short with respect to the excited state lifetimes. For laser beam diameters in the order of one centimeter, at room temperature this effect will typically broaden carbon dioxide lines to about 40 KHz HWHM [48]. Time of flight broadening will therefore be assumed negligible relative to the Doppler and collision broadening considered experimentally in this thesis.

Cell effects such as beam-wall interactions may be minimized by careful spectrometer design such that the Doppler width of the laser beam is well below the cell diameter.

With the possible exceptions of absorber isotope contamination and combination band overlaps, closed path absorption studies with pure gases and select binary mixtures can normally be structured to be free from spectroscopic interferences. The $C^{13}O_2$ ν_3 band is a potential interference in this case as it connects with the $C^{12}O_2$ band under consideration. The main overlap region occurs in the $C^{12}O_2$ ν_3 P branch, however, and the R branch region of interest is free of $C^{13}O_2$ absorption ([8][9]). Similarly, isotopic O^{17} and O^{18} substitution for O^{16} will lead to some overlap but will mainly interfere with the P branch as noted for C^{13}. Some allowed transitions for $C^{12}O^{16}O^{18}$ have been noted at energies above the ν_3 $C^{12}O_2^{16}$ R branch head [15], however, at

frequencies in the R(28) to R(32). ν_3 $C^{12}O_2{}^{16}$ region, absorption is dominated by the ν_3 $C^{12}O_2{}^{16}$ transition [43]. Dukuchaev and Tonkov [43] also note that the intensities of hot transitions in this region are negligibly small.

2.3. Practical Considerations

The preceding section presented the theoretical aspects of absorption line characterization in different molecular environments. This section reviews previous carbon dioxide ν_3 band studies and provides numerical estimates for the required constants in the describing equations. In this manner, absorption cell pathlengths, pure carbon dioxide and binary carbon dioxide-nitrogen gas mixture pressures and laser power requirements may be interrelated prior to system design.

As noted in the introduction, this thesis concerns primarily He-Ne laser beam absorption by CO_2-N_2 gas mixtures at pressures in the order of one atmosphere. An interesting sideline to this research is a comparison of pure carbon dioxide absorption data in different line broadening regimes. The pressure ranges examined for this latter system are dictated by acceptable signal to noise ratios for the processing electronics at fixed cell pathlengths[14]. Pressure broadened lineshapes are modelled by the Lorentz formula (Equation 2-9) and require preliminary estimates for linestrengths, broadening cross sections, correction terms, line centres and laser frequency. Pure carbon dioxide absorption is also examined in the Doppler region and will be treated with the Voigt formula as outlined in Section 2.2.5.

---

[14]Under high loading conditions (high CO_2 pressure or long pathlength), the spectrometer performance is limited by the minimum detectable signal at the detector. The instrument operates as a dual beam comparison type (Chapter 5). Low loading conditions require that the difference signal between sample and reference beams be above an acceptable minimum.

2.3.1. Line Strength

Total carbon dioxide ν_3 band strength $S^o_{v'' \rightarrow v'}$ has been determined by Burch et. al. [15] as 81.18 THz atm^{-1} cm^{-1} (2706 cm^{-1} atm^{-1} cm_{STP}^{-1}) at 273 °K and later remeasured by Rothman and Benedict [10] as 74.70 THZ atm^{-1} cm^{-1} (2490 atm^{-1} cm^{-2}) at 296 °K. Correction of the originally determined value to 296 °K [16] corresponds to less than 0.25% error between determinations, hence, the Rothman and Benedict $S^o_{v'' \rightarrow v'}$ will be used for the room temperature absorption tests.

The relative intensity coefficients $a_{v'',J'' \rightarrow v',J'}$ as defined by Equation (2-5) on page 10 have been calculated by Gray [16] for carbon dioxide $\Sigma \rightarrow \Sigma$ transitions at 300 °K and are listed with the results of Equation (2-5) for the appropriate R branch transitions as,

R(28) $a_{v'',J'' \rightarrow v',J'} = 0.02374$ $S_{v'',J'' \rightarrow v',J'} = 1.773$ THz atm^{-1} cm^{-1}

R(30) $a_{v'',J'' \rightarrow v',J'} = 0.02035$ $S_{v'',J'' \rightarrow v',J'} = 1.520$ THz atm^{-1} cm^{-1}

R(32) $a_{v'',J'' \rightarrow v',J'} = 0.01712$ $S_{v'',J'' \rightarrow v',J'} = 1.279$ THz atm^{-1} cm^{-1}

R(34) $a_{v'',J'' \rightarrow v',J'} = 0.01413$ $S_{v'',J'' \rightarrow v',J'} = 1.056$ THz atm^{-1} cm^{-1}

2.3.2. Collision Halfwidth Parameters

The pressure broadened halfwidths of carbon dioxide ν_3 R and P branch lines have been measured for both pure carbon dioxide and nitrogen broadened samples. Burch et. al. [15] report self broadened HWHM for R(28) to R(30) lines to be in the order of 2.1 GHz (0.07 cm^{-1}) at one atmosphere. The self broadening coefficient B was determined as 1.21 for nitrogen to give HWHM of about 1.75 GHz (0.058 cm^{-1}) for one atmosphere nitrogen broadened lines (Equation 2-10a).

Figure 2-5 illustrates measured nitrogen broadening cross sections as compiled by Dukuchaev and Tonkov [43]. For comparison purposes, the cross sections of three transitions are shown in the figure. The authors state that the equivalent width method used to measure the $00^0 0 \rightarrow 00^0 1$ transition halfwidths has baseline determination ambiguities and leads to low values. For this reason, they preferred to use the halfwidth measurements from laser studies of other transitions as indicated by the dashed line empirical fit in the figure[15]. Values of σ_{b_f}' in the region of the R(30) line are seen to vary between 1.8 GHz/atm (0.06 cm^{-1}/atm) and 2.4 GHz/atm (0.08 cm^{-1}/atm). The Dukuchaev and Tonkov empirical fit value is approximately 2.18 GHz/atm (0.0725 cm^{-1} atm^{-1}) at this point. Assuming the B value of 1.21 for nitrogen as determined by Burch et. al. [15], the modified self broadening cross section, σ_{b_a}', should lie in the range of 2.1 GHz/atm (0.07 cm^{-1}/atm) to 3.0 GHz/atm (0.1 cm^{-1}/atm) for these conditions.

---

[15] It is assumed that the nature of the collision broadening process leads to similar broadening coefficients for different transitions.

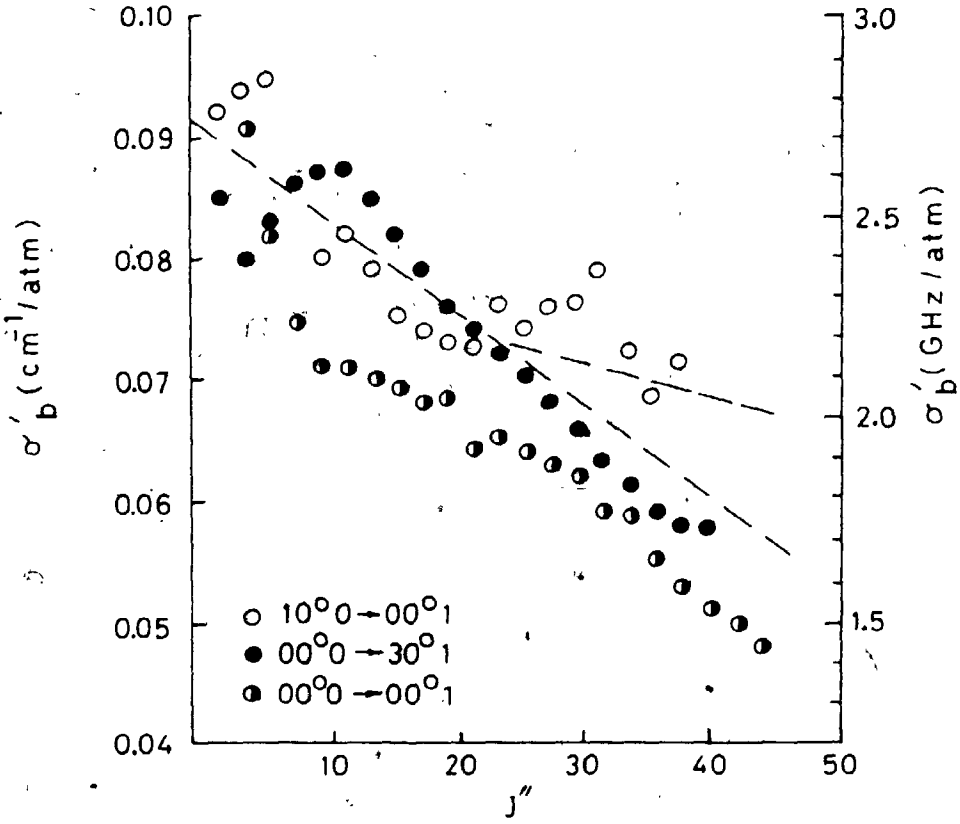

Figure 2-5: Values of $\sigma_b'(J'')$

2.3.3. Laser Line Absorption Band Frequency Coincidence

As noted in Section 2.2.4.1, the absorption line centre frequencies are assumed to be unshifted from the values determined by Plyler et. al. (Appendix A).

The He-Ne $3s_2 \rightarrow 3p_1$ transition frequency is listed by Moore [52] at 71.0694 THz (2370.62 cm^{-1}). To the author's knowledge, only one direct determination of the laser frequency has been reported; Brunet and Laures [50] in 1964 at 71.0910 THz (2371.47 cm^{-1}). The difference between observed and calculated wavelengths in this instance was attributed to atmospheric dispersion[16]. Another study of this specific laser action has not directly measured the output frequency but has assumed the calculated value [51]. The assignment in this case is based on carbon dioxide absorption data. Absorption trends indicate the main overlap between the carbon dioxide absorption spectrum and laser line to be in one of the individual absorption line wings.

2.3.4. Band Structure Simulation

The values for line centres at R(28), R(30), R(32) and R(34) have been assigned in Equation (2-9) and collision broadened shape factors have been calculated for a series of collision broadened HWHM that span the expected range of values at one atmosphere total pressure. The shape distortion factor χ is assumed to be unity. A normalized extinction coefficient $k^o(\nu)$ may be defined to remove the linear absorber pressure dependence of Equation (2-6) such that

---

[16] Brunet and Laures note strong carbon dioxide absorption and abnormal variance of atmospheric refractive index in this region.

$$k(\nu)^{o}_{v'',J''\rightarrow v',J'} = \frac{k(\nu)_{v'',J''\rightarrow v',J'}}{p_a} \qquad (2-12)$$

$$k(\nu)^{o}_{v'',J''\rightarrow v',J'} = S^{o}_{v'',J''\rightarrow v',J'} f_c(\gamma_c, \nu-\nu_o) \quad (\mathrm{cm^{-1}\ atm^{-1}})$$

Figure 2-6(a) shows the results of the calculation for total normalized extinction coefficient at one atmosphere pressure in the laser line spectral region where,

$$k(\nu)^{o}_{l} = \sum_{J''}{}_{28\rightarrow 34} k(\nu)^{o}_{v'',J''\rightarrow v',J'} \qquad (2-13)$$

given that $k(\nu)^{o}_{l}$ = normalized extinction coefficient at the laser frequency

Contributions by absorption lines other than those considered are negligible and collision HWHM are assumed to be the same for all three lines. The computer programs used to calculate and graph the curves are found in Appendix D.

Laser line frequencies as noted in Section 2.3.3 are indicated on the figure to illustrate the large difference in expected absorption at the two assignments. The Brunet and Laures determination at 71.0940 THz has a $k(\nu)^{o}_{l}$ value roughly fifteen times that at 71.0694 THz.

Evidence that the laser frequency lies in the wing of an individual line [51] indicates that the theoretical transition frequency at 71.0694 THz is a good

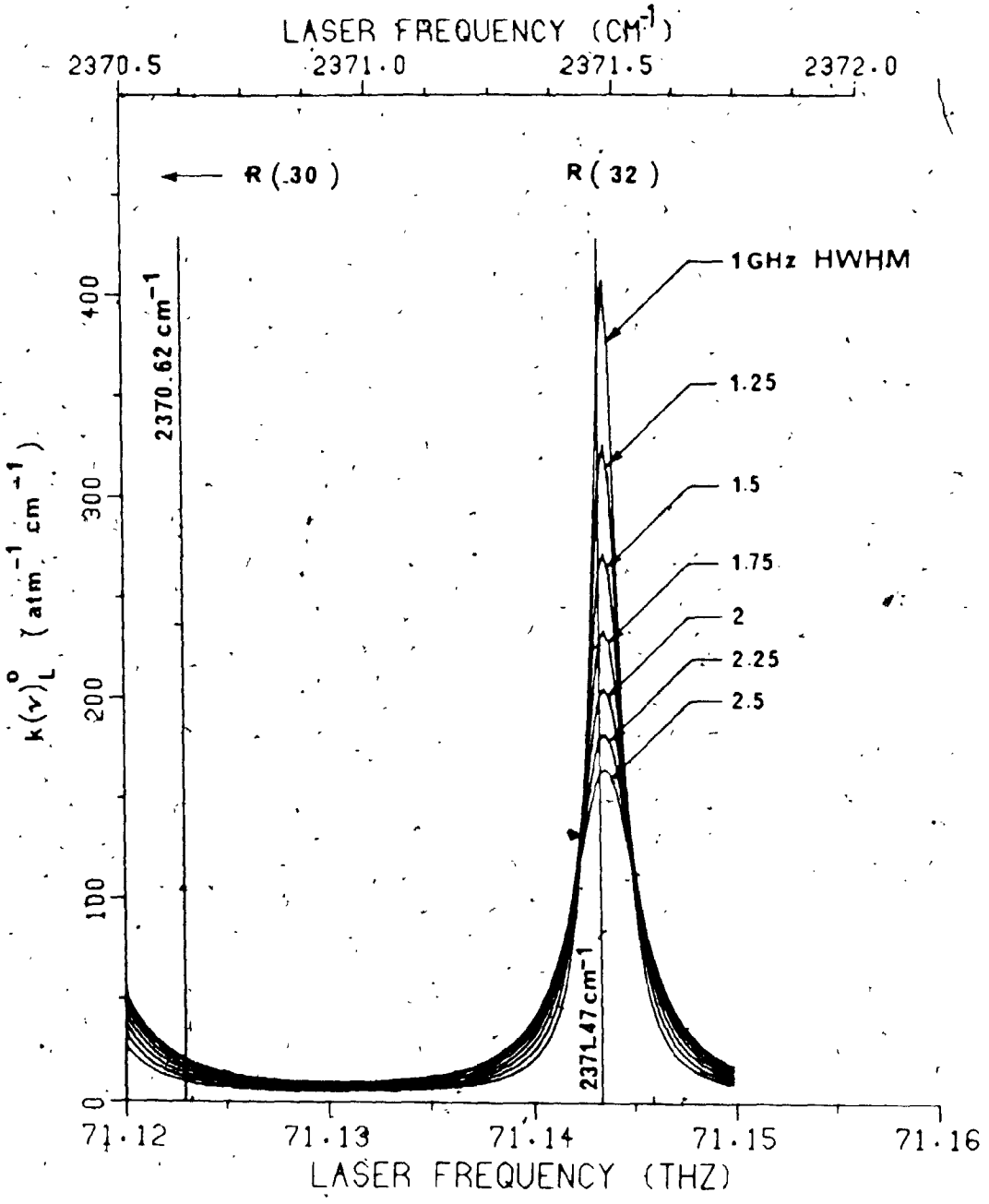

Figure 2-6: Normalized Extinction Coefficient as a Function of Frequency

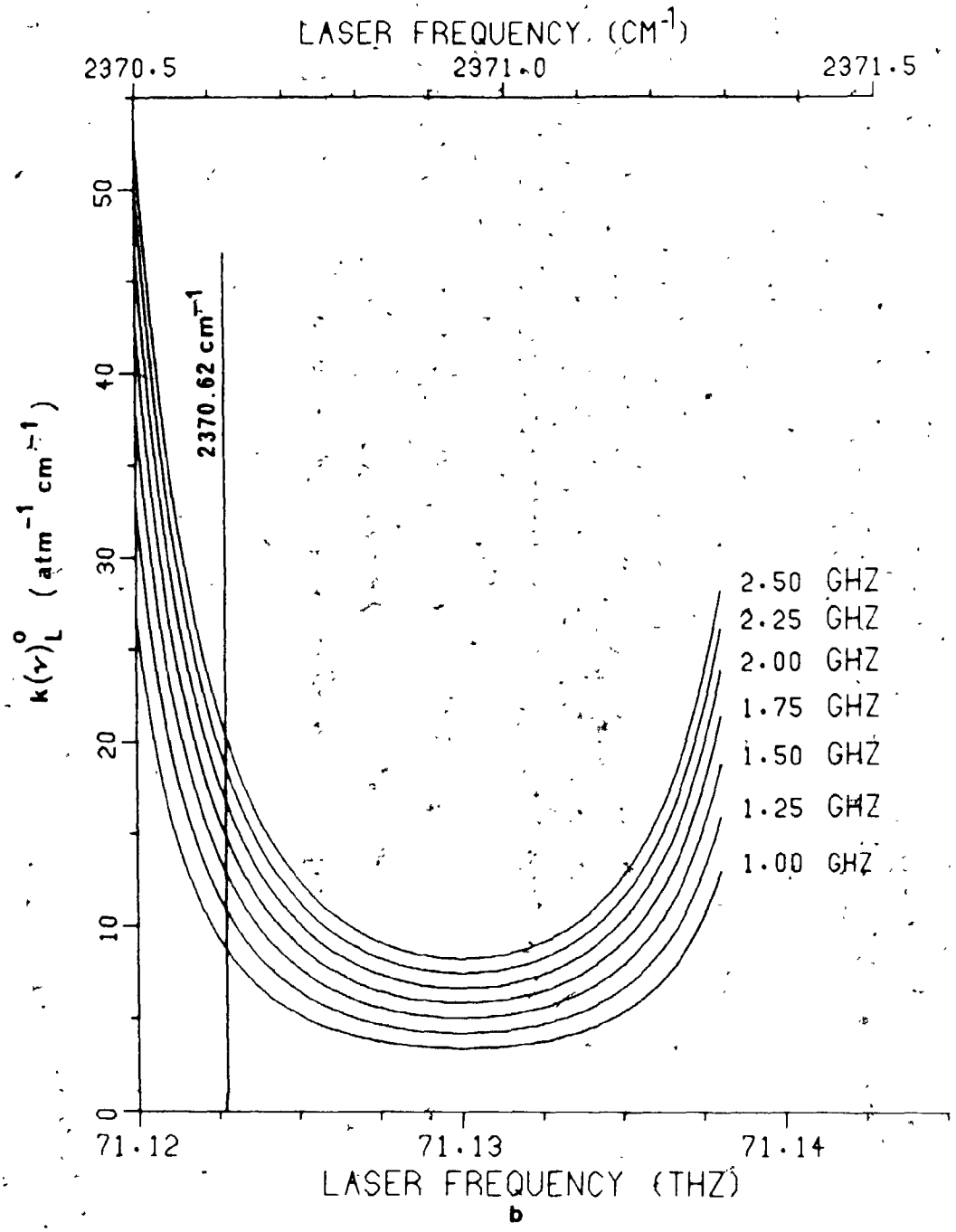

Figure 2-6. (con't)

starting point for spectrometer design. Belov et. al. [51] have determined $k(\nu)_L^o$ under self and nitrogen broadening conditions to be 14.5 cm^{-1} atm^{-1} and 11.5 cm^{-1} atm^{-1} respectively at one atmosphere total pressure. Reference to Figure 2-6(b) illustrates that these values correspond to line halfwidths of about 1.75 GHz. This corresponds well with the expected values as detailed in Section 2.3.2.

The formulations developed in this chapter to describe absorption band behaviour in different molecular environments will be referenced in Chapter 5. Prior to the presentation of spectrometer design and construction details, the helium neon laser source is examined in Chapters 3 and 4.

Chapter Three
The Helium Neon Laser Source

Laser action in helium neon gas dicharges was first reported in 1961 by Javan et. al. [53] and has since been the subject of a countless number of papers. Notable advancements in the design and analysis of He-Ne lasers which have led to the most commonly found present day commercial types include

1. the use of concave mirrors in place of plane parallel mirrors to better define laser beam geometry (Boyd and Gordon (1961) [56], Fox and Li (1961) [57])

2. sealed tube designs bounded by Brewster windows and external mirrors (Rigrod et. al. (1962) [58])

3. electron impact excitation (White and Gordon (1963) [59])

4. the discovery of the most commonly utilized laser transitions in both the visible at 632.8 nm (White and Rigden (1962) [60]) and the infrared at 3.39 μm (Bloom et. al. (1963) [61]).

The majority of the published literature concerns the report of newly observed He-Ne laser transition frequencies, the experimental observations of laser output power dependence on mixture ratios and total system pressures, pumping schemes and laser resonator design details. Reasonably complete listings of observed He-Ne laser action may be found in several sources ([54], [55]) to which the reader is referred for bibliographic information concerning specific studies.

Helium-neon laser action at 4.2 μm was first reported by Brunet and Laures in 1964 [50] and later "rediscovered" by Lis (1972) [62]. In both these

cases, the authors note that suppression of the competing superradiant line at 3.39 μm is required if the 4.2 μm laser transition is to be observed. To achieve this end, Brunet and Laures suggest the introduction of a dispersive element (a prism) in the laser resonator and an optical arrangement suitable for exclusive 4.2 μm radiation feedback. Lis uses polyethylene foil to block the beam in the laser cavity[1] in tandem with a prism setup. Neither paper provides details of the observed laser output characteristics at this wavelength with the exception of Brunet and Laures' comment that the laser action is strong.

In this thesis, a diffraction grating blazed for 4.2 μm is used in place of one of the resonator end mirrors to supply the required intracavity wavelength selection. The purpose of this chapter is to describe the design and construction of this laser with reference to design guidelines developed for other He-Ne systems. General descriptions of the theory of gas lasers may be found in the literature ([63]-[65]) and will not be treated here.

3.1. Helium Neon Laser Transition Pathways

Helium neon lasers are generally four level systems [66] with the basic transition pathways as shown in Figure 3-1. Electronic energy levels are designated by Russell-Saunders terms [67] for helium and both Paschen [68] and Racah [70] notations for neon on the left and right sides of the levels respectively. Descriptions of Russell-Saunders and Racah coupling schemes and appropriate selection rules for optically allowed dipole radiation transitions are found in Appendix B. Paschen labelling is a shorthand notation and does not convey any specific information to characterize the energy state. For

[1] This material is strongly absorbing at 3.39 μm but transparent at 4.2 μm

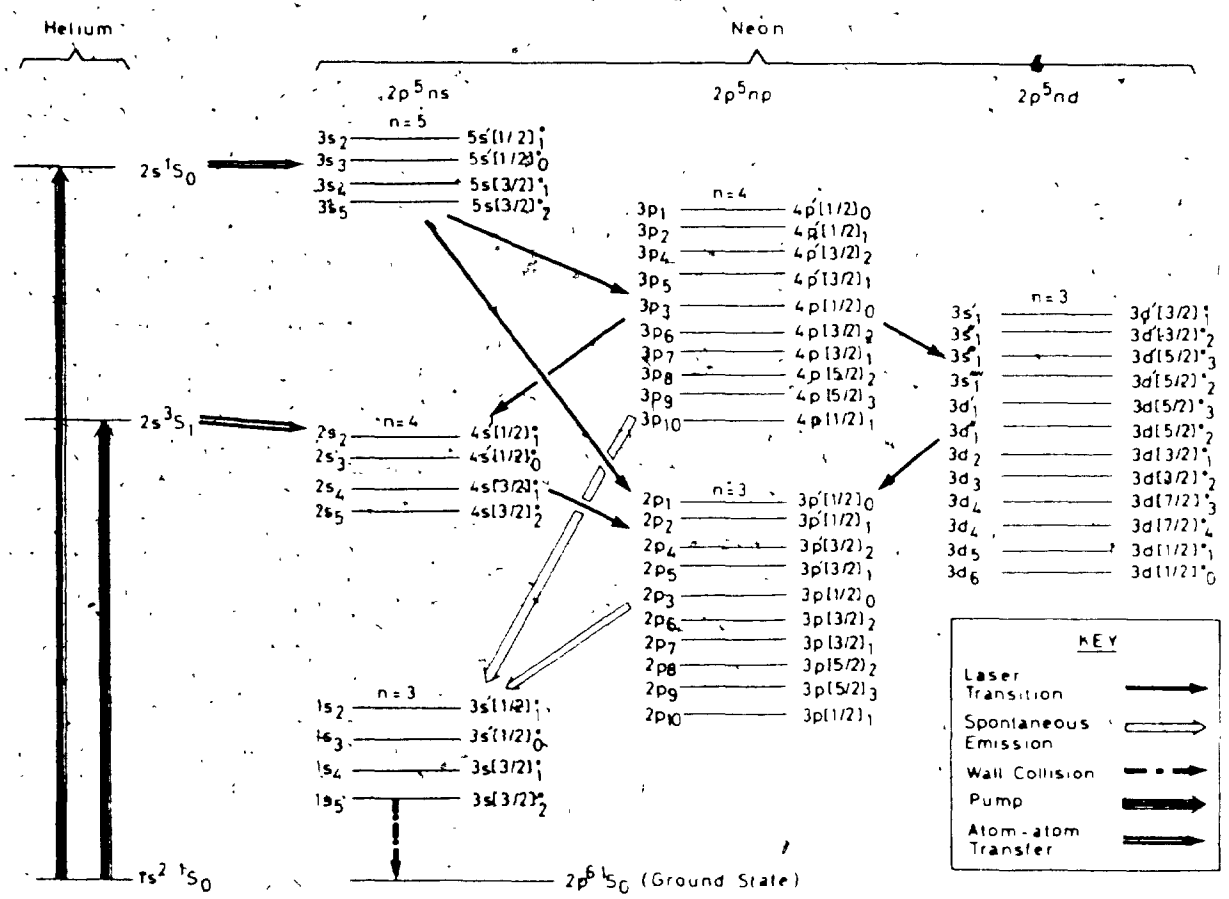

Figure 3-1: He-Ne Energy Level Diagram Showing Transition Pathways

convenience, neon levels are referred to here for the most part by the Paschen terms with spin pairings noted in some reactions to indicate preferred pathways.

3.1.1. General Overview of Neon Laser Transitions

A prerequisite to laser action is the existence of a population inversion between the desired upper and lower neon laser levels. The general scheme is initiated by the creation of helium excited state[2] metastable levels 2s $^3S_1$ and 2s $^1S_0$ by electron impact collisional energy transfer[3]. Population of neon 2s and 3s Paschen levels may then occur through helium-neon energy exchange by collisions of the second kind [51]. This pumping scheme is detailed with reference to the 4.2 μm laser transition in Section 3.1.2.

Observed neon laser transitions between the lower lying groups of neon energy levels are indicated in Figure 3-1. The strength or existence of individual laser oscillations is dependent on the degree of population inversion, the laser cavity Q and the transition probability between the states in question [77]. Foster and Statz suggest study of the latter consideration to aid in prediction of competing laser line strengths and present a method for approximate calculation of allowed s-p transition[4] probabilities [77]. This method has been used by Faust and McFarlane [78] to include neon p-d and f-

---

[2]Laser action has been observed in pure neon discharges ([72]-[75]), however, direct pumping of neon is less efficient than a helium neon mixture and does not always lead to population of the desired excited state neon levels.

[3]Early He-Ne laser designs used radio frequency radiation to pump helium to these levels [53]. Electron impact excitation is presently preferred as a more efficient and more convenient technique.

[4]This notation classifies energy levels by the orbital angular momentum of the promoted electron.

d transitions. Calculation details will not be given here, however, the technique assumes (J,l) or Racah coupling and builds up the wave functions via this coupling scheme as described in Appendix B.

The results of these calculations as tabulated by Faust and McFarlane [78] are shown in Figures 3-2 to 3-4. Observed laser transitions in the tables have been updated from the original by reference to more recent line compilations ([54], [55]). Transition probabilities have been calculated for laser lines that obey (J,l) coupling selection rules [71]

$$\Delta J_c = 0$$

$$\Delta J = 0, \pm 1 \qquad J=0 \leftarrow\!|\!\rightarrow J=0$$

$$\Delta K = 0, \pm 1 \qquad K=0 \leftarrow\!|\!\rightarrow K=0$$

The parity must also change.

Promotion of one electron leaves a tightly bound core or parent ion that is configured as a $^2P_{1/2}$ or $^2P_{3/2}$ state. The restriction on parent ion total angular momentum change ΔJ_c does not allow transitions between states associated with different parent ions, hence, $^2P_{1/2}$ and $^2P_{3/2}$ core state pathways may be listed separately in Figures 3-2 to 3-4. Violations of K rules are indicated by zeros in the tables and J rule violations by dashes. The figure does not specifically indicate the preferred laser pathways from common upper levels. Laser line observations are listed with the implication that strong lines may need to be supressed for laser action to occur at many of the transition wavelengths.

Faust and McFarlane [78] subdivide the tables along diagonals according

$^2P_{1/2}$ PARENT ION

RELATIVE LINE STRENGTHS IN 1/18 THS

UPPER LEVEL	LOWER LEVEL $p'[0\ 1/2]_0$	$p'[0\ 1/2]_1$	$p'[1\ 1/2]_1$	$p'[1\ 1/2]_2$
$s'[0\ 1/2]^{0'}_0$	–	● + 2	● + 4	–
$s'[0\ 1/2]^{0}_1$	● ▲ ■ 2	● ▲ ■ 4	● ▲ ■ 2	● ▲ ■ × 10

B A

$^2P_{3/2}$ PARENT ION

RELATIVE LINE STRENGTHS IN 1/18 THS

UPPER LEVEL	LOWER LEVEL $p[0\ 1/2]_0$	$p[0\ 1/2]_1$	$p[1\ 1/2]_1$	$p[1\ 1/2]_2$	$p[2\ 1\ 2]_2$	$p[2\ 1/2]_3$
$s[1\ 1/2]^{0}_1$	● ■ + 2	● ■ 1	● ■ + 5	● 1	● ■ 9	–
$s[1\ 1/2]^{0}_2$	–	● 5	+ 1	● ■ + 9	● + 1	● ■ + 14

C B A

● 4s — 3p
▲ 5s — 3p
■ 5s — 4p
\+ 6s — 5p
× 7s — 6p

A: $\Delta K = \Delta J = \Delta l$
B: $\Delta K = \Delta J = 0$
C: $\Delta K = \Delta J = -\Delta l$

Figure 3-2: Relative Strengths of Neon s-p Lines

$^2P_{1/2}$ PARENT ION

RELATIVE LINE STRENGTHS IN 1/900 THS

LOWER LEVEL	UPPER LEVEL $p'[0\ 1/2]_0$	$p'[0\ 1/2]_1$	$p'[1\ 1/2]_1$	$p'[1\ 1/2]_2$
$d'[1\ 1/2]^o_1$	●▲■▼♦ 100	50	25	5
$d'[1\ 1/2]^o_2$	–	●▲ 250 ■	5	▲ 5
$d'[2\ 1/2]^o_2$	–	0	●▲ 270 □	● 30
$d'[2\ 1/2]^o_3$	–	–	–	●▲ 420 ■

B

A

$^2P_{3/2}$ PARENT ION

RELATIVE LINE STRENGTHS IN 1/900 THS

LOWER LEVEL	UPPER LEVEL $p[0\ 1/2]_0$	$p[0\ 1/2]_1$	$p[1\ 1/2]_1$	$p[1\ 1/2]_2$	$p[2\ 1/2]_2$	$p[2\ 1/2]_3$
$d[0\ 1/2]^o_0$	–	50	■ 10	–	–	–
$d[0\ 1/2]^o_1$	50	● 100	5	25	0	–
$d[1\ 1/2]^o_1$	●▲ 50 ■▼	25	80	16	9	–
$d[1\ 1/2]^o_2$	–	●▲■▼ 125	16	144	● 1	14
$d[2\ 1/2]^o_2$	–	0	●▲▼♦ 189	●▲ 21	▲ 84 ○	○ 6
$d[2\ 1/2]^o_3$	–	–	–	●▲■▼♦ 294	6	120
$d[3\ 1/2]^o_3$	–	–	–	0	●▲■▼ 400	♦ 20
$d[3\ 1/2]^o_4$	–	–	–	–	–	●▲▼ 546 □

C

B

A

● 4p – 3d
▲ 5p – 4d
■ 6p – 5d
▼ 7p – 6d
♦ 8p – 7d

UNFILLED SYMBOLS INDICATE UNRESOLVED LINE PAIRS

A: $\Delta K = \Delta J = \Delta l$
B: $\Delta K = \Delta J = 0$
C: $\Delta K = \Delta J = -\Delta l$

Figure 3-3: Relative Strengths of Neon p-d Lines

$^2P_{1/2}$ PARENT ION

RELATIVE LINE STRENGTHS IN 1/132,300THS

UPPER LEVEL	LOWER LEVEL $d'[3/2]^o_1$	$d'[3/2]^o_2$	$d'[5/2]^o_2$	$d'[5/2]^o_3$
$f'[5/2]_2$	26,460 ▲	2940	1960	140
$f'[5/2]_3$	–	41,160 ▲	140	2800
$f'[7/2]_3$	–	0	42,000 ▲	2100
$f'[7/2]_4$	–	–	–	56,700 ▲

B

A

$^2P_{3/2}$ PARENT ION

RELATIVE LINE STRENGTHS IN 1/132,300THS

UPPER LEVEL	LOWER LEVEL $d[1/2]^o_0$	$d[1/2]^o_1$	$d[3/2]^o_1$	$d[3/2]^o_2$	$d[5/2]^o_2$	$d[5/2]^o_3$	$d[7/2]^o_3$	$d[7/2]^o_4$
$f[3/2]_1$	● 8820	4410	▲ 4410	882	378	–	–	–
$f[3/2]_2$	–	● 22050	882	▲ 7938	42	588	0	–
$f[5/2]_2$	–	0	● 21168	2352	▲ 7166	512	300	–
$f[5/2]_3$	–	–	–	● 32928	512	▲ 10240	15	405
$f[7/2]_3$	–	–	–	0	● 36000	1800	▲ 6075	225
$f[7/2]_4$	–	–	–	–	–	○ 48600	225	▲ 7875
$f[9/2]_4$	–	–	–	–	–	0	● 55125	○ 1575
$f[9/2]_5$	–	–	–	–	–	–	–	○ 69300

C

B

A

● $4f - 3d$

▲ Observed Spontaneous Emission

UNFILLED SYMBOLS INDICATE UNRESOLVED LINE PAIRS

A: $\Delta K = \Delta J = \Delta l$
B: $\Delta K = \Delta J = 0$
C: $\Delta K = \Delta J = -\Delta l$

Figure 3-4: Relative Strengths of Neon f-d Lines

to constant changes in J, K and l quantum numbers. Of note in the figure is that transition probabilities increase with higher J states with line strengths increasing in the sequence $\Delta J=\Delta K=-\Delta l \rightarrow \Delta J=\Delta K=0 \rightarrow \Delta J=\Delta K=\Delta l$. This corresponds well with experimental observation of relative laser line output powers [76]. The strongest lines occur in the s-p groups towards the lower right hand corners of the tables in Figure 3-2. Specifically, the $3s_2 \rightarrow 3p_4$ Paschen $(5s'[1/2]^o_1 \rightarrow 4p'[3/2]_2)$ transition at 3.39 μm and $3s_2 \rightarrow 2p_4$ Paschen $(5s'[1/2]^o_1 \rightarrow 3p'[3/2]_2)$ transition at 633 nm are two of the strongest He-Ne lines yet discovered [54].

The selection rules for J are inviolate in any coupling scheme and those for K hold well[5], however, not noted in the figure are several lines that originate from the $3s_2$ Paschen level $(5s'[1/2]^o_1)$ and violate the ΔJ_c rule ([54], [55]). Laser action may result for transitions with low probabilities or with minor selection rule violations if the population inversion between upper and lower states is very large ([76], [78]). Population of the $2s_2$ Paschen neon level in a gas discharge is made relatively efficient by collision with $2s\ ^1S_0$ helium metastables. This point is examined in greater detail in the following section.

3.1.2. The Helium Neon $3s_2$ - $3p_1$ System

The helium-neon $3s_2 \rightarrow 3p_1$ laser transition at 4.2 μm and associated reactions are outlined in Figure 3-5. The overall reaction pathways may be considered as a two level pump (1,2), laser transition (3) and fast lower laser level depopulation by sequential spontaneous emission (4a) and wall collision

---

[5]The single noted K rule violation is the observation of the He-Ne laser transition $3s_2 \rightarrow 2p_8$ $(5s'[1/2]^o_1 \rightarrow 3p[5/2]_2)$ at 594 nm $(\Delta K=-2, \Delta J_c=1)$ [75].

		ΔE (eV)
(1)	$He(1s^2\ ^1S_0) + e^- \longrightarrow He(2s\ ^1S_0) + e^- - \Delta E$	20.61
(2)	$He(2s\ ^1S_0)(1\downarrow) + Ne(2p^6\ ^1S_0)(1\downarrow) \longrightarrow He(1s^2\ ^1S_0)(1\downarrow) + Ne(3s_2)(1\downarrow) - \Delta E$	0.05
(3)	$Ne(3s_2) \xrightarrow{LASER} Ne(3p_1) + h\nu\ (4.2\ \mu m)$	0.20
(4a)	$Ne(3p_1) \longrightarrow Ne(1s_2) + h\nu\ (352\ nm)$	20.37
(4b)	$Ne(1s_2) \longrightarrow Ne(2p^6\ ^1S_0) + \Delta E$	

Figure 3-5: He-Ne Laser Transition Pathways

deactivation (4b). The purpose of this section is to outline this laser scheme with reference to the individual steps. Considerations for final laser design will follow in the next section.

The equations in Figure 3-5 are balanced with respect to reactant/product energy differences as listed in the right column. Endothermic reactions have energy supplied by the electrons (1) or gas discharge (2). Exothermic reactions involve emitted radiation (3, 4a) or energy absorption by the walls of the laser tube (4b).

Population of the neon $3s_2$ level through electrical pumping as outlined in Figures 3-1 and 3-5 has been studied experimentally (White and Gordon [59] [79], Labuda and Gordon [80]) and summarized in several sources ([54], [63]-[65]). Although the exact nature of gas laser pumping processes can be complex, general observations concerning this specific system pumping behaviour and upper level $3s_2$ neon laser transitions may be listed as follows.

1. Transitions between helium ground states to $2s\ ^1S_0$ and $2s\ ^3S_0$ levels are optically forbidden (Appendix B). Electron excitation by collisions of the first kind[6] for optically forbidden transitions favour the pathway that conserves spin ($1s^2\ ^1S_0 \rightarrow 2s\ ^1S_0$) [63].

2. The production rate of helium metastables is directly proportional to gas discharge electron current and is optimized at a specific value of the product of tube diameter and total gas pressure[7] (pD). Level destruction occurs predominantly through both processes independent of discharge current (second kind collisions with neon

---

[6] A collision of the first kind transfers kinetic energy from one species to potential energy of the other. Second kind collisions involve an exchange of potential energy between the collision partners.

[7] Gordon and White [79] note that an optimum pD product for laser operation implies an optimum average electron energy that is independent of discharge current. A brief analysis of electron behaviour in a gas discharge is given in Reference [63].

ground state atoms and diffusion to the laser tube walls) and those showing linear current dependency (superelastic collisions such as $He(2s\ ^1S_0 + e^- \rightarrow He(1s^2\ ^1S_0) + e^-)$. The current dependence of steady state helium metastable population may be expressed in the form $Nk_1I/(k_2 + k_3I)$ where N is the ground state helium population [79]. Metastable population is therefore seen to reach a saturated value at high current levels.

3. The energy transfer efficiency of second kind collisions is greatly increased if spin is conserved by the collision partners (Wigner spin rule [54]). This consideration favours population of the neon $3s_2$ Paschen level with respect to the other three 3s levels on collision with $2s\ ^1S_0$ helium atoms. The $3s_2$ level is not appreciably populated by first kind collisions between electrons and neon ground state atoms [59].

4. Steady state operation of the laser requires an equilibrium population inversion between the upper and lower laser levels. Lifetimes of the upper 3s levels are typically ten times those of the lower 3p states [63] and this condition is fulfilled if the upper level is efficiently pumped.

5. The gain of the line is proportional to the population difference between the laser levels [59]. At high current levels, the lower state population increases by direct electron pumping of neon ground state levels and cascading from higher neon levels that have also been directly excited by electron collision. As noted in point 2 above, the upper state population tends to saturate at high current levels, hence, the population inversion and laser gain go through a maximum at an optimum current level. This optimum current is generally in the order of 50 to 100 mA for helium neon systems [81].

6. Reference to Figure 3-2 indicates that the $3s_2 \rightarrow 3p_1$ $(5s'[1/2]_1^o \rightarrow 4p'[1/2]_0)$ transition is allowed, however, on the basis of transition probability, the laser transition $3s_2 \rightarrow 3p_4$ $(5s'[1/2]_1^o \rightarrow 4p'[3/2]_0)$ is the preferred pathway from the common upper level. Simultaneous observation of several lines originating from the same upper level is rare, as the population of the upper level is reduced by laser action at the stronger transition frequency

[62]. The $3s_2 \rightarrow 3p_4$ transition must therefore be supressed in the laser cavity as noted in the chapter introduction.

7. Depopulation of the lower laser level occurs by spontaneous emission to the lower lying neon states and cascade to the 1s Paschen levels. Lis [62] has monitored the intensity of spontaneous emission at the $3p_1 \rightarrow 1s_2$ neon transition wavelength (352 nm) under $3s_2 \rightarrow 3p_1$ lasing and nonlasing conditions. These results indicate that the $3p_1 \rightarrow 1s_2$ transition does depopulate the $3p_1$ level to an appreciable degree as given by Equation 4a in Figure 3-5.

8. The transition to neon ground state from the 1s Paschen levels is optically disallowed and occurs through collision between neon atoms and the walls of the laser tube. Equations 4a and 4b in Figure 3-5 are bracketed to indicate the possibility of alternate pathways between neon $3p_1$ and ground state.

3.2. Design Considerations

The preceding section considered general helium-neon laser transition pathways with emphasis on systems that have a common $3s_2$ neon upper laser level. This section will examine the control parameters available to the experimenter for output power optimization[8] of a specific laser line. For convenience, these parameters may be subdivided into two categories according to the ease of adjustment after laser resonator design and construction. Easily adjusted parameters in an unsealed variable gas fill system as described below include total gas pressure, gas mixture ratios and discharge current. As noted in Section 3.1.2, both discharge current and pD product have optimum values that are most generally determined experimentally. The main design constraint in system specification for these cases is the capability of the discharge tube

[8] This approach ignores the spectral purity requirements as will be discussed on page 58.

high voltage power supply. High current levels may be required to scan through the current maximum and high voltages to break down the laser gas fill mixture under higher pressure/lower tube diameter constant pD conditions.

General observations of $3s_2$ upper level He-Ne laser output powers indicate that optimum pDs lie between 3.8 x 10^{-3} - 4.7 x 10^{-3} atm mm (2.9 - 4.0 Torr mm) ([59] [87]). Optimum He:Ne mixture ratios vary from approximately 5:1 to 10:1 depending on the tube bore diameter and the strength of the laser transition. Higher helium fractions may be required for the weaker lines in that the upper level in these cases must be more strongly pumped for laser action.

3.2.1. Laser Resonator Specification

The parameters that are more difficult to adjust during experimentation are associated mainly with the dimensions of the laser tube. Additionally, the optical properties of the elements that I) seal and complete the laser resonator system (mirrors, gratings and windows) and II) determine the internal cavity and output coupling losses tend to be fixed. Given the expense and inconvenience of changing the laser optics, the design scheme will be conservative with respect to selection of these elements.

The guidelines for moderate and low gain He-Ne lasers are well known [82] and are most easily outlined with reference to a general schematic diagram of the proposed system (Figure 3-6). This configuration may be considered as a hemispherical type[9] with the resonator optics defined by a semi-transparent mirror (M1) and plane optical element (diffraction grating G1). This grating is

---

[9]The hemispherical configuration consists strictly of a plane mirror and spherical concave mirror separated by a distance equal to the concave mirror radius of curvature. In this work, hemispherical type refers to any stable combination of concave and plane elements.

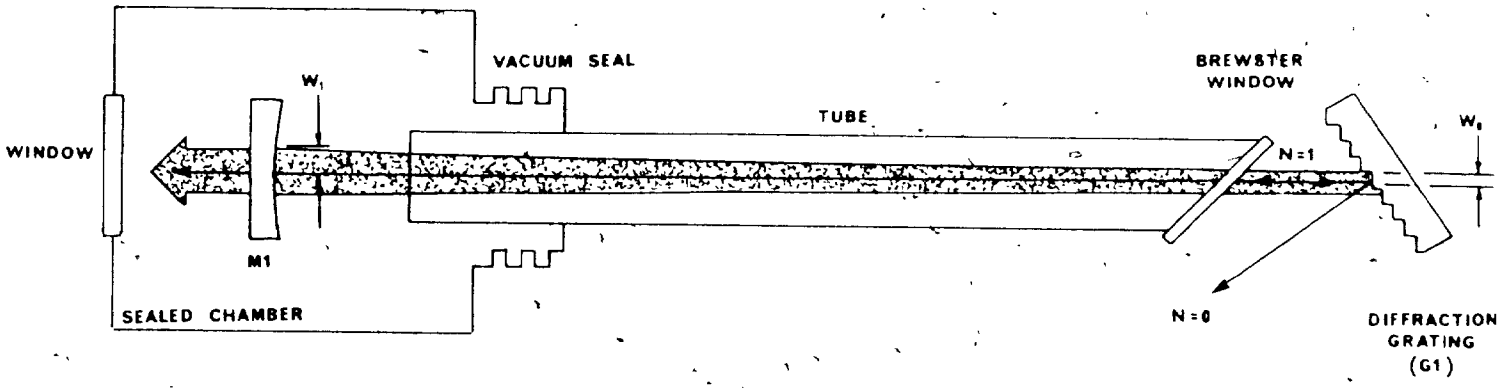

Figure 3-6: Laser Schematic Diagram

in Littrow configuration [83] such that the first order reflection of the selected wavelength is coincident with the incoming radiation path. The laser tube is permanently sealed at one end by a Brewster window that partially polarizes transmitted radiation in the horizontal plane [84]. This polarization plane is properly oriented with respect to the grating blaze direction as shown in Figure 3-6 for maximum first order reflection [85]. The combined effect of the Brewster window and diffraction grating leads to a laser output that is almost exclusively plane polarized in the horizontal direction.

A simple and good approximation of laser cavity wave behaviour may be made with both a geometrical optics approach and wavefront modelling as a gaussian spherical beam. The stability of the beam focussing system is generally analyzed geometrically with reference to the resonator g values as detailed in Appendix C. For resonator types considered here, the $0 \leq g_1 g_2 \leq 1$ criterion for stability is met if the coupling mirror M1 is concave and has a radius of curvature greater than or equal to the laser length (L).

The laser system is designed such that the tube diameter restricts laser operation to the lowest order transverse mode [86]. In this sense, the transverse amplitude variation across the wavefront at any point in the cavity may be described by a gaussian distribution with a minimum spot size[10] or waist, w_0, at the surface of the diffraction grating. An elementary ray diffraction analysis as outlined by Siegman [86] considers the laser cavity electric field pattern of Figure 3-6 as a gaussian plane wave at the beam waist propagating as a gaussian spherical wave to a maximum spot size, w_1, at the output mirror. The

[10]The spot size is defined as the distance from the centre of the beam at which the electric field vector falls to $1/e$ of the centre value.

mathematical equations describing the behaviour of such a system in terms of light intensity may be summerized for a cross-sectionally circular beam as

$$I(r) = I_o \exp(-2r^2 / w^2) \qquad (3-1)$$

where $I(r)$ = light intensity at cross sectional distance r from the beam centre

I_o = light intensity at the beam centre

w = spot size

and

$$w_o = (L\lambda / \pi)^{1/2} (g_1 / (1-g_1))^{1/4} \qquad (3-2)$$

$$w_1 = (L\lambda / \pi)^{1/2} (g_1 (1-g_1))^{-1/4} \qquad (3-3)$$

where g_1 = g parameter of M1

This formulation assumes that the diameters of M1 and G1 are far larger than w_1 and w_o respectively. The g parameter of the diffraction grating has also been assigned as unity (Appendix C).

The relevant characteristics of neutral gas lasers in terms of resonator dimensions are [82]

1. the gain is proportional to the laser length and the inverse of bore diameter

2. the output power is proportional to the gain-volume product and varies as $(\text{length})^{3/2}$.

Based on high gain and power output considerations alone these guidelines indicate that the bore diameter should be as small as possible for a long active lasing length. The spot sizes w_o and w_1 should also be close in value such that a high percentage of the discharge volume is occupied by the laser cavity pattern.

Of special importance is the requirement that the laser medium open loop gain be higher than the cavity losses for CW laser operation to be successful[11]. Firstly, cavity losses should be reduced by careful Brewster window orientation, clean optics and low coupling fractions. Secondly, power loss from the gaussian wings occurs as the beam propagates down a finite diameter tube. As an estimate of this power loss, the beam may be considered as passing through a circular aperture of radius a_r, such that with reference to Equation (3-1)

$$\frac{I(a)}{I_o} = 1 - \exp(-2a_r^2/w^2) \qquad (3-4)$$

The tube diameter selection is complicated by the practicality of finding a source of straight quartz or Pyrex tubing with the required high length to diameter ratio. In the author's experience, this task is virtually impossible and the alternate route taken is the selection of bent tubing that may be straightened during alignment by means of periodically spaced adjustable supports. This approach requires adequate tube flexibility to permit minor alignment adjustments without breaking the glass yet sufficient rigidity to

---

[11] This point is discussed on page 56.

minimize sagging between the support points. A large diameter thin walled tube suits these requirements and a design compromise with more efficient small bore diameters must be made. The final design selection is a medium wall Pyrex tube with an inside diameter of 8.8 mm. The tube is constructed with one open end and sealed to the laser gas supply system through a vacuum lock as shown in Figure 3-6. This is a precautionary arrangement such that, if higher system gain is necessary, smaller diameter inserts may be slid down the inside of the tube without major disruption.

To approximate beam losses to the laser tube walls, Equation (3-4) may be solved for different spot sizes passing through a 4.4 mm radius aperture. Figure 3-7 graphs this relationship and notes that appreciable power loss occurs only after the spot size exceeds 2.25 mm. The graph falls off rapidly above this point and, hence, 2.5 mm was selected as a conservative spot size upper bound for acceptable tube wall losses. To maximize the active volume of the laser discharge, the spot size should be in the range of 2.25 to 2.50 mm at all points along the tube axis.

The beam waist radius, w_o, and maximum beam radius, w_l, as defined by Equations (3-2) and (3-1) respectively are shown as functions of mirror radius for constant values of resonator length[12] in Figure 3-8. These curves may be used to maximize allowable laser tube length in terms of mirror radius given the above restrictions on spot sizes as follows

1. A four sided figure bounded by beam waist radii of 2.25 and 2.5 mm is defined in Figure 3-8(a) (ABCD).

---

[12] It may seem more natural to plot lines of constant mirror radius and continuously vary mirror separation distance. Unfortunately, the trough or foldback noted in Figure 3-8 makes interpretation less clear when this projection is shown.

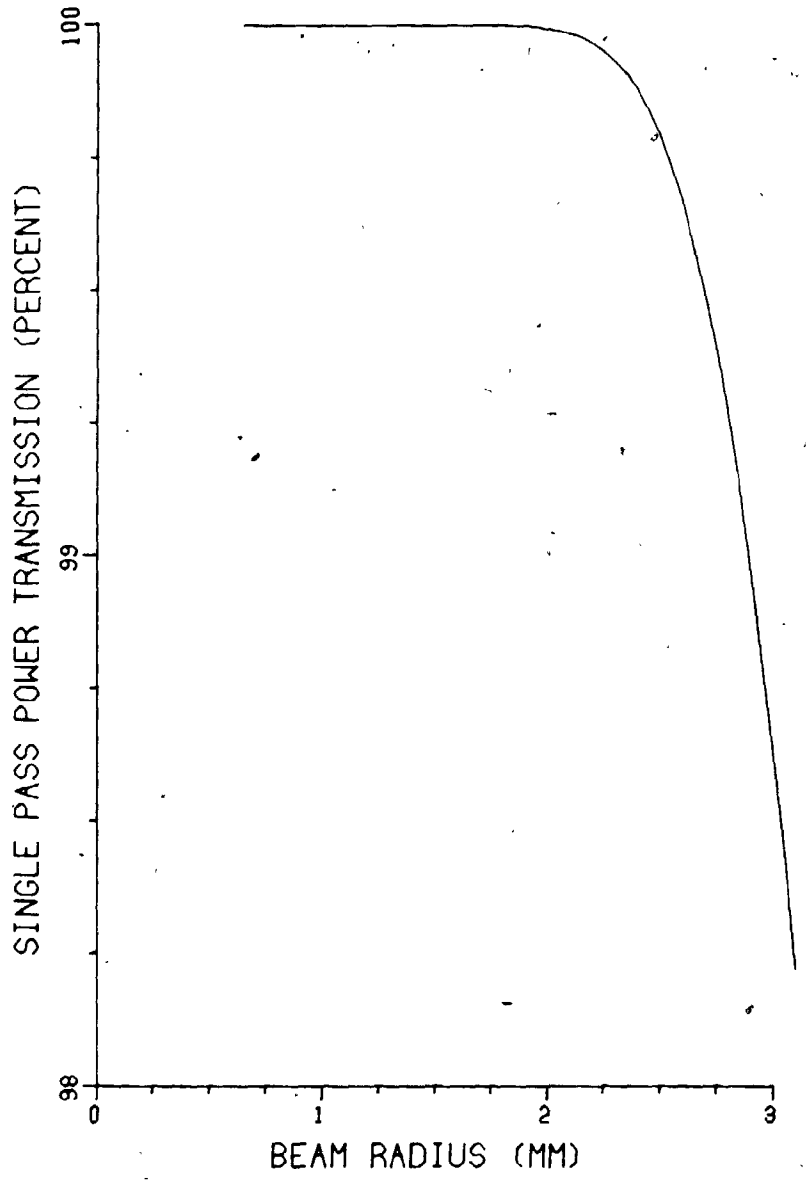

Figure 3-7: Power Transmission Through an 8.8 mm Aperture

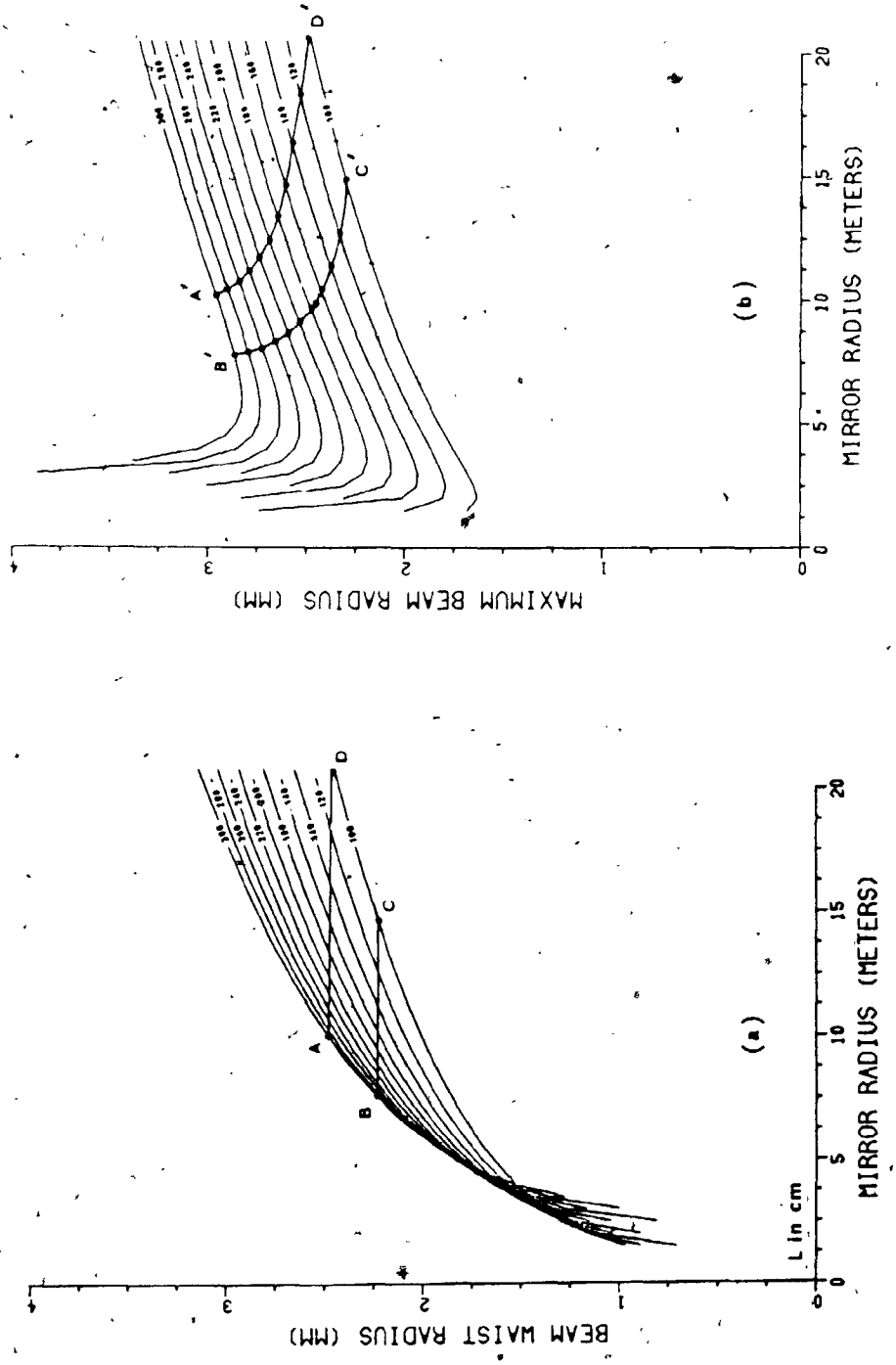

Figure 3-8: Spot Size Determination

2. A point by point mapping of mirror radii values for constant resonator lengths is made from Figure 3-8(a) to Figure 3-8(b) (A'B'C'D').

3. The area within A'B'C'D' bounded by lines at w_1 equals 2.25 and 2.5 mm respectively defines the mirror radius-resonator length combinations that correspond to allowed values for both spot sizes.

4. The maximum laser tube length is selected from the bounded area and corresponding mirror radius value noted.

The selected values using this technique from Figure 3-8 correspond to a mirror separation distance of 180 cm and M1 radius of 10 m. The spot sizes w_o and w_1 are 2.27 and 2.5 mm respectively in this configuration. These values will be used for resonator design as outlined in Chapter 4.

3.2.2. Output Coupling

Calculation of the optimum output coupling fraction requires knowledge of the dominant laser gain curve broadening mechanisms of the specific system. For the expected optimum pD range as noted on page 46, this gain curve is inhomogeneously broadened [90] with a contour that may be described by a Doppler broadened bandshape factor f_d (Equation (2-7) page 12). This broadening mechanism leads to the well known hole burning effect in the laser gain curve with hole positions determined by the axial modes of the laser cavity[13]. Ultimately, laser operation is restricted to axial mode frequencies[14] that are spaced discretely at intervals of Δf and governed by the cavity

[13] This effect is discussed in standard textbooks on laser physics ([63]-[65]).

[14] For the sake of brevity, it is assumed that frequency shifting of the axial modes by the laser transition is small and may be regarded as inconsequential for the present purposes [88].

length, L, such that[15]

$$\Delta f = \frac{c}{2 n_o L} \tag{3-5}$$

where n_o : refractive index of the medium

c : speed of light

As noted previously, an additional requirement is that the open loop laser gain be large enough to overcome losses at a specific axial mode frequency for steady state lasing to occur at this frequency. The output spectrum of an inhomogeneously broadened laser will be examined briefly in Section 3.2.3.

Increasing the coupling fraction, T_c, from the laser has competing effects on the actual observed output power. Output power will tend to increase with higher transmission through the laser end mirror, however, this action removes a number of photons contributing to laser amplification and decreases the available power to be coupled out [89]. A solution for optimum T_c in the inhomogeneously broadened case has been proposed by Rigrod [91] with certain simplifying assumptions in the multifrequency case and has been shown to hold well for experiments with He-Ne lasers operating at the 1.15 μm transition. Explicit solution of these relationships requires knowledge of the unsaturated laser gain coefficient and saturation parameter; parameters that are generally determined experimentally by feeding radiation from a laser already working at the desired wavelength into a laser amplifier of the same type. For this

---

[15] Briefly stated, the axial mode frequencies satisfy the closed loop zero phase shift requirement for stable oscillation.

reason, initial design values for T_c are somewhat speculative given that the gain coefficient for the He-Ne $3s_2 \rightarrow 3p_4$ transition has not been reported. It is worthwhile, however, to examine the nature of inhomogeneously broadened laser operation and note the sensitivity of output power on total cavity losses. For convenience, the laser gain curves referred to in the following discussion are assumed to be exclusively inhomogeneously broadened.

In the presense of a radiation field intensity, $w(\nu)$, the saturated laser gain coefficient per unit length at frequency ν within the gain curve is generally expressed[18] as [91]

$$G_s(\nu) = G_o(\nu)\,(1 + w/w_o)^{-1/2} \qquad (3\text{-}6)$$

where $G_o(\nu)$: unsaturated gain coefficient at frequency ν

$G_s(\nu)$: saturated gain coefficient at frequency ν

$w_o(\nu)$: saturation parameter

(the cavity radiation intensity for $G_s = G_o/\sqrt{2}$)

The net gain coefficient as radiation flux is directed through an amplifying medium without optical feedback is given simply as the difference between saturated gain and cavity losses. During steady state laser operation, feedback at the axial mode frequencies burns holes in the gain curve such that the net gain coefficients at the hole frequencies exactly balance the cavity losses. As cavity losses are reduced, the number of atoms in the vicinity of the hole

---

[18] Gain saturation occurs at the probe frequency ν as the width of the holes in the gain curve approach the Doppler width of the laser transition

centre frequency with sufficient gain to oscillate also increases and available power in the laser cavity rises considerably. This power rise continues with decreasing cavity loss until the hole widths begin to overlap or exceed the Doppler width. These observations indicate in a qualitative sense the importance of low cavity loss and small coupling fractions for inhomogeneously broadened lasers.

Reference to Figure 3-6 on page 47 illustrates that cavity losses occur for this specific system at the Brewster window interface, by M1 surface absorption and tube-wall beam truncation and through zeroeth order reflection from the diffraction grating. Minimum cavity loss is achieved by making M1 fully reflecting and defining the output beam as the radiation coupled out of the cavity in the zeroeth order reflection. This approach suffers most notably in that the beam detection optics must be continuously realigned as the diffraction grating is rotated to scan through different laser lines. This is particularly awkward if superradiant lines at 3.39 μm (He-Ne) or 3.51 μm (He-Xe [92]) are used to roughly align the resonator and mirror M1 prior to attempted lasing at the much weaker He-Ne 4.2 μm wavelength. Coupling out in this fashion was reserved as a more desperate approach to be used only if laser action could not be observed with a very small transmission fraction through M1.

The initial design transmissivity of M1 was conservatively selected to be less than 1 per cent. This value was chosen on the basis of observed transmission of about 2 per cent for commercial high gain 3.39 μm He-Ne lasers such as the Spectra Physics Model 120.

3.2.3. Expected Output Characteristics

For a resonator length of 180 cm, the axial mode frequencies are separated by 83 MHz if the refractive index of the medium is approximated as unity (Equation (3-5). The Doppler full width at half maximum of the laser gain curve as calculated by Equation (2-7) has a value[17] of about 225 MHz and, hence, this laser could oscillate simultaneously at several axial mode frequencies. For the purposes of this work, it will be noted simply that i) the laser output frequency is located within the Doppler width of the gain curve, and ii) if the output is multimode, it will be assumed that the carbon dioxide extinction coefficient does not differ appreciably between axial mode frequencies.

The output beam diameter and angular divergence determine the minimum required aperture size of the optical elements in the spectrometer. If it is assumed that the beam geometry is diffraction limited, the beam divergence half angle, α_d is given by [1]

$$\alpha_d = \frac{1.22\lambda}{D_o} \tag{3-7}$$

where D_o : output beam diameter ($2w_1$)

and the beam diameter at distance z from the output of the laser, $D(z)$, is [1]

---

[17] The discharge temperature is assigned as 400 °K in this calculation in keeping with typically observed values for He-Ne lasers [93].

$$D(z) = D_o + 2L\tan(\alpha_d) \qquad (3-8)$$

The calculated beam divergence solid half angle is 1 mrad for this system. Equation (3-8) is used as a design guideline to approximate the maximum optical pathlength in the dual beam spectrometer. Details of the spectrometer design and construction are presented in Chapter 5.

3.3. Summary

The initial design parameters and expected output characteristics of the low gain He-Ne $3s_2 \rightarrow 3p_1$ laser discussed in this chapter may be summarized as

1. Material : Quartz or Pyrex cylindrical tubing
2. Resonator Dimensions : 180 cm in length with an 8.8 mm inside bore diameter
3. Resonator Optics : Semitransparent spherical concave coupling mirror (10 m radius, < 1 % transmission) and echellette diffraction grating in Littrow configuration
4. Pumping Technique : Electron excitation
5. Expected Optimum Discharge Current : 50 - 100 mA DC
6. Expected Optimum Total Gas Pressure : 4.3×10^{-4} - 6.0×10^{-4} atm, (330 - 450 mTorr)
7. Expected Optimum Gas Mixture Ratio : He:Ne at 5:1 to 10:1
8. Output Characteristics : TEM_{oo} multimode operating within a 225 MHz bandwidth

granite[1] surfaces is the selection of metal channel beams as shown in Figure 4-2. Aluminum is chosen for this application on the basis of cost, availability and machining ease. The beams form a 226 cm by 56.5 cm surface that is held in place by three steel bars. Six adjustable legs level the entire table. A 221 cm by 25.5 cm area and 56.5 cm by 45.4 cm area on the tabletop are reserved for the laser resonator and spectrometer respectively as shown in Figure 4-2.

4.1.3. Laser Tube

The laser tube was fabricated by Laurie Harnick of the University of Western Ontario glassblowing shop and is shown in finished form in Figure 4-3. The discharge and gas fill region is defined by an 8.8 mm inside diameter pyrex tube, 170 cm long and cut at one end to Brewster's angle (54.5°) for calcium fluoride (CaF_2) at 4.2 μm. Calcium fluoride is chosen as the window material on the basis of expense, durability and high transmissivity at 4.2 μm. The optical properties of CaF_2 and Brewster angle calculations are included in Appendix E. The window is attached to the tube with flexible epoxy (Techkits, New Jersey [94]). An advantage of this design is that the exact orientation of the Brewster cut plane is not critical as with tubes having both ends sealed in this fashion.

The cathode is formed by a hollowed aluminum rod (15 cm long; 23 mm o.d., 19 mm i.d.) closed at one end and sandblasted to roughen the surface [95]. It lies freely at the bottom of a 25 mm diameter sidearm tube and is riveted to a nickel strap to provide an electrical connection with a tungsten electrode (10

---

[1] During the initial stages of this work, the author contacted several monument makers who will supply custom slabs of polished granite at prices considerably lower than those of scientific companies. Unfortunately, transportation arrangements for very large items of this sort can be very difficult.

Chapter Four
Laser Construction and Test Details

The complete laser system requires a gas mixing and intake manifold, vacuum system, optical bench, resonator support structure, laser tube, power supply and an optical detection unit. With the exception of the power supply, these components were designed and fabricated by the author with facilities available at the University of Western Ontario. The first half of this chapter outlines the design details of these individual component systems.

4.1. Construction Details

4.1.1. Gas Intake Manifold and Vacuum System

This system was designed to provide both controlled flow and sealed laser tube conditions to a minimum total pressure limit of 1×10^{-4} atm (76 mTorr). A rotary pump (Welsh Scientific Duo Seal) has sufficient capability to meet these requirements.

A schematic diagram of the general system layout is shown in Figure 4-1. Two liquid nitrogen cold traps are included as a precautionary measure; CT1 to freeze impurities such as water vapour from the intake gases and CT2 to prevent oil leakage into the system in the event of pump failure. The vacuum and gas inlet lines are predominantly copper tubing and aluminum Edwards Speedivac O-ring junction connectors. These materials provide an adequate vacuum seal for the required pressure range. A heat gun was used to outgas the system after installation.

A large volume (2 liter) mixing chamber is installed between the gas intake

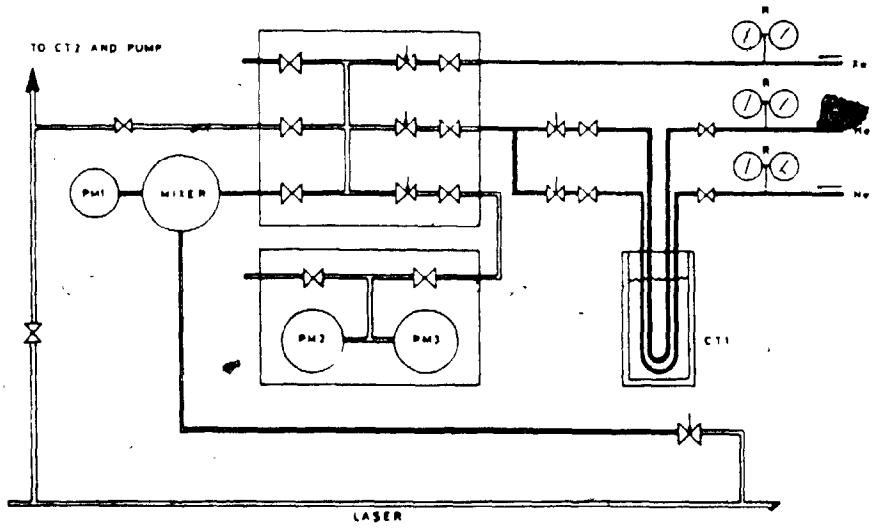

Figure 4-1: Gas Intake Manifold and Vacuum System

and laser tube to allow for premixing a fixed ratio of helium-neon gas. The total pressure dependence of laser output power may then be examined by leaking a specific gas combination from the chamber to the laser tube. A needle valve between the chamber and tube is included such that similar fixed ratio measurements may be made for flowing conditions.

Gas mixing in this arrangement is turbulent as the higher pressure gas fraction (helium) is added to the low pressure neon in the chamber. Propeller agitation will provide a more uniform gas mixture than this technique, however, coupling the propeller shaft to a driving motor through the chamber wall while maintaining a vacuum seal can be difficult. Fear of atmospheric poisoning of the laser fill gas was the overriding factor in the selection of mixing chamber type.

The chamber and laser tube pressures are directly monitored by a 0-10 Torr capacitance manometer (PM1 - MKS Baratron 222B). Two additional pressure gauges (PM2 and PM3 - Wallace and Tiernan 0.1-20 Torr and 0-800 Torr ranges respectively) serve the dual purpose of extending the range of PM1 and measuring the pressure of the intake lines when the mixing chamber is isolated from the system.

Overnight leak testing of the completed system established a leak rate of approximately 200 mTorr per hour from initial pressures of 100 mTorr.

4.1.2. Optical Bench

The main requirements of the optical bench are to provide a level working surface to support the laser resonator framework and to isolate the laser from low frequency room vibrations. A compromise, with prohibitively expensive

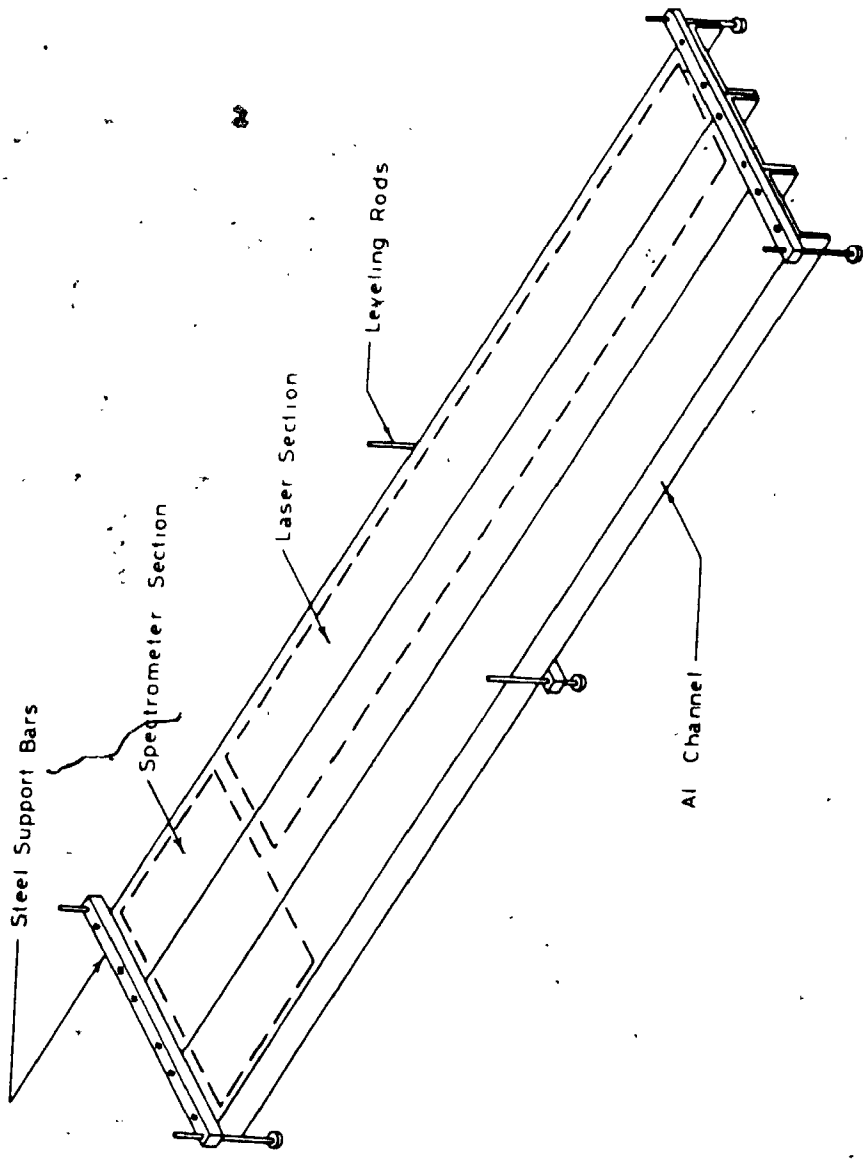

Figure 4-2: Optical Bench

granite[1] surfaces is the selection of metal channel beams as shown in Figure 4-2. Aluminum is chosen for this application on the basis of cost, availability and machining ease. The beams form a 226 cm by 56.5 cm surface that is held in place by three steel bars. Six adjustable legs level the entire table. A 221 cm by 25.5 cm area and 56.5 cm by 45.4 cm area on the tabletop are reserved for the laser resonator and spectrometer respectively as shown in Figure 4-2.

4.1.3. Laser Tube

The laser tube was fabricated by Laurie Harnick of the University of Western Ontario glassblowing shop and is shown in finished form in Figure 4-3. The discharge and gas fill region is defined by an 8.8 mm inside diameter pyrex tube, 170 cm long and cut at one end to Brewster's angle (54.5°) for calcium fluoride (CaF_2) at 4.2 μm. Calcium fluoride is chosen as the window material on the basis of expense, durability and high transmissivity at 4.2 μm. The optical properties of CaF_2 and Brewster angle calculations are included in Appendix E. The window is attached to the tube with flexible epoxy (Techkits, New Jersey [94]). An advantage of this design is that the exact orientation of the Brewster cut plane is not critical as with tubes having both ends sealed in this fashion.

The cathode is formed by a hollowed aluminum rod (15 cm long, 23 mm o.d., 19 mm i.d.) closed at one end and sandblasted to roughen the surface [95]. It lies freely at the bottom of a 25 mm diameter sidearm tube and is riveted to a nickel strap to provide an electrical connection with a tungsten electrode (10

---

[1] During the initial stages of this work, the author contacted several monument makers who will supply custom slabs of polished granite at prices considerably lower than those of scientific companies. Unfortunately, transportation arrangements for very large items of this sort can be very difficult.

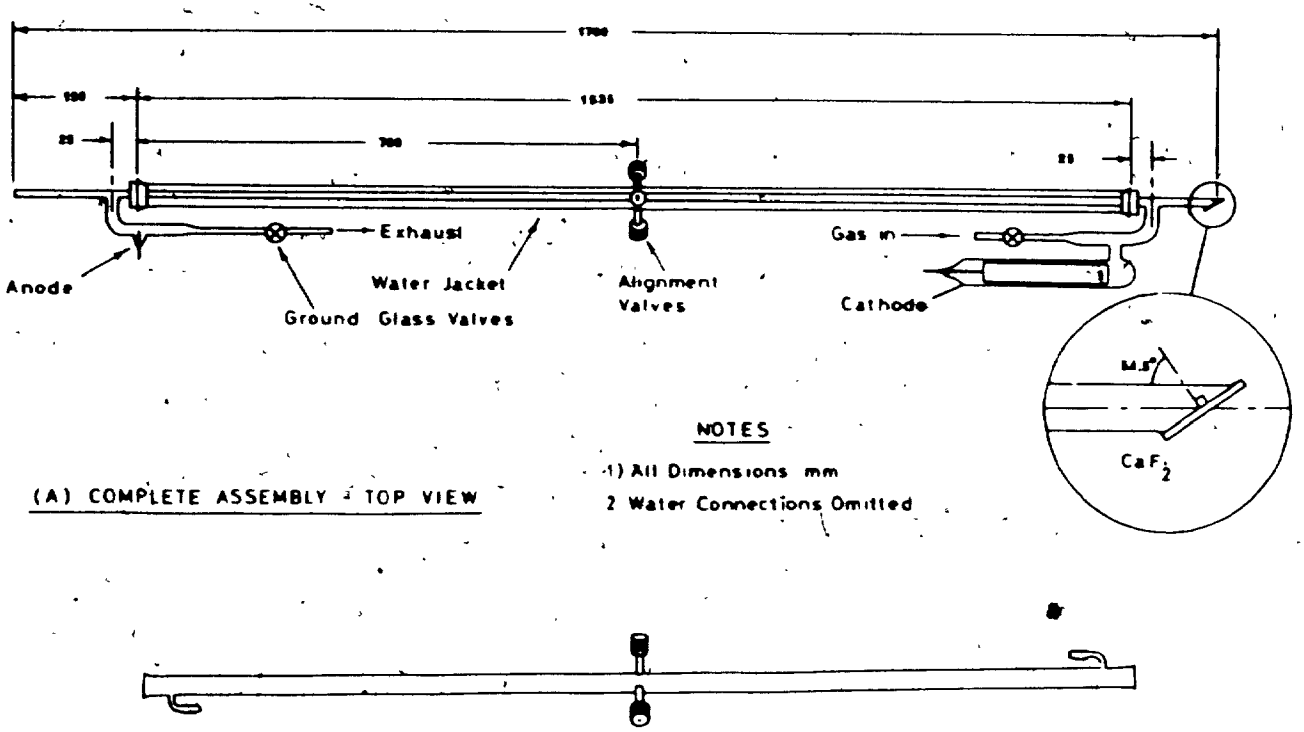

Figure 4-3: Laser Tube

cm long, 2 mm diameter). The electrode is anchored to the end of the sidearm tube by a graded glass seal. The cathode and gas inlet port are attached to the sealed end of the laser as shown in Figure 4-3. The gas exhaust and anode sidearm completes the electrical and gas flow circuits. The anode is identical to the cathode tungsten feed-through post except in length (5 cm). Two ground glass valves (Eck and Krebs Co.) allow the tube to be isolated from the intake manifold and vacuum system.

Prior to attachment of the anode sidearm, the water jacket is installed loosely over the laser tube. On completion of the glassblowing, two one hole stoppers are cut through one side and slipped over the central tube. A water seal is formed by bonding the stoppers with epoxy to both the jacket and laser tube.

Three teflon needle valves support the tube at midpoint. This arrangement allows for tube alignment and yet maintains a waterproof seal.

4.1.4. Laser Resonator Support Framework

The laser resonator support system should provide a rigid framework to protect the tube and minimize changes in cavity length with temperature to stabilize the axial mode frequencies as defined by Equation (3-5). In this section, individual components of the framework are described with reference to isometric drawings: detailed orthographic projections are available from the author on request.

The main support system is formed by four rod supports and three invar rods (220 cm long, 15.8 mm dia) as shown in Figure 4-4. Invar is used to

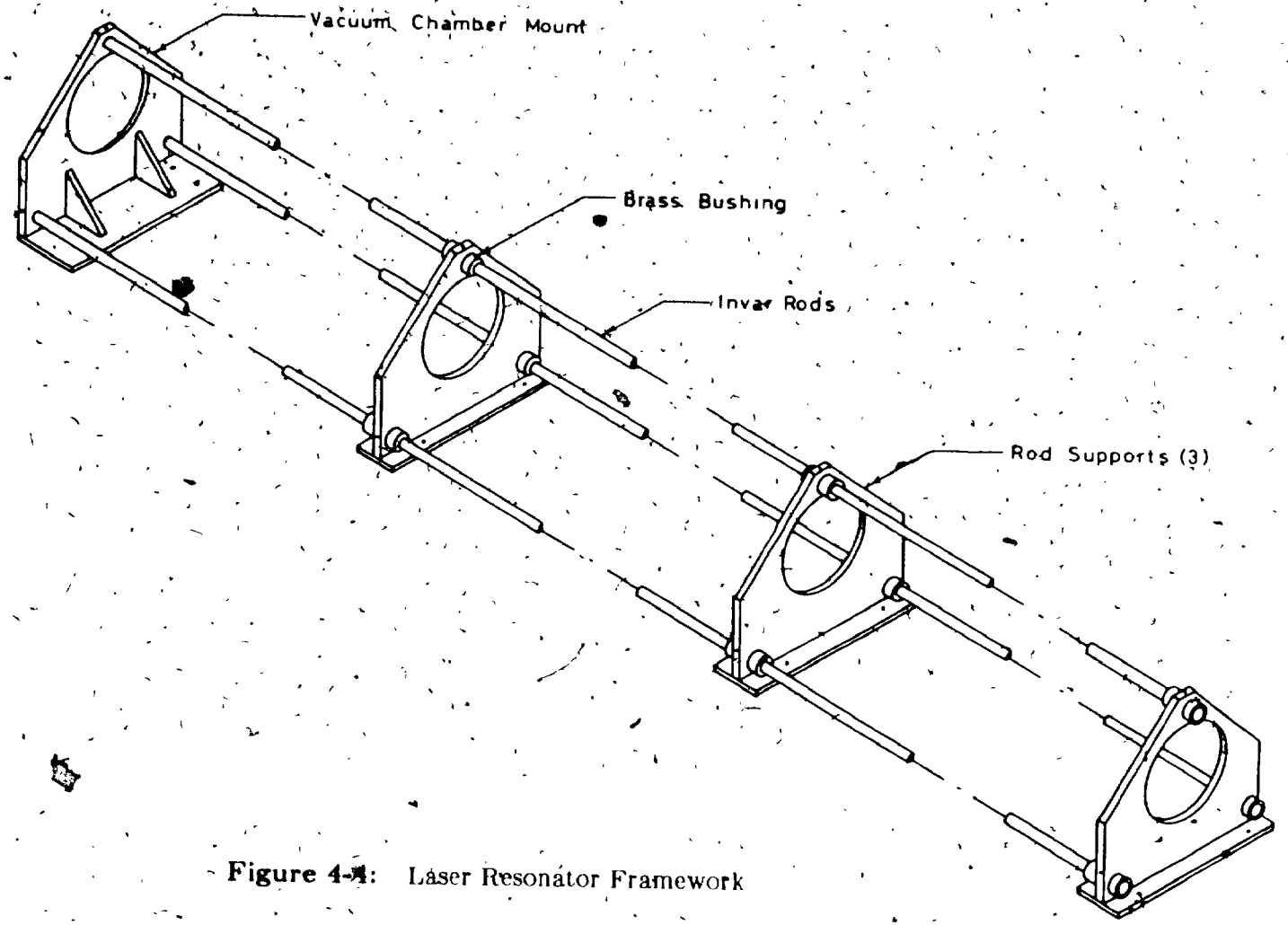

Figure 4-4: Laser Resonator Framework

establish a low thermal expansion coefficient for the network[2]. If the thermal properties of the invar are to be exploited fully, the rods must be allowed to expand and contract independently of the aluminum optical bench. This may be accomplished in the following manner. The rod supports are equally spaced and fastened with machine screws to the optical bench to define the laser area marked in Figure 4-2. Three of the rod support plates are drilled at the rod positions and fitted with brass bushings. The bushings are locked to the plates with set screws and reamed to produce a sliding fit with the invar rods. The rods are then pushed through the bushings and secured to the vacuum chamber mount. Components mounted directly on the rods are now referenced in distance to the vacuum chamber mount face by the invar alone.

The open end of the laser tube is connected to the gas fill system by the output coupler and tube support shown in cross section by Figure 4-5. The seal between the tube and vacuum chamber is made by two spaced O-rings that are compressed by a threaded vacuum lock nut. The tube end is aligned by three positioning screws located around the outside of a circular mirror mount support. A rear gimbal serves to keep the laser tube coaxial with the rear section of the vacuum chamber. This feature relieves stress at the tube-chamber junction and maintains the quality of the O-ring seal when the opposite end of the tube is moved during alignment. A brass bellows decouples motion of the rear section from the front gimbal.

The vacuum chamber is designed to accomodate circular mirrors of 25.4

---

[2] The thermal expansion coefficient for invar (3.6×10^{-7} cm/cm/°C) is about two times better than that of quartz ($.49 \times 10^{-7}$ cm/cm/°C) and seventy times better than that of aluminum (240×10^{-7} cm/cm/°C). For the 220 cm invar lengths considered here, the total length of invar shows a temperature dependence of 0.8 μm/°C.

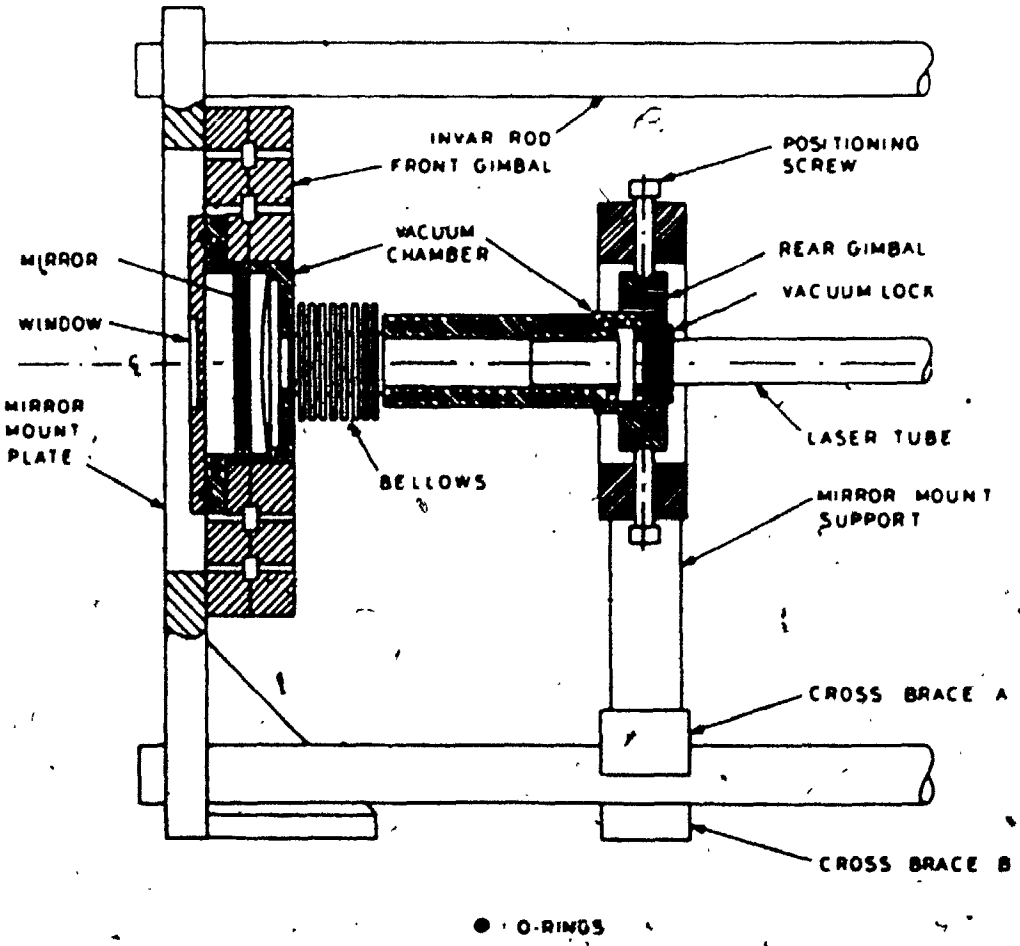

Figure 4-5: Output Coupler and Tube Support

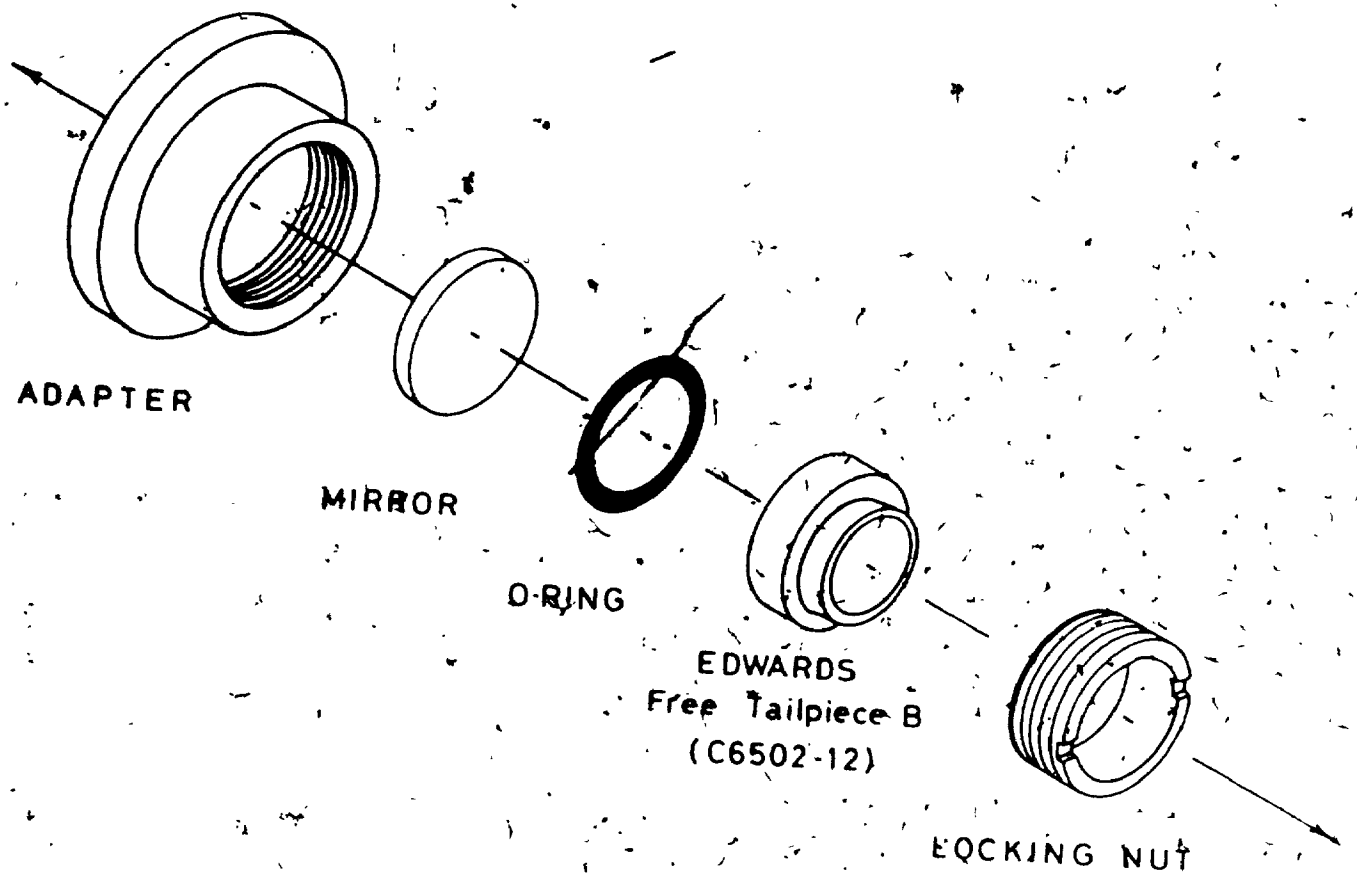

Figure 4-6: Output Mirror Adapter

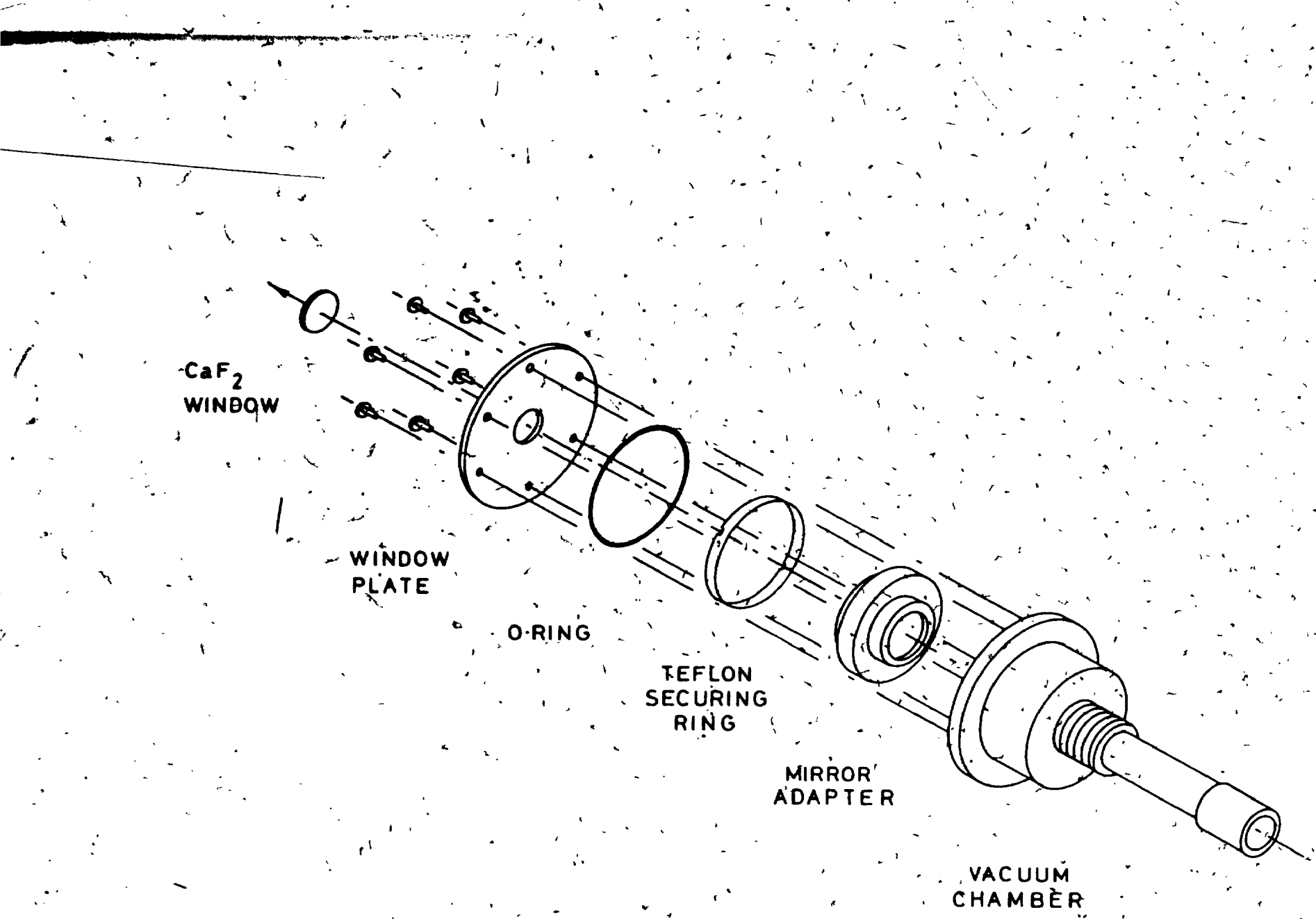

Figure 4-7: Mirror Seating Geometry

mm (1 inch) and 50.8 mm (2 inch) in diameter. The smaller diameter mirrors are increased in diameter to match the larger ones by the output mirror adapter as shown in Figure 4-6. This adapter also allows for convenient handling of the output mirror outside the chamber mount without fear of fingerprint contamination. The mirror or mirror adapter is seated in the vacuum chamber and secured with a threaded teflon ring (Figure 4-7). The chamber is sealed by an O-ring and window plate. The laser output beam passes through a calcium fluoride window (50 mm diameter, 3 mm thick) epoxied to the centre hole of the window plate.

The vacuum chamber is mounted directly to a large front gimbal. This gimbal provides mirror tilt and rotation functions by micrometer adjustment[3]. The system is completed by mounting this entire assembly to the mirror mount plate as shown in Figure 4-5.

The Brewster angle end of the laser tube is secured by a teflon clamp and positioned horizontally and vertically by an X-Y translator mount. Additional support for the cathode sidearm is provided by a teflon Y brace mounted to the invar rods.

The diffraction grating is held by a rotary mount (Lansing AOD 10.203) and secured to a large turntable and base arrangement as shown in Figure 4-8. The base plate is bolted to horizontal crossbracing in the laser resonator framework. The distance between the grating face and the laser tube Brewster window should be as short as possible to minimize the effects of atmospheric carbon dioxide absorption in the resonator. A minimum distance of 5 cm is possible with this mounting hardware.

---

[3]The micrometers have been omitted from Figure 4-5 for clarity.

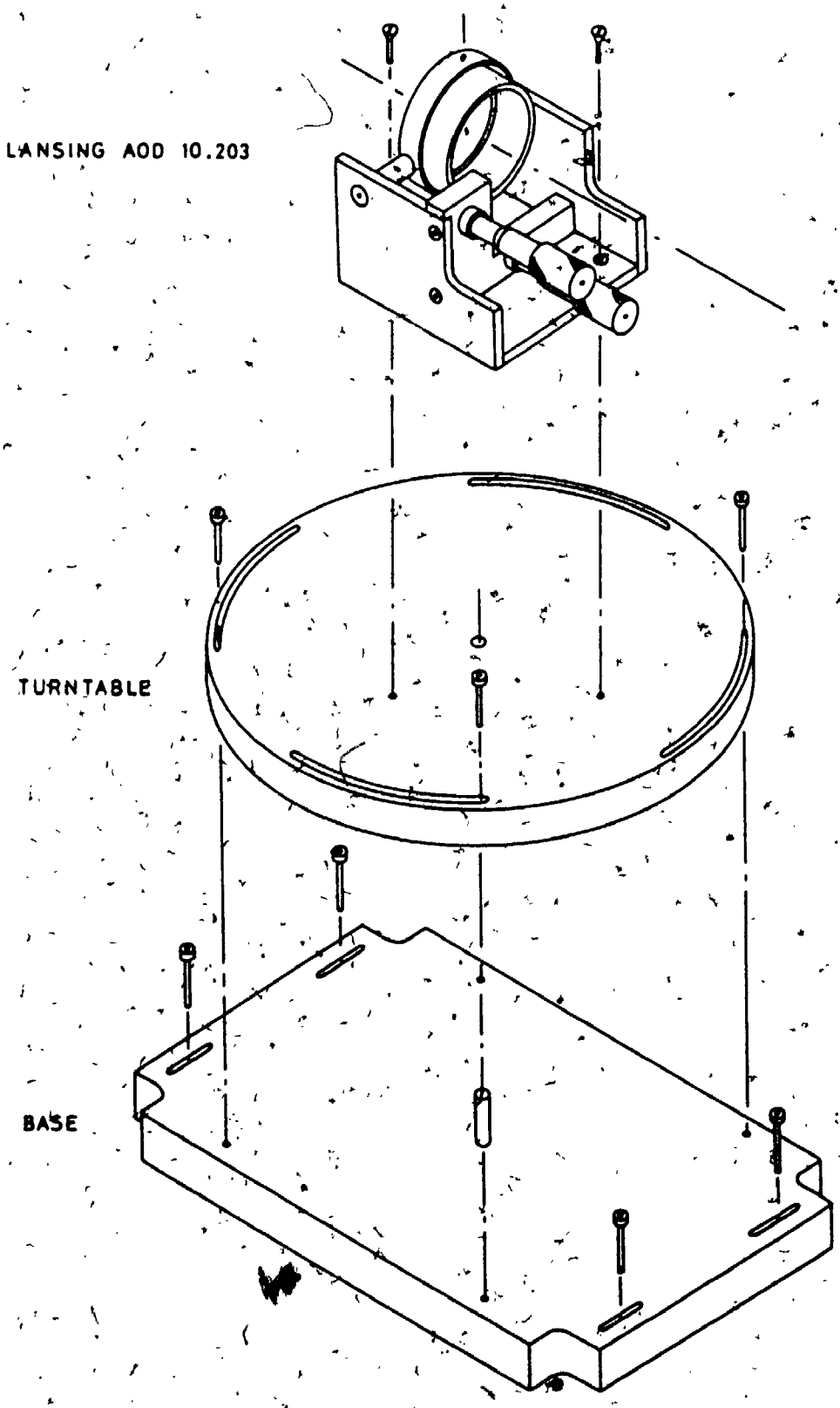

Figure 4-8: Diffraction Grating Mount

4.1.5. Power Supply

In the interest of safety, the optical bench and laser support framework are electrically grounded to the laboratory water supply system. In this design, it is important to note that the laser tube anode is connected directly by the laser fill gas to the support framework. The anode should therefore be grounded to prevent a discharge path between this electrode and the vacuum chamber. The cathode must then be maintained at a negative voltage to establish proper polarity for the tube.

A power supply on loan from the University of Western Ontario Department of Physics (Sorenson and Co. Model 1012-50, maximum rating -12kV and 50 mA) is used in series with a resistor (150 kΩ, 200 W) to power the laser tube. This power supply is unlikely to have the current capability to find the optimum current levels as noted on page 44, however, at 50 mA the laser output power should be close to maximum for a specific gas mixture. It was considered unnecessary to incure the additional expense of upgrading the supply for this application.

4.1.6. Laser Optics

Several output coupling mirrors were tested in the laser resonator. All mirror surfaces were prepared by low temperature gold deposition (Edwards Model E12E3 Vacuum Coating Unit). The transmission fractions were established by relative intensity measurements at 3.39 μm with a commercial He-Ne Spectra Physics Model 120 radiation source. It is assumed in this approach that the optical properties of the substrate materials and gold do not differ appreciably between 3.39 μm and 4.2 μm (Appendix E).

All coupling mirrors are spherical concave types with 10 meter radii of curvature. Three mirrors that were tested with varying degrees of success may be listed as

1. a 50.8 mm (2 inch) diameter circular copper substrate with a fully reflective gold surface layer. Output coupling in this case is through a central 0.5 mm diameter pinhole. The main advantage of this approach is the insensitivity of the coupling fraction to laser output wavelength[4]. The coupling hole should be shifted slightly off the laser tube centreline for laser operation in the TEM_{oo} mode[5].

2. a 25.4 mm (1 inch) diameter planoconcave zinc selenide (ZnSe) substrate deposited with gold to be partially transmitting (1%). This material transmits well at 4.2 μm (70% - Appendix E) but is difficult to clean prior to redeposition and does not adhere well to gold.

3. a 25.4 mm (1 inch) planoconcave germanium (Ge) partially transmitting (0.5 %) gold coated substrate. Uncoated Ge is only about 50% transmitting at 4.2 μm (Appendix E), however, the mirror surface is easy to prepare and wears well.

The diffraction grating (Bausch and Lomb 35-63-05-860) is a 50.8 mm (2 inch) diameter disc that will mount directly in the Lansing AOD 10.203 mount described in Section 4.1.4. The grating is an echellette type with 210 grooves/mm and 26° 45′ blaze angle.

---

[4]The small diameter of the output beam for this system leads to large divergence angles (Equation 3-7) and to potential beam handling problems. A beam expander [1] located at the output of the laser may be required to reduce beam divergence.

[5]The laser preferentially oscillates in the lowest loss transverse modes. Coupling the power from the centre of the beam reduces the TEM_{oo} intensity in the resonator but will not affect some of the higher order transverse modes. Shifting the coupling hole to the wing of the TEM_{oo} mode corrects this problem.

A 10 meter radius of curvature fully reflective spherical concave mirror is used in place of the diffraction grating for preliminary alignment of the coupling mirror and laser tube.

4.2. Laser Test Results

Laser beam intensity measurements are made by first amplitude modulating the beam (100%) with a tuning fork chopper (Bulova ONT-L8C, 200 Hz) and subsequently detecting the chopped radiation with a lead selenide (PbSe) photoconductor and AC coupled preamplifier (100x). A phase lock amplifier (Keithley Autoloc 840) converts the detector preamplifier output voltage to a DC signal that is proportional to laser output intensity. Details pertaining to the detector mounting system and preamplifier design may be found in previous work by the author [99].

The phase lock amplifier output may be recorded directly with a chart recorder (Watanabe Servocorder 652) to examine the time behaviour and output amplitude stability for specific gas mixtures in the resonator. A power supply constructed for the mixing chamber pressure gauge (PM1 - Figure 4-1) is also equipped with an output monitor port to provide a DC voltage signal that is directly proportional to total chamber pressure. This voltage is used as the X input to an X-Y recorder (Hewlett - Packard Moseley 7005B) such that laser output intensity - total pressure graphs may be recorded directly. All experimental details and instrument settings for the tests are found in Appendix F.

Laser action at 3.39 μm (He-Ne) and 3.51 μm (He-Xe) is observed for all coupling mirror and grating - fully reflective mirror combinations. With proper resonator and optical element alignment, the laser output power at these

wavelengths is sufficiently strong to saturate the detector preamplifier at 50 mA discharge current levels. These lines are used simply to align the resonator prior to attempted lasing at 4.2 μm: the observation of both lines has been fully documented ([59], [87], [92]) and further characterization is considered unnecessary.

Lasing at the 4.2 μm He-Ne transition is observed only with the combination of the germanium substrate output coupling mirror and diffraction grating. General observations of the Laser behaviour may be summarized as follows.

1. Under sealed conditions, the output power rises slowly with time to a maximum at approximately twenty minutes after initiation. Output power decreases as the fill gas becomes contaminated by atmospheric gases leaking through the O-Ring seal at the open end of the tube (Figure 4-5). The maximum sealed run time before failure due to atmospheric poisoning is one hour.

2. Higher output powers are achieved by converting from sealed operation to a continuous flow condition. Calibration for continuous flow measurements is done by premixing the desired He-Ne gas ratio in the mixing chamber, filling the laser tube from the chamber to pressures higher than required ($\sim$ 10 Torr) and slowly pumping the laser tube to lower pressures through the mixing chamber. At low evacuation rates, it is assumed that pressures of the tube and vacuum chamber are approximately equal.

3. Under all experimental conditions, the laser output power increases with discharge current. The current limitations of the power supply (50 mA) do not allow for investigation of the current optimum predicted in Section 3.1.2.

4. The laser tube must be water cooled for successful laser operation at 4.2 μm.

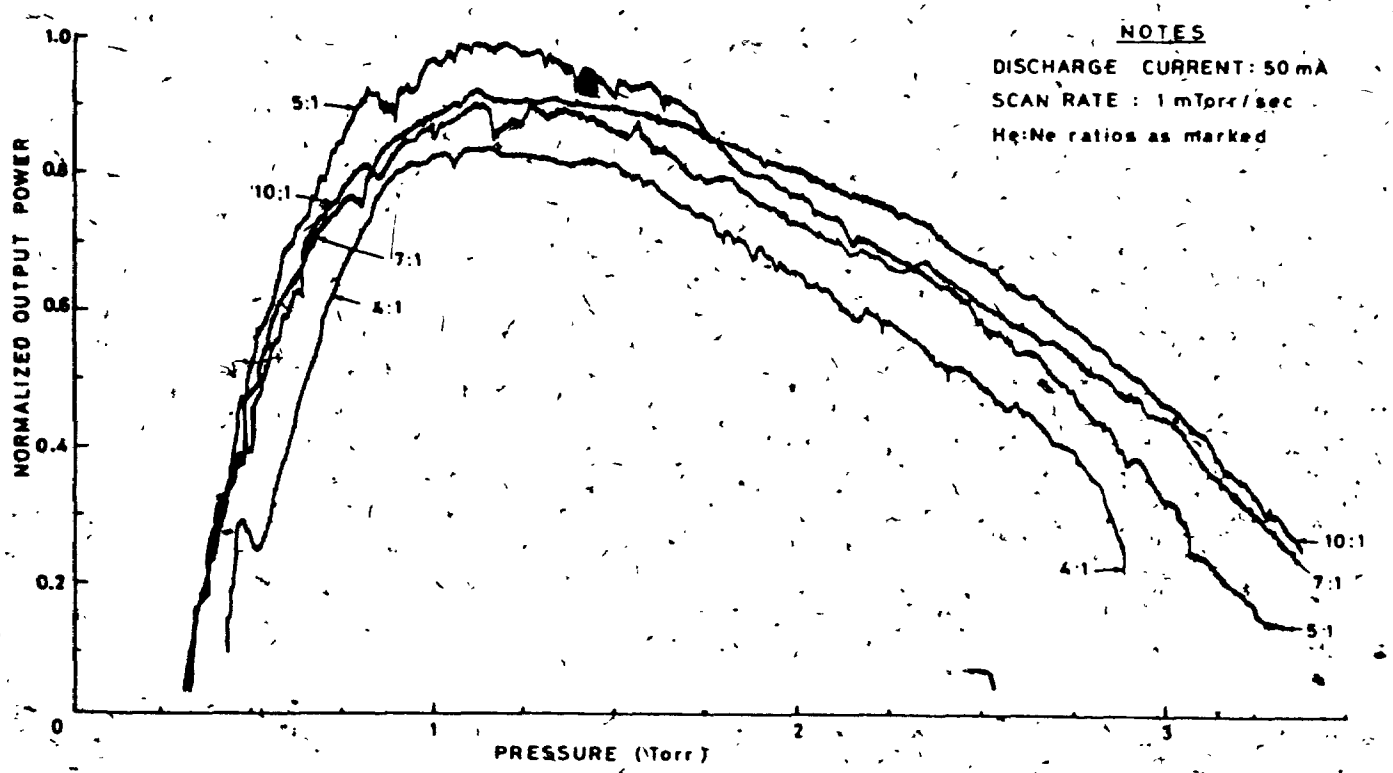

Figure 4-9: Laser Output Power Dependence at 4.2 μm on Total Pressure

The output power dependence at 4.2 μm on total laser tube pressure for several fixed He-Ne gas ratios is shown in Figure 4-9. These curves are obtained for low flow rate conditions (1 mTorr/sec total system pressure drop) in the fashion described by point 2 above and are recorded by the X-Y recorder. The laser tube is filled to approximately 10 Torr from the mixing chamber with the appropriate gas mixture and slowly evacuated until laser action is observed. The tube and chamber are then sealed until the laser output power stabilizes. The system evacuation is continued to the point of failure as indicated in the figure. For He-Ne gas mixtures in the span of 4:1 to 10:1, the peak output power does not differ by more than 20% with the maximum recorded for 5:1 at 1 Torr total pressure. This gas ratio was used for all subsequent laser output power and carbon dioxide absorption tests.

All curves in Figure 4-9 have been normalized with respect to the maximum observed output intensity noted above. A beam splitter (Ge) was positioned at the output of the laser and the PbSe detector and preamplifier output compared to the response of an absolute laser power monitor (Scientech 352). This test determined the sensitivity of the PbSe detector system to be 2 $V_{\text{peak to peak}}$/mW for radiation at 4.2 μm. The maximum power noted in Figure 4-9 is approximately 3 mW given this calibration factor.

Further characterization of the He:Ne 5:1 mixture ratio is shown in Figure 4-10 and 4-11 for both sealed and low evacuation rate operation. Under sealed conditions, the recorded output intensity is the observed maximum before failure due to fill gas contamination.

Laser action at a 50 mA discharge current level occurs in the pressure region outlined by the solid contour in Figure 4-10. Of particular interest is

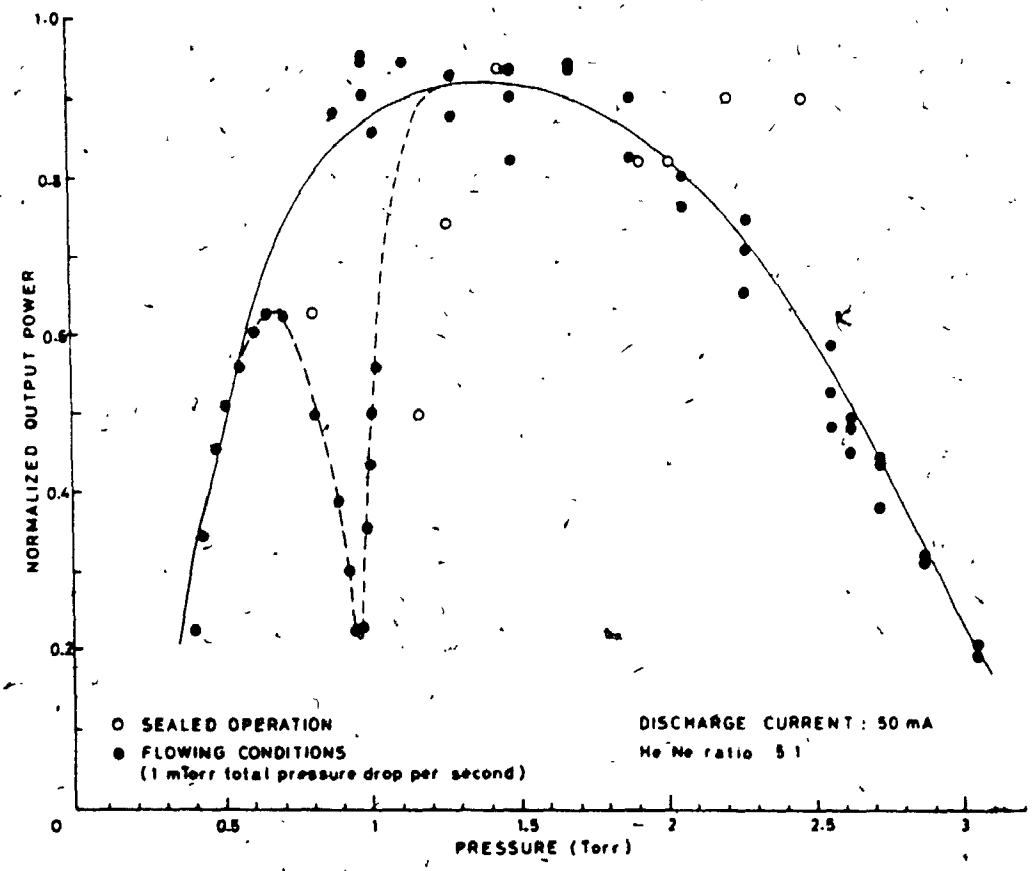

Figure 4-10: Output Power Versus Total Pressure at 50 mA

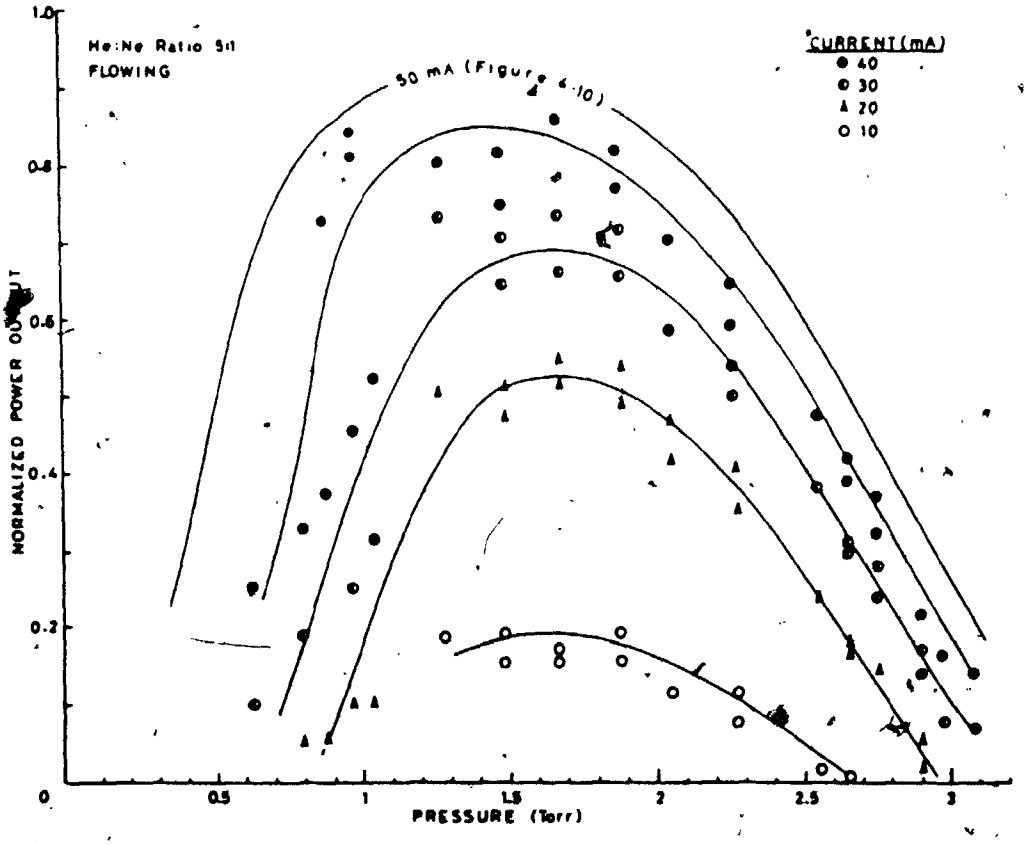

Figure 4-11: Output Power Versus Total Pressure : Variable Current

the presence of a small side peak on the low side of the working region. With the exception of the small observed satellite at 500 mTorr for the 4:1 He:Ne mixture, this increase in power is not evident for the flowing measurement tests as shown in Figure 4-9. The peak is clearly resolved only when a specific gas mixture in the laser tube is quickly evacuated to approximately 1 to 1.5 Torr, sealed until the laser power stabilizes and then slowly pressure scanned to below 500 mTorr. Given that the expected pressure optimum lies approximately at the centre value of the observed side peak (500 mTorr, page 46), this behaviour is interpreted as the competing effects of increasing laser gain as the pD optimum is approached and laser failure as the fill gas is more quickly poisoned at lower tube pressures. For maximum output power and amplitude stability, the laser should be run under low flow conditions with evacuation occurring between 2 to 1 Torr.

The current dependence of laser output power for the working pressure region is shown in Figure 4-11. As evident in the figure, maximum output power is achieved at the power supply maximum of 50 mA.

4.3. Summary

Laser action at the helium neon $3s_2 \rightarrow 3p_1$ transition (4.2 μm) has been successfully demonstrated. A maximum output power of 3 mW at 50 mA discharge current levels has been achieved for He:Ne gas mixtures of 5:1 in the pressure range of 1 to 2 Torr. The output power was also found to be relatively insensitive to the gas mixture ratio in the region of 5:1 to 10:1 He:Ne.

The final laser design consists of a water cooled pyrex tube (170 cm long, 8.8 mm inside diameter) sealed at one end with a Brewster window (CaF_2), a

2

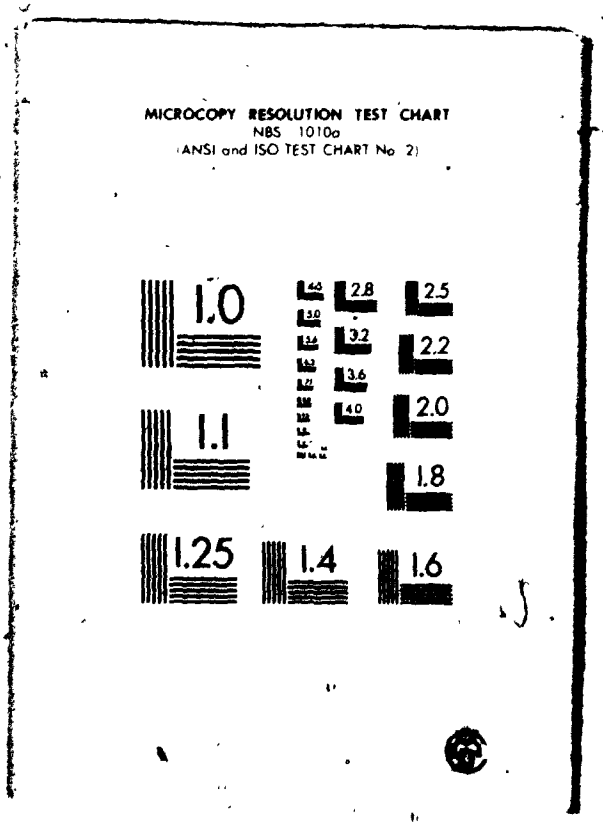
MICROCOPY RESOLUTION TEST CHART
NBS 1010a
(ANSI and ISO TEST CHART No 2)
1.0
1.1
1.25
1.4
1.6
2.8
3.2
3.6
4.0
2.5
2.2
2.0
1.8

0.5% transmissive planoconcave Germanium output coupling mirror (10 meter radius of curvature) and reflective echellette diffraction grating blazed for 4.2 μm. The optical elements and laser tube assemble to form a resonator 180 cm in length.

Maximum operation time before failure due to atmospheric gas poisoning is one hour. The main source of poisoning gas is thought to be through the double O-Ring seal locking the laser tube to the vacuum chamber. More permanent laser installations should consider the sealing of both ends of the laser tube with Brewster windows to avoid this problem.

The laser is used as the probe radiation source for the resonance absorption spectrometer as detailed in the following chapter.

Chapter Five
Carbon Dioxide Absorption Tests

Carbon dioxide analysis by absorption of 4.2 μm helium neon laser radiation requires both an optical spectrometer and appropriate signal processing unit to relate gas concentration to beam transmission through the sample. A complete system to provide this function has been designed and constructed by the author at the University of Western Ontario. This chapter initially describes the final design and concludes with the results of carbon dioxide absorption tests.

5.1. Optical Spectrometer

5.1.1. General System Overview

The optical spectrometer is a dual beam - single detector arrangement that has been fully documented in principle previously by the author [1]. The operational details of the specific system are most easily described by reference to a general schematic diagram of the spectrometer optical and gas intake sections as shown in Figure 5-1. The complete framework is delineated by the solid boundary in the figure and is designed to be mounted directly on the optical bench as described in Chapter 3. A junction box (I/O) at the left side of the figure provides a vacuum seal for electrical connections to the signal processing unit. The complete system may be isolated from the atmosphere and purged with nitrogen gas to minimize carbon dioxide absorption of the laser radiation outside the sampling path.

The laser beam enters the spectrometer at the right side of the figure and is amplitude modulated by a Bulova modulator (ONT-L8C). This modulation

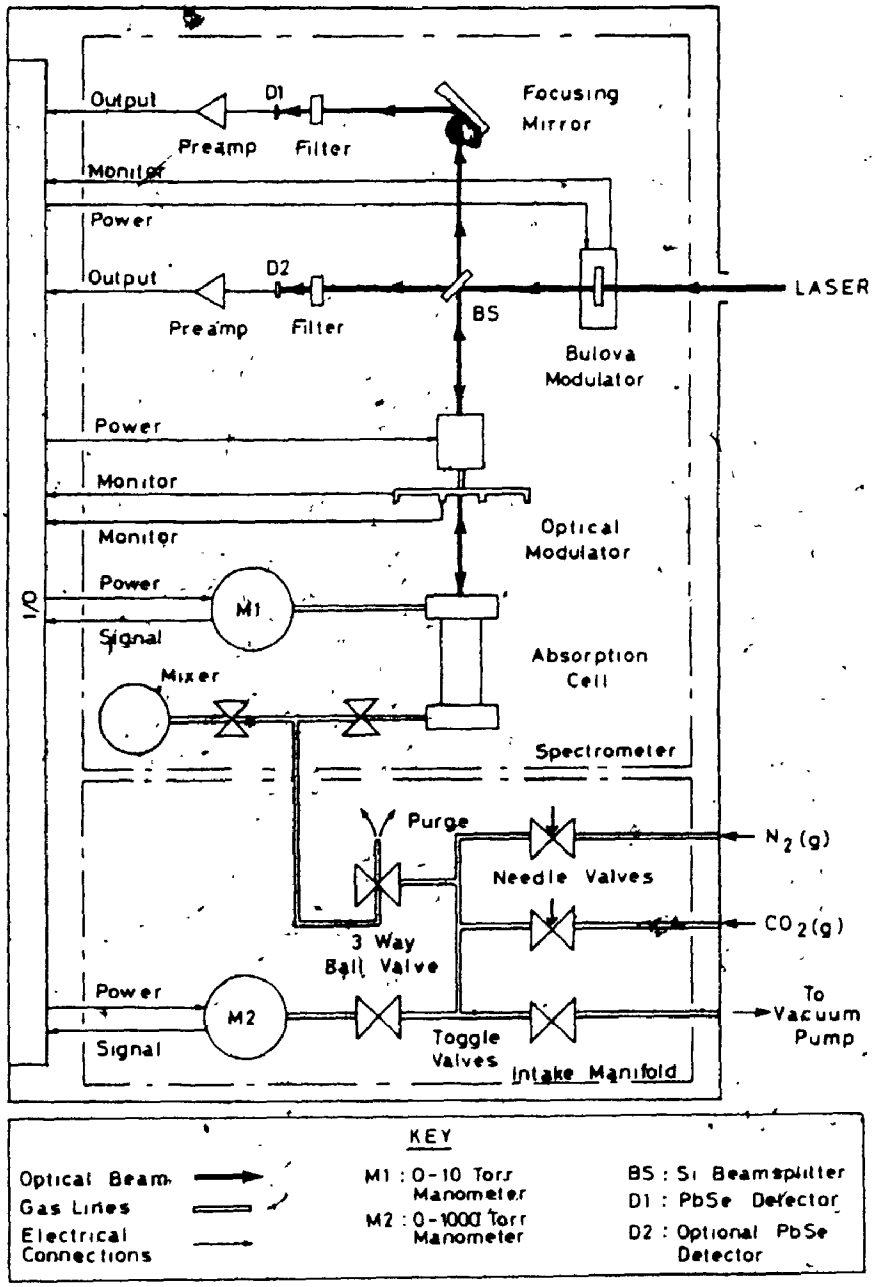

Figure 5-1: Spectrometer Plan View

(100%, 200 Hz) encodes the laser radiation intensity as an AC signal in order to avoid the electronic drifting problems inherent in the detection of DC signals. The beam passes through the modulator and falls on the face of a 50% transmitting beamsplitter. The transmitted radiation is optically filtered and monitored by a lead selenide detector. In actuality this signal does not play a part in the analysis of carbon dioxide absorption data but is included as a convenience. Simple removal of the beamsplitter from the system allows for direct observation of the laser output power in this arrangement as described in Chapter 4.

The radiation reflected from the face of the beamsplitter is directed towards a multi-bladed fully reflective chopping wheel (optical modulator [100]). This modulator splits the radiation into sample and reference paths. Sample radiation passes between the reflective blades of the rotating wheel and enters an absorption cell. The rear wall of the cell consists of a fully reflecting plane mirror that directs the sample beam back through the cell to the optical modulator. The radiation passing between the chopping wheel blades becomes coincident with the reference beam pathway. This combined beam contains the intensity information of both sample and reference paths time multiplexed at the chopping wheel blade rotation frequency. The radiation passes back through the beamsplitter and is focused to the face of a lead selenide detector. The detected signal is preamplified and fed through a single cable to the input of the signal processing unit.

An intake manifold and gas mixing network is housed inside the spectrometer to prepare gas samples for absorption testing. The particular combination of valves and vacuum tubing allows for accurate measurement of cell pressures from 0 - 1.32 atm (0 - 1000 Torr). A mixer adjacent to the

absorption cell ensures uniform gas mixtures for nitrogen broadened carbon dioxide determinations. A purging line connecting the nitrogen gas supply or vacuum pump to the interior of the spectrometer is also included.

5.1.2. Detailed Component Descriptions

Individual descriptions and construction details for all components with the exception of the absorption cell, mixer and beamsplitter have been published by the author ([99], [100]) and will not be repeated here.

The spectrometer framework system is shown in Figure 5-2. Six aluminum rods (15.9 mm (0.625 in) dia, 40.6 cm (16 in) long, c1-c6) are positioned by four rod supports (e1-e4) to form a cage structure 55.9 cm (22 in) (length) by 40.6 cm (16 in) (width) by 26.7 cm (10.5 in) (height). The framework is rigidly braced by three aluminum end plates (f1, f2, h) that are attached to the rod supports with machine screws. The end plates also serve to support the gas intake valves (h) and electronic junction box (f2, g) and to provide an entrance aperture for the laser beam (f1). The dimensions of the cage are such that the cross bracing designed for the laser resonator (Chapter 4) may be used to support and align the optical components inside the spectrometer. A component table (d) is centred under the entrance axis of the laser beam and supports the Bulova modulator, beamsplitter and optional detector described by Figure 5-1. The beamsplitter is an uncoated polished germanium optical flat (2 mm thick, 50 mm dia) mounted directly in a circular mirror mount (Opticon Co.). The optical properties of germanium at 4.2 μm are included in Appendix E.

The absorption cell consists of a brass cell body as shown in Figure 5-3. Radiation enters the cell through a calcium fluoride window (25.4 mm dia, 3

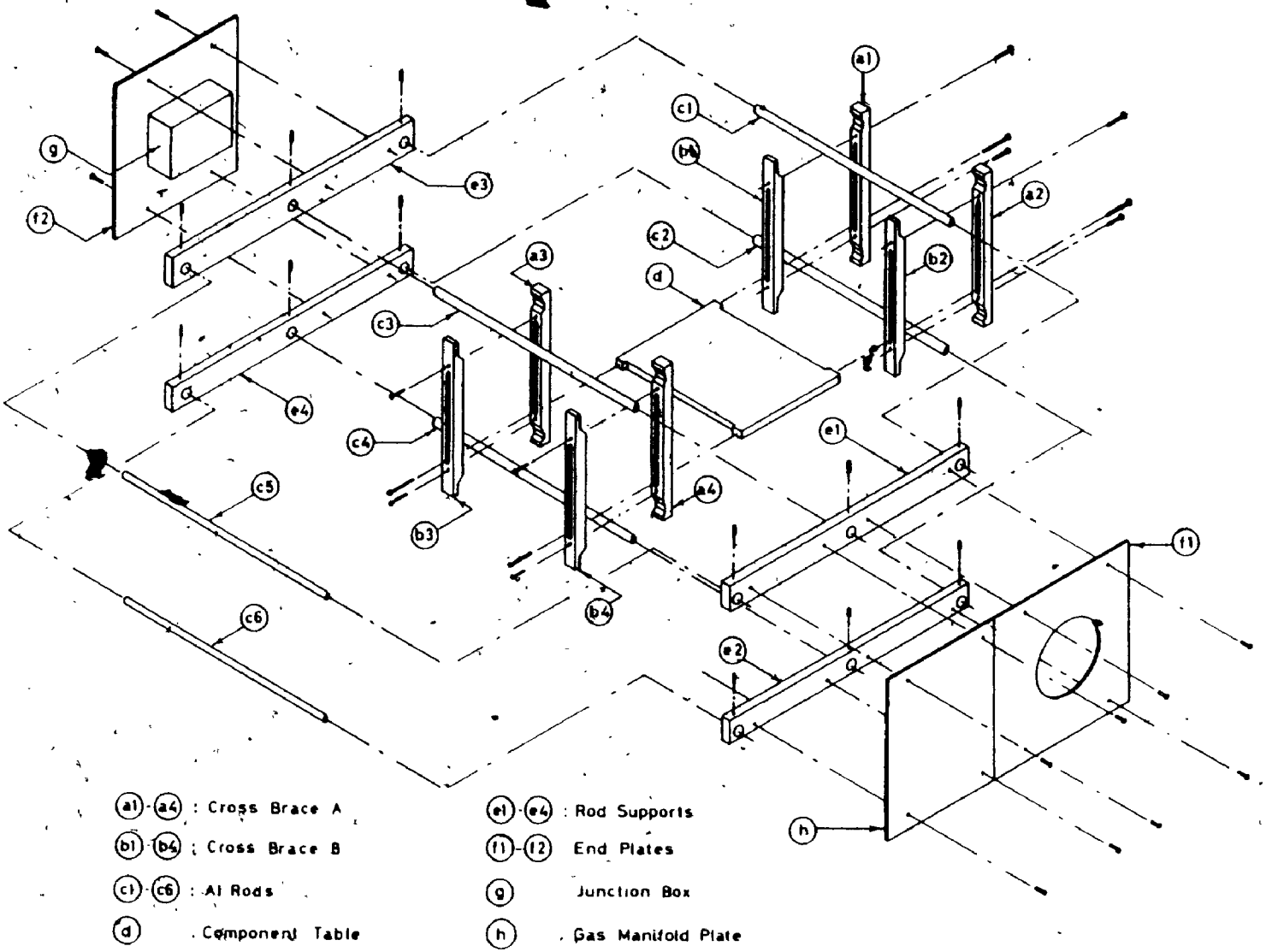

Figure 5-2: Spectrometer Framework : Exploded View

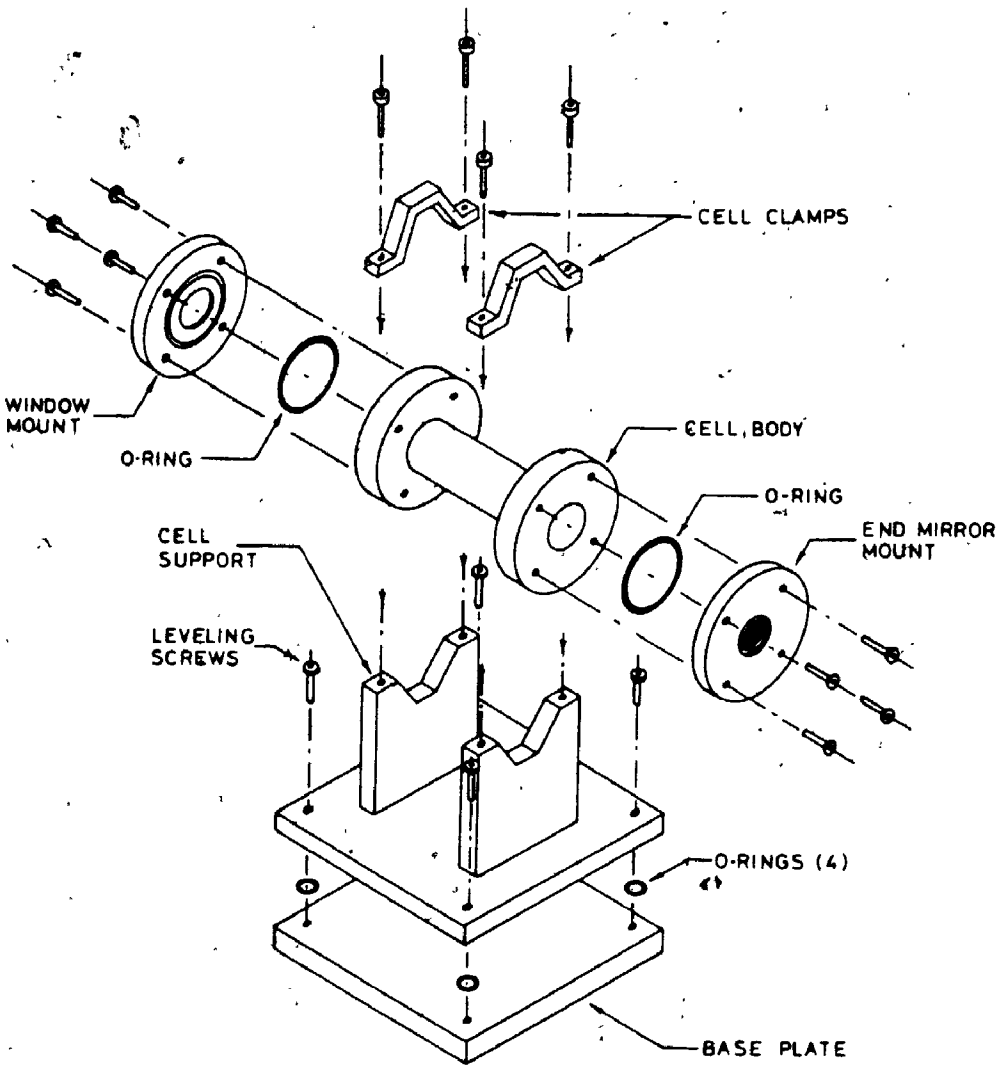

Figure 5-3: Absorption Cell

mm thick) epoxied to the centre hole of the window mount. The window mount is sealed to the front face of the cell body by an O-Ring. The end mirror mount is constructed and installed in identical fashion to the window mount with the exception that the calcium fluoride window is replaced by a fully reflective first surface gold plane mirror. The cell body is clamped to the cell support and the entire assembly mounted to horizontal cross bracing in the spectrometer framework. Alignment of the end mirror is accomplished by the leveling screws and O-Ring combination outlined in the figure. A hole drilled perpendicularly to the cell body axis through one side of the larger diameter rear section is fitted with 6.35 mm (0.250 in) diameter copper tubing. The tubing is soldered to the cell body to provide a gas intake/gas exhaust port. In a similar manner, the opposite end of the cell body is connected to a pressure meter (M1 - Figure 5-1). The gas flow and pressure meter connections have been omitted from Figure 5-3 for reasons of clarity.

The absorption cell defines a cylindrical volume 22.2 mm in diameter and 9.9 cm in length with the end mirror and window mounts in place. The total absorbing pathlength through the cell is 19.8 cm.

The range of carbon dioxide pressures that may be tested is limited by exclusive determination over a single absorbing pathlength. Both an absolute minimum signal level at the detector and minimum difference signal level should be established as reliable operational bounds for the spectrometer. Initial testing of the complete optical system with the evacuated 9.9 cm cell in place determined the signal levels at the detector for sample and reference beams to be approximately 17% and 21% respectively of the laser output intensity. Given a conservative average output intensity of 2 mW for the laser at 50 mA discharge current (Chapter 4), this translates to detected signals of

approximately 340 mV_{peak} and 420 mV_{peak} for the sample and reference beams respectively under no absorption conditions. For accurate signal processing, the transmission through the gas sample is set to be bounded by 10% and 90% of the unattenuated signal. The expected range of signal levels with these constraints is approximately 35 mV_{peak} to 300 mV_{peak} for the sample beam. This range is easily handled by conventional signal processing techniques.

To increase the pressure range capability of the system, the absorption cell is modified by the variable pathlength assembly as shown in Figure 5-4. The fixed end mirror is replaced by a sliding plug with a gold plane mirror mounted to the forward surface. The plug is positioned in the cell body by the dual threaded rod configuration and fixed to the rear plate. A longer cell body (30 cm) similar in other dimensions to that described previously is also required. The combination of this cell body and rod lengths (18 cm) allows for total pathlengths from 0 to 22 cm. The spectrometer processing range is now limited only at the low loading end of carbon dioxide pressures at 22 cm pathlengths.

The absorption cell is located 32 cm from the output of the laser. At a maximum absorption pathlength of 22 cm, the laser beam diameter is calculated to be 6 mm (Equation 3-8) on exit from the cell. The cell diameter of 22.2 mm is sufficiently large to ensure that the beam does not contact the cell walls. All optics in the system can handle beam diameters at least twice the value of the laser beam diameter at the respective positions along the optical pathlength.

Orientation of the cell with the calcium fluoride window perpendicular to

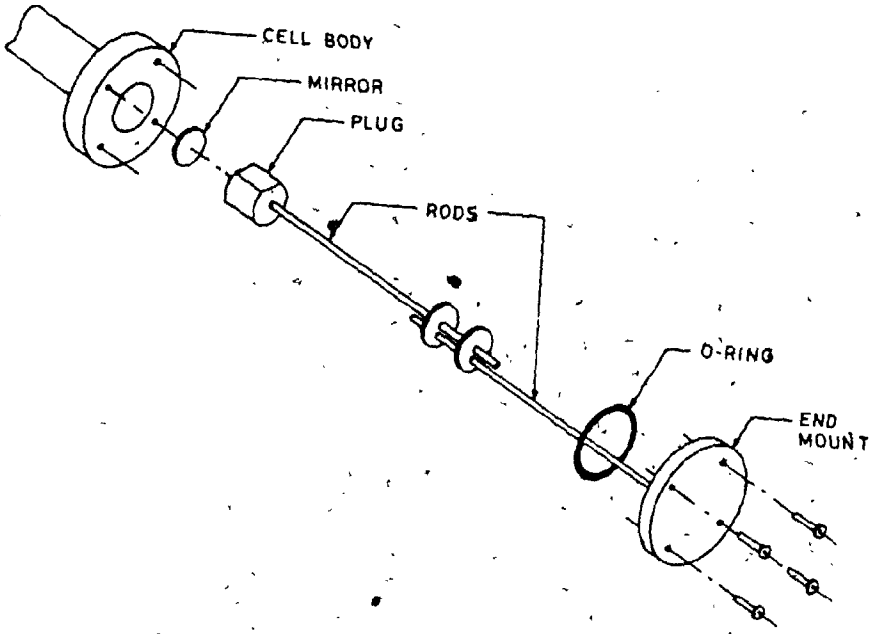

Figure 5-4: Absorption Cell Variable Pathlength Adaptor

the input axis of the laser beam leads to the problem of back reflection of radiation from the window surface to the detector. This radiation is interpreted by the spectrometer as having passed through the sample and causes a small offset voltage in the processing electronics. This problem is typically solved by tilting the window to remove the reflected signal from the beam return path. This solution, however, may lead to large errors in cell pathlength assignments as the zero pathlength condition is approached by the variable length cell. It was decided in this work to maintain a perpendicular window orientation and to compensate for the back reflected radiation in the sample path with the signal processor. This point is further considered in Section 5.2.

Initial absorption measurements with nitrogen-carbon dioxide mixtures were performed by directly mixing the gases in the absorption cell. This method of sample preparation was found to be unsatifactory as the mixture required a considerable time period before uniformly distributing in the cell volume. A mixer (Figure 5-1) with propeller agitation solved this problem.

5.2. The Signal Processor

5.2.1. Preprocessing

The signal processing unit is required to separate the detector preamplifier output signal into sample and reference streams and to calculate a real time ratio of sample to reference beam intensities. An electronic device to perform these functions has been described previously by the author [101]. A general description of the processor operation is briefly presented here for the convenience of the reader. Detailed circuit diagrams of the individual system blocks are found in the original literature.

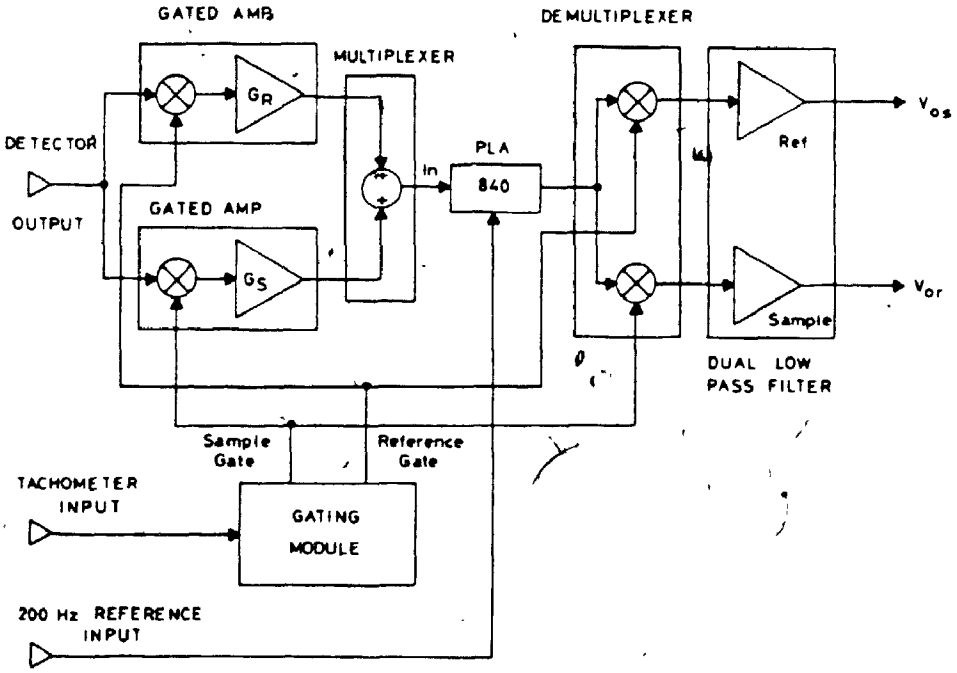

Figure 5-5: Signal Processor Block Diagram

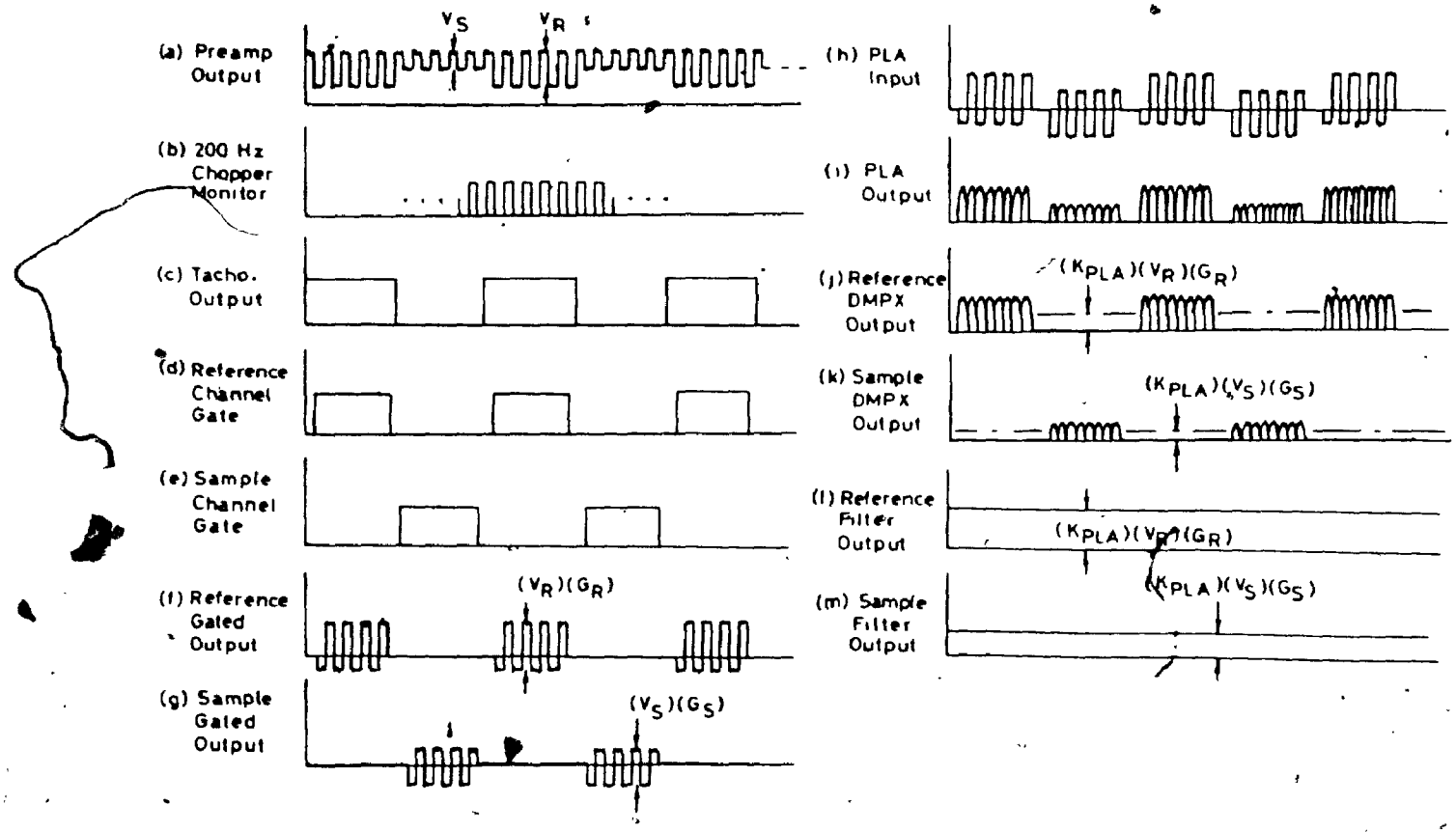

Figure 5-6: Individual Component Output Waveforms

A schematic diagram of the processor and associated waveforms of the individual components have been reproduced as Figures 5-5 and 5-6 respectively. The detector preamplifier output may be seen as the sequentially switched sample (V_S) and reference (V_R) beam intensities modulated at the Bulova modulator frequency. An optical sensor attached to the optical modulator returns a signal to the processor to indicate if the spectrometer is in sample or reference mode (Tacho Output). The gating module provides the signals required to demultiplex the detector preamplifier output into separate sample and reference paths. These pulses are narrowed slightly with respect to the optical modulator synchronization signal to remove switching spikes from the demultiplexed signals. Variable gain gated amplifiers provide the signal separation function. This arrangement allows for independent sample and reference beam amplification (G_S and G_R respectively) prior to amplitude decoding. The signals are recombined (Multiplexer) and processed by a phase lock amplifier (Keithley Autoloc-840) operating with the 200 Hz reference frequency supplied by the Bulova modulator. This recombination removes the phase lock amplifier gain settings from the final system transfer function and avoids mismatch errors present in a system employing separate phase lock amplifiers for sample and reference beam channels. The unfiltered phase lock amplifier output is again separated (Demultiplexer) and filtered (Dual Low Pass Filter) to yield two DC signals that are proportional to sample (V_{os}) and reference (V_{or}) laser beam intensities. The ratio of these signals defines the required expression for sample transmission as given by Equation (2-1).

Knowledge of the sample to reference signal ratio under no carbon dioxide absorption conditions is necessary for final calibration of the absorption data.

The logarithmic difference amplifier previously described [101] to directly

calculate absorbing molecule concentration levels from the spectrometer output signal has been omitted in the present scheme. This point is examined in the following subsection.

5.2.2. Computer Preprocessing

Direct calculation of sample transmission from the decoded sample and reference signals described above neglects the back reflection contribution from the absorption cell window to the sample beam signal. A simple correction factor may be applied to the data if it is assumed that the reflection coefficient from the cell window does not vary appreciably during the course of the experiment. In this sense, the sample signal at the input to the preprocessor, V_S, may be expressed as,

$$V_S = V_S' + \alpha V_R \tag{5-1}$$

where : V_S' : actual sample signal

αV_R : window reflection contribution to sample signal

V_R : measured reference signal

Uncalibrated transmission, $T_{un}(\nu)$, is defined as,

$$T_{un}(\nu) = \frac{V_S'}{V_R} \tag{5-2}$$

$$= \frac{V_{os}}{V_{or}} \frac{G_R}{G_S} - \alpha \tag{5-3}$$

The proportionality constant, α, may be measured by removing the fully reflecting mirror from the absorption cell[1].

The uncalibrated transmission is related to the actual transmission as defined by Equation (2-1) by correction for the mismatch between the sample and reference paths such that [101]

$$T(\nu) = \frac{T_{un}(\nu)}{T_L} \tag{5-4}$$

given that

$$T_{un}(\nu) = T_L \exp(-k(\nu)L) \tag{5-5}$$

where T_L : sample to reference beam mismatch factor

The T_L value is established by measuring the transmission under zero carbon dioxide loading conditions.

The DC signals from the signal preprocessor unit are stored as permanent records by a two channel chart recorder (Watanabe Servocorder 652). The curves are digitized with a flatbed digitizer (Tektronix 4115B) and stored as data files on the University of Western Ontario PDP 10 computer system. The complete processing scheme is shown in Figure 5-7 with reference to the individual processing programs that are listed in Appendix

[1]The actual sample signal is zero under these conditions and the direct ratio of preprocessor output voltages, V_{os}/V_{or}, equals $\alpha G_S/G_R$. It is assumed in this formulation that the reference signal intensity is constant over one cycle of the optical modulator switching frequency.

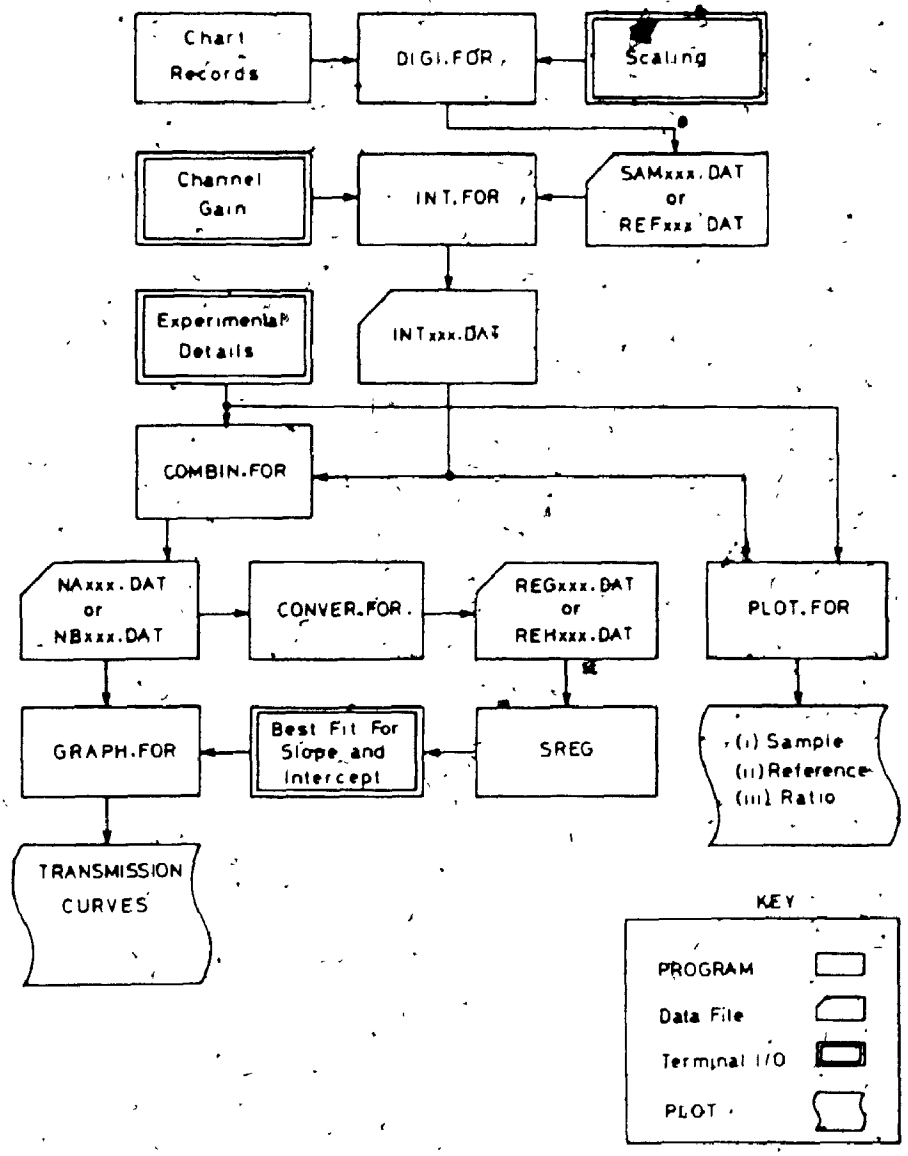

Figure 5-7: Data Processing Pathways

The sample and reference signal files are scaled by the individual channel gain factors and the calculated transmission fraction corrected with the back reflection coefficient (α) (INT.FOR). These curves are plotted directly (PLOT.FOR) as sample signal, reference signal and calculated ratio as functions of time. The mean value of the ratio over the test duration is also listed with the standard deviation of the sampled points.

Analysis of the nitrogen broadened carbon dioxide absorption data is simplified if the relative concentration of carbon dioxide in the nitrogen matrix is kept small for a constant total gas pressure. With this constraint, Equations (2-1) and (2-12) may be expressed as

$$T(\nu) = \exp(-k_{pf}(\nu)^{o}_{l}\, p_a\, L) \qquad (5-6)$$

where $k_{pf}(\nu)^{o}_{l}$: normalized extinction coefficient for constant total nitrogen pressure ($atm^{-1}\, cm^{-1}$)

p_a : carbon dioxide pressure (atm)

L : pathlength (cm)

The slope of the natural logarithm of $T(\nu)$ versus p_a graph for $p_a \ll p_f \approx P_e$ (Equation 2-10a) at constant P_e yields the value $-k_{pf}(\nu)^{o}_{l} \cdot L$. Programs COMBIN.FOR and CONVER.FOR prepare the data for linear regression analysis (SREG) and GRAPH.FOR plots the individual transmission points and best fit line. This data may be used to determine the foreign gas broadening coefficient, σ_{b_f}', and laser line frequency as described by Equation (2-9). These calculations will follow the test details and a discussion of the preliminary results.

For pure carbon dioxide absorption tests, the normalized extinction coefficient, $k_{pa}(\nu)^{o}_{l}$, is calculated point by point for each sampling pressure. Sample signal, reference signal and ratio graphs are produced in the same manner as for nitrogen broadened tests. The modified self broadening coefficient, $\sigma_{b_a}{}'$, and laser line frequency determinations follow in Section 5.3.2.

5.3. Experimental Details and Test Results

5.3.1. N_2 Broadened CO_2 Absorption Tests

5.3.1.1. Experimental Details

Gas mixtures are prepared by first purging the intake manifold and overpressuring the mixer with carbon dioxide. The mixer is evacuated to the desired carbon dioxide pressure and isolated from the system. The intake manifold is then purged with nitrogen and overpressured. Nitrogen is rapidly admitted to the required pressure for a specific CO_2-N_2 mixture. The mixer is again isolated and the remainder of the intake manifold evacuated. The absorption cell and mixer are connected and the final cell pressure recorded.

Total pressures investigated are from 0.13 atm (100 Torr) to 1.18 atm (900 Torr) in discrete steps of 0.13 atm (100 Torr). The single discontinuity in the sequence is at 1.05 atm (800 Torr): it was elected to substitute 1 atm (760 Torr) for this value so that a direct comparison with previously published results could be made.

Carbon dioxide partial pressures in the range of 1.3×10^{-3} to 9.2×10^{-3} atm (1 - 7 Torr) provide a good range of transmission values for a 20.0 pathlength over the selected total pressure range. One additional CO_2 pressure reading of 1.18×10^{-2} atm (9 Torr) is included for the 0.13 atm (100

Torr) determination to increase the total transmission range. Given the expected self to foreign gas broadening cross section ratio of 1.2 (page 26), a CO_2 concentration of 10% total pressure is assumed to introduce negligible error in the determination of σ_{b_f}'.

The transmission at 1 atm (760 Torr) is determined over a 2.0 cm pathlength to check the value established for $k_{p_f}(\nu)^{\circ}_{l}$ by the 20 cm test. A range of pressures from 6.6×10^{-3} atm (5 Torr) to 6.8×10^{-2} atm (50 Torr) is suitable for this test.

After the cell is prepared, the laser tube is filled to 3.9×10^{-3} atm (3 Torr) with a 5:1 He:Ne gas mixture and evacuated slowly at a 50 mA discharge current. Absorption test results are recorded to the point of laser failure as described in Chapter 4. At several points during the course of transmission determination for a single total pressure, the absorption cell is filled with nitrogen and the beam mismatch factor, T_L, measured (Calibration Tests - Appendix G).

5.3.1.2. Experimental Results

The back reflection coefficient is determined to be $0.0013 \pm < 1\%$. The error assignment in this case is based on the standard deviation for sampled points for the one specific test. Actual error over the course of many tests should be somewhat higher as the beam wanders across the face of the detector as a function of time. Maximum back correction deviation from the established mean value is assumed to be less than $\pm$ 0.01.

Each absorption test is calibrated by the appropriate value of T_L as noted in Appendix G. The calculated transmissions and best fit slopes are shown for

Total Pressure (Torr)	Path (cm)	Slope ($Torr^{-1}$)	$K_{pf}(\nu)_l^\circ$ (atm^{-1} cm^{-1})
100 ± 10	20.0 ± 0.5	-0.0361 ± 6.3	1.37 ± 17.
200 ± 5		-0.0712 ± 5.2	2.71 ± 11.
300 ± 3.3		-0.0978 ± 3.0	3.72 ± 7.0
400 ± 2.5		-0.133 ± 4.5	5.05 ± 7.5
500 ± 2.0		-0.166 ± 2.5	6.31 ± 5.
600 ± 1.7		-0.203 ± 4.4	7.71 ± 6.6
700 ± 1.4		-0.235 ± 6.4	8.93 ± 8.3
760 ± 1.3		-0.242 ± 7.2	9.20 ± 9
900 ± 1.1		-0.276 ± 4.1	10.5 ± 5.7
760 ± 1.3	2.0 ± 5.0	-0.0278 ± 2.7	10.6 ± 9

Note: At 760 Torr, average $K_{pf}(\nu)_l^\circ$ = 9.90 ± 15 atm^{-1} cm^{-1}

: All errors in per cent

Table 5-1: Nitrogen Broadened Absorption Test Results

each of the total pressure tests in Appendix H for the 20.0 and 2.0 cm pathlengths. Table 5-1 summarizes the experimental results and indicates the associated error for the final determinations of $k_{pf}(\nu)^{o}_{l}$. Error assignments are based on 95% confidence levels for the linear regression analysis for best slope, a given value of ± 10 Torr for the pressure measurements by the manufacturer (MKS Baratron 0-1000 Torr 222B) and a cell length measuring precision of ± 0.5 mm. Total error is assigned as the sum of these individual component parts.

5.3.1.3. Calculations and Discussion

This section describes the technique used to calculate the unknown coefficients in Equation (2-9) given the experimentally determined values of $k_{pf}(\nu)^{o}_{l}$ for the nitrogen broadened carbon dioxide spectrum. Two assumptions are made with respect to the original formulation to expedite the solution of the problem.

1. The foreign gas broadening cross sections for the lines R(28) to R(34) are assumed to be approximately equal. An average value for this parameter will be calculated.

2. The laser frequency is assumed to lie between the peak frequencies of R(30) and R(32). Reference to Figures (2-6) (30) and (2-8) (7) indicates that the calculated $k_{pf}(\nu)^{o}_{l}$ values are approximately symmetrical about the function minimum (transparency window) at 71.1276 THz (2370.92 cm^{-1}) [43]. It is expected that minimization of the error function defined by the difference between experimental points and calculated values will result in the observation of two optimum laser frequencies, i.e. on the high frequency side of R(30) and the low frequency side of R(32). This point illustrates the danger of absolute laser frequency determination by the experimental technique described in this thesis. Solution of the normalized extinction coefficient expression is done in two stages with allowed laser frequency restricted to either the wing of the

R(30) or R(32) lines respectively. A final computation of the global minimum is also included by removing any boundary conditions on the laser frequency in the analysis.

Equation (2-9) may be reformulated with the individual parameter assignments listed here for convenience as

$$k_{pf}(\nu)^{o}_{l} = \sum_{J''=28 \rightarrow 32} S^{o}_{v''J'' \rightarrow v'J'} f_c(P_T, \nu_l - \nu_R) \qquad (5-7)$$

where

$$f_c(P_T, \nu_l - \nu_R) = \frac{1}{\pi} \frac{P_T \sigma_{b_f}'}{(\nu_l - \nu_R)^2 + (P_T \sigma_{b_f}')^2} \qquad (5-8)$$

and ν_l : laser frequency (cm^{-1})

ν_R : frequency of line R(J'') (cm^{-1}) (Appendix A)

P_T : total system pressure (atm)

σ_{b_f}' : average nitrogen broadening cross section (R(28) to R(32)) (cm^{-1}/atm)

The constant values for $S^{o}_{v''J'' \rightarrow v'J'}$ are listed on page 25.

The optimization technique chosen for the evaluation of best fit estimates of ν_l and σ_{b_f}' for the experimental data is the Fletcher-Powell (FP) Method [97]. Implementation software for this routine was supplied by Mr. A. C. Simmons of Maverik Software Inc., Toronto, Ontario.

The specific FP method used in this work maps an error surface that is established by the square of the difference between estimates for the function and the actual experimental points. Optimum solutions are defined as points on the surface at which the two dimensional function gradient equals zero. Details of the mechanics of the method are given by the original reference and textbooks on numerical analysis [98].

The boundary conditions for σ_{b_f}' are set to be 0.02 to 1.4 cm^{-1}/atm. Initial attempts to determine the optimum values of σ_{b_f}' and ν_l for ν_l bounded by the peak frequency of R(30) (2370.38 cm^{-1}) and the central transparency window (2370.92 cm^{-1}) were unsuccessful. Examination of the simulated normalized extinction coefficient curves (Figure 2-6) indicates that for laser frequencies located in the wing of an absorption band, the error surface will be fairly flat[2] along a series of points connecting specific combinations of σ_{b_f}' and ν_l. Given the experimental scatter of sampled points, this condition may not allow the optimization routine to find a zero gradient condition in two dimensions within the assigned parameter boundaries. The absolute error may, however, be very small at several points on the surface.

A second trial with the laser frequency bounded by the peak frequencies of the R(30) and R(32) lines quickly converged to an optimum solution for σ_{b_f}' and ν_l of 0.079 cm^{-1}/atm (2.40 GHz/atm) and 2371.09 cm^{-1} (71.0835 THz) respectively. The curve representing the results of substituting these values into Equations (5-7) and (5-8) is shown[3] along with the experimentally

[2]A restatement of this observation is that as the optimization method shifts the laser frequency away from the centre of the absorption peak towards the transparency window, broadening the line will lead to a low error condition for the function fit.

[3]This is the curve labelled as **UNSHIFTED** in the figure.

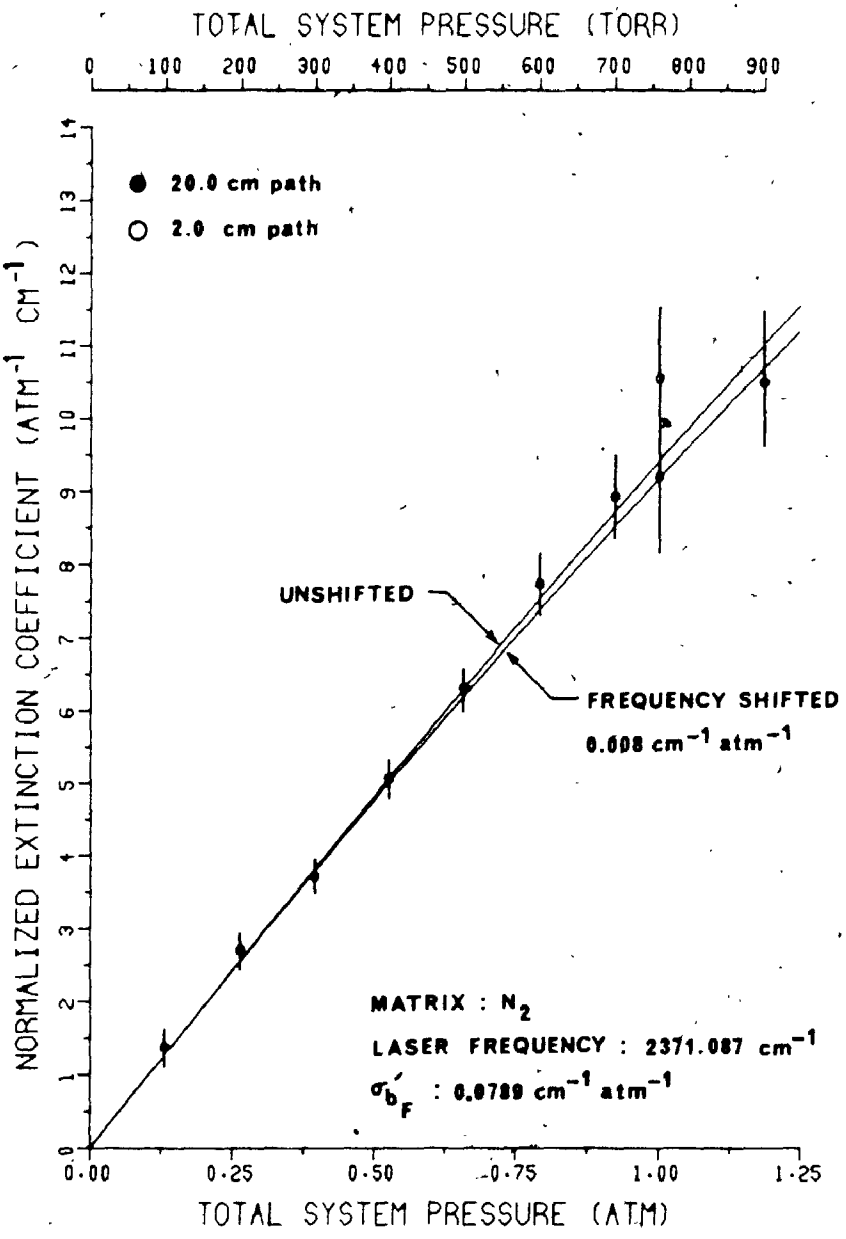

Figure 5-8: N_2 Broadened Experimental Results and Fit Functions

observed points in Figure 5-11. The curve lies within experimental error boundaries (Table 5-1) of all the observed experimental values.

Examination of the major sources of error for the two individual pathlength determinations of $k_{p\int(\nu)^0_l}$ is instructive prior to further interpretation of the experimental results. At 20.0 cm pathlengths, the high pressure tests have a wide range of transmission values over the input range of experimental carbon dioxide partial pressures. At transmissions in the region of 0.1, the back correction factor affects the detected signal by as much as 10%. Small absolute errors in α ($\sim \pm$ 0.01) are reflected as large errors in the final calculation of $k_{p\int(\nu)^0_l}$. This effect is accentuated for small absolute errors in low transmission values by the logarithmic transformation. The short pathlength determination of $k_{p\int(\nu)^0_l}$ for 1 atm (760 Torr) total pressure suffers large inaccuracies ($\pm$ 5%) in the measurement of absolute pathlength. Comparison of the two test results at 1 atm total pressure indicates an offset error in either the measurement of the 2.0 cm pathlength or the 20.0 cm pathlength assignment of the back reflection coefficient. The two determinations do overlap within the estimated individual error bounds and the average $k_{p\int(\nu)^0_l}$ equals 9.90 $\pm$ 15% cm^{-1} atm^{-1} (Table 5-1). This determination compares well to the published results of $k_{p\int(\nu)^0_l}$ equals 11.5 cm^{-1} atm^{-1} for small carbon dioxide concentrations in 1 atm air[4] by Belov. et. al. [43].

A better point fit is possible by introducing a pressure dependent frequency shift (Equation 2-8) to the absorption band peaks in the

---

[4]The line broadening effects of nitrogen and oxygen have been shown to be approximately the same for carbon dioxide 4.2 μm spectra [102].

denominator of Equation (5-8). This function is shown in Figure 5-8 for an assigned frequency shift cross section of one tenth the value of the originally determined nitrogen broadening cross section of 0.079 $cm^{-1}.atm^{-1}$. The curve is included here simply as a curiosity: such speculation may be dangerous without direct observation of the higher pressure absorption spectrum as noted in Chapter 2.

The best fit value of 2.40 GHz/atm (0.079 cm^{-1}/atm) for the modified nitrogen broadening cross section is within the range of previously determined cross sections as noted in Chapter 2. The results of a third series of function optimizations is shown in Figure 5-9 where the value of σ_{b_f} has been fixed in a series of discrete steps between 1.35 GHz/atm (0.045 cm^{-1}/atm) and 3.0 GHz/atm (0.01 cm^{-1}). The FP method finds the best fit laser frequencies for these tests with consistency only when the data range is restricted to below total pressures of 0.79 atm (600 Torr). Given experimental errors for $k_{pf}(\nu)^0_l$ determinations (Table 5-1), the accuracy of σ_{b_f}' is assumed to be at best ± 10%. This translates to an absolute determination of σ_{b_f}' equals 2.40 ± 0.20 GHz/atm (0.079 ± 0.008 cm^{-1}/atm). The upper and lower optimum laser frequencies for the extreme bounds of σ_{b_f}' are found by linearly interpolating between the points of Figure 5-9 to be 71.0802 THz (2371.11 cm^{-1}) and 71.0784 THz (2371.05 cm^{-1}). A conservative assignment for laser frequency therefore is given by ν_l equals 71.0835 ± 0.0012 THz (2371.09 ± 0.04 cm^{-1}).

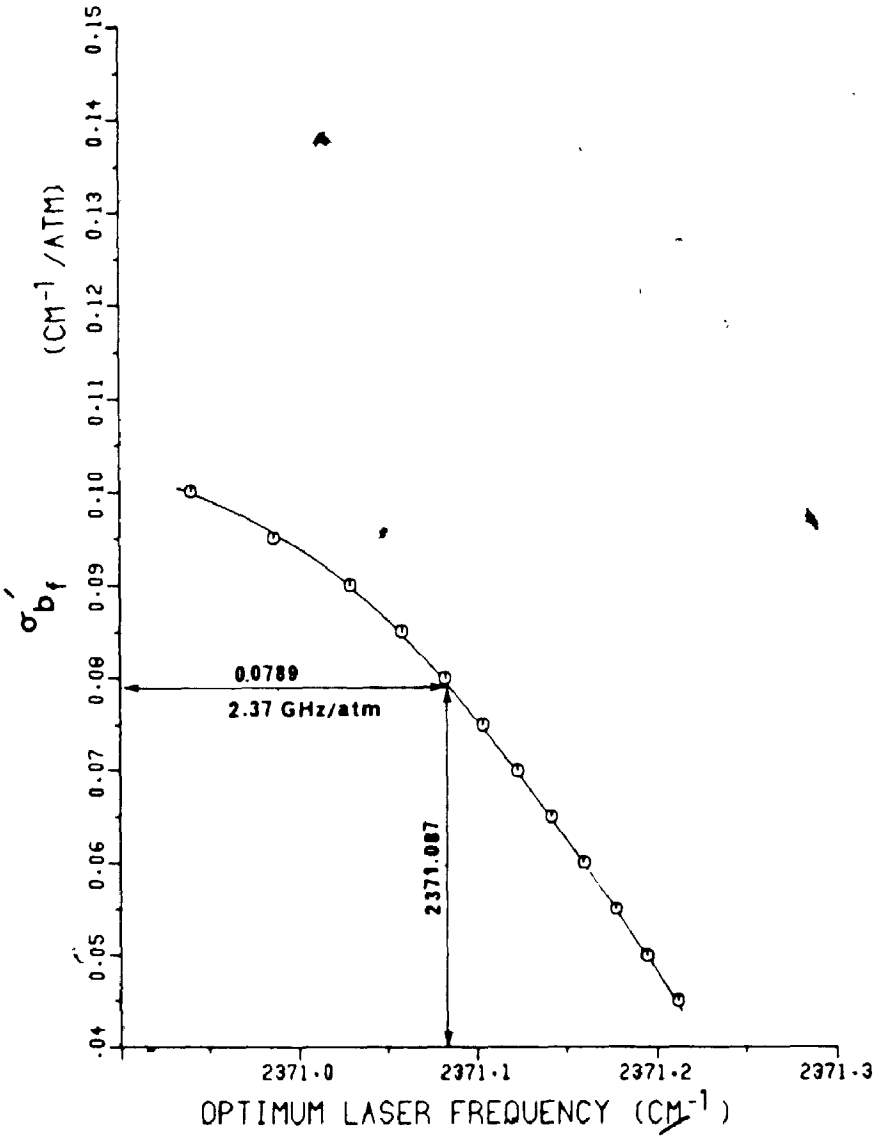

Figure 5-9: Optimization Results : Nitrogen Matrix

5.3.2. Pure CO_2 Absorption Tests

The experimental and data processing details for pure carbon dioxide tests are for the most part the same as previously described for nitrogen broadened determinations.

5.3.2.1. Experimental Details

For pure CO_2 testing, the spectrometer intake manifold is evacuated, purged and the sample cell filled to the required pressure.

Two pathlengths are used for the determination of $k_{pa}(\nu)^{o}_{l}$. The fixed cell (19.8 cm) is used to examine a pressure range of 0.0013 atm (1 Torr) to 0.12 atm (90 Torr). The variable length cell is set to a pathlength of 2.0 cm and a range of 0.033 atm (25 Torr) to 0.33 atm (250 Torr) carbon dioxide pressures is tested. The sample absorption at higher carbon dioxide pressures is too strong for reliable measurements at the 2.0 cm pathlength. At shorter absorption cell pathlengths, the calculated $k_{pa}(\nu)^{o}_{l}$ values become less precise as the relative pathlength measuring error increases.

Below pressures of approximately 0.0013 atm (1 Torr), the absorption line bandwidths become so small that the laser line frequency is located in the extreme absorption line wings. Increasing the pathlength to 60 cm provides very little decrease in the observed transmission under these low concentration conditions[5]. Given these considerations, the final tested pressure range is restricted to between 0.0013 atm (1 Torr) and 0.33 (250 Torr).

---

[5]It was not possible to decrease the sample transmission to below 0.9 for carbon dioxide pressures in the range of 0.00066 atm (500 mTorr) to 0.0013 atm (1 Torr) at the 60 cm pathlength.

Laser operation and initial data processing are as described previously for nitrogen broadening tests.

5.3.2.2. Experimental Results

All transmission test results, specific instrument settings and calibration tests are found in Appendix G. To expedite the data processing stage, the 2.0 cm pathlength data is digitized only at two points on the sample and reference curves and a mean ratio calculated. Reference to the standard deviations listed for previous tests and previously published preprocessor calibration curves indicates that this will not introduce significant error to the final calculations.

The calculated transmissions at individual tested pressures are shown for the 2.0 cm and 19.8 cm paths in Figures 5-10 and 5-11 respectively. The curves superimposed on the points in both of the figures are described in the following section.

5.3.2.3. Calculations and Discussion

The initial pressure range chosen for the function optimization[6] is from 0.099 atm (75 Torr) to 0.33 atm (250 Torr) for the 2.0 cm pathlength. The normalized extinction coefficient $k_{pa}(\nu)^{o}_{l}$ is calculated from the appropriate form of Equation (5-6) for each experimental pressure.

The simplification of assigning an average value of σ_{b_a}' over the four absorption peaks under consideration and the boundary conditions imposed on σ_{b_a}' and ν_l are in effect as described in Section 5.3.1.3.

---

[6]The higher pressure range is selected to ensure that the gas sample is predominantly pressure broadened as described in Chapter 2

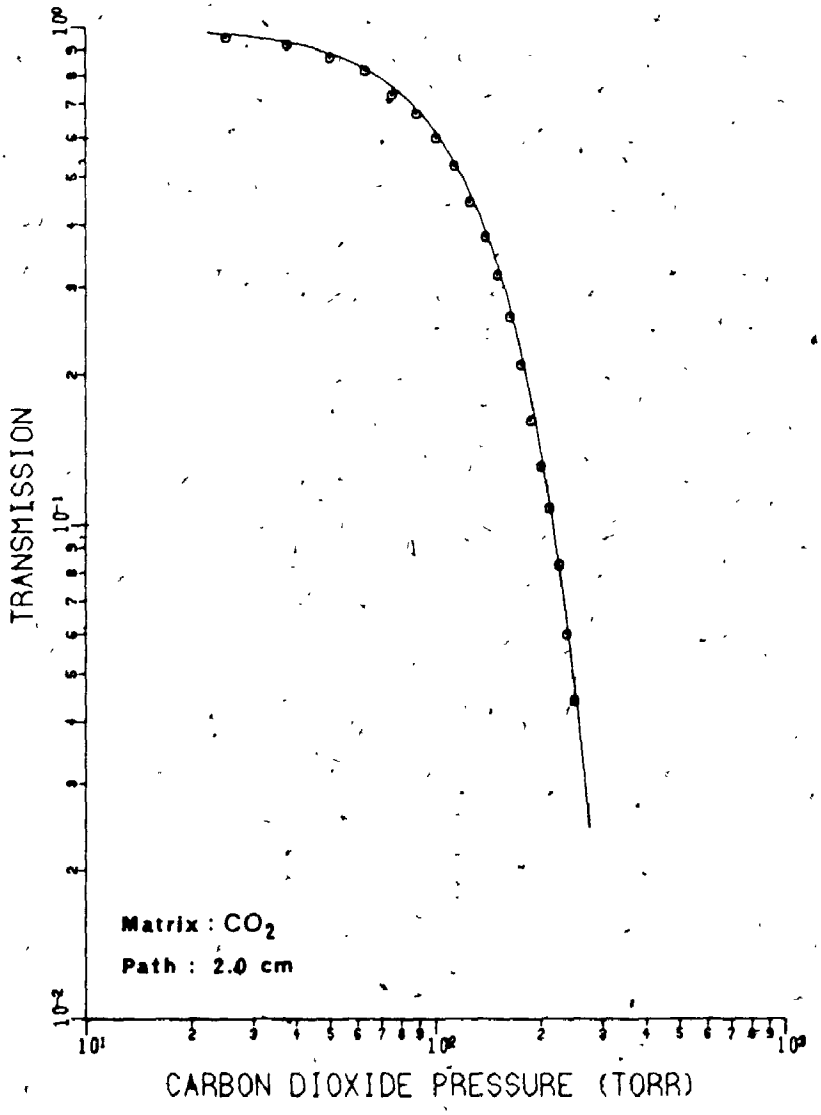

Figure 5-10: Pure CO_2 Transmission versus Pressure : 2.0 cm Path

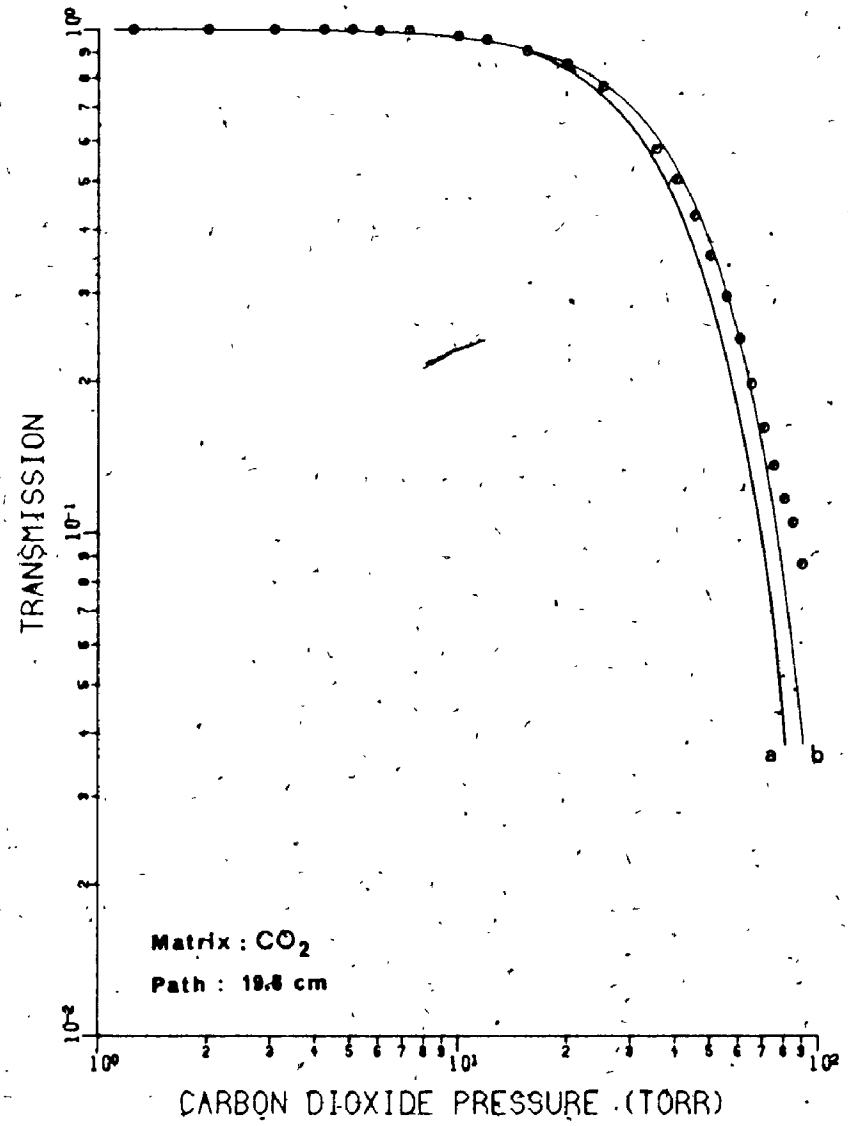

Figure 5-11: Pure CO_2 Transmission versus Pressure : 19.8 cm Path

The FP Method finds a global optimum for σ_{b_a}' and ν_l of 3.00 GHz/atm (0.100 cm^{-1}/atm) and 71.0847 THz (2371.13 cm^{-1}) respectively. By restricting the laser frequency allowed range to the wing of the R(30) absorption line, a local optimum is found for σ_{b_a}' and ν_l equal to 2.97 GHz/atm (0.099 cm^{-1}/atm) and 71.0730 THz (2370.74 cm^{-1}). These two function solutions are approximately symmetrical about the transparency window as expected.

The calculated values of $k_{pa}(\nu)^o_l$ and best function fits (Equation 5-8) for the two solutions are shown in Figures 5-12 and 5-13. Both curves show a strong linear trend as expected for location of the laser frequency in the wing of an absorption band. A good empirical relationship to describe the curve in the considered pressure range as found by the FP method is

$$k_{pa}(\nu)^o_l = 15.6\,p_a - 4.11\,p_a^2 \qquad (5-9)$$

where p_a : CO_2 pressure in atmospheres

Error bars are not shown in Figures 5-12 and 5-13, however, at higher pressures and associated low transmissions, the calculated values are limited to $\pm$ 10% as discussed for the nitrogen broadened data. The results of optimum laser frequency determinations for fixed σ_{b_a}' are shown for the R(30) and R(32) line overlaps in Figures 5-14 and 5-15 respectively. As noted in Section 5.3.1.3, the error bounds may be estimated and the results summarized as

$$\sigma_{b_a}' = 3.00 \pm 0.30 \text{ GHz/atm}$$
$$\sigma_{b_a}' = 0.100 \pm 0.010 \text{ cm}^{-1}\text{/atm}$$
$$\nu_l = 71.0847 \pm 0.0008 \text{ THz}$$

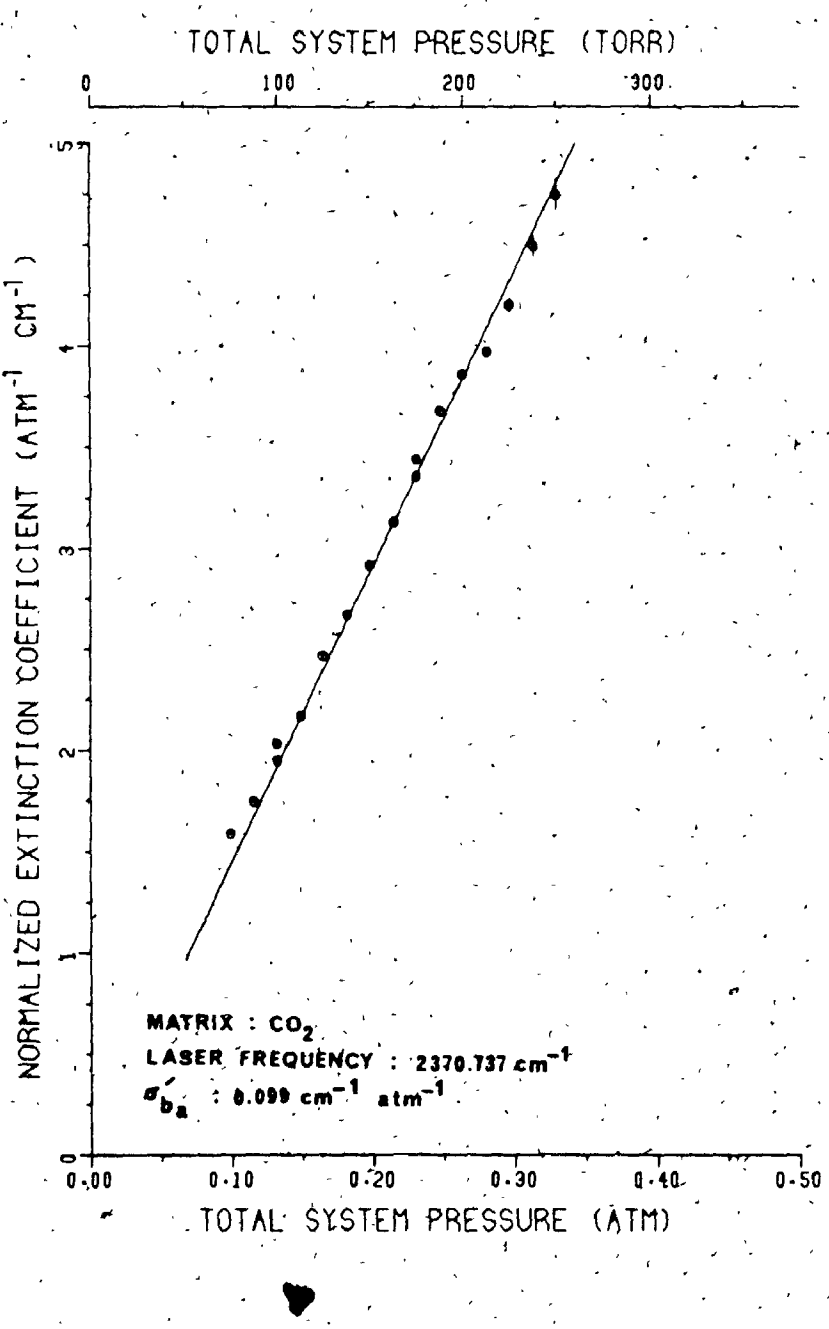

Figure 5-12: Normalized Extinction Coefficients : Pure CO_2 (1)

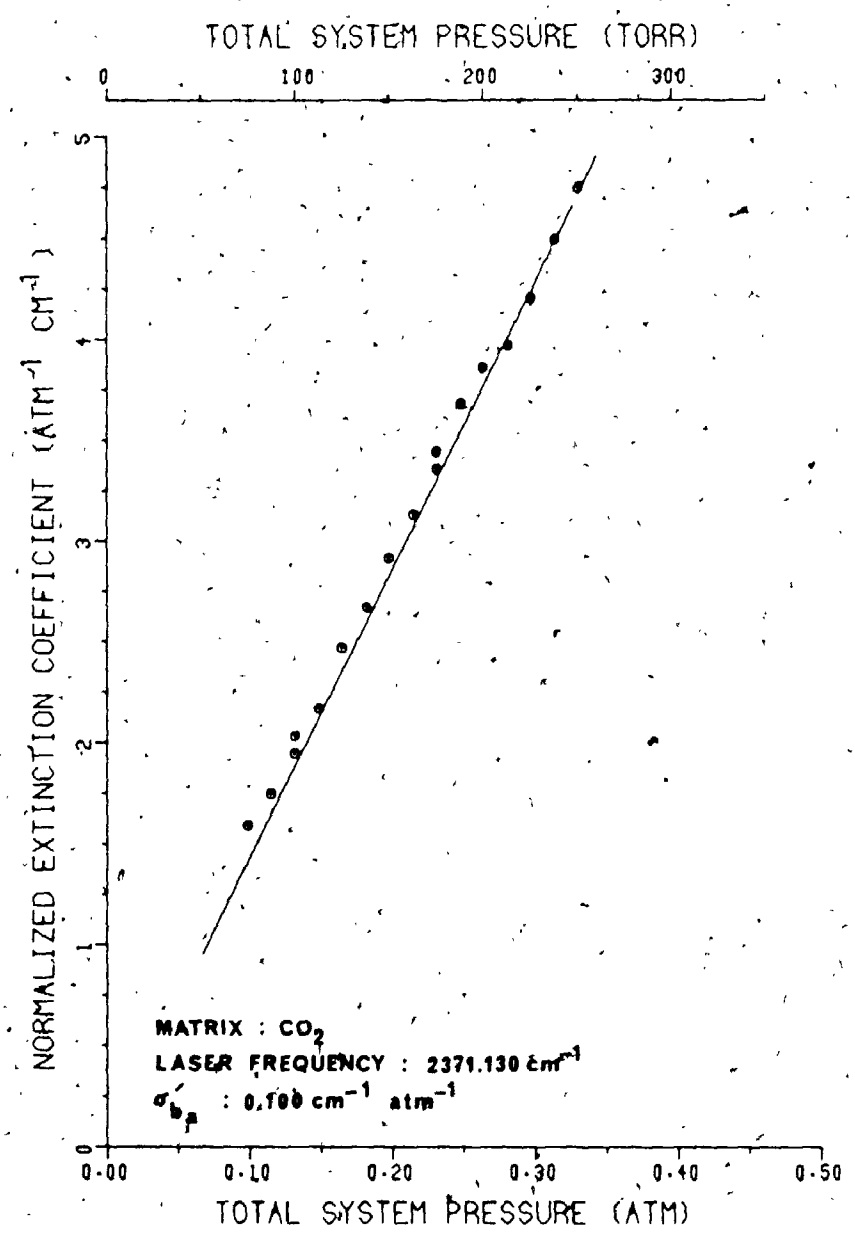

Figure 5-13: Normalized Extinction Coefficients : Pure CO_2 (2)

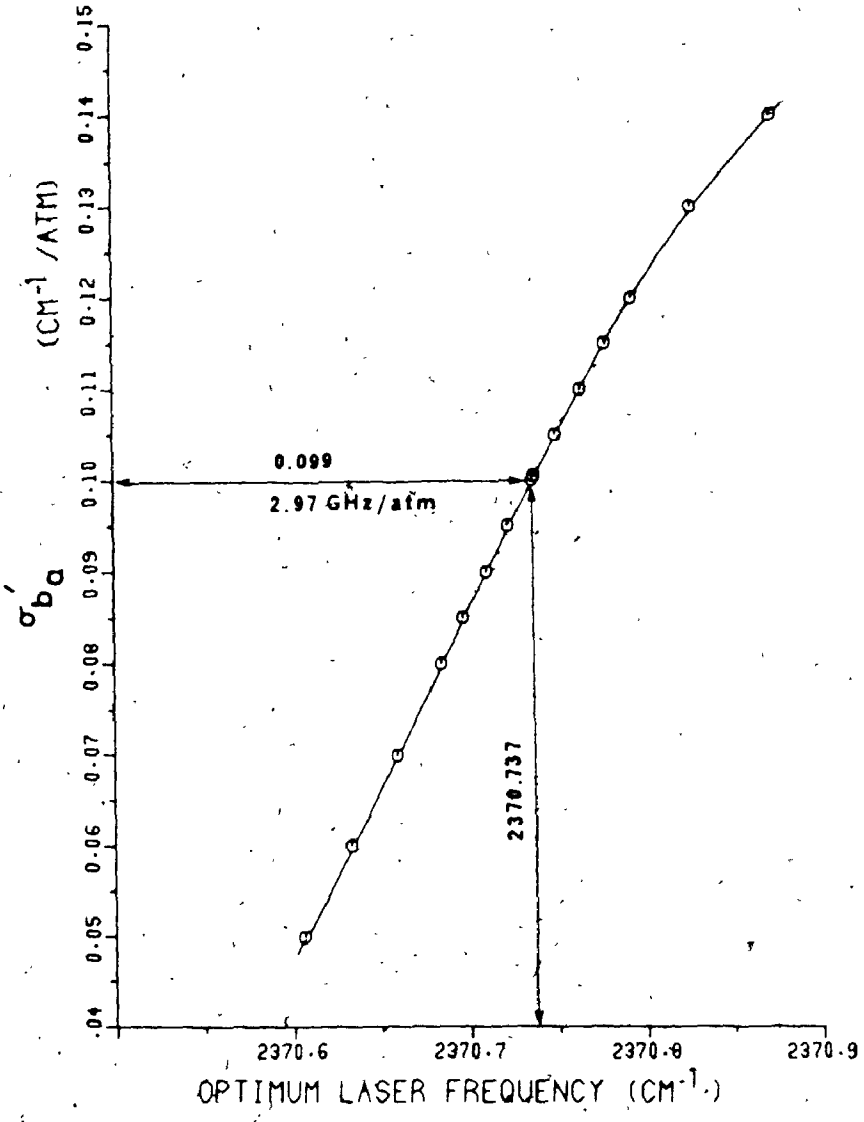

Figure 5-14: Optimization Results : Pure CO_2

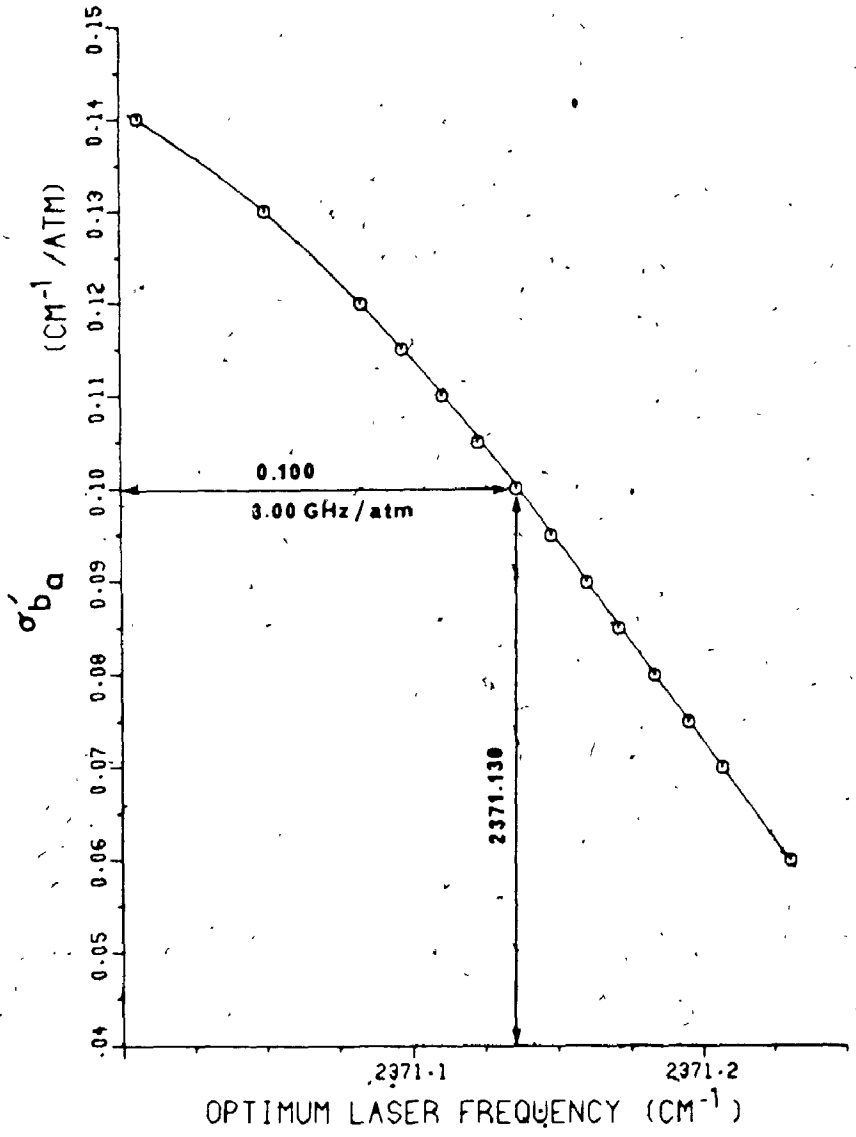

Figure 5-15: Optimization Results : Pure CO_2

$$\nu_l = 2371.13 \pm 0.03 \text{ cm}^{-1}$$

and

$$\sigma_{b_a}' = 2.97 \pm 0.80 \text{ GHz/atm}$$

$$\sigma_{b_a}' = 0.099 \pm 0.010 \text{ cm}^{-1}/\text{atm}$$

$$\nu_l = 71.0730 \pm 0.0008 \text{ THz}$$

$$\nu_l = 2370.74 \pm 0.03 \text{ cm}^{-1}$$

A calculated ratio of 1.27 for $\sigma_{b_a}'/\sigma_{b_f}'$ compares well to the published values of 1.21 (Burch et. al. [15]) and 1.25 (Belov et. al. [51]) (26).

The optimum values for σ_{b_a}' are substituted into Equations (5-6) to (5-8) and the expected transmissions calculated for the entire range of pressures for both 2.0 and 19.8 cm pathlengths. The curves are superimposed on the experimental data points in Figures 5-10 and 5-11 (Curve a). The results calculated for the two optimum laser frequencies cannot be distinguished in graphical form with this scaling and have been plotted as one curve.

The curve fit for the 2.0 cm path is excellent over the entire data range and further processing with more complex models[7] is considered unnecessary. Curve a in Figure 5-11 is shifted slightly towards the low pressure side of the graph: Curve b is a plot of the same function with the pathlength decreased by 5%. The fit is within experimental error in both cases for these data points with the parameters calculated at the shorter pathlength. As with the higher pressure carbon dioxide absorption data, further processing of the low pressure points will not provide further insight into the absorption process.

---

[7] An example would be the Voigt function described in Section 2.2.5.

Chapter Six
Conclusions and Recommendations

The laser resonance absorption spectrometer has been shown to be a viable instrument for the quantitative analysis of carbon dioxide. The unit functions accurately between sample transmissions of 10% to 90%. The low transmission boundary may be decreased by tilting the front window of the absorption cell to remove back reflected radiation from the beam path.

For pure carbon dioxide samples in the pressure range of 0.0016 atm (1.25 Torr) to 0.33 atm (250 Torr), a fixed frequency Lorentzian pressure broadening model provided a good characterization of the bandshape function. The laser frequency cannot be located absolutely with this type of absorption data but may be determined relative to the centre frequency of one of two overlapping carbon dioxide absorption lines. The best Lorentzian function fit as found by the Fletcher-Powell [97] optimization method corresponds to a determined laser frequency located in the CO_2 R(32) line shoulder of 71.0847 ± 0.0008 THz (2371.13 ± 0.03 cm^{-1}). An average pressure dependent broadening cross section, σ_{b_a}', over the R(28), R(30), R(32) and R(34) CO_2 absorption lines of 3.00 ± 0.30 GHz/atm (0.100 ± 0.010) was determined for CO_2 absorption at this laser frequency.

A second function optimum for the absorption data was found in the wing of the R(30) line at a laser frequency of 71.0730 ± 0.0008 THz (2370.74 ± 0.03 cm^{-1}) with a self broadening cross section of 2.97 ± 0.30 GHz/atm (0.099 ± 0.010 cm^{-1}/atm). The two determined laser frequencies are approximately symmetrical about the extinction coefficient minimum (transparency window)

at 71.0743 THz (2370.92 cm^{-1}) as predicted in Section 5.3.1.3. Both determined laser frequency optima lie between the theoretical [52] and previously observed [52] $3s_2 \rightarrow 3p_1$ laser transition frequencies.

The normalized extinction coefficient for 1 atmosphere total pressure nitrogen broadened carbon dioxide absorption at the laser frequency has been determined as 9.90 ± 1.49 cm^{-1} atm^{-1}. The experimental data over a range of 0.13 atm (100 Torr) to 1.18 atm (900 Torr) total pressure at low carbon dioxide concentrations fits well with the Lorentzian model as described for the pure CO_2 case. The optimum laser frequency and broadening cross section, σ_{b_f}', for the experimental data are 71.0835 ± 0.0012 THz (2371.09 ± 0.04 cm^{-1}) and 2.40 ± 0.24 GHz/atm (0.079 ± 0.008 cm^{-1}/atm). The self broadening coefficient of carbon dioxide with respect to nitrogen was determined as 1.27 by the method.

The laser delivers 3 mW of power under low flow rate conditions with a 50 mA discharge current. The output power is not sensitive to helium:neon concentration ratios in the region of 5:1 to 10:1 and is a maximum at total pressures between 0.0013 atm (1 Torr) and 0.0026 atm (2 Torr).

The laser fill gas becomes poisoned by atmospheric gases over a time period of roughly one half hour until failure occurs. It is recommended that permanent laser installations utilize a sealed tube design for longer laser lifetimes.

Appendix A
Carbon Dioxide Assymetric Stretching Frequencies

LINE	P		R	
	Obs.	Calc.	Obs.	Calc.
0	N/A	N/A	--------	2349.97
2	--------	2347.63	--------	51.50
4	--------	46.04	--------	53.01
6	--------	44.42	--------	54.49
8	--------	42.78	--------	55.95
10	--------	41.12	--------	57.38
12	--------	39.43	--------	58.78
14	--------	37.71	--------	60.16
16	--------	35.97	--------	61.52
18	--------	34.20	--------	62.86
20	--------	32.41	--------	64.16
22	--------	30.60	--------	65.44
24	--------	28.77	--------	66.70
26	--------	26.91	--------	67.93
28	--------	25.02	--------	69.13
30	--------	23.11	2370.36	--------
32	--------	21.17	71.48	--------
34	--------	19.21	72.65	--------
36	--------	17.23	73.71	--------
38	--------	15.22	74.79	--------
40	--------	13.19	75.83	--------
42	--------	11.13	76.87	--------
44	--------	09.05	77.88	--------
46	2306.96	--------	78.86	--------
48	04.84	--------	79.80	--------
50	02.70	--------	80.74	--------
52	00.56	--------	81.65	--------
54	2298.38	--------	82.51	--------
56	96.03	--------	83.38	--------
58	93.81	--------	84.21	--------
60	--------	--------	85.01	--------
62	89.23	--------	85.79	--------
64	86.93	--------	86.55	--------
66	--------	--------	87.26	--------
68	82.21	--------	87.97	--------
70	--------	--------	88.64	--------
72	--------	--------	89.32	--------
74	--------	--------	89.91	--------
76	--------	--------	90.49	--------
78	--------	--------	91.10	--------
80	--------	--------	91.61	--------
82	--------	--------	92.16	--------
84	--------	--------	--------	--------
86	--------	--------	93.09	--------
88	--------	--------	93.55	--------
90	--------	--------	93.96	--------

From Reference 8 Frequencies - cm^{-1} - vacuum

Appendix B
Electronic Energy State Classification of Helium and Neon

The electronic energy levels of an atom are determined by the shell level number, orbital angular momentum (am) and spin am of each electron about the nucleus. These discrete quantities are characterized by quantum numbers n, l, and s respectively. Nucleus-electron and electron-electron interactions lead to atomic energies that, in general, may be classified according to overall orbital (L), spin (S) and total (J) am quantum numbers.

Helium is a two electron atom with single electron excited state energies classified by the Russell-Saunders (RS) coupling scheme [67]. In this notation, individual electron orbital am vectors are assumed to strongly couple to form **L**, individual spin vectors couple to form **S**, and the total am vector **J** is defined by the vector sum **L+S** such that J is allowed the values (L+S), (L+S+1),....., |L-S|. The energy state is represented by the symbol $nl\ ^{2S+1}L_J$ where, in addition to previously defined variables

n : main orbital quantum number of the promoted electron

l : orbital am quantum number of the promoted electron

(s=0, p=1, d=2, f=3)

2S+1 : multiplicity

L is designated by a capital letter following the sequence as noted for l above. In addition, the parity of the state is determined by summing the individual electron orbital am quantum numbers, $\sum_i l_i$. Odd parity (odd sum)

is listed by a superscript o at the right side of the term symbol. For the three helium energy levels considered in Figure 3-1, $\sum_i l_i$ equals zero in all cases and the superscript is omitted.

General selection rules for dipole radiation in the RS coupling scheme are [69]

$$\Delta l = \pm 1 \qquad \Delta L = 0, \pm 1$$

$$\Delta S = 0 \qquad S=0 \leftarrow | \rightarrow S=0$$

$$\Delta J = 0, \pm 1 \qquad J=0 \leftarrow | \rightarrow J=0$$

The parity must also change.

In the higher atomic number inert gases, promotion of one electron leaves a tightly bound core around which the electron circulates. Coupling in this instance is the interaction of the total am vector of the core $\mathbf{j}_c$ with first $\mathbf{l}$ and then $\mathbf{s}$ of the promoted electron. An intermediate quantum number K may be defined such that $\mathbf{K}=\mathbf{j}_c+\mathbf{l}$. $\mathbf{K}$ is then coupled with the electron spin to yield the total am $\mathbf{J}$ of magnitude $K \pm 1/2$.

This coupling scheme (J,l) as proposed by Racah [70] designates the energy levels as $nl[K]_J$ where the symbols are as defined previously. For neon levels, the promoted electron am l is listed as a primed value for levels belonging to the $^2P_{1/2}$ core; unprimed for those belonging to the $^2P_{3/2}$ parent [76]. Selection rules applicable to this coupling type are found on page 37.

Appendix C
Laser Cavity g Parameters

The stability of a periodic focussing system may be determined geometrically in terms of g parameters. For the purpose of this work, a two mirror optical system (M1, M2) is considered with both mirror focal points sharing a common axis connecting the centre points of both mirrors, and

$$g_1 = 1 - L/R_1 \qquad \text{(C-1)}$$

$$g_2 = 1 - L/R_2 \qquad \text{(C-2)}$$

where R_1 : M_1 radius of curvature

R_2 : M_2 radius of curvature

L : Mirror separation distance

The stability criterion in the configuration is defined as

$$0 \leq g_1 g_2 \leq 1 \qquad \text{(stable)}$$

$$g_1 g_2 < 0 \text{ or } g_1 g_2 > 1 \qquad \text{(unstable)}$$

A hemispherical type resonator as considered in Chapter 3 has one flat element of infinite radius of curvature (M_2) such that $g_2 = 1$. Reference to Equations (C-1) and (C-2) indicates that stable hemispherical type resonators require that the concave mirror (M_1) have a radius of curvature greater than the mirror separation distance.

Appendix D
Computer Programs

Absorption Band Simulation

```
C   BROAD FOR
C
C   This pprogram simulates the extinction coefficient
C   curve for carbon dioxide at nu3 in the laser region.
C
    DIMENSION ARRAY(7,80),Y(80)
    DIMENSION FREQL(80),A(3),FREQ(3),BHALF(7)
    FCTR=1.
    PI=3.14
    BIG=0.
    S=2706.
    FREQ(1)=2369.13
    FREQ(2)=2370.36
    FREQ(3)=2371.48
    A(1)=0.02374
    A(2)=0.02035
    A(3)=0.01712
    DO 3 J=1,7
    BHALF(J)=.75+FLOAT(J)*.25
    TOT=BHALF(J)/30.
    DO 2 K=1,80
    FREQL(K)=2370.49+FLOAT(K)*0.01
    SUM=0.
    DO 1 I=1,3
    DFSQ=(FREQL(K)-FREQ(I))**2
    SHAPE=TOT/(PI*(TOT**2+DFSQ))
    VK=A(I)*S*SHAPE
    SUM=SUM+VK
1   CONTINUE
    IF(SUM.GT.BIG) BIG=SUM
    ARRAY(J,K)=SUM
2   CONTINUE
3   CONTINUE
    SX=5.
    XMIN1=71.12
    DT1=.5
    K1=4
    DX1=0.025/SX
    CALL PLOTS(30,0,5,11.,3)
    CALL PLOT(2.,2.4,-3)
    CALL FACTOR(FCTR)
    CALL AXIS4(0.,0.,21HLASER FREQUENCY (THZ),21,-.15,-.125,
    1SX,0.,XMIN1,DX1,2,DT1,K1)
    SY=7.
    YMIN=0.
    DY=55./SY
    DTY=SY/11.
    KY=2
    CALL AXIS4(0.,0.,1H ,0,0.,.125,7.,90.,YMIN,DY,-1,DTY,KY)
    XMIN2=2370.5
    DX2=1./SX
    DT2=.5
    K2=5
    CALL AXIS4(0.,7.,21HLASER FREQUENCY (CM ),21,.15,.125,SX,0.,
    1XMIN2,DX2,1,DT2,K2)
    DO 5 J=1,7
    DO 4 K=1,80
    Y(K)=ARRAY(J,K)
4   CONTINUE
    CALL PLOT(0.,0.,3)
    CALL LINE4(FREQL,Y,80,1,XMIN2,DX2,YMIN,DY,0,0,0)
    IF(J.GT.1) GO TO 6
    CALL WHERE(PENX,PENY,FCTR)
    PKEEP=PENX+.15
    CALL NUMBER(PKEEP,PENY,.125,BHALF(J),0.,2)
```

```
      CALL WHERE(PENX,PENY,FCTR)
      PENX=PENX+.15
      CALL SYMBOL(PENX,PENY,.125,3HCHZ,0.,3)
      GO TO 5
    6 YNEW=Y(80)/DY
      CALL NUMBER(PKEEP,YNEW,.125,BHALE(J),0.,2)
      CALL WHERE(PENX,PENY,FCTR)
      PENX=PENX+.15
      CALL SYMBOL(PENX,PENY,.15,3HCHZ,0.,3)
    5 CONTINUE
      XL1=(2370.62-XMIN2)/DX2
      XL2=(2371.47-XMIN2)/DX2
      CALL PLOT(XL1,0.,3)
      CALL PLOT(XL1,6.,2)
      CALL ENDPLT
      STOP
      END
```

Laser Resonator Calculations

Waist Size

```
C       PROGRAM WAIST1.F10
C
C       THIS PROGRAM CALCULATES THE WAIST RADIUS OF A
C       HEMISPHERICAL GAUSSIAN BEAM
C
        DIMENSION R(40),W0(40),W1(40)
        PI=3.1415927
        RLAMDA=4.2
        XMIN=0.
        XDA=4.0
        YMIN=0.
        YDA=0.5
        CALL PLOTS(15.8,10.75,2)
        CALL PLOT(2.,1.5,-3)
        CALL AXIS4(0.,0.,22HMIRROR RADIUS (METERS),22,-.175,
       1-.125,5.,0.,XMIN,XDA,-1,.3125,4)
        CALL AXIS4(0.,0.,22HBEAM WAIST RADIUS (mm),25,.175,
       1.125,8.,90.,YMIN,YDA,-1,.5,4)
        DO 1 I=1,11
        N=0
        RL1=0.8+I*0.2
        SCALE=SQRT(RL1*RLAMDA/PI)
        DO 3 J=1,40
        R1=0.5*J+0.5
        G=1.-RL1/R1
        IF(G.LE.0.) GO TO 3
        IF(G.GE.1.) GO TO 3
        N=N+1
        R(N)=R1
        W0(N)=SCALE*(G/(1.-G))**(.25)
        WI(N)=SCALE*(1./(G*(1.-G)))**(.25)
        IF(W0(N).LT.4.) GO TO 3
        N=N-1
3       CONTINUE
        CALL LINE4(R,W0,N,1,XMIN,XDA,YMIN,YDA,0,0,0)
2       CONTINUE
1       CONTINUE
        CALL PLTERR(1)
        CALL ENDPLT
        STOP
        END
```

Beam Maximum Size

```
C       PROGRAM MAX.F10
C
C       THIS PROGRAM CALCULATES THE MAXIMUM BEAM
C       RADIUS OF A HEMISPHERICAL RESONATOR
C
        DIMENSION R(40),W0(40),W1(40)
        PI=3.1415927
        RLAMDA=4.2
        XMIN=0.
        XDA=4.0
        YMIN=0.
        YDA=0.5
        CALL PLOTS(15.8,10.75,2)
        CALL PLOT(2.,1.5,-3)
        CALL AXIS4(0.,0.,22HMIRROR RADIUS (METERS),22,-.175,
       1-.125,5.,0.,XMIN,XDA,-1,.3125,4)
        CALL AXIS4(0.,0.,24HMAXIMUM BEAM RADIUS (mm),24,.175,
       1.125,8.,90.,YMIN,YDA,-1,.5,4)
        DO 1 I=1,11
        N=0
        RL1=0.8+I*0.2
        SCALE=SQRT(RL1*RLAMDA/PI)
        DO 3 J=1,40
        R1=0.5*J+0.5
        G=1.-RL1/R1
        IF(G.LE.0.) GO TO 3
        IF(G.GE.1.) GO TO 3
        N=N+1
        R(N)=R1
        W0(N)=SCALE*(G/(1.-G))**(.25)
        W1(N)=SCALE*(1./(G*(1.-G)))**(.25)
        IF(W1(N).LT.4.) GO TO 3
        N=N-1
3       CONTINUE
        CALL LINE4(R,W1,N,1,XMIN,XDA,YMIN,YDA,0,0,0)
2       CONTINUE
1       CONTINUE
        CALL PLTERR(1)
        CALL ENDPLT
        STOP
        END
```

Beam Power Loss

```
C       PROGRAM POW.F10
C
C       THIS PROGRAM CALCULATES THE SINGLE PASS TRANSMISSION
C       FOR A GAUSSIAN BEAM AS A FUNCTION OF BEAM WAIST
C       RADIUS IN A 4.4 mm RADIUS TUBE.
C
        DIMENSION POW(60),W(60)
        N=0
        A=4.4
        DO 1 I=1,60
        W(I)=0.600+I*0.05.
        POW(I)=100.*(1.-EXP(-2.*(A/W(I))**2))
        IF(POW(I).LE.98.) GO TO 2
        N=N+1
1       CONTINUE
2       CALL PLOTS(15,8.,10.75,2)
        CALL PLOT(2.,1.5,-3)
        XMIN=0.
        DX=0.6
        YMIN=98.
        DY=0.25
        CALL AXIS4(0.,0.,16HBEAM RADIUS (mm),16
       1,-.175,-.125,5.,0.,XMIN,DX,-1,0.4166,4)
        CALL AXIS4(0.,0.,40HSINGLE PASS POWER
       1 TRANSMISSION (PERCENT),40,.175,.125,8.,90.,YMIN,DY,
       1-1,1.,4)
        CALL LINE4(W,POW,N,1,XMIN,DX,YMIN,DY,0,0,0)
        CALL PLTERR(1)
        CALL ENDPLT
        STOP
        END
```

Absorption Data Processing

The general interrelationships of the computer programs are given by Figure (5-7).

Digitizing Routine

```
C       PROGRAM DIGI.FOR
C
C       THIS PROGRAM ACCEPTS INPUT FROM A TEKTRONIX DIGITIZING
C       TABLET VIA A TEK 4010 TERMINAL AND STORES ABSOLUTE
C       SCALED VALUES IN A DESIGNATED FILE.
C
C       TO RUN THIS PROGRAM, TYPE: EX DIGI,REL:PLOT10/SEARCH
C
        DOUBLE PRECISION IFIL
        DIMENSION XP(4),YP(4)
        DATA IG/'Y'/
C
C       OPEN FILE AND CHECK VALIDITY
C
        WRITE(6,1017)
1       WRITE(6,1000)
        READ(6,1001) IFIL
        IF(IFIL.EQ.'          ') GO TO 1
        OPEN(UNIT=1,FILE=IFIL)
C
C       INITIALIZE PLOT10
C
        CALL INITT(120)
C
C       ACCEPT PAGE BOUNDARIES IN ANY ORDER FROM DIGITIZER
5       WRITE(6,1002)
C
        WRITE(6,1006)
        DO 2 I=1,4
        CALL ECHOFF
        CALL TABINT(0,0,0)
        CALL TABARM(0)
        CALL GETPNT(IH,IX,IY)
        CALL TABOFF
        CALL ECHON
        WRITE(6,1007) IH,IX,IY
        XP(I)=FLOAT(IX)
        YP(I)=FLOAT(IY)
2       CONTINUE
        WRITE(6,1009)
        READ(6,1015) IANS
        IF(IANS.NE.IG) GO TO 5
C
C       SORT THE SCALING POINTS
C
        CALL PAGE(XP,YP)
C
C       INPUT THE SCALING DATA
C
        WRITE(6,1003)
        WRITE(6,1004)
        READ(6,1010) XLL
        WRITE(6,1005)
        READ(6,1010) YLL
        YLR=YLL
```

```
      WRITE(6,1008)
      READ(6,1010) XUR
      WRITE(6,1005)
      READ(6,1010) YUR
      XUL=XLL
      YUL=YUR
      XLR=XUR
      YLR=YLL
C
C     COMPENSATE FOR MISALIGNMENT OF GRAPH AND TABLE AXES
C
      RAT=(YP(2)-YP(1))/(XP(2)-XP(1))
      ALPHA=ATAN(RAT)
C
C     CALCULATE ABSOLUTE SCALING FACTORS
C
      XSCALE=(XP(2)-XP(1))/(COS(ALPHA)*(XLR-XLL))
      YSCALE=(YP(4)-YP(1))/(COS(ALPHA)*(YUL-YLL))
C
C     PREPARE TO DIGITIZE POINTS
C
      WRITE(6,1018)
      WRITE(6,1016)
3     CALL ECHOFF
      CALL TABINT(0,0,0)
      CALL TABARM(0)
      CALL GETPNT(IH,IX,IY)
      CALL TABOFF
      CALL ECHON
      IF(IH.NE.29) GO TO 4
      IF(IH.EQ.32) GO TO 4
      ICOUNT=ICOUNT+1
C
C     ALIGN GRAPH AXES
C
      XT=FLOAT(IX)
      YT=FLOAT(IY)
      RAT2=(YT-YP(1))/(XT-XP(1))
      THETA=ATAN(RAT2)
      ANGLE=THETA-ALPHA
      XC=COS(ANGLE)*(XT-XP(1))/COS(THETA)
      YC=SIN(ANGLE)*(XT-XP(1))/COS(THETA)
C
C     SCALE THE ALIGNED POINTS
C
      XACT=(XC/XSCALE)+XLL
      YACT=(YC/YSCALE)+YLL
C     WRITE TO FILE
C
      WRITE(2,1012) XACT,YACT
C
C     WRITE TO SCREEN
C
      WRITE(6,1013) XACT,YACT
C
```

```
C       LOOP TO CONTINUE DIGITIZING
C
        GO TO 3
500     WRITE(6,1011)
        GO TO 1
4       CLOSE(UNIT=2,STATUS='KEEP')
        WRITE(6,1014) ICOUNT,IFIL
        CALL FINITT(0,0)
C
C       FORMAT STATEMENTS
C
1000    FORMAT('0','OUTPUT FILENAME : ',$)
1001    FORMAT(A10)
1002    FORMAT('0','ENTER PAGE BOUNDARY POINTS VIA TABLET PEN')
1003    FORMAT('0','ASSIGN PAGE BOUNDARY VALUES')
1004    FORMAT('0','LOWER LEFT : X VALUE :',$)
1005    FORMAT(12X,': Y VALUE :',$)
1006    FORMAT('0','HEADER',2X,'X VALUE',2X,'Y VALUE')
1007    FORMAT('0',3X,I2,5X,I4,5X,I4)
1008    FORMAT('0','UPPER RIGHT: X VALUE :',$)
1009    FORMAT(' ','BOUNDARIES OK? (Y/N):  ',$)
1010    FORMAT(F10.3)
1011    FORMAT(' ','I/O ERROR - TRY AGAIN')
1012    FORMAT(1X,E14.7,5X,E14.7)
1013    FORMAT('0',1X,F10.3,5X,F10.3)
1014    FORMAT(1X,'THERE WERE ',I4,' POINTS STORED IN FILE:   ',A10)
1015    FORMAT(A2)
1016    FORMAT('0','    X VALUE',8X,'Y VALUE')
1017    FORMAT('+','DIGITIZING PROGRAM')
1018    FORMAT('0','ENTER POINTS FROM TABLET')
C
C
        STOP
        END
```

```
C
C
      SUBROUTINE PAGE(X,Y)
C
C       THIS SUBROUTINE SCALES THE PAGE SIZE FOR DIGITLZING
C     CHART RECORDER GRAPHS USLNG PROGRAM DIG.FOR.
C     POINTS ARE PASSED AS ARRAYS X AND Y, EACH WITH 4 ELEMENTS
C     THAT ARE INPUT IN ANY ORDER. THE ROUTINE SORTS THE POINTS AS
C
C               X(4),Y(4) .---------------. X(3),Y(3)
C                         |               |
C                         |               |
C                         |               |
C               X(1),Y(1) .---------------. X(2),Y(2)
C
C        OUTPUT IS REWRITTEN INTO THE INPUT ARRAYS AS SHOWN.
C
      DIMENSION X(4),Y(4)
      ISTORE=0
      IFLAG=0
      K=4
1     I1=0
      DO 3 I=1,K
      I1=I1+1
      IF(I1.EQ.ISTORE) I1=I1+1
      J1=0
      DO 2 J=1,K
      J1=J1+1
      IF(J1.EQ.ISTORE) J1=J1+1
      IF(X(I1).LT.X(J1)) GO TO 3
2     CONTINUE
      IF(IFLAG.EQ.1) GO TO 5
      XMAX1=X(I1)
      ISTORE=I1
      IFLAG=1
      GO TO 4
3     CONTINUE
4     K=3
      GO TO 1
5     XMAX2=X(I1)
      IF(Y(ISTORE).LT.Y(I1)) GO TO 6
      XLR=X(I1)
      YLR=Y(I1)
      XUR=X(ISTORE)
      YUR=Y(ISTORE)
      GO TO 7
6     XLR=X(ISTORE)
      YLR=Y(ISTORE)
      XUR=X(I1)
      YUR=Y(I1)
7     IFLAG=0
      DO 8 L=1,4
      IF(L.EQ.I1) GO TO 8
      IF(L.EQ.ISTORE) GO TO 8
      IF(IFLAG.EQ.1) GO TO 9
```

```
            ISAVE=L
            IFLAG=1
    8       CONTINUE
    9       IKEEP=L
            IF(Y(ISAVE).LT.Y(IKEEP)) GO TO 10
            XLL=X(IKEEP)
            YLL=Y(IKEEP)
            XUL=X(ISAVE)
            YUL=Y(ISAVE)
            GO TO 11
   10       XLL=X(ISAVE)
            YLL=Y(ISAVE)
            XUL=X(IKEEP)
            YUL=Y(IKEEP)
   11       X(1)=XLL
            X(2)=XLR
            X(3)=XUR
            X(4)=XUL
            Y(1)=YLL
            Y(2)=YLR
            Y(3)=YUR
            Y(4)=YUL
            RETURN
            END
```

Scaling and Preliminary Calculations

```
C       PROGRAM INT.FOR
C
C       This program takes digitized data from program DIGI.FOR
C       in the form of REFERENCE and SAMPLE files, sorts both files
C       in ascending values of X and removes any double values of X
C       by assigning an average Y value.
C       The SAMPLE and REFERENCE files are then aligned to yield common
C       values of X by linearly interpolating the SAMPLE file to
C       correspond to REFERENCE file X values.
C       The program calculates the ratio of SAMPLE/REFERENCE at
C       every point, a corrected ratio, average ratio and standard
C       deviation. Output is in the form
C
C       LINE 1:(  0f points) (average ratio) (standard deviation)
C              (average percent error in ratio)
C
C              FORMAT(1X,I3,3(5X,E14.7))
C
C       LINES 2-EOF:(X value)(Y Reference value(YR))(Y Sample Value(YS))
C                   (Corrected ratio YC/YR)
C
C              FORMAT(1X,6E14.6)
C
        DOUBLE PRECISION IFIL1,IEIL2,IOFIL
        DIMENSION XR(500),YR(500)
        DIMENSION XS(500),YS(500)
        DIMENSION TX(500), TYS(500),TYR(500)
        DIMENSION CRAT(500)
C
C       ASSIGN CORRECTION FACTOR
C
        ALPHA=0.013
C
C       ASSIGN I/O DEVICE NUMBERS
C
        IN1=2
        IN2=2
        IOUT=2
C
C       ASSIGN INPUT FILENAMES AND READ DATA
C
1       WRITE(6,1000)
        READ(6,1001) IFIL1
        WRITE(6,1010)
        READ(6,1011,ERR=4) ICS
        WRITE(6,1012)
        READ(6,1013) TOTS
        IF(IFIL1.NE.'          ') GO TO 2
        WRITE(6,1002)
        GO TO 1
2       OPEN(UNIT=IN1,FILE=IFIL1)
        DO 3 I=1,500
        READ(IN1,1003,END=5,ERR=4) XS(I),YS(I)
3       CONTINUE
        GO TO 5
```

```
4       WRITE(6,1004)
        GO TO 1
5       NS=I-1
        WRITE(6,1005) NS,IFIL1
        CLOSE(UNIT=IN1,DISPOSE='SAVE')
6       WRITE(6,1006)
        READ(6,1001) IFIL2
        WRITE(6,1010)
        READ(6,1011,ERR=9) IGR
        WRITE(6,1012)
        READ(6,1013) TOTR
        IF(IFIL2.NE.'            ') GO TO 7
        WRITE(6,1002)
        GO TO 6
7       OPEN(UNIT=IN2, FILE=IFIL2)
        DO 8 I=1,500
        READ(IN2,1003,END=10,ERR=9) XR(I),YR(I)
8       CONTINUE
        GO TO 10
9       WRITE(6,1004)
        GO TO 6
10      NR=I-1
        WRITE(6,1005) NR,IFIL2
        CLOSE(UNIT=IN2,DISPOSE='SAVE')
C
C       SORT THE INPUT FILES FROM LOW TO HIGH AND REMOVE
C       DOUBLE VALUES
C
        CALL SORT(XR,YR,NR,NNR)
        CALL SORT(XS,YS,NS,NNS)
C
C       ALIGN THE SAMPLE AND REFERENCE FILES BY LINEARLY
C       INTERPOLATING THE SAMPLE DATA
C
        CAVE=0.
        K=1
        I=1
        J=1
11      IF(XS(J).LE.XR(I)) GO TO 12
        I=I+1
        IF(I.GT.NNR) GO TO 14
        GO TO 11
12      IF(XS(J+1).GE.XR(I)) GO TO 13
        J=J+1
        IF(J.GE.NNS) GO TO 14
        GO TO 12
13      SLOPE=(YS(J+1)-YS(J))/(XS(J+1)-XS(J))
        TYS(K)=(SLOPE*(XR(I)-XS(J))+YS(J))/FLOAT(IGS)
        TYR(K)=YR(I)/FLOAT(IGR)
        TYS(K)=TYS(K)-ALPHA*TYR(K)
        TX(K)=XR(I)
C
C       APPLY CORRECTION FACTORS
C
        CRAT(K)=TYS(K)/TYR(K)
```

```
C
C       CALCULATE AVERAGES
C
        CAVE=CAVE+CRAT(K)
        I=I+1
        IF(I.GT.NNR) GO TO 15
        K=K+1
        GO TO 11
14      K=K-1
15      AVE=AVE/FLOAT(K)
        CAVE=CAVE/FLOAT(K)
C
C       ASSIGN OUTPUT FILE AND DEVICE
C
16      WRITE(6,1007)
        READ(6,1001) IOFIL
        IF(IOFIL.NE.'           ') GO TO 17
        GO TO 16
17      OPEN(UNIT=IOUT,FILE=IOFIL)
C
C       CALCULATE STANDARD DEVIATIONS
C
        RERR=0.
        SERR=0.
        SD2=0.
        DO 18 I=1,K
        RERR=RERR+TOTR*500./TYR(I)
        SERR=SERR+TOTS*500./TYS(I)
        SD2=(CRAT(I)-CAVE)**2+SD2
18      CONTINUE
        TERR=(RERR+SERR)/FLOAT(K)
        SD2=SQRT(SD2/FLOAT(K))
        WRITE(IOUT,1008) K,CAVE,SD2,TERR
        DO 19 I1=1,K
        WRITE(IOUT,1009) TX(I1),TYR(I1),TYS(I1),CRAT(I1)
19      CONTINUE
        CLOSE(UNIT=IOUT,DISPOSE='SAVE')
C
C       FORMAT STATEMENTS
C
1000    FORMAT(1X,'SAMPLE FILENAME :',$)
1001    FORMAT(A10)
1002    FORMAT('0','FILE NOT FOUND - TRY AGAIN')
1003    FORMAT(1X,E14.7,5X,E14.7)
1004    FORMAT('0','I/O ERROR - TRY AGAIN')
1005    FORMAT('0','THER ARE  ',I3,' POINTS IN FILE  ',A10)
1006    FORMAT('0','REFERENCE FILENAME :',$)
1007    FORMAT('0','OUTPUT DATA FILENAME : ',$)
1008    FORMAT(1X,I3,3(5X,E14.7))
1009    FORMAT(1X,4E14.6)
1010    FORMAT(1X,'REMOTE GAIN : ',$)
1011    FORMAT(I3)
1012    FORMAT(' ','CHART RECORDER FSD? (VOLTS) : ',$)
1013    FORMAT(F10.3)
        STOP
```

```
      END
C
C
C
      SUBROUTINE SORT(T,Y,NOLD,NNEW)
      DIMENSION T(500),Y(500)
      N=NOLD
1     BIG=0.
      DO 3 I=1,N
      IF(T(I).GE.BIG) GO TO 2
      GO TO 3
2     BIG=T(I)
      BIGY=Y(I)
      ISAVE=I
3     CONTINUE
      TEMP1=T(N)
      TEMP2=Y(N)
      T(N)=BIG
      Y(N)=BIGY
      T(ISAVE)=TEMP1
      Y(ISAVE)=TEMP2
      N=N-1
      IF(N.EQ.1) GO TO 10
      GO TO 1
10    ISAVE=1
      J=1
4     ICOUNT=1
5     IF(T(J).NE.T(J+1)) GO TO 6
      J=J+1
      ICOUNT=ICOUNT+1
      IF(J.EQ.NOLD) GO TO 6
      GO TO 5
6     T(ISAVE)=T(J)
      TEMP=0.
      DO 7 I=1,ICOUNT
      K=J-ICOUNT+I
      TEMP=TEMP+Y(K)
7     CONTINUE
      Y(ISAVE)=TEMP/FLOAT(ICOUNT)
      ISAVE=ISAVE+1
      J=J+1
      IF(J.GT.NOLD) GO TO 8
      GO TO 4
8     NNEW=ISAVE-1
      RETURN
      END
```

Organizing Routines

```
C   CONVER.FOR
C
C   This program prepares data for the PDP10 SREG linear
C   regression program.
C
    DIMENSION X(20),Y(20)
    DOUBLE PRECISION IFIL
C
C   ASK FOR OLD FILENAME
C
1   WRITE(6,1000)
    READ(6,1001) IFIL
    IF(IFIL.NE.'          ') GO TO 2
    WRITE(6,1003)
    GO TO 1
2   OPEN(UNIT=IN,FILE=IFIL)
    READ(IN,1004) NP
    X(1)=0.
    Y(1)=0.
    I=NP+1
    DO 3 J=1,NP
    READ(IN,1005) X(J+1),CRAP,Y(J+1),CRAP2
3   CONTINUE
    CLOSE(UNIT=IN,DISPOSE='SAVE')
C
C   ASK FOR NEW FILENAME
4   WRITE(6,1006)
    READ(6,1001) IFIL
    IF(IFIL.NE.'          ') GO TO 5
    WRITE(6,1003)
    GO TO 4
5   OPEN(UNIT=IN,FILE=IFIL)
    DO 6 K=1,I
    WRITE(IN,1007) X(K),Y(K)
6   CONTINUE
    CLOSE(UNIT=IN,DISPOSE='SAVE')
C
C   FORMAT STATEMENTS
C
1000        FORMAT(' ','INPUT FILENAME? : ',$)
1001        FORMAT(A10)
1003        FORMAT(' ','FILE NOT FOUND - TRY AGAIN')
1004        FORMAT(1X,I3)
1005        FORMAT(1X,4(5X,E14.7))
1006        FORMAT('0','NEW FILENAME? : ',$)
1007        FORMAT(1X,2E16.8)
    STOP
    END
```

```
C       PROGRAM COMBIN.FOR
C
C       This program takes input from the user that has
C       been generated by INT.FOR and combines it into
C       one file for plotting by GRAPH.FOR.
C
C       To run, type EX COMBIN.FOR
C
        DIMENSION PP(25),PPE(25),T(25),TE(25),TLN(25)
        DOUBLE PRECISION IFIL
        DATA IC/'Y '/
C
C       ASSIGN I/O DEVICE NUMBERS
C
        IN=2
C
C       INITIALIZE VARIABLES AND FLAGS
C
        I=0
1       IFLAG=0
        TERR=0.
        CAV=0.
C
C       ASK FOR INPUT FILE TO BE SORTED
C
        WRITE(6,1000)
2       READ(6,1001) IFIL
        OPEN(UNIT=IN,FILE=IFIL)
        READ(IN,1002) NP,AV,SD,ABSERR
        CLOSE(UNIT=IN,DISPOSE='SAVE')
C
C       CALCULATE PERCENT ERROR ABOUT THE MEAN
C
        SERR=100 *SD/(AV*SQRT(FLOAT(NP)))
C
C       ESTIMATE TOTAL PERCENT ERROR
C
        ABSERR=ABSERR+SERR
C
C       PATH TO DATA OR CALIBRATION
C
        IF(IFLAG.EQ.0) GO TO 3
        GO TO 4
C
C       ASSIGN TEMP PARAMETERS TO DATA
C
3       TERR=ABSERR
        DAV=AV
        IFLAG=1
C
C       ASK FOR CALIBRATION FILENAME
C
        WRITE(6,1005)
C
C       LOOP TO CALCULATE RATIO
```

```
C
      GO TO 2
C
C     CALCULATE CALIBRATION VALUES
C
4     TERR=ABSERR+TERR
      CAV=(AV+CAV)/FLOAT(IFLAG)
C
C     LEAVE LOOP IF CALIBRATION COMPLETE
C
      IF(IFLAG.EQ.2) GO TO 5
C
C     DETERMINE IF ANOTHER CALIBRATION IS REQUIRED
C
      WRITE(6,1006)
      READ(6 1007) IANS
      IF(IANS.NE.IG) GO TO 5
C
C     SET FLAG FOR LAST LOOP INDICATOR
C
      IFLAG=2
C
C     LOOP LAST TIME
C
      WRITE(6,1005)
      GO TO 2
C
C     INPUT DATA NOT IN RAW FILES FOR STORAGE
C
5     I=I+1
      WRITE(6,1008)
      READ(6,1004) PP(I)
C
C     ASSIGN ELEMENT NUMBERS FOR STORAGE
C
      T(I)=DAV/CAV
      TE(I)=TERR
      TLN(I)=ALOG(T(I))
C
C     DETERMINE IF MORE FILES ARE TO BE ENTERED
C
      WRITE(6,1009)
      READ(6,1007) IANS
      IF(IANS.NE.IG) GO TO 6
C
C     START AGAIN IF NEW FILE INPUT
C
      GO TO 1
C
C     ACCEPT OUTPUT FILENAME
C
6     WRITE(6,1010)
      READ(6,1001) IFIL
      OPEN(UNIT=IN,FILE=IFIL)
C
```

```
C       DUMP POINT TOTAL AT TOP OF FILE
C
        WRITE(IN,1011) I
C
C       WRITE DATA POINTS INTO FILE
C
        DO 7 J=1,I
        WRITE(IN,1012) PP(J),T(J),TLN(J),TE(J)
7       CONTINUE
C
C       SHUT DOWN
        CLOSE(UNIT=IN,DISPOSE='SAVE')
C
C       FORMAT STATEMENTS
C
1000    FORMAT(' ','INPUT FILENAME? : ',$)
1001    FORMAT(A10)
1002    FORMAT(1X,I3,3(5X,E14.7))
1004    FORMAT(F10.3)
1005    FORMAT(' ','CALIBRATION FILENAME? : ',$)
1006    FORMAT(' ','IS THERE ANOTHER CALIBRATION FILE? (Y/N) :',$)
1007    FORMAT(A2)
1008    FORMAT('0','CO2 PARTIAL PRESSURE? (TORR) : ',$)
1009    FORMAT('0','MORE DATA FILES? (Y/N) : ',$)
1010    FORMAT('0','OUTPUT FILENAME? : ',$)
1011    FORMAT(1X,I3)
1012    FORMAT(1X,4(5X,E14.7))
        STOP
        END
```

Graphical Output

```
C       PROGRAM GRAPH.FOR
C
C       This program graphs data files generated by
C       COMBIN.FOR in the form of pressure vs transmission.
C       To run, type:
C
C       DO TEK GRAPH (Terminal Output) or
C       DO PLOT GRAPH (Calcomp PLotter)
C
        DOUBLE PRECISION IFIL
        DIMENSION PP(20,20),T(20,20),TE(20,20)
        DIMENSION SL(20),FINT(20),ISAVE(20),PT(20)
        DATA IC/'Y '/
C
C       ASSIGN I/O DEVICE NUMBERS AND INITIALIZE VARIABLES
C
        IN=2
        TMIN=1.
        J=1
        PERR=0.1
C
C       ASSIGN GRAPH SCALING PARAMETERS
C
        SX=8.
        SY=5.5
        XMIN=0.
        DX=10./SX
        DTX=SX/20.
        HGT=.1
        HGT1=.125
        HGTS=.04
C
C       READ INPUT FILENAMES
C
1       WRITE(6,1000)
        READ(6,1001) IFIL
        OPEN(UNIT=IN,FILE=IFIL)
C
C       DETERMINE THE NUMBER OF POINTS IN FILE
C
        READ(IN,1002) NP
C
C       PAD THE BEGINNIG OF ARRAY FOR ZERO ABSORPTION
C
        PP(J,1)=0.
        T(J,1)=1.
        TE(J,1)=0.
C
C       READ PRESSURE/TRANSMISSION VALUES FOR TEST J
C
        ISAVE(J)=NP+1
        DO 2 K=2,ISAVE(J)
        READ(IN,1003) PP(J,K),T(J,K),GRAP,TE(J,K)
        IF(T(J,K).LE.TMIN) TMIN=T(J,K)
2       CONTINUE
```

```
C
C       ACCEPT DATA FROM TERMINAL
C
        WRITE(6,1011)
        READ(6,1007) CELL
        WRITE(6,1004)
        READ(6,1005) IPT
        PT(J)=FLOAT(IPT)
        WRITE(6,1006)
        READ(6,1007) SL(J)
        WRITE(6,1008)
        READ(6,1007) FINT(J)
C
C       ASK IF MORE POINTS COMING
C
        WRITE(6,1009)
        READ(6,1010) IANS
        IF(IANS.NE.IG) GO TO 3
        J=J+1
        GO TO 1
C
C       PREPARE TO PLOT
C
3       YMIN=-1.
        DY=SY
        IF(TMIN.GT.0.1) GO TO 4
        YMIN=-2.
        DY=SY/2.
4       CONTINUE
        CALL PLOTS(30.11.,8.5,1)
        CALL PLOT(1.5,1.5,-3)
        CALL AXIS4(0.,0.,29HPARTIAL PRESSURE - CO2 (TORR),
        129.,-.175,-.125,SX,0.,XMIN,DX,-1,DTX,2)
        CALL AXIS4(0.,0.,12HTRANSMISSION,12,.175,.125,
        1SY,90.,YMIN,DY,-2,0.,0)
        CALL SYMBOL(.25,.25,HGT1,17HMATRIX : NITROGEN,0.,17)
        CALL SYMBOL(.25,.5,HGT1,18HPATHLENGTH (CM) :  ,0.,18)
        CALL WHERE(PENX,PENY,FCTR)
        CALL NUMBER(PENX,PENY,HGT1,CELL,0.,1)
        CALL PLOT(0.,SY,-3)
        DO 6 I1=1,J
        BIG=0.
        DO 5 I2=1,ISAVE(I1)
        Y=ALOG10(T(I1,I2))*DY
        X=PP(I1,I2)/DX
        IF(X.GE.BIG) BIG=X
        CALL SYMBOL(X,Y,HGTS,1,0.,-1)
        IF(I2.EQ.1) GO TO 5
        B1=X-PERR/DX
        B2=X+PERR/DX
        CALL SYMBOL(B1,Y,0.03,13,0.,-1)
        CALL SYMBOL(B2,Y,0.03,13,0.,-2)
        YERR1=ALOG10(T(I1,I2)*(1.+0.01*TE(I1,I2)))*DY
        YERR2=ALOG10(T(I1,I2)*(1.-0.01*TE(I1,I2)))*DY
        CALL SYMBOL(X,YERR1,0.03,13,90.,-1)
```

```
      CALL SYMBOL(X,YERR2,0.03,13,90.,-2)
5     CONTINUE
      SET=BIG+0.25
      YNEW=(SET*DX*SL(I1)+FINT(I1))*DY/2.303
      GLABEL=SET+.25
      CALL NUMBER(GLABEL,YNEW,HGT1,PT(I1),0.,-1)
      CALL WHERE(PENX,PENY,FCTR)
      CALL SYMBOL(PENX,PENY,HGT1,5H TORR,0.,5)
      YY=PENY-1.5*HGT1
      CALL SYMBOL(GLABEL,YY,HGT1,5HTOTAL,0.,5)
      CALL PLOT(SET,YNEW,3)
      YNEW=FINT(I1)*DY/2.303
      CALL PLOT(0.,YNEW,2)
6     CONTINUE
C
C     FORMAT STATEMENTS
C
1000  FORMAT(' ','INPUT FILENAME? : ',$)
1001  FORMAT(A10)
1002  FORMAT(1X,I3)
1003  FORMAT(1X,4(5X,E14.7))
1004  FORMAT('0','SYSTEM TOTAL PRESSURE? (TORR) (I4): ',$)
1005  FORMAT(I4)
1006  FORMAT(' ','BEST FIT SLOPE? (F15.8) : ',$)
1007  FORMAT(F15.8)
1008  FORMAT(' ','BEST FIT INTERGEPT? (F15.8) : ',$)
1009  FORMAT('0','IS THERE MORE TO COME? (Y/N) : ',$)
1010  FORMAT(A2)
1011  FORMAT(' ','PATHLENGTH (CM)? (F15.8): ',$)
      CALL PLTERR(1)
      CALL ENDPLT
      STOP
      END
```

```
C       PROGRAM PLOT.FOR
C
C       This  program takes data from INT.FOR and plots
C       SAMPLE, REFERENCE, and INTENSITY RATIO GRAPHS.
C
C       To run on TEK, type DO TEK PLOT1, or the full
C       command of EX PLOT1,@REL:TEK
C
        DOUBLE PRECISION IFIL1,IPT,IT,IC,IC1
        DATA IC/'Y '/
        DIMENSION X(500),YR(500),YS(500)
        DIMENSION CRAT(500)
C
C       INITIALIZE FLAGS
C
        IFLAG1=0
C
C       ASSIGN Y AXIS LENGTH FOR INTENSITY GRAPH
C
        SI=3.
C
C       ASSIGN SCALING FACTOR TO DETERMINE PAGE SIZE
C
        HGT=.130
        YY=8.75
        XX=0.
        FCTR=.9
C
C       ASSIGN SCALING FACTORS FOR SAMPLE/REFERENCE GRAPHS
C
        XMIN=0.
        YMIN=0.
        DX=10.
        DY=0.222222
        IN1=2
C
C       ACCEPT INPUT FILE
C
1       WRITE(6,1000)
        READ(6,1001) IFIL1
        IF(IFIL1.NE.'          ') GO TO 2
        WRITE(6,1002)
        GO TO 1
2       OPEN(UNIT=IN1,FILE=IFIL1)
        READ(IN1,999) NP,CRINT,SD2,BULL
C
C       NORMALIZE CURVES
C
        SMC=1.
        BIGC=0.
        BIGYR=0.
        BIGYS=0.
        DO 3 I=1,NP
        READ(IN1,1003) X(I),YR(I),YS(I),CRAT(I)
        IF(YR(I).GE.BIGYR) BIGYR=YR(I)
```

```
      IF(YS(I).GE.BIGYS) BIGYS=YS(I)
      IF(CRAT(I).GE.BIGC) BIGC=CRAT(I)
      IF(CRAT(I).LE.SMC) SMC=CRAT(I)
3     CONTINUE
      BIG=AMAX1(BIGYR,BIGYS)
      ZERO=X(1)
      DO 4 I=1,NP
      YR(I)=YR(I)/BIG
      YS(I)=YS(I)/BIG
      X(I)=X(I)-ZERO
4     CONTINUE
C
C     ACCEPT GRAPH HEADERS
C
5     WRITE(6,1006)
      READ(6,1007,ERR=5) IT
6     WRITE(6,1009)
      WRITE(6,1016)
      WRITE(6,1021)
      WRITE(6,1017)
      READ(6,1015,ERR=6) IFLAG
      IF(IFLAG.EQ.2) GO TO 11
      IF(IFLAG.EQ.3) GO TO 11
7     WRITE(6,1008)
      READ(6,1022,ERR=7) PP
8     WRITE(6,1011)
      WRITE(6,1012)
      WRITE(6,1013)
      WRITE(6,1014)
      READ(6,1015,ERR=8) MT
      IF(MT.EQ.3) GO TO 10
9     WRITE(6,1010)
      READ(6,1001,ERR=9) IPT
10    WRITE(6,1023)
      READ(6,1007,ERR=10) IC
      WRITE(6,1024)
      READ(6,1025) IANS
      IF(IANS.NE.IC) GO TO 11
      IFLAG1=1
      WRITE(6,1023)
      READ(6,1007) IC1
11    WRITE(6,1018)
      READ(6,1022,ERR=11) CELL
C
C     INITIALIZE PLOTTER
C
      CALL PLOTS(30,8.5,11.,3)
      CALL PLOT(2.,2.,3)
      CALL FACTOR(ECTR)
C
C     WRITE OUT HEADINGS
C
12    CALL SYMBOL(XX,YY,HGT,14HTRIAL NUMBER =,0.,14)
      CALL WHERE(PENX,PENY,ECTR)
      CALL SYMBOL(PENX,YY,HGT,IT,0.,10).
```

```
      CALL WHERE(PSAVE,PENY,FCTR)
      PSAVE=PSAVE+0.5
      YDOWN=YY-1.5*HGT
      CALL SYMBOL(XX,YDOWN,HGT,11HPATH (CM) :,0.,11)
      CALL NUMBER(PENX,YDOWN,HGT,CELL,0.,1)
      IF(IFLAG.NE.1) GO TO 12
      YDOWN=YDOWN-1.5*HGT
      CALL SYMBOL(XX,YDOWN,HGT,14HCALIBRATION  :,0.,14)
      CALL SYMBOL(PENX,YDOWN,HGT,IC,0.,7)
      IF(IFLAG1.NE.1) GO TO 13
      YDOWN=YDOWN-1.5*HGT
      CALL SYMBOL(PENX,YDOWN,HGT,IC1,0.,7)
13    IF(IFLAG.EQ.1) GO TO 14
      IF(IFLAG.EQ.3) GO TO 18
      CALL SYMBOL(PSAVE,YY,HGT,11HCALIBRATION,0.,11)
      GO TO 19
14    CALL SYMBOL(PSAVE,YY,HGT,21HCO2 PRESSURE (TORR) :,0.,21)
      CALL WHERE(PENX,PENY,FCTR)
      CALL NUMBER(PENX,YY,HGT,PP,0.,2)
      YY=YY-1.5*HGT
      IF(MT.EQ.3) GO TO 15
      CALL SYMBOL(PSAVE,YY,HGT,21HCELL PRESSURE (TORR):,0.,21)
      CALL SYMBOL(PENX,YY,HGT,IPT,0.,10)
      YY=YY-1.5*HGT
      GO TO 16
15    CALL SYMBOL(PSAVE,YY,HGT,12HMATRIX : CO2,0.,12)
      GO TO 19
16    IF(MT.NE.1) GO TO 17
      CALL SYMBOL(PSAVE,YY,HGT,17HMATRIX : NITROGEN,0.,17)
      GO TO 19
17    CALL SYMBOL(PSAVE,YY,HGT,12HMATRIX : AIR,0.,12)
      GO TO 19
18    CALL SYMBOL(PSAVE,YY,HGT,10HBACKGROUND,0.,10)
19    CALL AXIS4(0.,0.,14HTIME (SECONDS),14,-.175,-.125,6.,0.,XMIN,
     1DX,-1,.5,2)
      CALLAXIS4(0.,0.,20HNORMALIZED INTENSITY,20,.175,.125,4.5,90.,
     1YMIN,DY,1,.45,2)
      CALL LINE4(X,YS,NP,1,XMIN,DX,YMIN,DY,0,0,0)
      X0=X(NP)/DX+0.25
      Y0=YS(NP)/DY
      CALL SYMBOL(X0,Y0,.125,6HSAMPLE,0.,6)
      CALL LINE4(X,YR,NP,1,XMIN,DX,YMIN,DY,0,0,0)
      Y0=YR(NP)/DY
      CALL SYMBOL(X0,Y0,.125,9HREFERENCE,0.,9)
C
C     WRITE VALUES TO TERMINAL
C
      X6=0.5
      Y6=5.
      CALL SYMBOL(X6,Y6,HGT,9H(I) MEAN=,0.,9)
      CALL WHERE(PENX,PENY,FCTR)
      CALL NUMBER(PENX,PENY,HGT,CRINT,0.,4)
      CALL WHERE(PENX,PENY,FCTR)
      PENX=PENX+0.5
      CALL SYMBOL(PENX,Y6,HGT,2HS=,0.,2)
```

```
      CALL WHERE(PENX,PENY,FCTR)
      CALL NUMBER(PENX,Y6,HGT,SD2,0.,6)
      CALL WHERE(PENX,PENY,FCTR)
      PENX=PENX+0.5
      CALL SYMBOL(PENX,Y6,HGT,12H  OF POINTS=,0.,12)
      CALL WHERE(PENX,PENY,FCTR)
      XNUM=FLOAT(NP)
      CALL NUMBER(PENX,PENY,HGT,XNUM,0.,-1)
C
C     DO RATIO GRAPHS
C
      SCALE1=10.*SMC
      SCALE2=10.*BIGC+1.
      LOW=INT(SCALE1)
      IHIGH=INT(SCALE2)
      DI=FLOAT(IHIGH-LOW)/(SI*10.)
      IF(DI.NE.0.) GO TO 20
      DI=0.1/SI
20    YMIN=FLOAT(LOW)/10.
      DT=.02/DI
      K=5
      CALL PLOT(0.,5.1,-3)
      CALL AXIS4(0.,0.,15HINTENSITY RATIO,15,.175,.125,
     1SI,90.,YMIN,DI,2,DT,K)
      CALL LINE4(X,CRAT,NP,1,XMIN,DX,YMIN,DI,0,0,0)
21    CALL PLTERR(0)
      CALL ENDPLT
C
C     FORMAT STATEMENTS
C
999   FORMAT(1X,I3,3(5X,E14.7))
1000  FORMAT(1X,'INPUT FILENAME :',$)
1001  FORMAT(A10)
1002  FORMAT('0','FILE NOT FOUND - TRY AGAIN')
1003  FORMAT(1X,4E14.6)
1004  FORMAT('0','I/O ERROR - TRY AGAIN')
1005  FORMAT('0','THERE ARE  ',I3,' POINTS IN FILE  ',A10)
1006  FORMAT('0','TRIAL NUMBER? :',$)
1007  FORMAT(A10)
1008  FORMAT('0','CARBON DIOXIDE PRESSURE (TORR)? : ',$)
1009  FORMAT('0','RUN TYPE : (1) DATA')
1010  FORMAT(' ','TOTAL SYSTEM PRESSURE (TORR)? : ',$)
1011  FORMAT('0','MATRIX : (1) NITROGEN')
1012  FORMAT(' ',9X,'(2) AIR')
1013  FORMAT(' ',9X,'(3) CARBON DIOXIDE')
1014  FORMAT('0','MATRIX TYPE NUMBER? : ',$)
1015  FORMAT(I1)
1016  FORMAT(' ',11X,'(2) CALIBRATION')
1017  FORMAT('0','TYPE? : ',$)
1018  FORMAT('0','PATHLENGTH (CM)? :',$)
1019  FORMAT('0','DO YOU WISH TO ENABLE THE PLOTTER? (Y/N) :',$)
1020  FORMAT(A2)
1021  FORMAT(' ',11X,'(3) BACKGROUND')
1022  FORMAT(F5.2)
1023  FORMAT('0','CALIBRATION FILE NUMBER? :',$)
```

```
1024    FORMAT(' ','IS THERE ANOTHER CALIBRATION FILE? (Y/N): ',$)
1025    FORMAT(A2)
C
        STOP
        END
```

Appendix E
Transmission Curves

Note: From Reference [96]

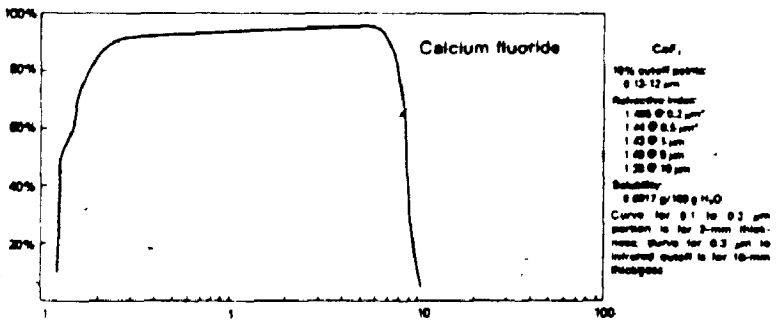

$$n_{CaF_2} \approx 1.40\ (4.2\ \mu m)\ ,\ \theta_b = \tan^{-1}(1.40)$$

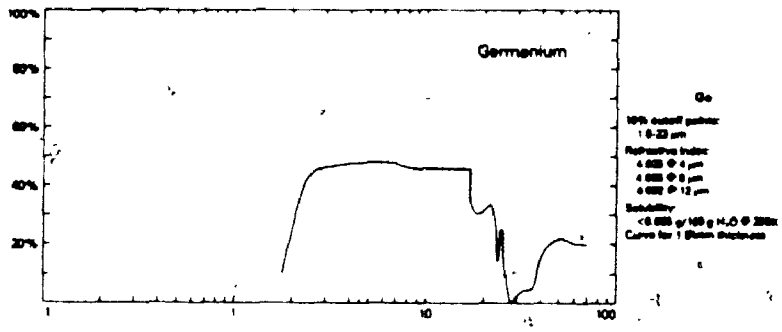

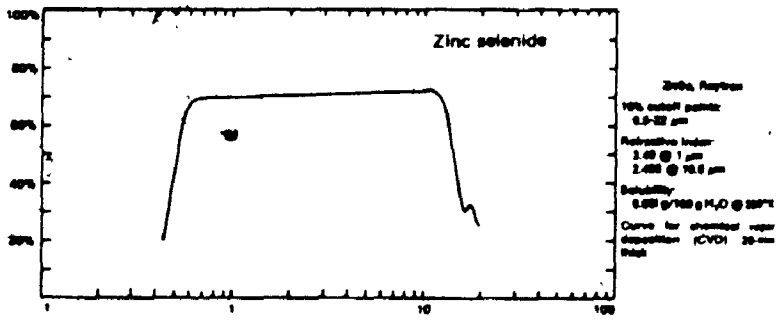

Appendix F
Laser Power Test Details

This appendix presents the experimental details for the helium neon $3s_2 \rightarrow 3p_1$ power measurements.

Detector

Type:PbSe Series 1000 Plate

(Infrared Industries Inc., Orlando, FL, USA)

Active Area: 4 x 4 mm

Resistance: 500 kΩ

D* (298 °K, 4.2 μm): 3 x 10^9 cm $Hz^{1/2}$/Watt

Preamplifier Gain: 100 (V/V)

High Frequency Modulator

Type: Bulova ONT-L8C

Frequency: 200 Hz

Modulation Depth: 100 %

Phase Lock Amplifier

Type: PAR Model 126

Sensitivity: 500 mV

Input LPF: 10 Hz

Input HPF: 3 KHz

Output Time Constant: 1 second

Zero Supress: Off

Chart Recorder

Type: Watanabe Servocorder 652

Full Scale Deflection: 5 V

XY Recorder

Type: Hewlett-Packard 7005B

Full Scale Deflection (X): 10 V

Full Scale Deflection (Y): 10 V

Appendix G
Absorption Test Data

This appendix presents the experimental details and test results for carbon dioxide absorption at 4.2 μm.

G.1. General Test Conditions

Detector

Type:PbSe Series 1000 Plate

(Infrared Industries Inc., Orlando, FL, USA)

Active Area: 4 x 4 mm

Resistance: 500 kΩ

D* (298 K, 4.2 μm): 3 x 10^9 cm $Hz^{1/2}$/Watt

Preamplifier Gain: 100 (V/V)

High Frequency Modulator

Type: Bulova ONT-L8C

Frequency: 200 Hz

Modulation Depth: 100 %

Phase Locked Dicke Chopper

Chopping Frequency: 13 Hz

Pulse Delay: 2 msec

Pulse Width: 73 msec

Duty Cycle (High): 90 %

Gated Amplifiers

Remote Gain: Sample (G_S): Variable

Reference (G_R): 1 (V/V)

Phase Lock Amplifier

Type: Keithley 840 Autoloc

Sensitivity: 100 mV

Input Mode: Wideband

Output Time Constant: Off

Zero Supress: Off

Trigger: Positive

Phase: 242

Output Low Pass Filter Module

Time Constant: 1 second

Chart Recorder

Type: Watanabe Servocorder 652

Full Scale Deflection:Sample (FSD_S): Variable

Reference (FSD_R): 2 volts

Speed: 120 mm/min

G.2. Background Correction Test Data

Override Values

Remote Gain : Reference (G_R): 0.1 (V/V)

(Note: A 20 dB attenuator was used at the input to the Reference Channel Gated Amplifier to prevent phase lock amplifier overload.)

Phase Lock Amplifier Sensitivity: 10 mV

Trial Values

Trial Number: BC.1

Remote Gain : Sample (G_S): 2 (V/V)

FSD_S: 500 mV

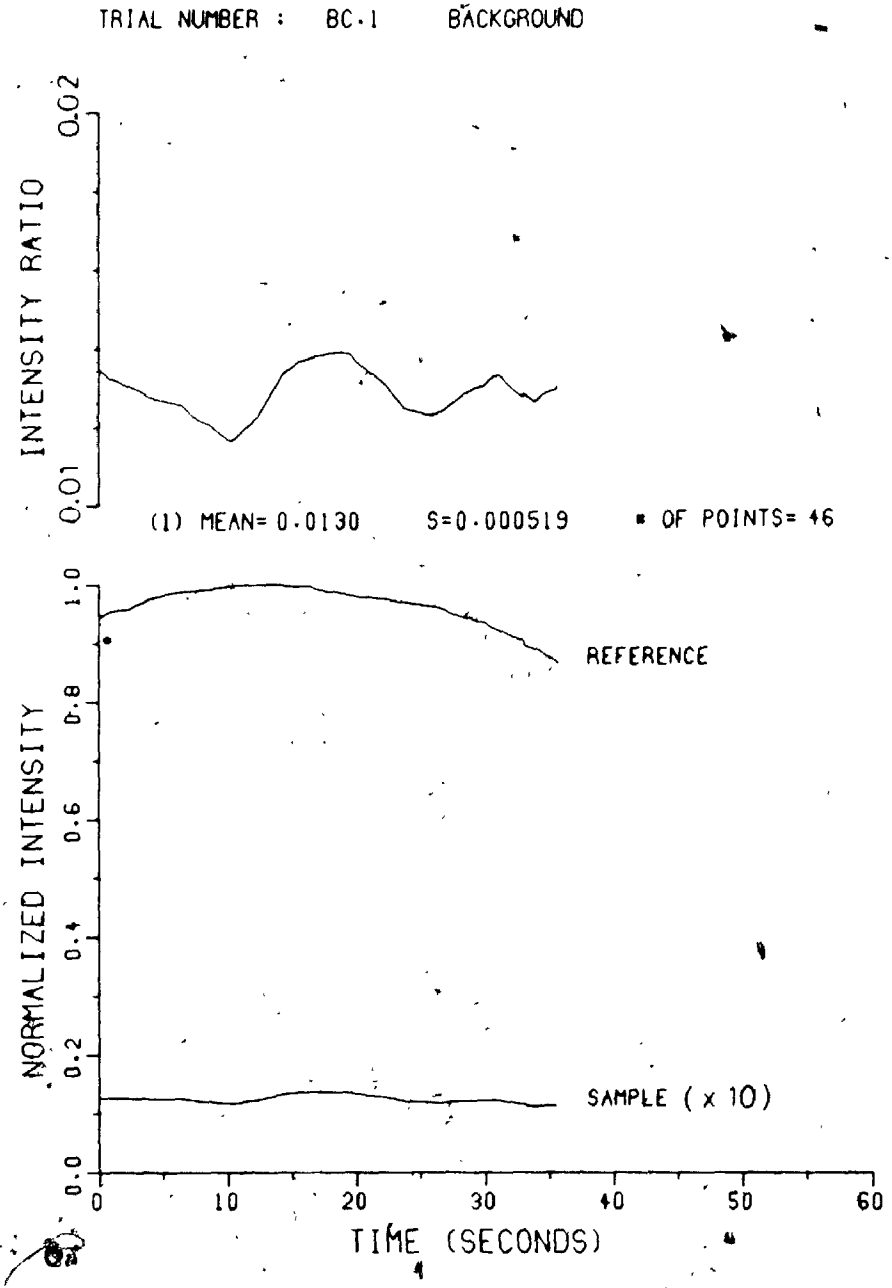
TRIAL NUMBER : BC-1 BACKGROUND
INTENSITY RATIO
0.02
0.01
(1) MEAN= 0.0130 S=0.000519 # OF POINTS= 46
NORMALIZED INTENSITY
1.0
0.8
0.6
0.4
0.2
0.0
REFERENCE
SAMPLE (x 10)
0
10
20
30
40
50
60
TIME (SECONDS)

G.3. Nitrogen Broadened Absorption Bands

G.3.1. Pathlength - 20 cm

Calibration Files

Trial Numbers: NC20.1-NC20.27

Remote Gain: Sample (G_S): 1 (V/V)

FSD_S: 2

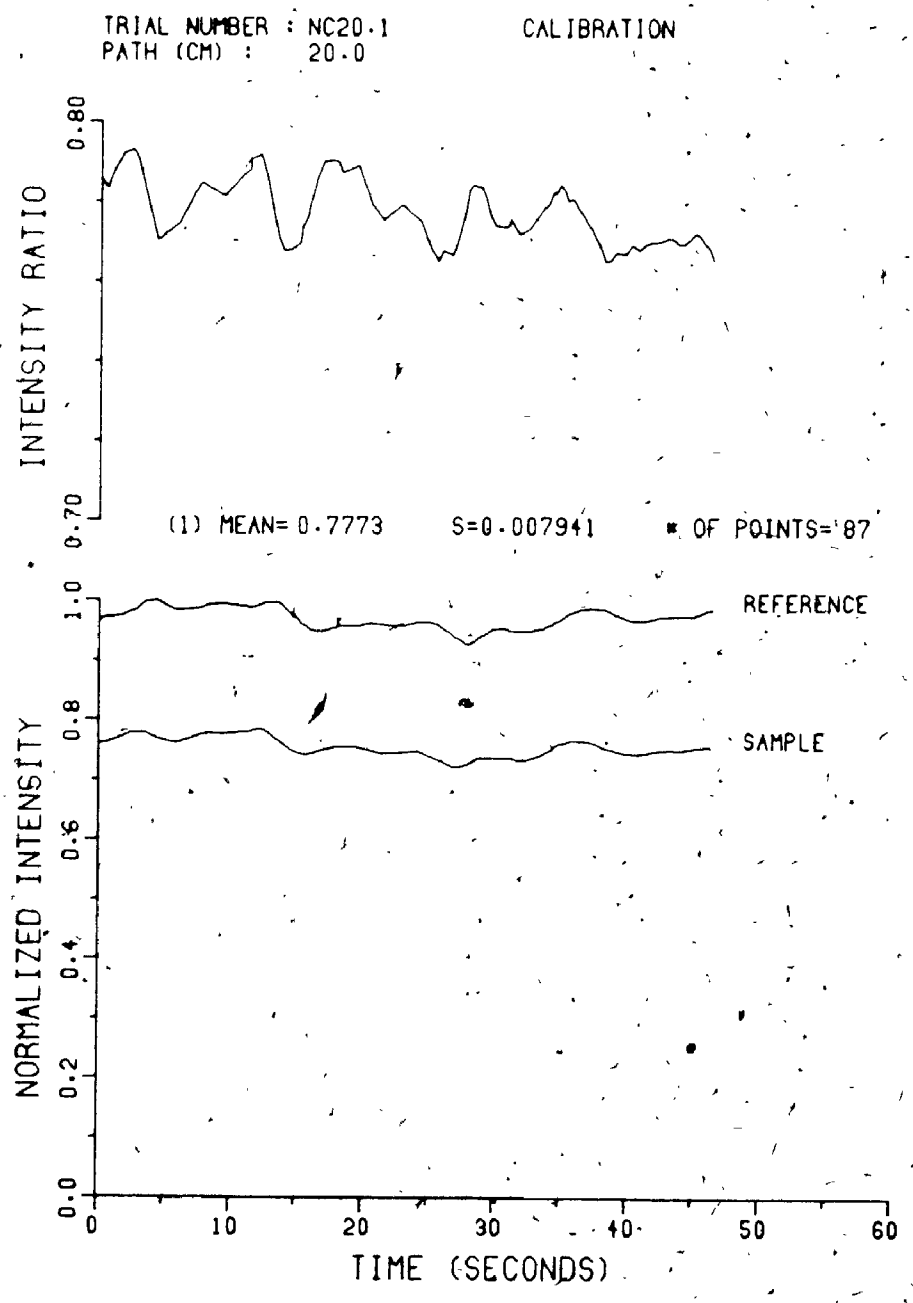
TRIAL NUMBER : NC20.1
PATH (CM) : 20.0
CALIBRATION
INTENSITY RATIO
0.80
0.70
(1) MEAN= 0.7773
S=0.007941
# OF POINTS= 87
REFERENCE
SAMPLE
NORMALIZED INTENSITY
1.0
0.8
0.6
0.4
0.2
0.0
0
10
20
30
40
50
60
TIME (SECONDS)

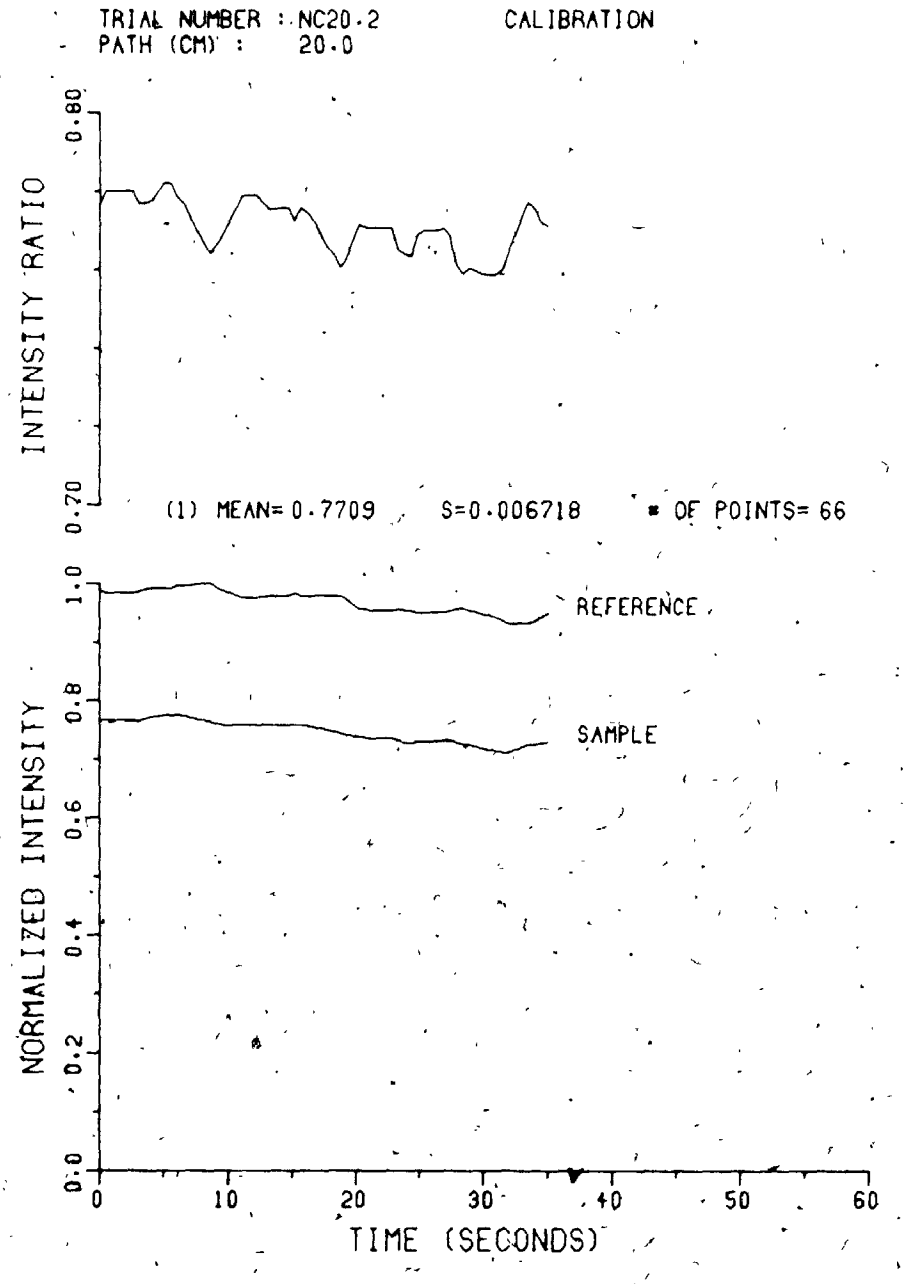
TRIAL NUMBER : NC20.2
PATH (CM) : 20.0
CALIBRATION
INTENSITY RATIO
0.80
0.70
(1) MEAN= 0.7709 S=0.006718 # OF POINTS= 66
NORMALIZED INTENSITY
1.0
0.8
0.6
0.4
0.2
0.0
REFERENCE
SAMPLE
0
10
20
30
40
50
60
TIME (SECONDS)

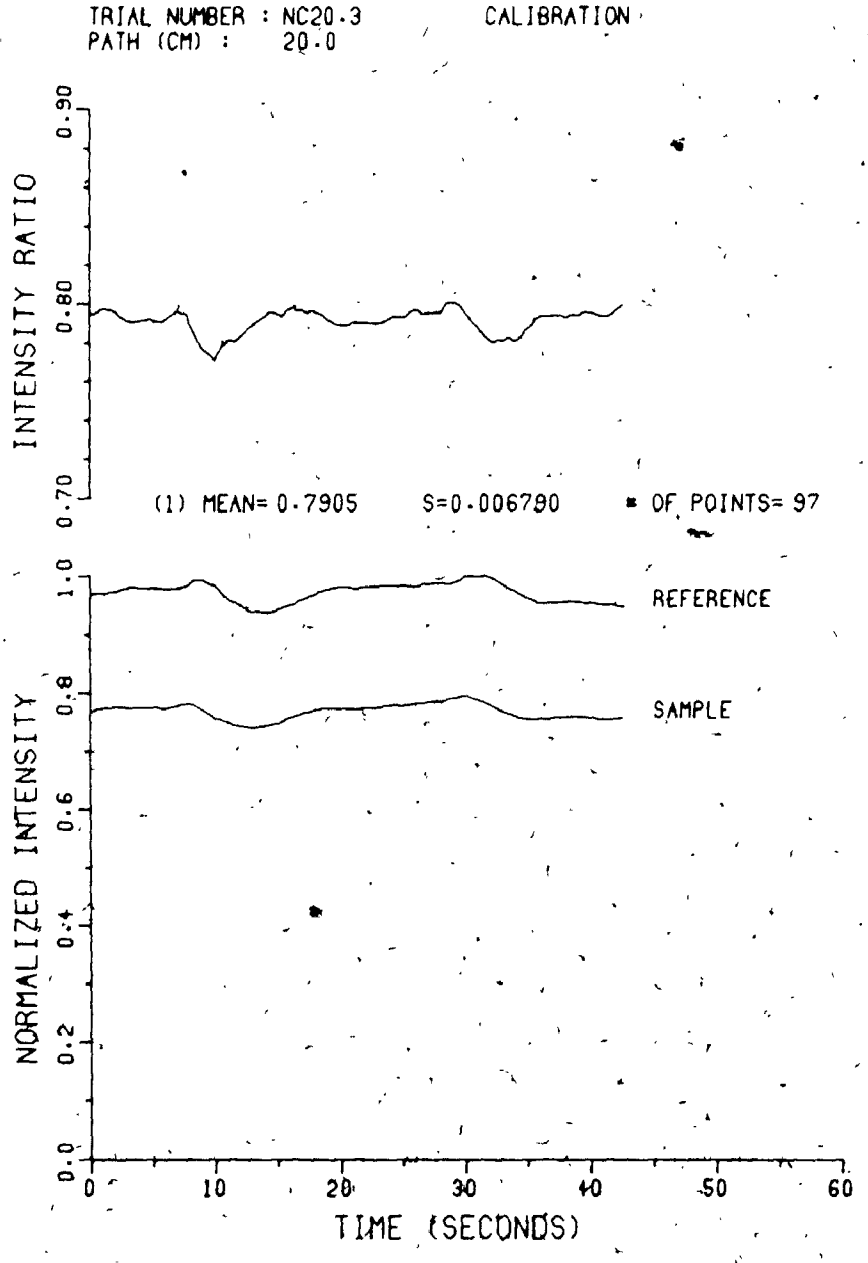
TRIAL NUMBER : NC20.3
PATH (CM) : 20.0
CALIBRATION
INTENSITY RATIO
0.90
0.80
0.70
(1) MEAN= 0.7905
S=0.006780
# OF POINTS= 97
NORMALIZED INTENSITY
1.0
0.8
0.6
0.4
0.2
0.0
REFERENCE
SAMPLE
0
10
20
30
40
50
60
TIME (SECONDS)

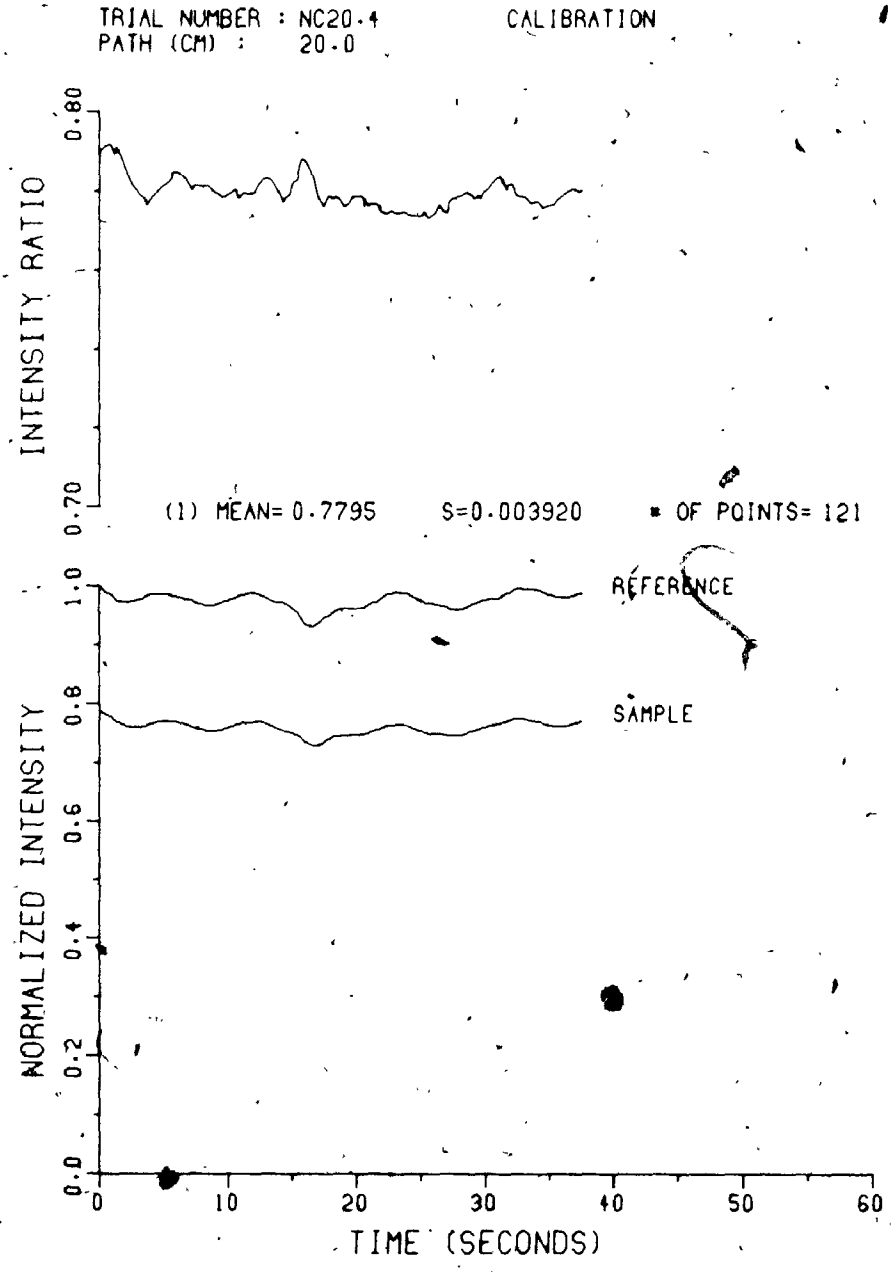
TRIAL NUMBER : NC20-4
PATH (CM) : 20.0
CALIBRATION
INTENSITY RATIO
0.80
0.70
(1) MEAN= 0.7795 S=0.003920 # OF POINTS= 121
REFERENCE
SAMPLE
NORMALIZED INTENSITY
1.0
0.8
0.6
0.4
0.2
0.0
0
10
20
30
40
50
60
TIME (SECONDS)

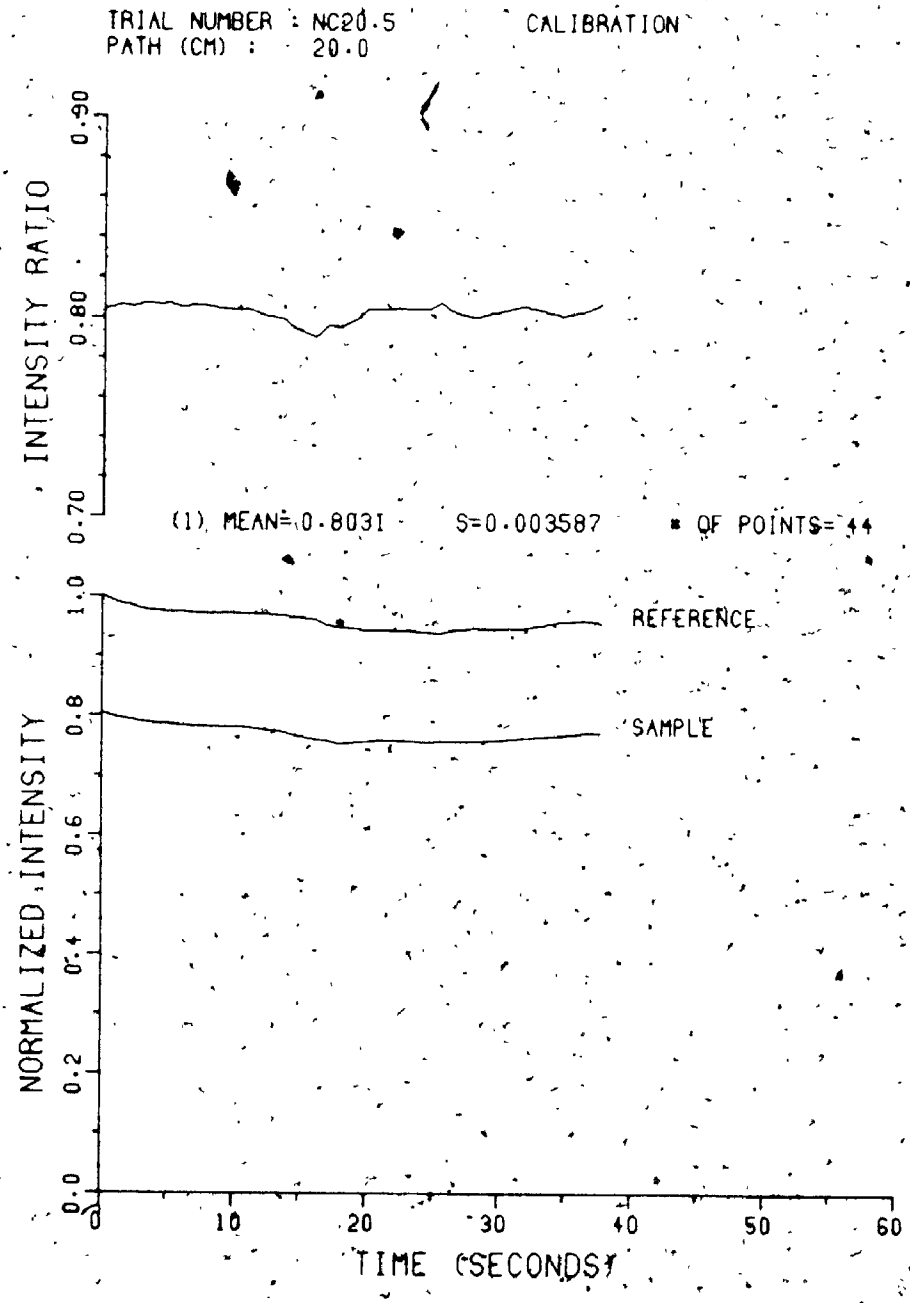
TRIAL NUMBER : NC20.5
PATH (CM) : 20.0
CALIBRATION
INTENSITY RATIO
0.90
0.80
0.70
(1) MEAN=0.8031
S=0.003587
# OF POINTS= 44
NORMALIZED INTENSITY
1.0
0.8
0.6
0.4
0.2
0.0
REFERENCE
SAMPLE
0
10
20
30
40
50
60
TIME (SECONDS)

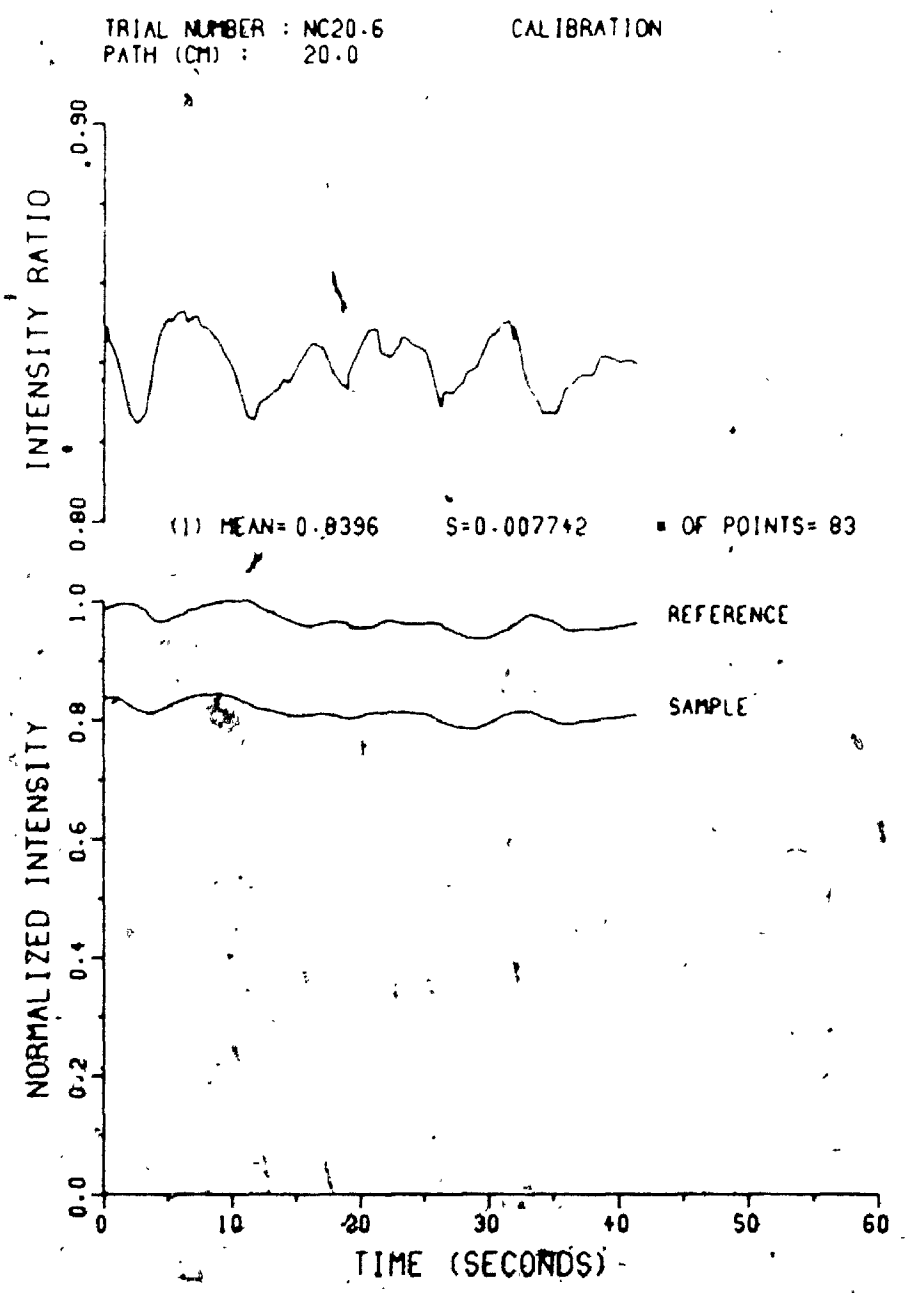
TRIAL NUMBER : NC20-6
PATH (CM) : 20.0
CALIBRATION
INTENSITY RATIO
0.90
0.80
(1) MEAN= 0.8396 S=0.007742 # OF POINTS= 83
NORMALIZED INTENSITY
1.0
0.8
0.6
0.4
0.2
0.0
REFERENCE
SAMPLE
0
10
20
30
40
50
60
TIME (SECONDS)

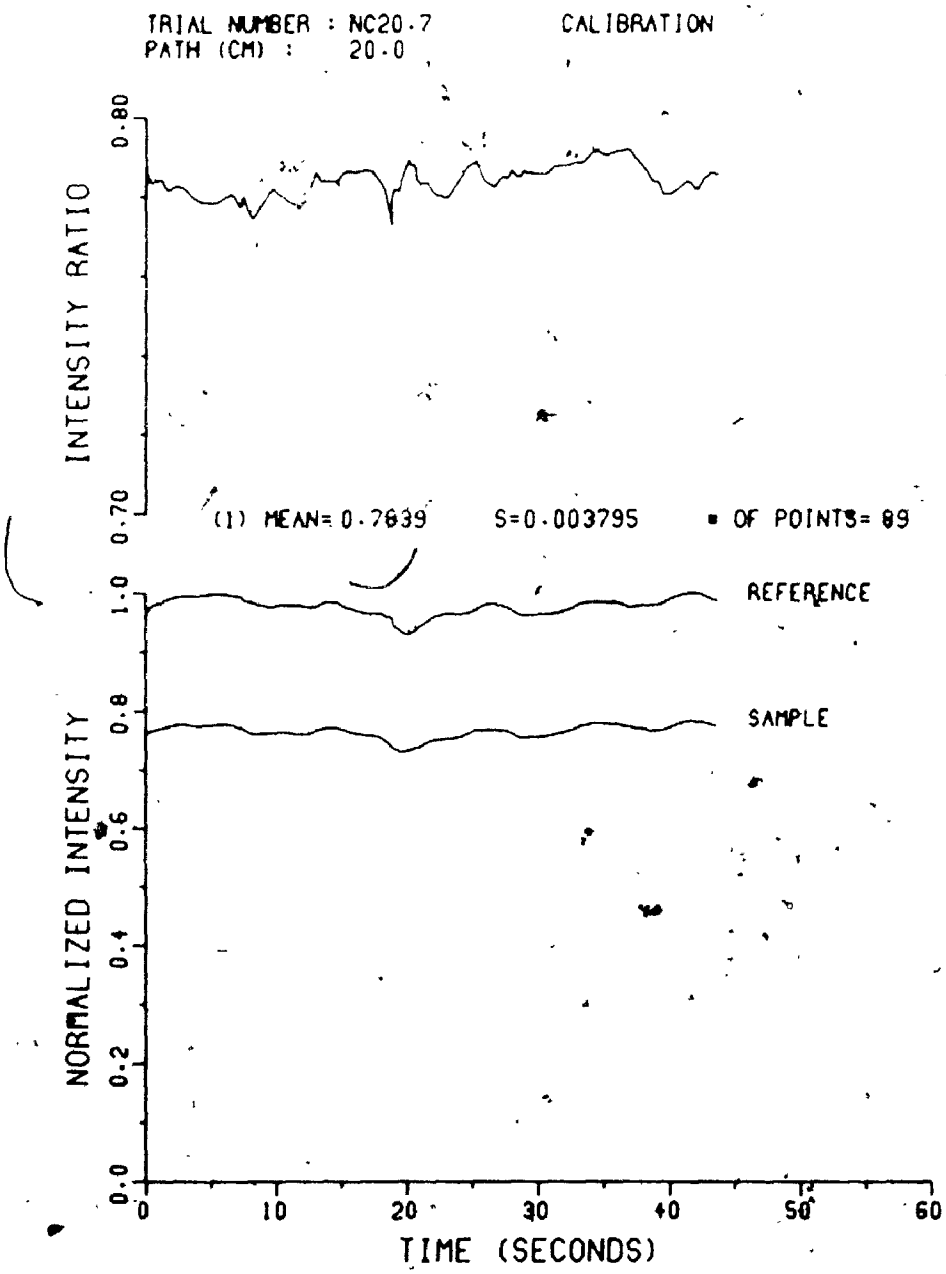
TRIAL NUMBER : NC20.7
PATH (CM) : 20.0
CALIBRATION
INTENSITY RATIO
0.80
0.70
(1) MEAN= 0.7639
S=0.003795
# OF POINTS= 89
REFERENCE
SAMPLE
NORMALIZED INTENSITY
1.0
0.8
0.6
0.4
0.2
0.0
0
10
20
30
40
50
60
TIME (SECONDS)

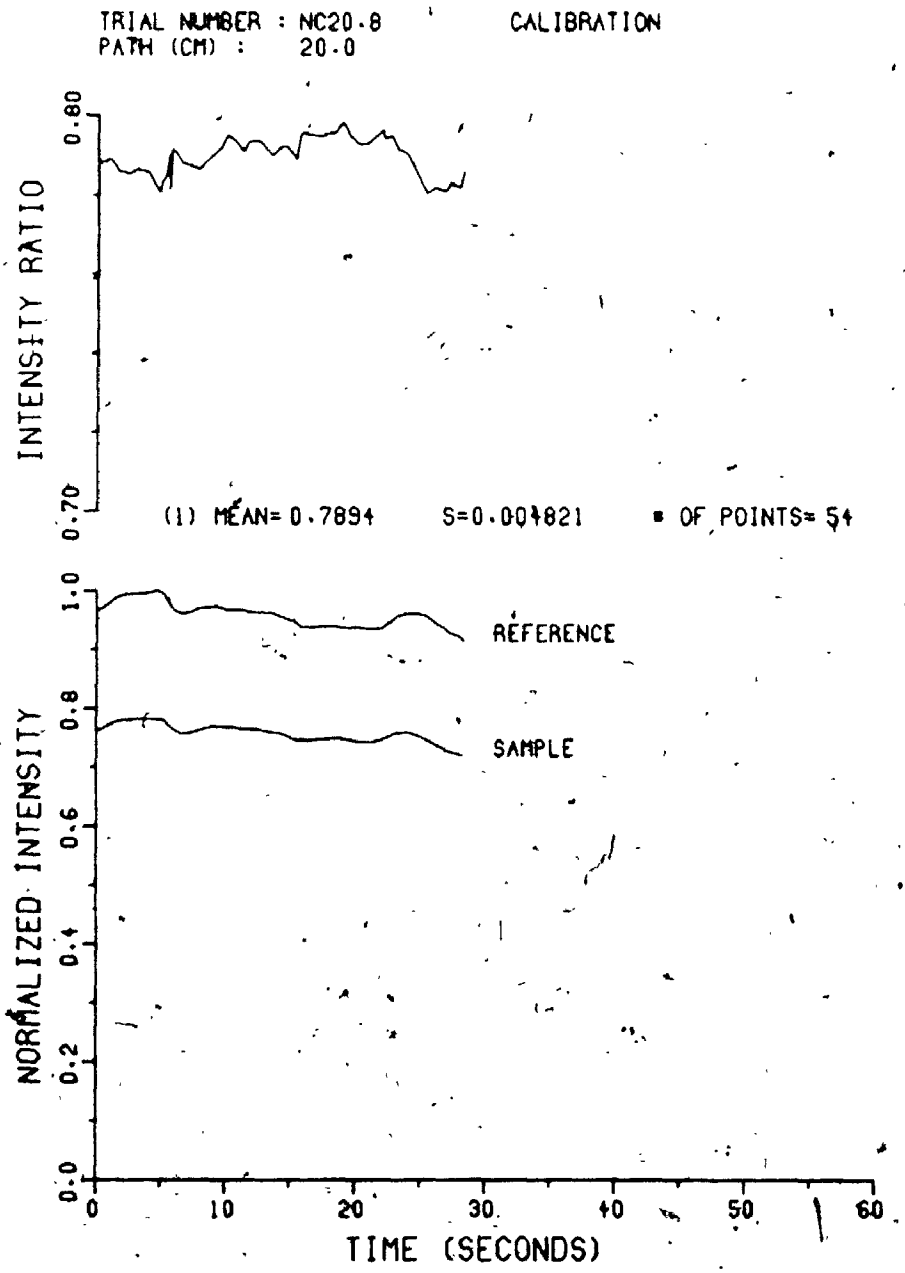
TRIAL NUMBER : NC20.8
PATH (CM) : 20.0
CALIBRATION
INTENSITY RATIO
0.80
0.70
(1) MEAN= 0.7894
S=0.001821
# OF POINTS= 54
NORMALIZED INTENSITY
1.0
0.8
0.6
0.4
0.2
0.0
REFERENCE
SAMPLE
0
10
20
30
40
50
60
TIME (SECONDS)

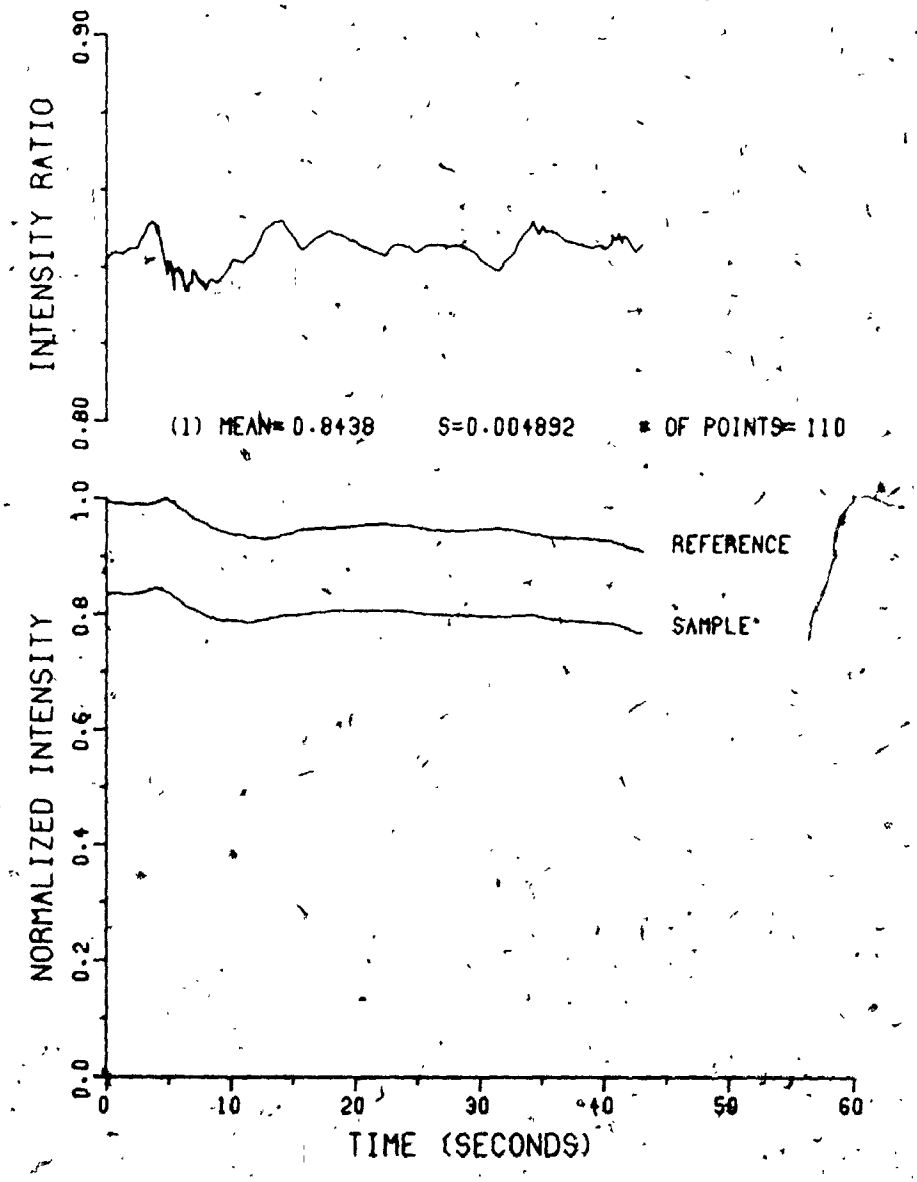
TRIAL NUMBER : NC20.9
PATH (CM) : 20.0
CALIBRATION
INTENSITY RATIO
0.90
0.80
(1) MEAN= 0.8438 S=0.004892 # OF POINTS= 110
NORMALIZED INTENSITY
1.0
0.8
0.6
0.4
0.2
0.0
REFERENCE
SAMPLE
0
10
20
30
40
50
60
TIME (SECONDS)

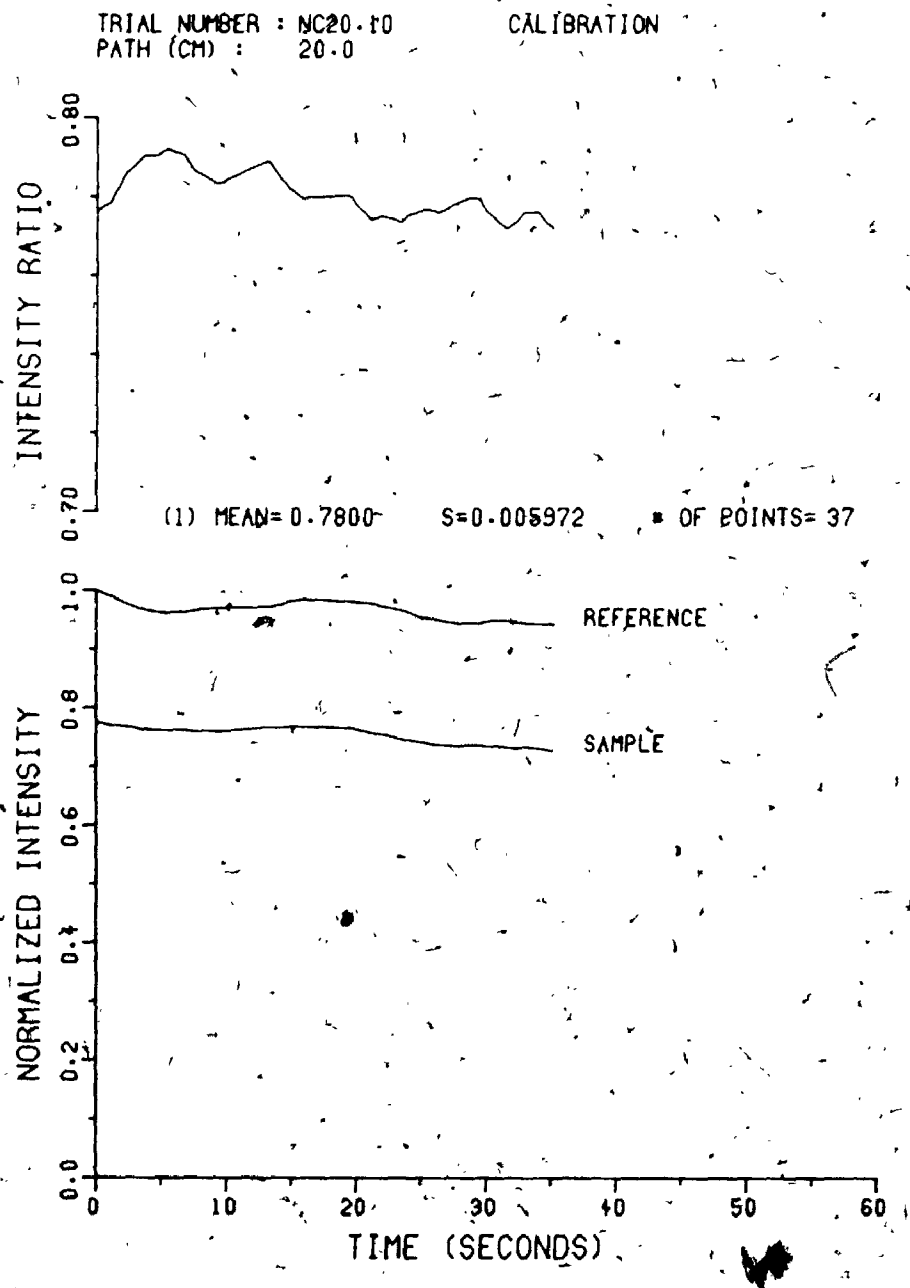
TRIAL NUMBER : NC20.10
PATH (CM) : 20.0
CALIBRATION
INTENSITY RATIO
0.80
0.70
(1) MEAN= 0.7800
S=0.005972
# OF POINTS= 37
NORMALIZED INTENSITY
1.0
0.8
0.6
0.4
0.2
0.0
REFERENCE
SAMPLE
0
10
20
30
40
50
60
TIME (SECONDS)

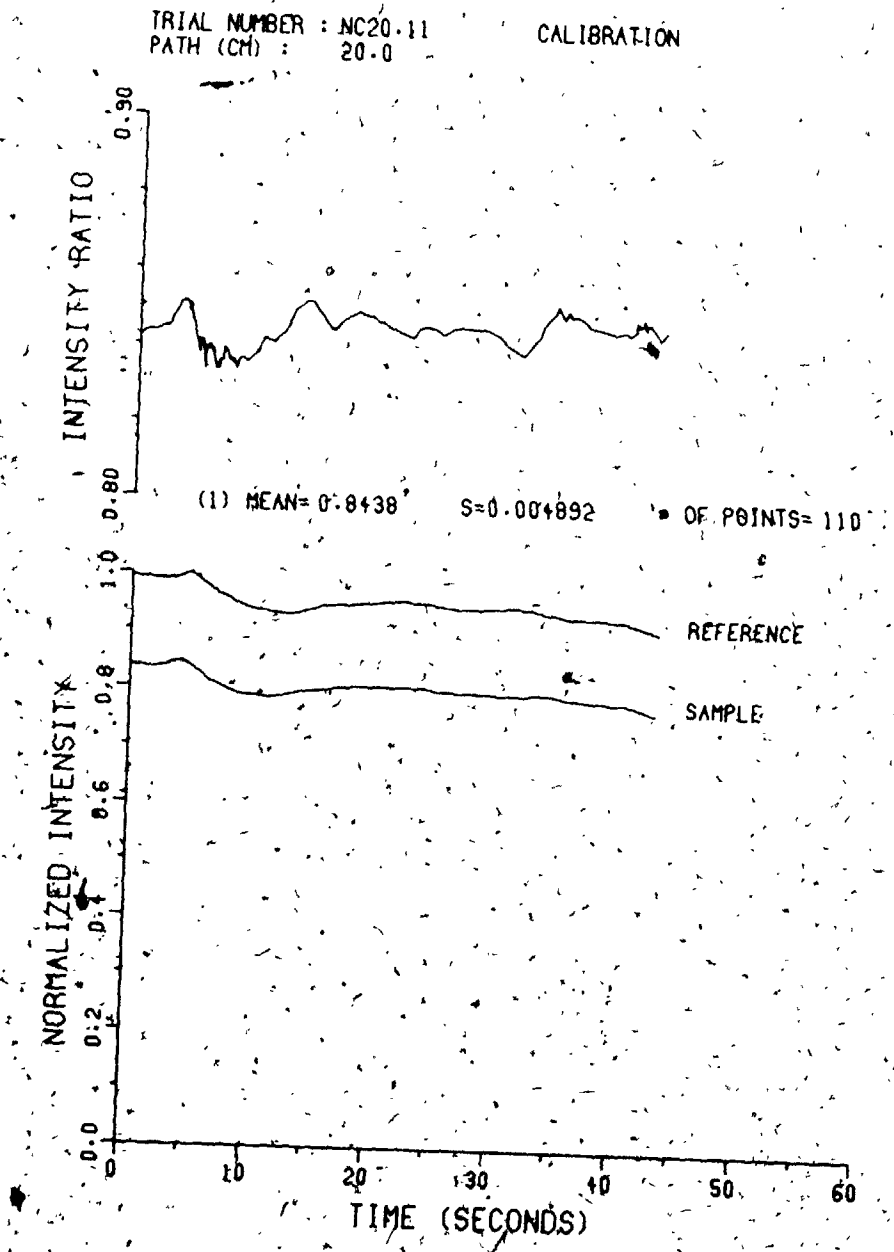
TRIAL NUMBER : NC20.11
PATH (CM) : 20.0
CALIBRATION
INTENSITY RATIO
0.90
0.80
(1) MEAN= 0.8438
S=0.004892
# OF POINTS= 110
REFERENCE
SAMPLE
NORMALIZED INTENSITY
1.0
0.8
0.6
0.4
0.2
0.0
0
10
20
30
40
50
60
TIME (SECONDS)

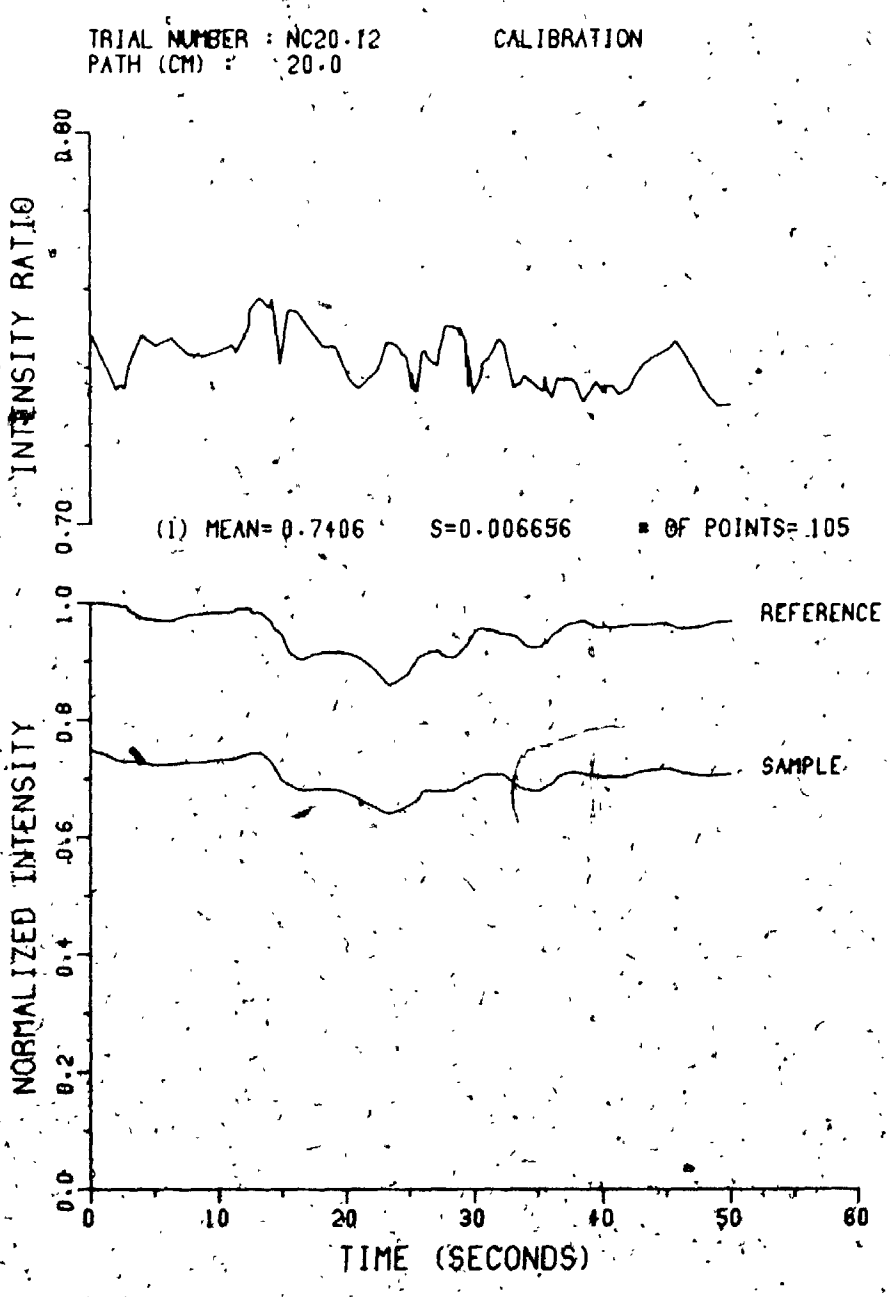
TRIAL NUMBER : NC20-12
CALIBRATION
PATH (CM) : 20.0
INTENSITY RATIO
0.80
0.70
(I) MEAN= 0.7406
S=0.006656
# OF POINTS= 105
NORMALIZED INTENSITY
1.0
0.8
0.6
0.4
0.2
0.0
REFERENCE
SAMPLE
0
10
20
30
40
50
60
TIME (SECONDS)

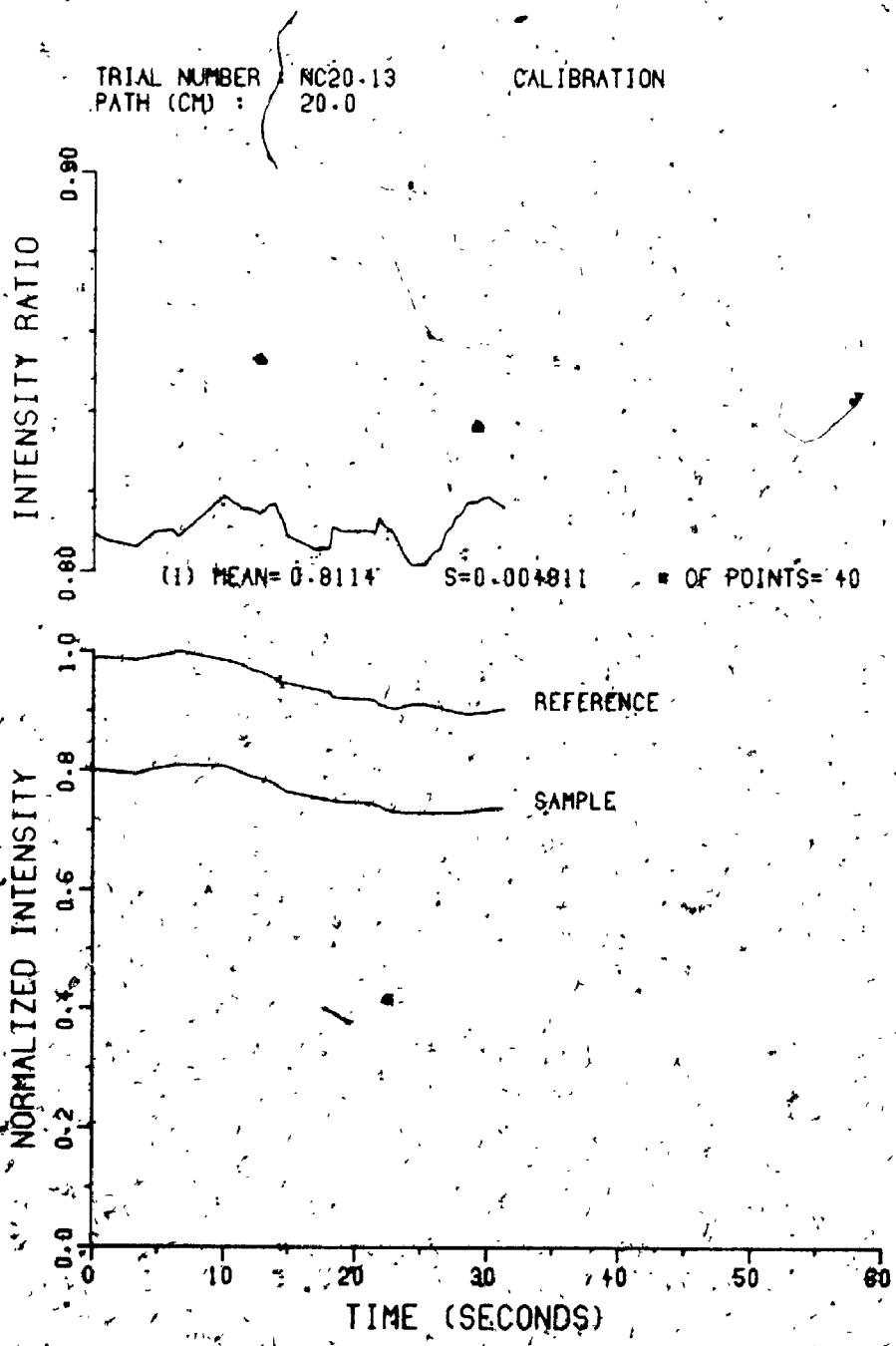
TRIAL NUMBER : NC20-13
PATH (CM) : 20.0
CALIBRATION
INTENSITY RATIO
0.90
0.80
(1) MEAN= 0.8114 S=0.004811 # OF POINTS= 40
NORMALIZED INTENSITY
1.0
0.8
0.6
0.4
0.2
0.0
REFERENCE
SAMPLE
0
10
20
30
40
50
60
TIME (SECONDS)

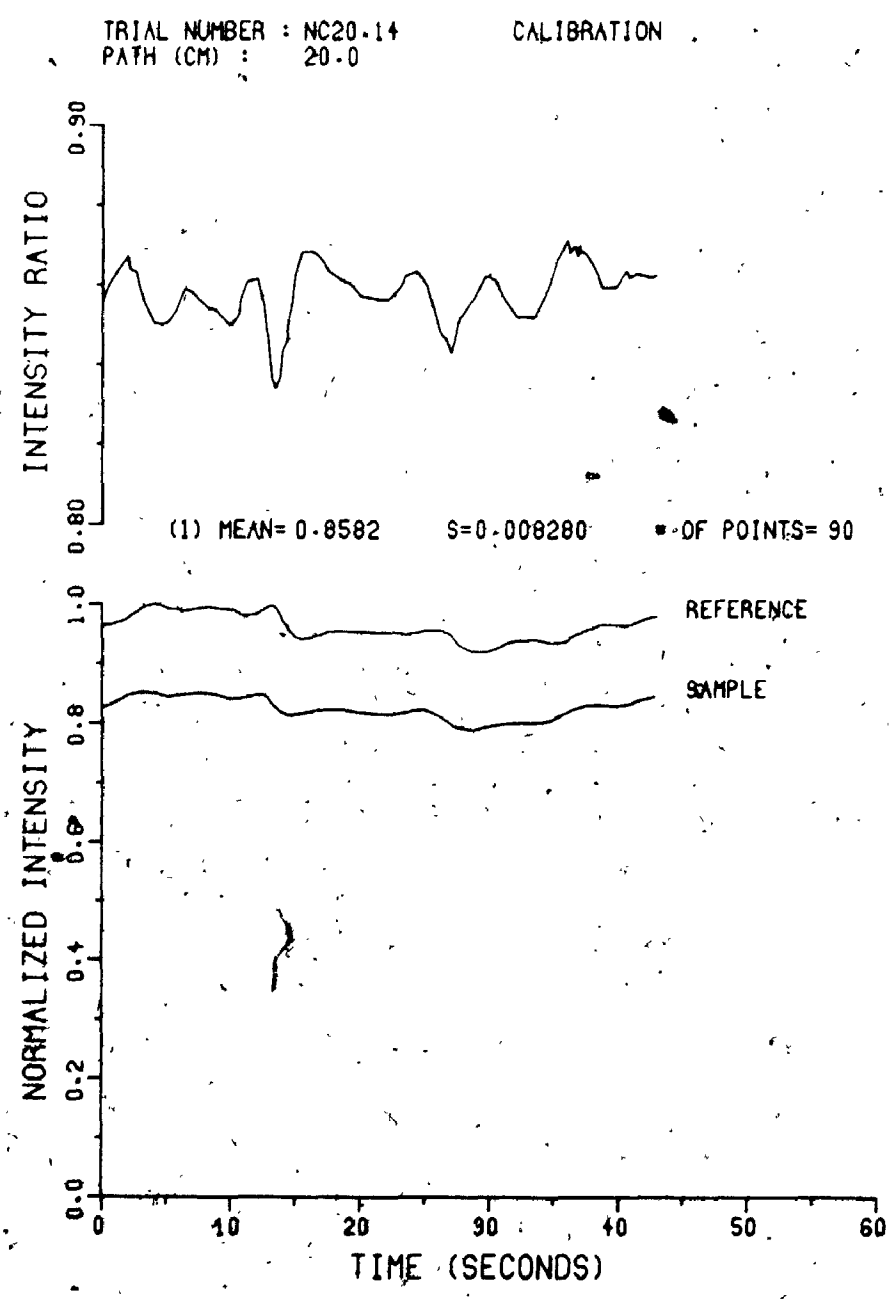
TRIAL NUMBER : NC20.14
PATH (CM) : 20.0
CALIBRATION
INTENSITY RATIO
0.90
0.80
(1) MEAN= 0.8582
S=0.008280
# OF POINTS= 90
NORMALIZED INTENSITY
1.0
0.8
0.6
0.4
0.2
0.0
REFERENCE
SAMPLE
0
10
20
30
40
50
60
TIME (SECONDS)

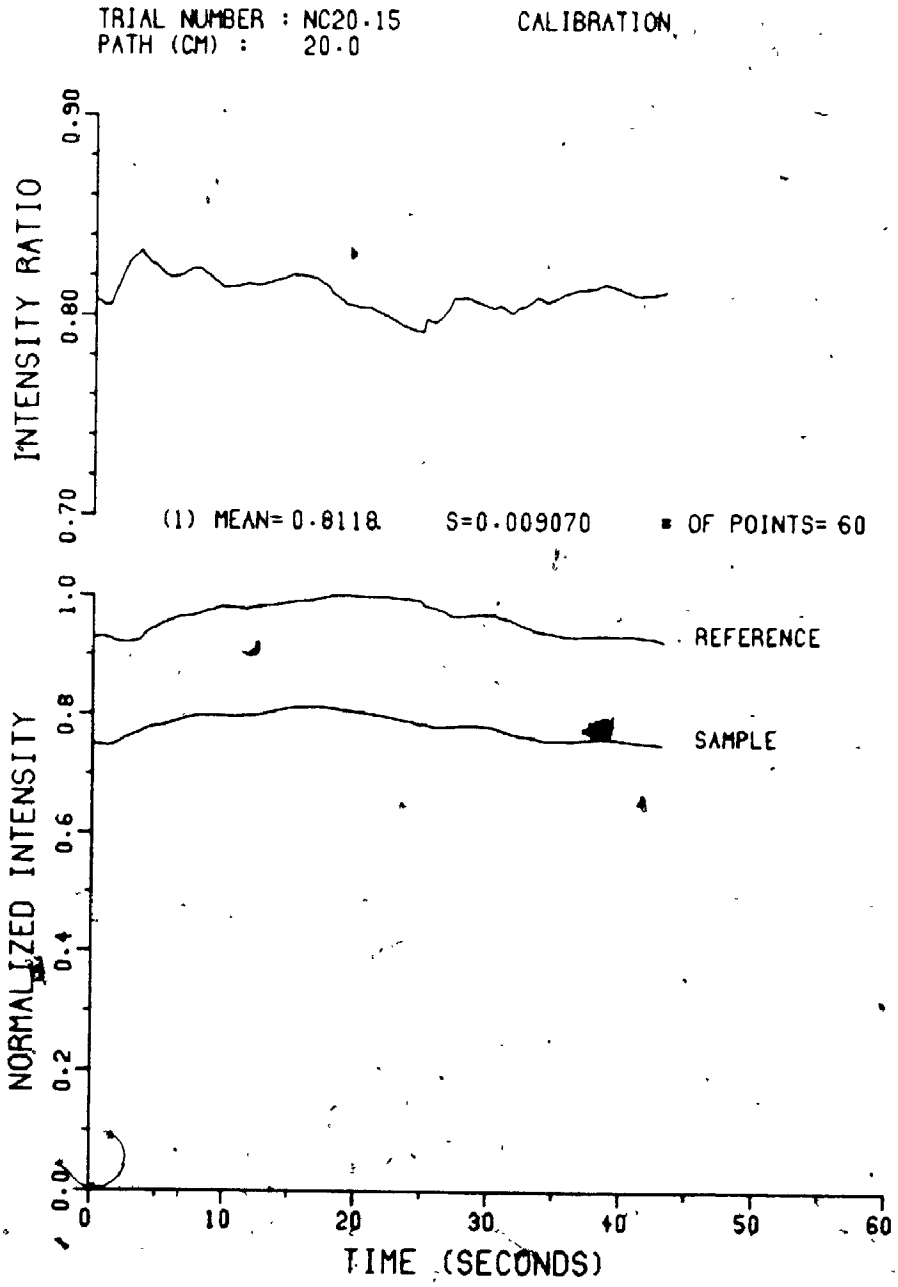
TRIAL NUMBER : NC20.15
PATH (CM) : 20.0
CALIBRATION
INTENSITY RATIO
0.90
0.80
0.70
(1) MEAN= 0.8118 S=0.009070 # OF POINTS= 60
NORMALIZED INTENSITY
1.0
0.8
0.6
0.4
0.2
0.0
REFERENCE
SAMPLE
0
10
20
30
40
50
60
TIME (SECONDS)

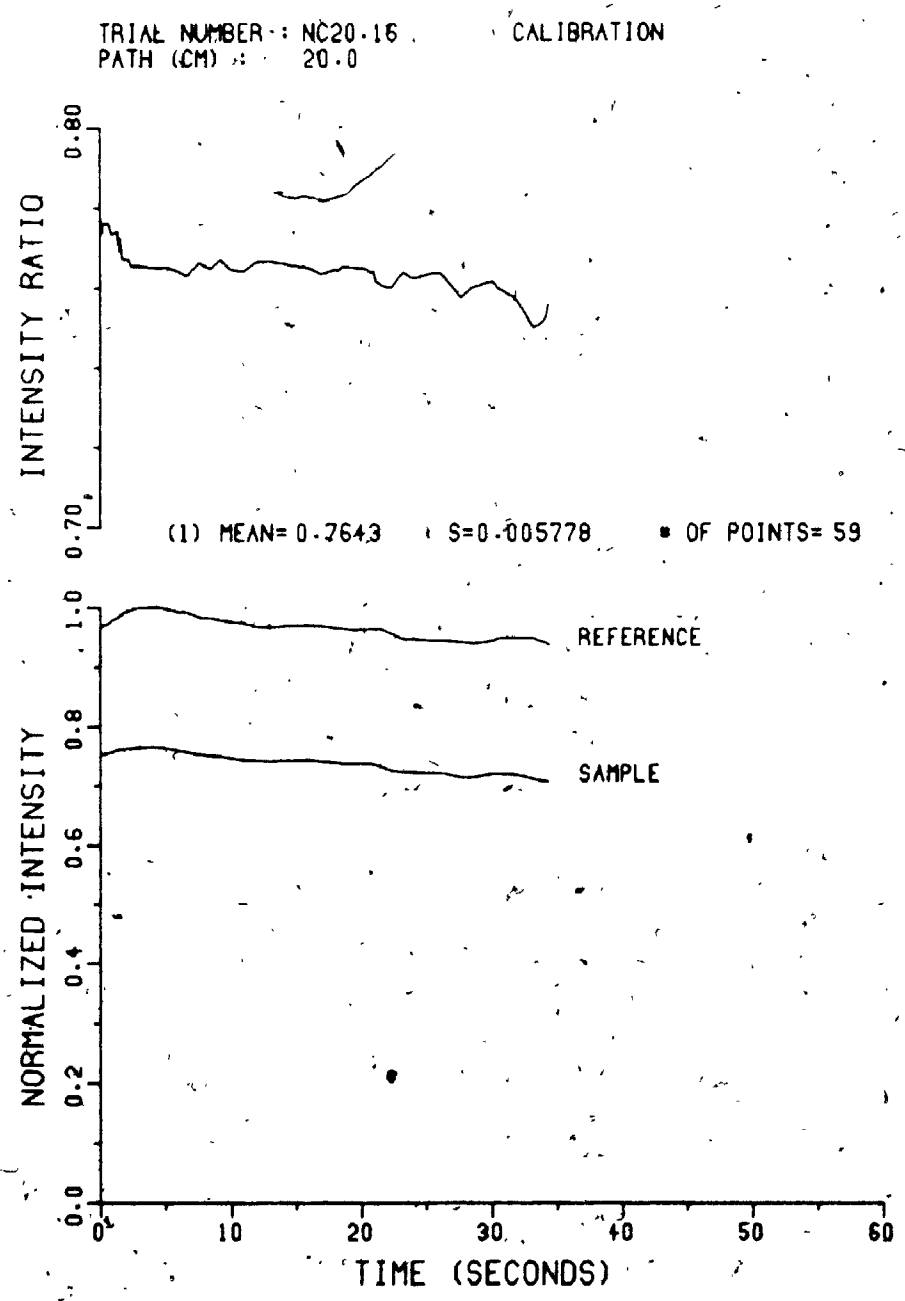
TRIAL NUMBER : NC20-16
CALIBRATION
PATH (CM) : 20.0
INTENSITY RATIO
0.80
0.70
(1) MEAN= 0.7643
S=0.005778
# OF POINTS= 59
NORMALIZED INTENSITY
1.0
0.8
0.6
0.4
0.2
0.0
REFERENCE
SAMPLE
0
10
20
30
40
50
60
TIME (SECONDS)

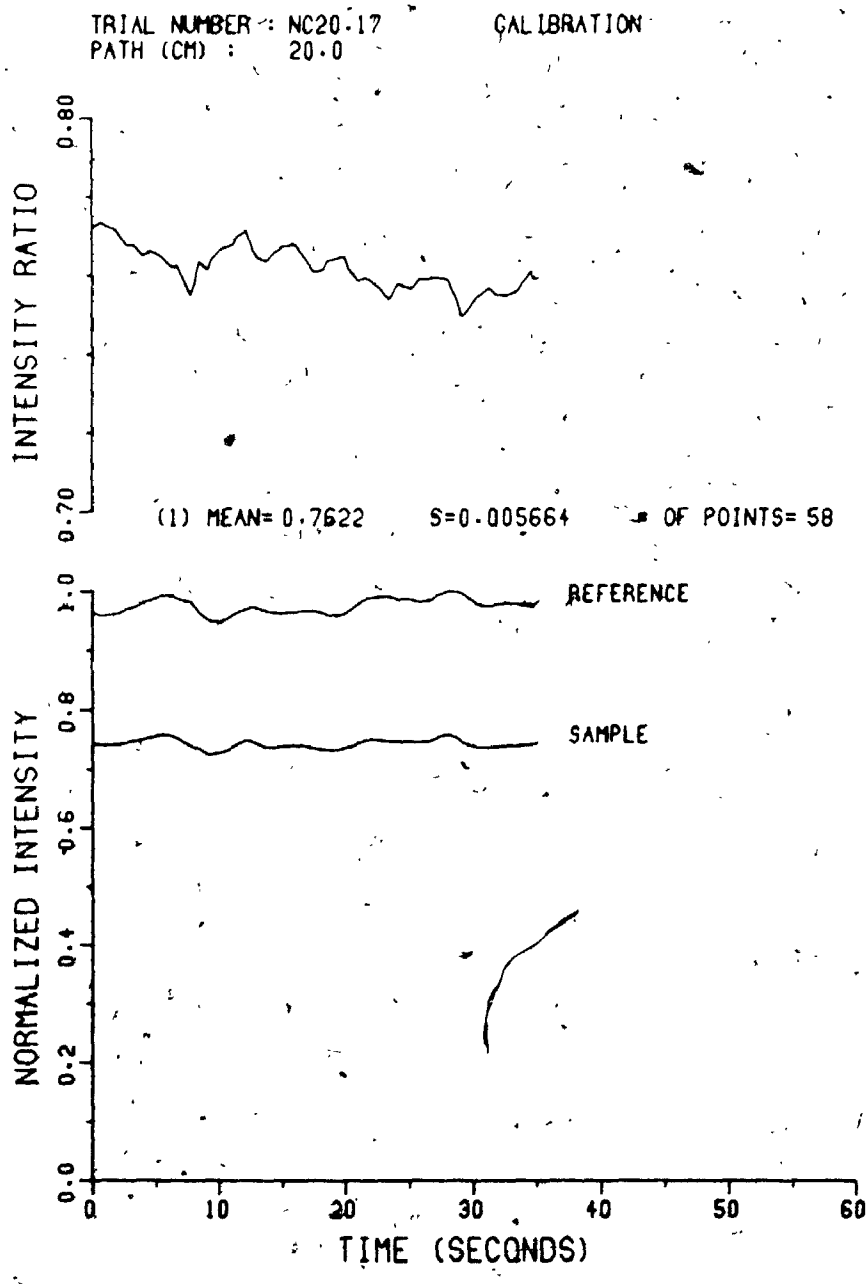
TRIAL NUMBER : NC20.17
PATH (CM) : 20.0
CALIBRATION
INTENSITY RATIO
0.80
0.70
(1) MEAN= 0.7622 S=0.005664 # OF POINTS= 58
REFERENCE
SAMPLE
NORMALIZED INTENSITY
1.0
0.8
0.6
0.4
0.2
0.0
0
10
20
30
40
50
60
TIME (SECONDS)

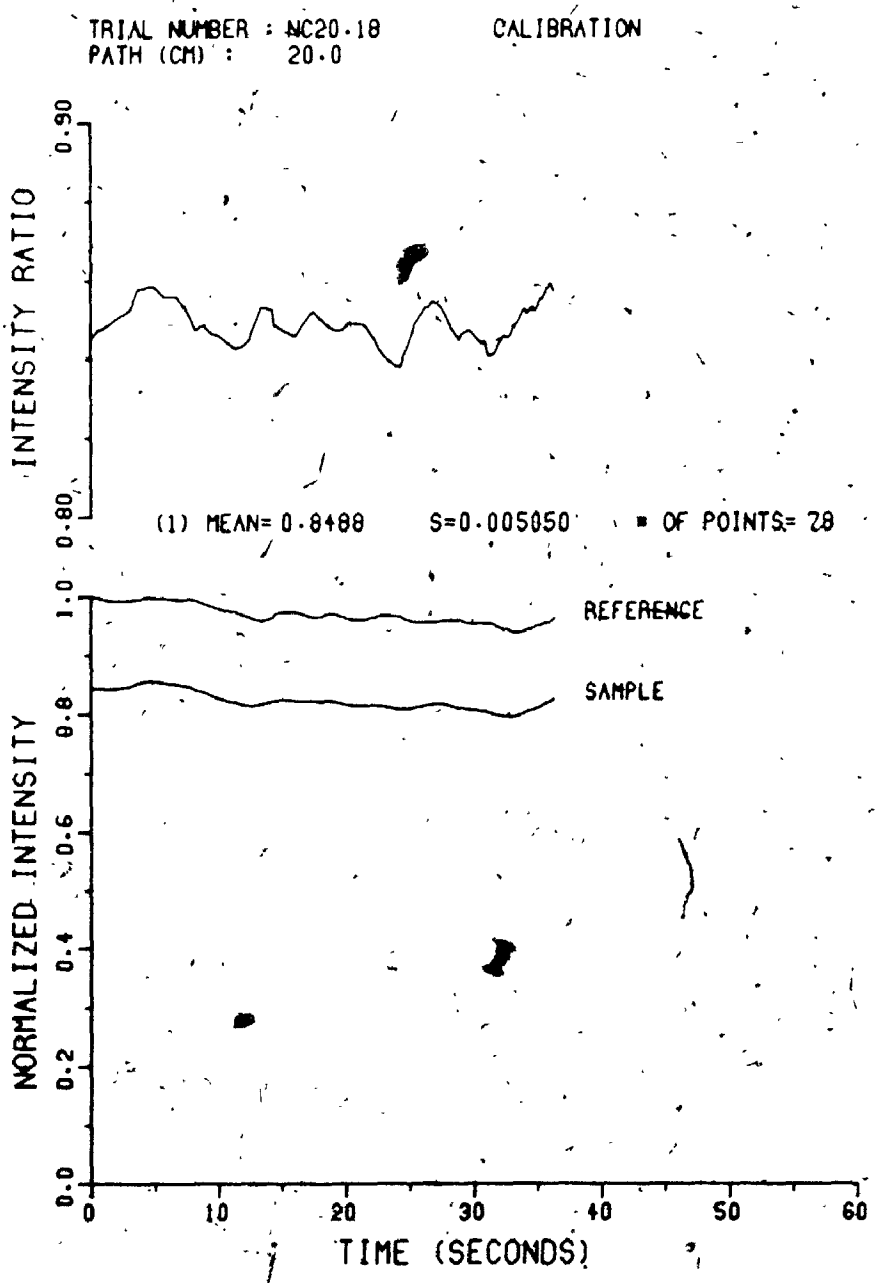
TRIAL NUMBER : NC20-18
PATH (CM) : 20.0
CALIBRATION
INTENSITY RATIO
0.90
0.80
(1) MEAN= 0.8488
S=0.005050
# OF POINTS= 28
1.0
0.8
0.6
0.4
0.2
0.0
NORMALIZED INTENSITY
REFERENCE
SAMPLE
0
10
20
30
40
50
60
TIME (SECONDS)

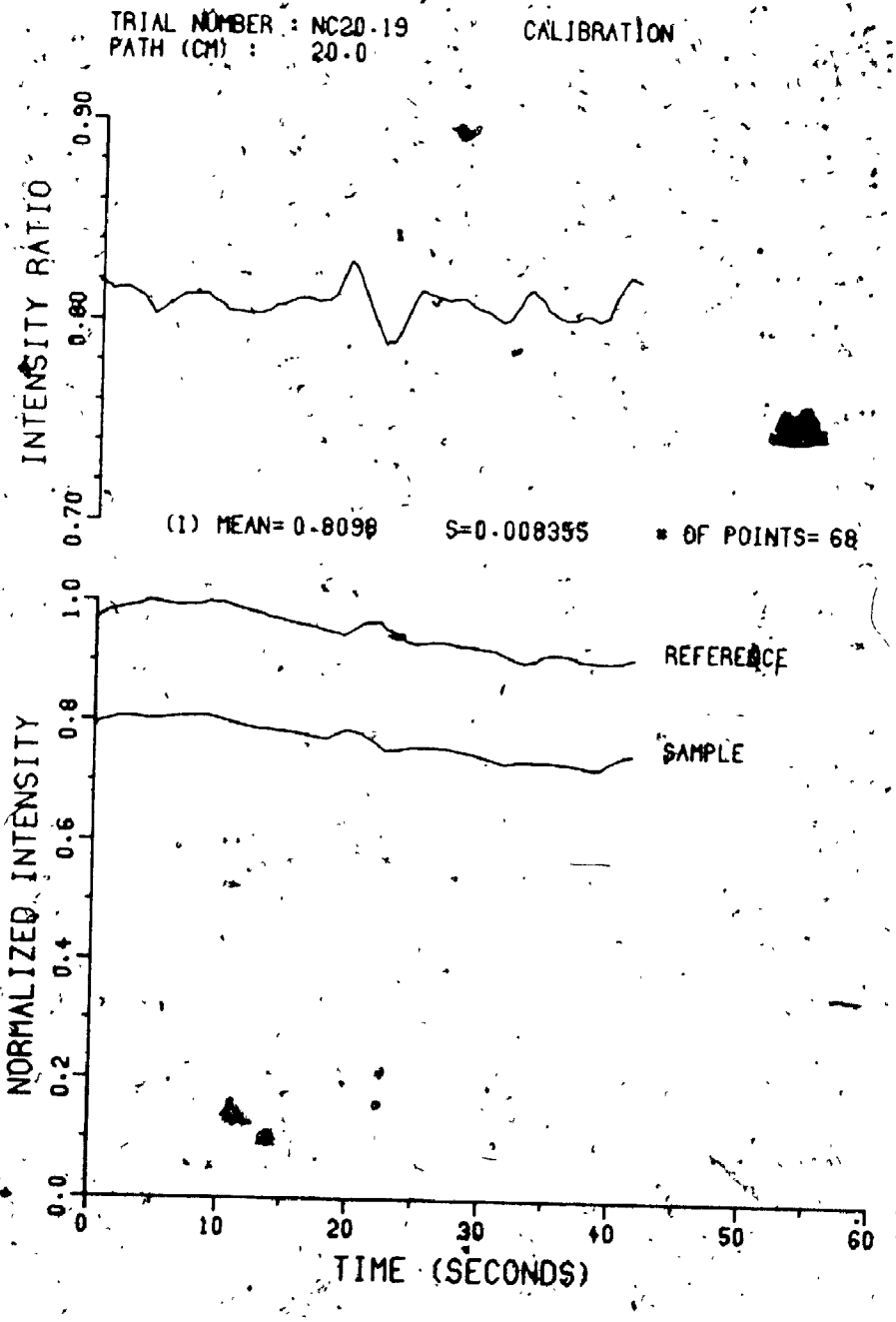
TRIAL NUMBER : NC20-19
PATH (CM) : 20.0
CALIBRATION
INTENSITY RATIO
0.90
0.80
0.70
(1) MEAN= 0.8098
S=0.008355
# OF POINTS= 68
NORMALIZED INTENSITY
1.0
0.8
0.6
0.4
0.2
0.0
REFERENCE
SAMPLE
0
10
20
30
40
50
60
TIME (SECONDS)

(100%, 200 Hz) encodes the laser radiation intensity as an AC signal in order to avoid the electronic drifting problems inherent in the detection of DC signals. The beam passes through the modulator and falls on the face of a 50% transmitting beamsplitter. The transmitted radiation is optically filtered and monitored by a lead selenide detector. In actuality this signal does not play a part in the analysis of carbon dioxide absorption data but is included as a convenience. Simple removal of the beamsplitter from the system allows for direct observation of the laser output power in this arrangement as described in Chapter 4.

The radiation reflected from the face of the beamsplitter is directed towards a multi-bladed fully reflective chopping wheel (optical modulator, [100]). This modulator splits the radiation into sample and reference paths. Sample radiation passes between the reflective blades of the rotating wheel and enters an absorption cell. The rear wall of the cell consists of a fully reflecting plane mirror that directs the sample beam back through the cell to the optical modulator. The radiation passing between the chopping wheel blades becomes coincident with the reference beam pathway. This combined beam contains the intensity information of both sample and reference paths time multiplexed at the chopping wheel blade rotation frequency. The radiation passes back through the beamsplitter and is focused to the face of a lead selenide detector. The detected signal is preamplified and fed through a single cable to the input of the signal processing unit.

An intake manifold and gas mixing network is housed inside the spectrometer to prepare gas samples for absorption testing. The particular combination of valves and vacuum tubing allows for accurate measurement of cell pressures from 0 - 1.32 atm (0 - 1000 Torr). A mixer adjacent to the

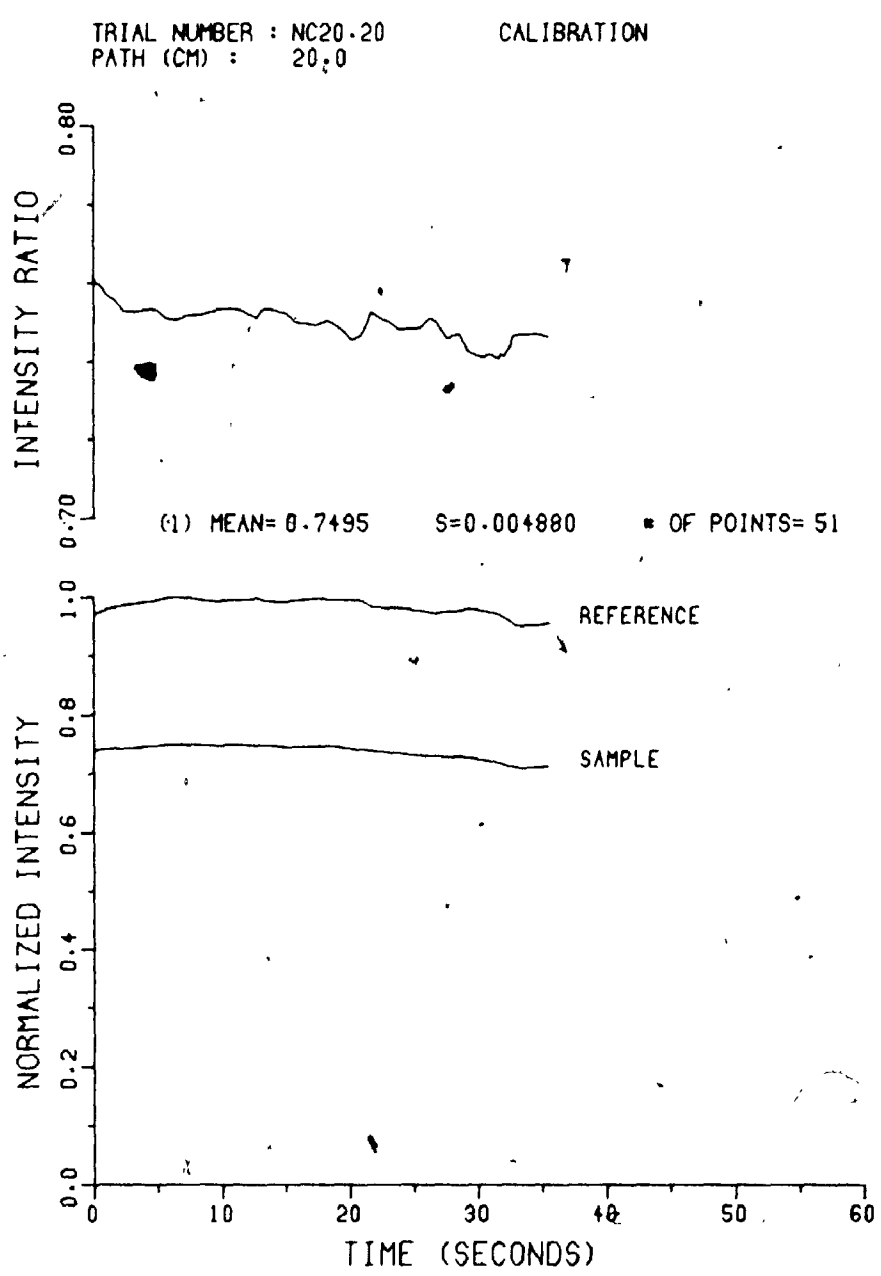
TRIAL NUMBER : NC20-20
CALIBRATION
PATH (CM) : 20.0
INTENSITY RATIO
0.80
0.70
(1) MEAN= 0.7495
S=0.004880
# OF POINTS= 51
NORMALIZED INTENSITY
1.0
0.8
0.6
0.4
0.2
0.0
REFERENCE
SAMPLE
0
10
20
30
40
50
60
TIME (SECONDS)

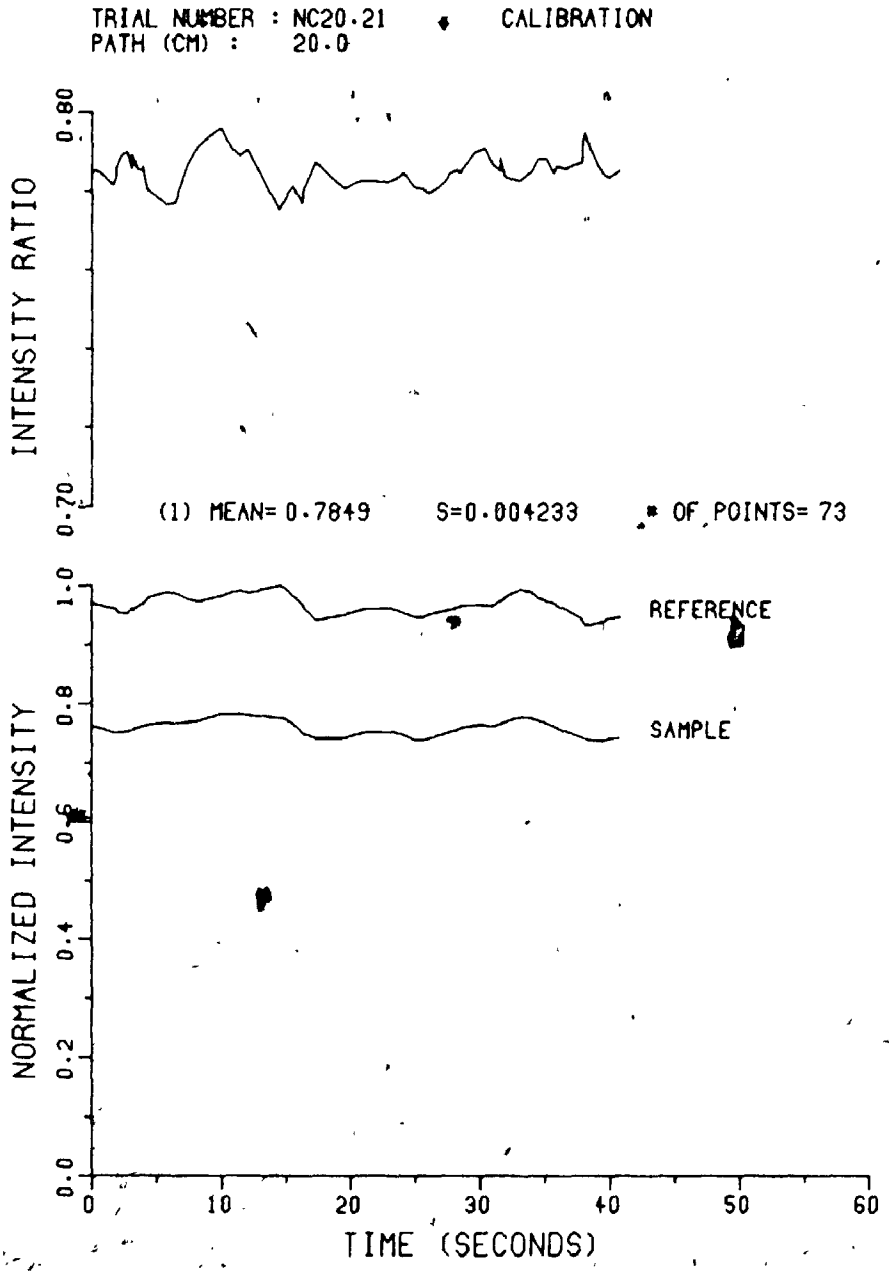
TRIAL NUMBER : NC20.21
PATH (CM) : 20.0
CALIBRATION
INTENSITY RATIO
0.80
0.70
(1) MEAN= 0.7849
S=0.004233
# OF POINTS= 73
NORMALIZED INTENSITY
1.0
0.8
0.6
0.4
0.2
0.0
REFERENCE
SAMPLE
0
10
20
30
40
50
60
TIME (SECONDS)

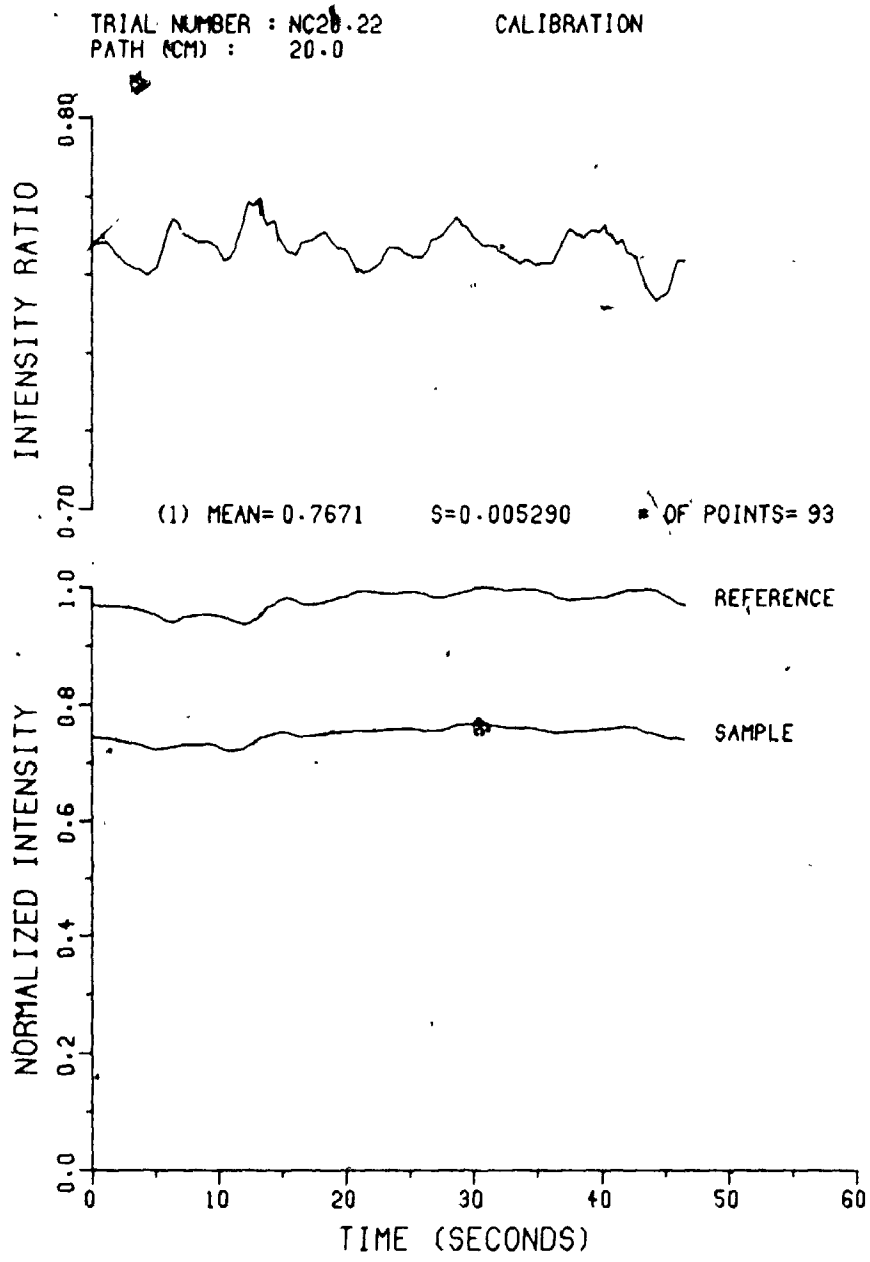
TRIAL NUMBER : NC20.22
PATH (CM) : 20.0
CALIBRATION
INTENSITY RATIO
0.80
0.70
(1) MEAN= 0.7671
S=0.005290
# OF POINTS= 93
REFERENCE
SAMPLE
NORMALIZED INTENSITY
1.0
0.8
0.6
0.4
0.2
0.0
0
10
20
30
40
50
60
TIME (SECONDS)

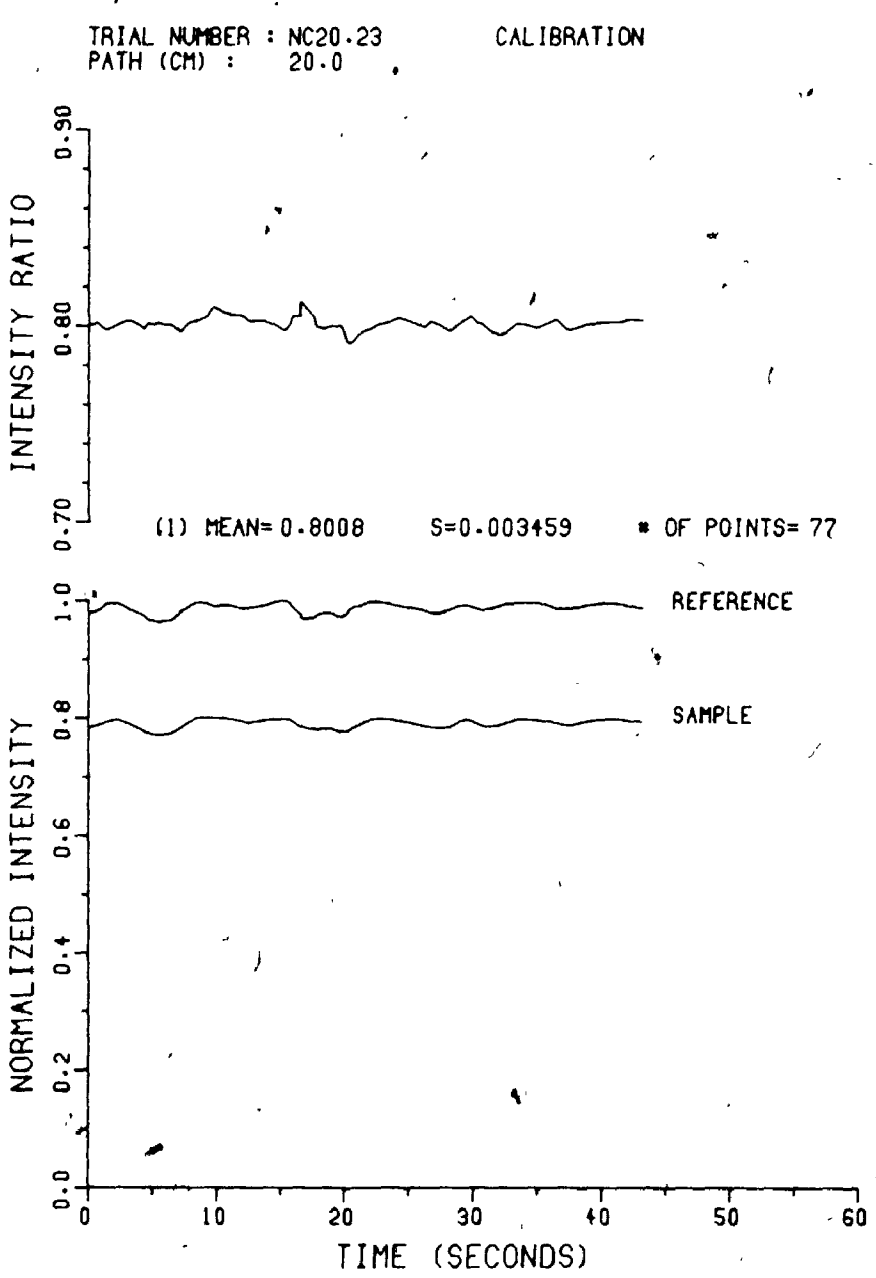
TRIAL NUMBER : NC20.23
PATH (CM) : 20.0
CALIBRATION
INTENSITY RATIO
0.90
0.80
0.70
(1) MEAN= 0.8008
S=0.003459
# OF POINTS= 77
NORMALIZED INTENSITY
1.0
0.8
0.6
0.4
0.2
0.0
REFERENCE
SAMPLE
0
10
20
30
40
50
60
TIME (SECONDS)

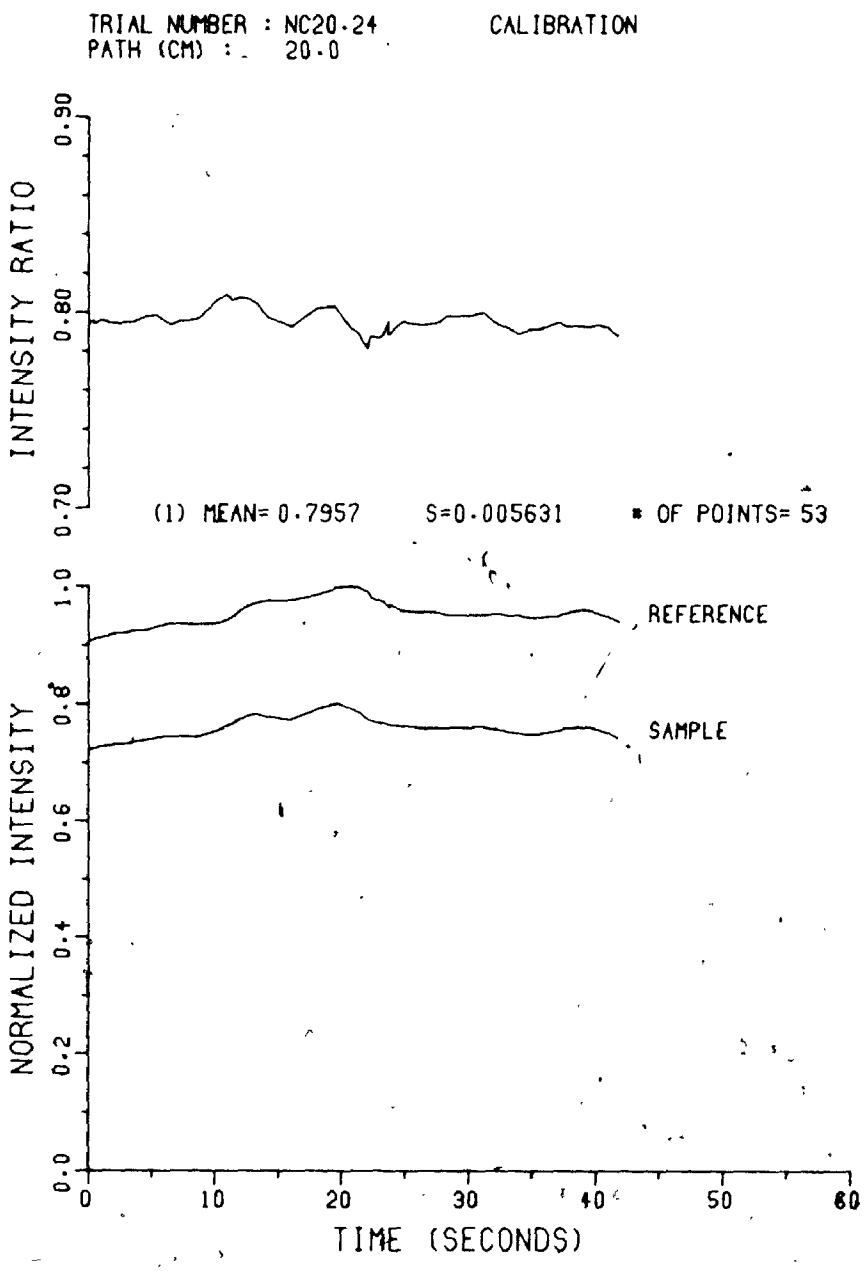
TRIAL NUMBER : NC20-24
PATH (CM) : 20.0
CALIBRATION
INTENSITY RATIO
0.90
0.80
0.70
(1) MEAN= 0.7957
S=0.005631
# OF POINTS= 53
NORMALIZED INTENSITY
1.0
0.8
0.6
0.4
0.2
0.0
REFERENCE
SAMPLE
0
10
20
30
40
50
60
TIME (SECONDS)

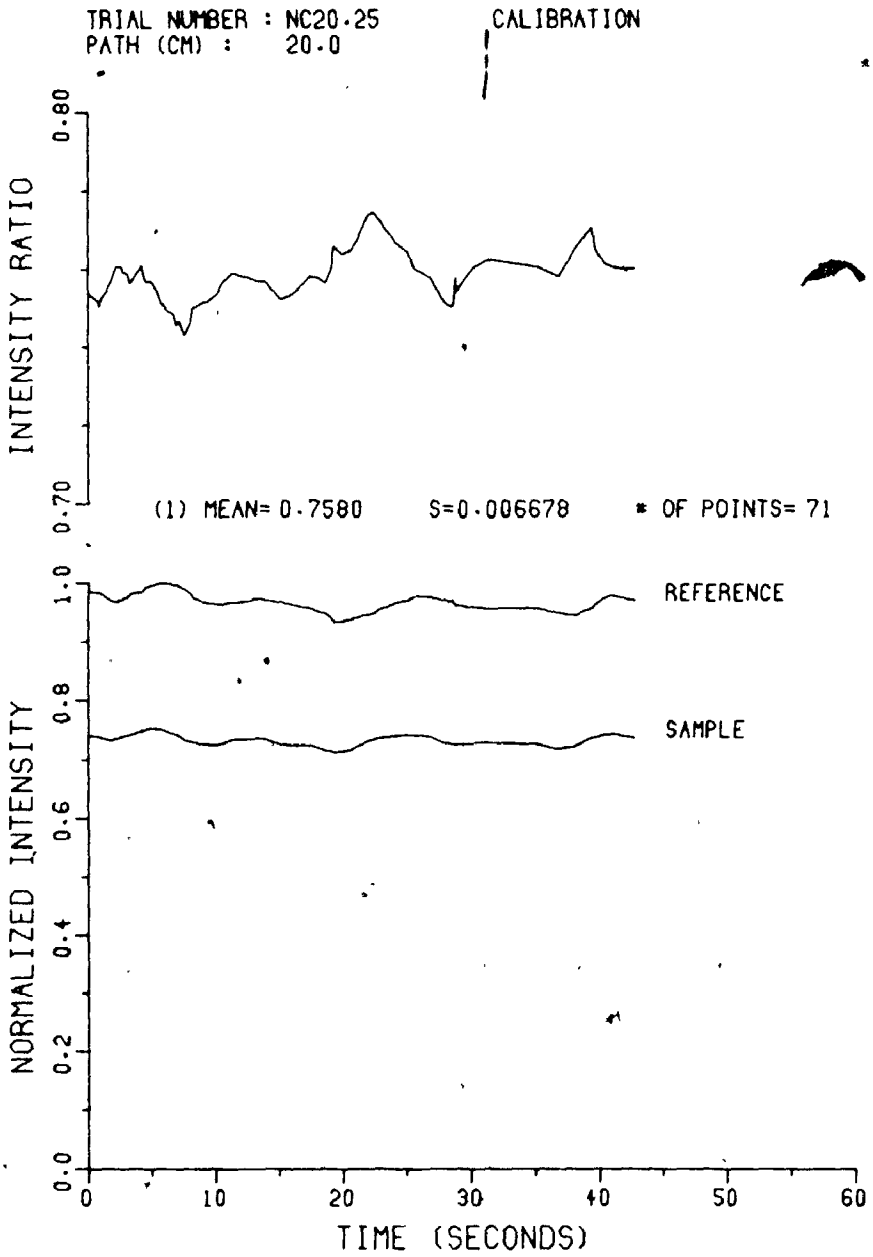
TRIAL NUMBER : NC20.25
PATH (CM) : 20.0
CALIBRATION
INTENSITY RATIO
0.80
0.70
(1) MEAN= 0.7580 S=0.006678 # OF POINTS= 71
NORMALIZED INTENSITY
1.0
0.8
0.6
0.4
0.2
0.0
REFERENCE
SAMPLE
0
10
20
30
40
50
60
TIME (SECONDS)

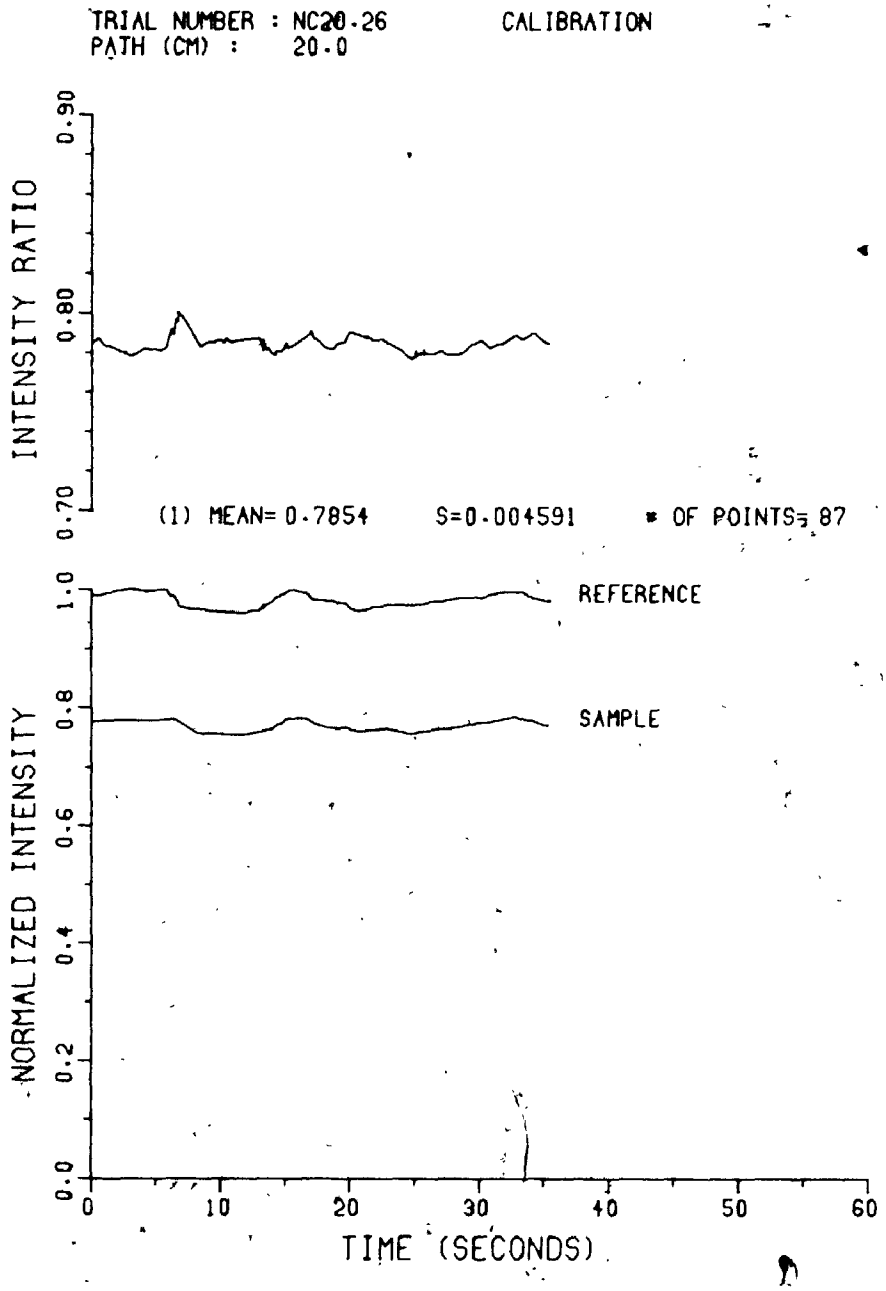
TRIAL NUMBER : NC20-26
PATH (CM) : 20.0
CALIBRATION
INTENSITY RATIO
0.90
0.80
0.70
(1) MEAN= 0.7854
S=0.004591
# OF POINTS= 87
NORMALIZED INTENSITY
1.0
0.8
0.6
0.4
0.2
0.0
REFERENCE
SAMPLE
0
10
20
30
40
50
60
TIME (SECONDS)

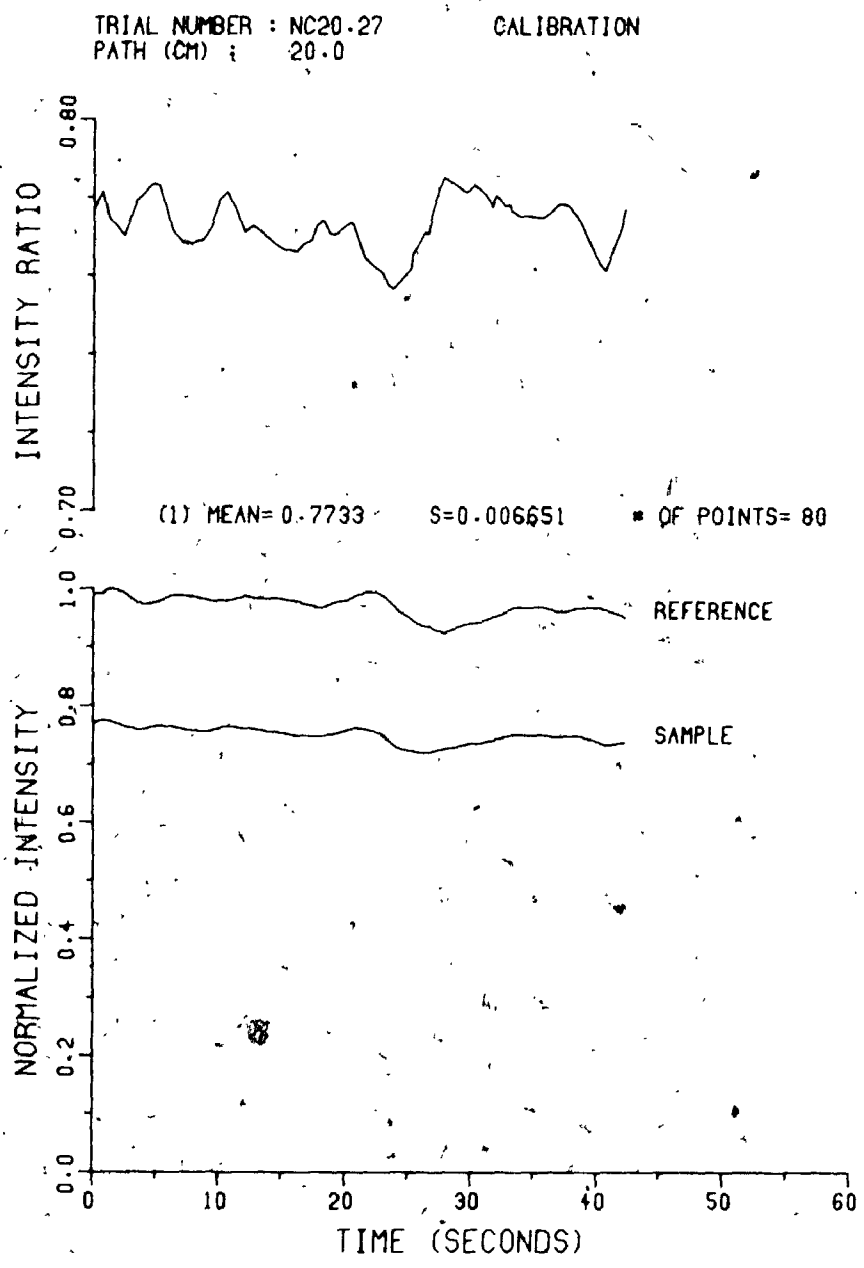
TRIAL NUMBER : NC20.27
CALIBRATION
PATH (CM) : 20.0
INTENSITY RATIO
0.80
0.70
(1) MEAN= 0.7733
S=0.006651
# OF POINTS= 80
NORMALIZED INTENSITY
1.0
0.8
0.6
0.4
0.2
0.0
REFERENCE
SAMPLE
0
10
20
30
40
50
60
TIME (SECONDS)

Data Files - Total Pressure: 100 Torr

Trial Numbers: N20.100.1-N20.100.4

Remote Gain: Sample (G_S): 1 (V/V)

FSD_S: 2

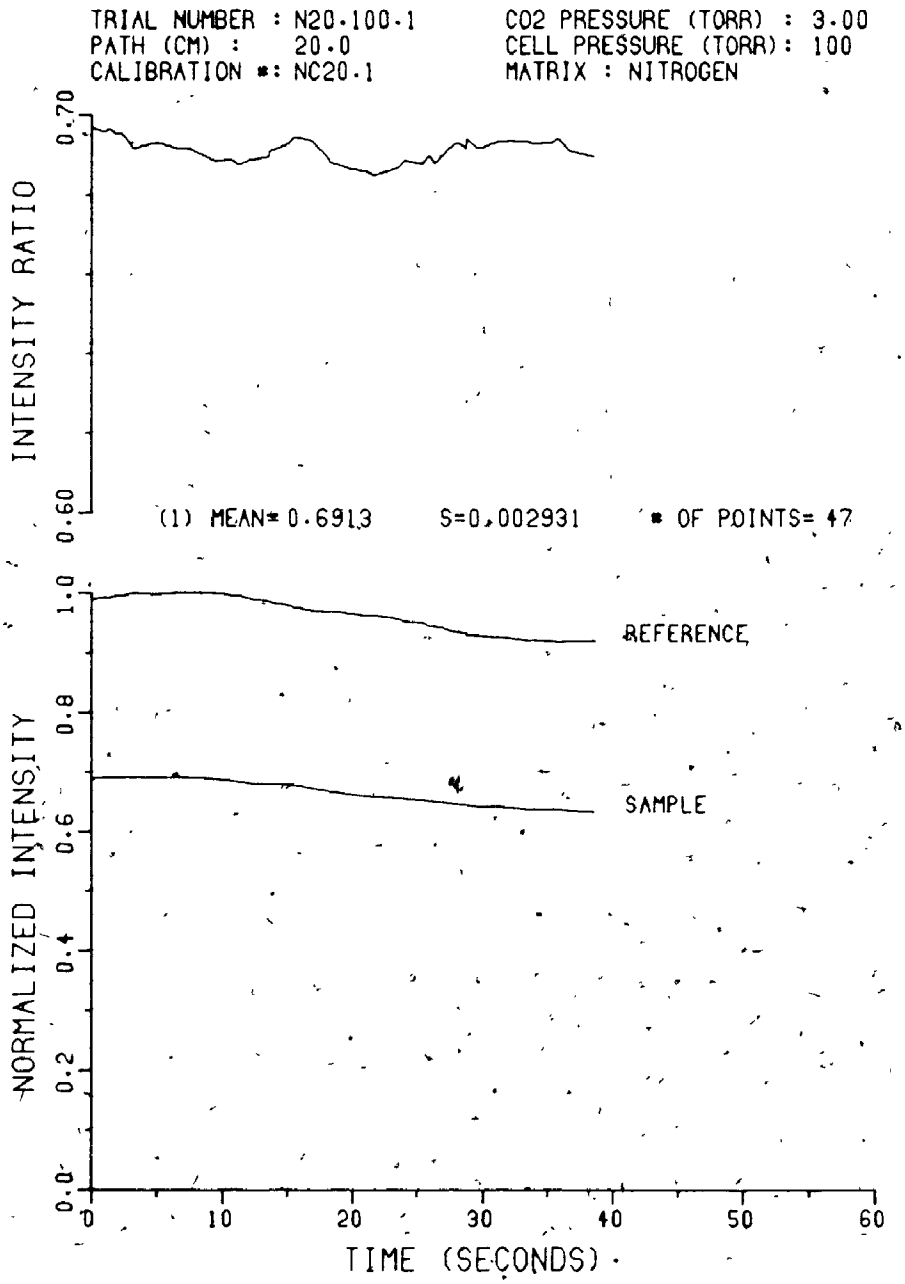
TRIAL NUMBER : N20.100.1
PATH (CM) : 20.0
CALIBRATION #: NC20.1
CO2 PRESSURE (TORR) : 3.00
CELL PRESSURE (TORR): 100
MATRIX : NITROGEN
INTENSITY RATIO
0.70
0.60
(1) MEAN= 0.6913 S=0.002931 # OF POINTS= 47
NORMALIZED INTENSITY
1.0
0.8
0.6
0.4
0.2
0.0
REFERENCE
SAMPLE
0
10
20
30
40
50
60
TIME (SECONDS)

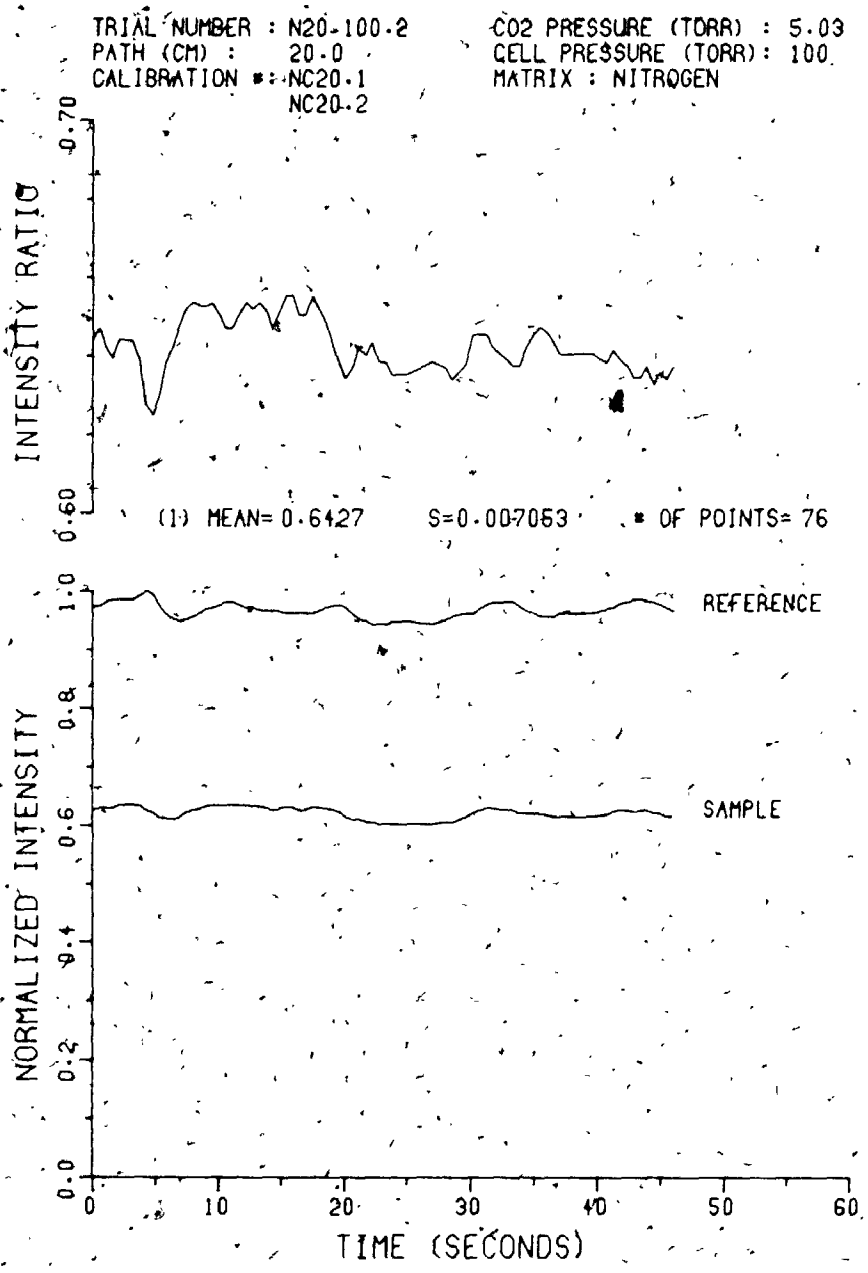
TRIAL NUMBER : N20-100-2
PATH (CM) : 20.0
CALIBRATION #: NC20-1
NC20-2
CO2 PRESSURE (TORR) : 5.03
CELL PRESSURE (TORR): 100.
MATRIX : NITROGEN
INTENSITY RATIO
0.70
0.60
(1) MEAN= 0.6427 S=0.007053 # OF POINTS= 76
NORMALIZED INTENSITY
1.0
0.8
0.6
0.4
0.2
0.0
REFERENCE
SAMPLE
0
10
20
30
40
50
60
TIME (SECONDS)

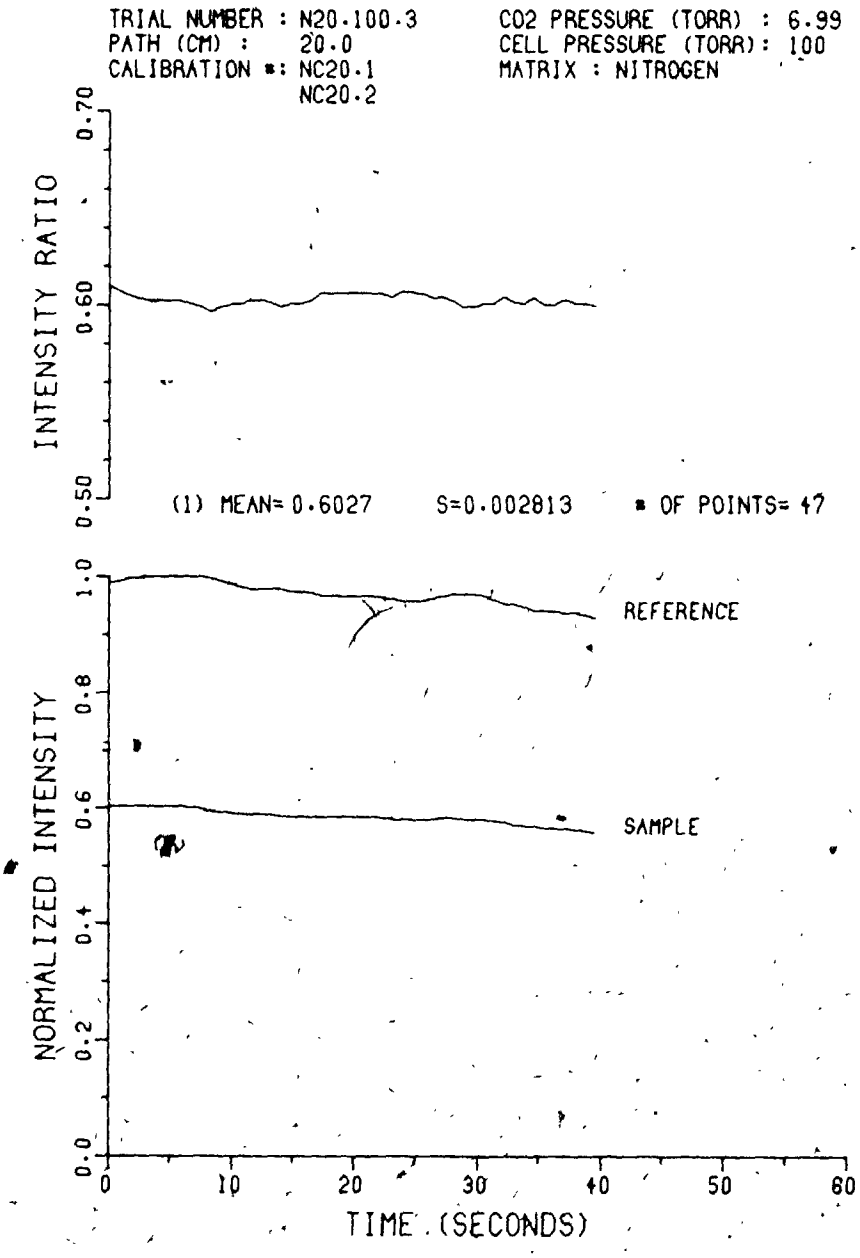
TRIAL NUMBER : N20.100.3
PATH (CM) : 20.0
CALIBRATION #: NC20.1
NC20.2
CO2 PRESSURE (TORR) : 6.99
CELL PRESSURE (TORR): 100
MATRIX : NITROGEN
INTENSITY RATIO
0.70
0.60
0.50
(1) MEAN= 0.6027 S=0.002813 # OF POINTS= 47
NORMALIZED INTENSITY
1.0
0.8
0.6
0.4
0.2
0.0
REFERENCE
SAMPLE
0
10
20
30
40
50
60
TIME (SECONDS)

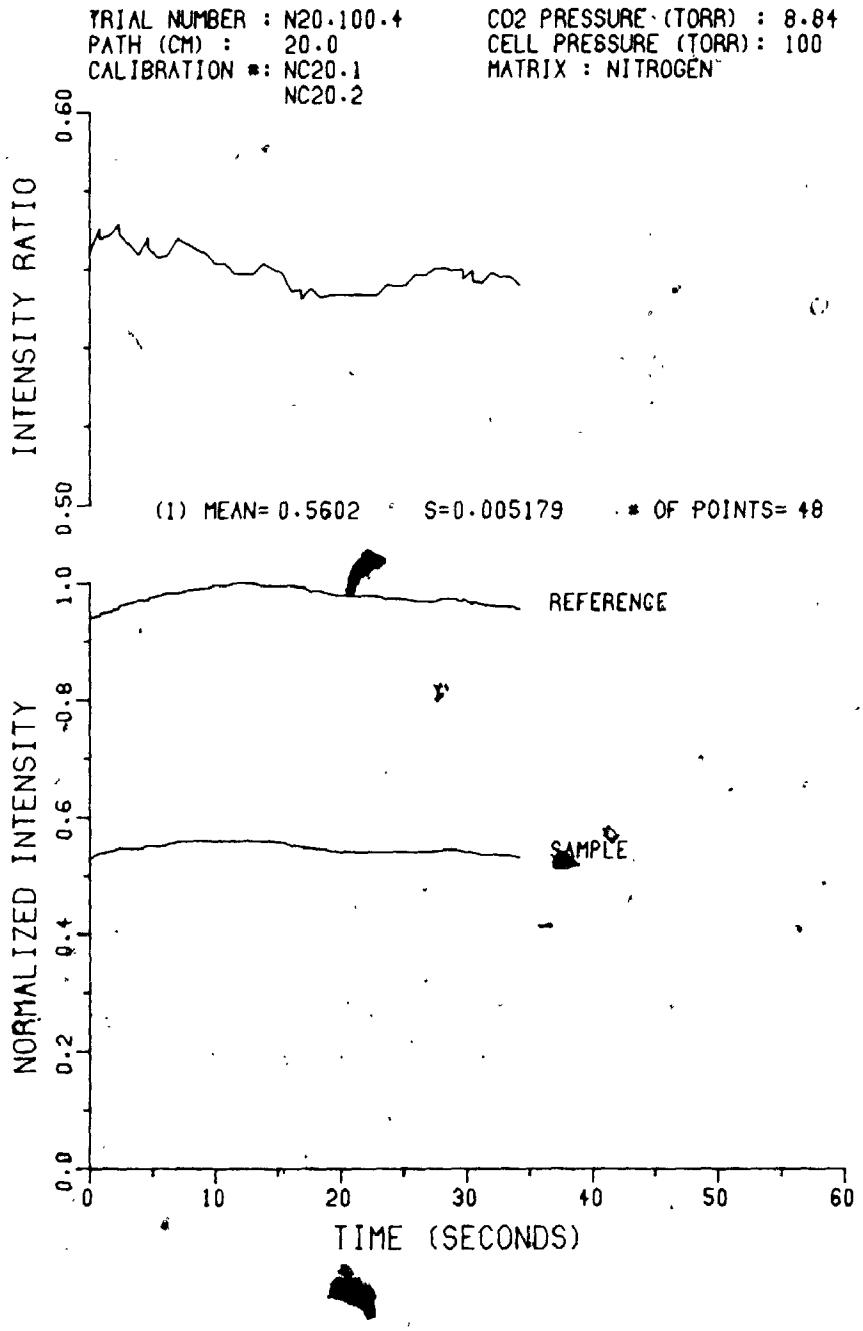
TRIAL NUMBER : N20.100.4
PATH (CM) : 20.0
CALIBRATION #: NC20.1
NC20.2
CO2 PRESSURE (TORR) : 8.84
CELL PRESSURE (TORR): 100
MATRIX : NITROGEN
INTENSITY RATIO
0.60
0.50
(1) MEAN= 0.5602 S=0.005179 # OF POINTS= 48
NORMALIZED INTENSITY
1.0
0.8
0.6
0.4
0.2
0.0
REFERENCE
SAMPLE
0
10
20
30
40
50
60
TIME (SECONDS)

Data Files - Total Pressure: 200 Torr

Trial Numbers: N20.200.1-N20.200.7

Remote Gain: Sample (G_S): 1 (V/V)

FSD_S: 2

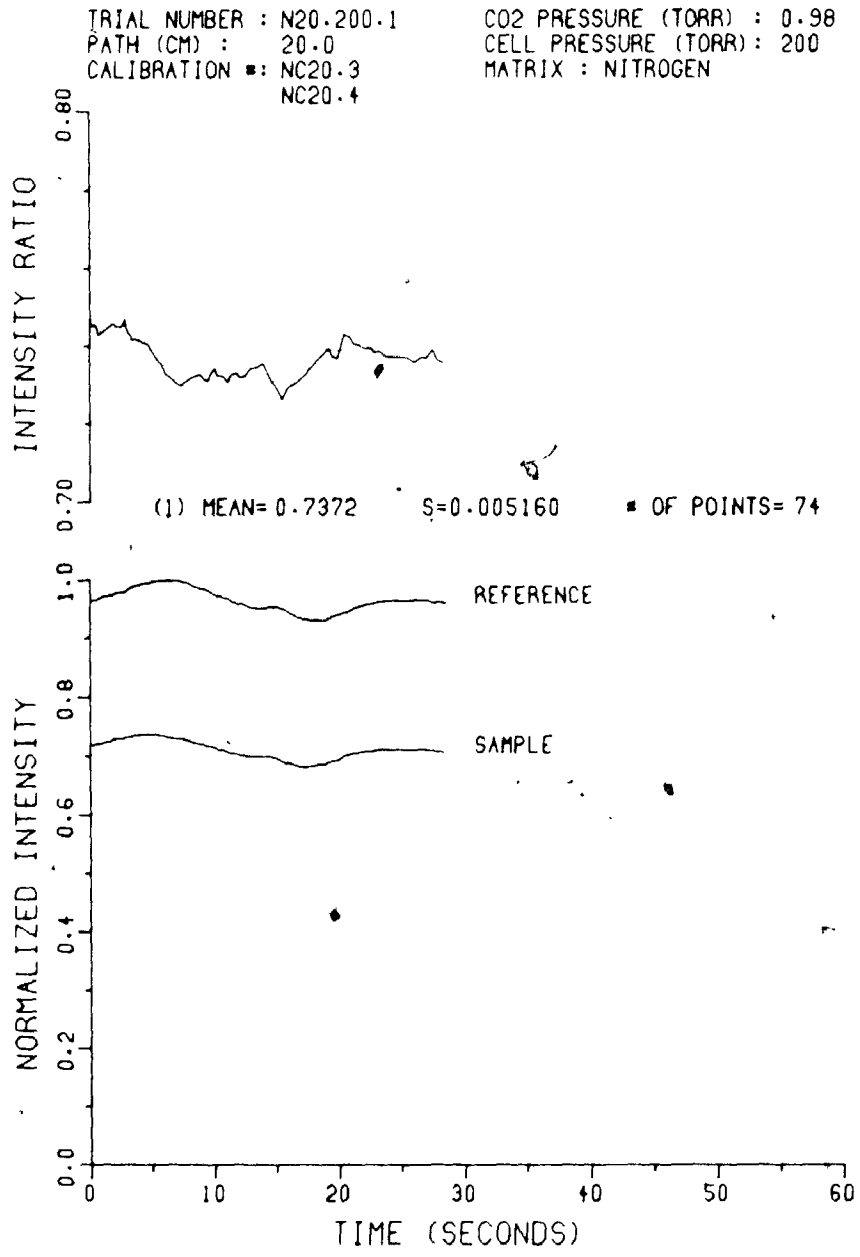

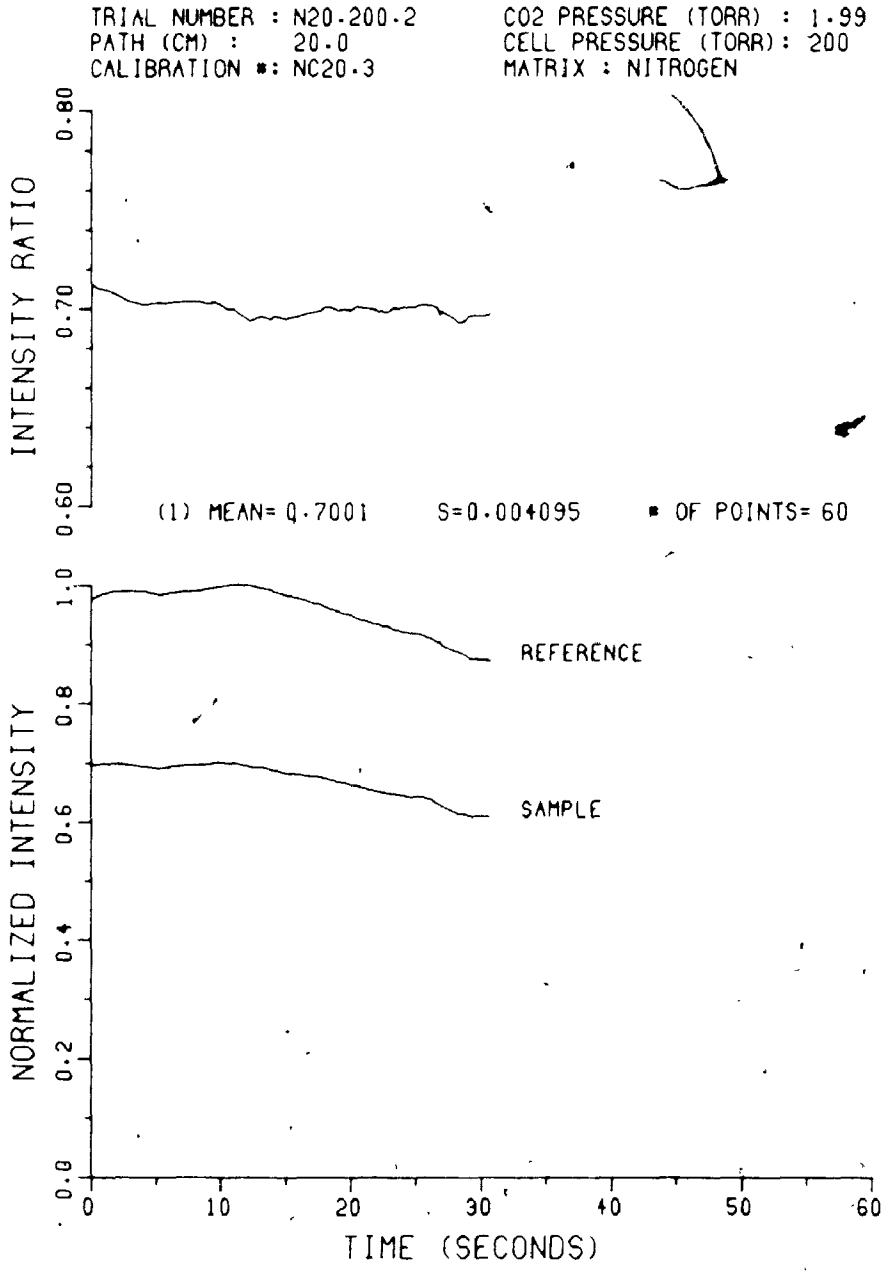
TRIAL NUMBER : N20-200-2
PATH (CM) : 20.0
CALIBRATION #: NC20-3
CO2 PRESSURE (TORR) : 1.99
CELL PRESSURE (TORR): 200
MATRIX : NITROGEN
INTENSITY RATIO
0.80
0.70
0.60
(1) MEAN= 0.7001 S=0.004095 # OF POINTS= 60
NORMALIZED INTENSITY
1.0
0.8
0.6
0.4
0.2
0.0
REFERENCE
SAMPLE
0
10
20
30
40
50
60
TIME (SECONDS)

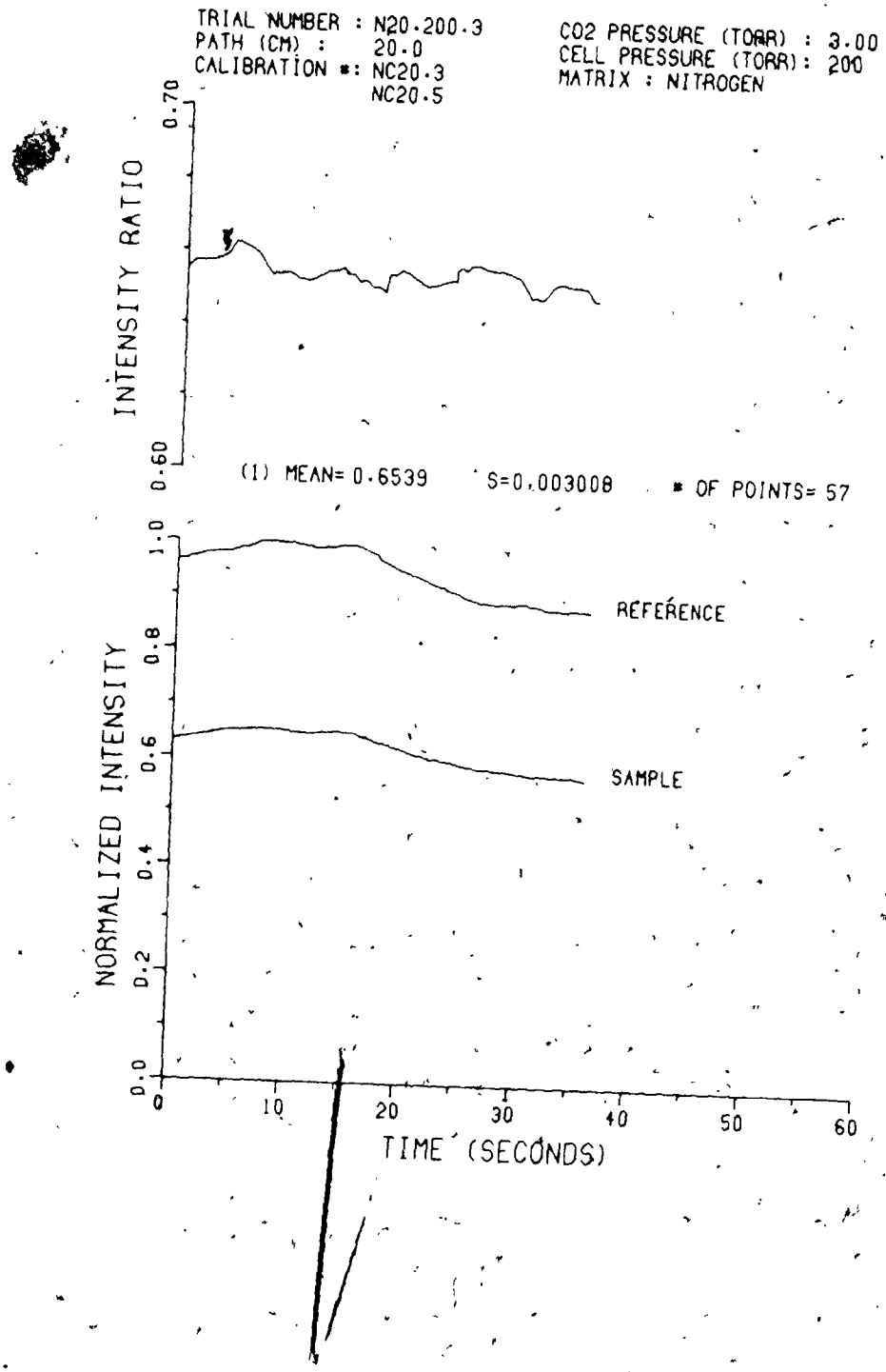
TRIAL NUMBER : N20.200.3
PATH (CM) : 20.0
CALIBRATION #: NC20.3
NC20.5
CO2 PRESSURE (TORR) : 3.00
CELL PRESSURE (TORR): 200
MATRIX : NITROGEN
INTENSITY RATIO
0.70
0.60
(1) MEAN= 0.6539 S=0.003008 # OF POINTS= 57
NORMALIZED INTENSITY
1.0
0.8
0.6
0.4
0.2
0.0
REFERENCE
SAMPLE
0
10
20
30
40
50
60
TIME (SECONDS)

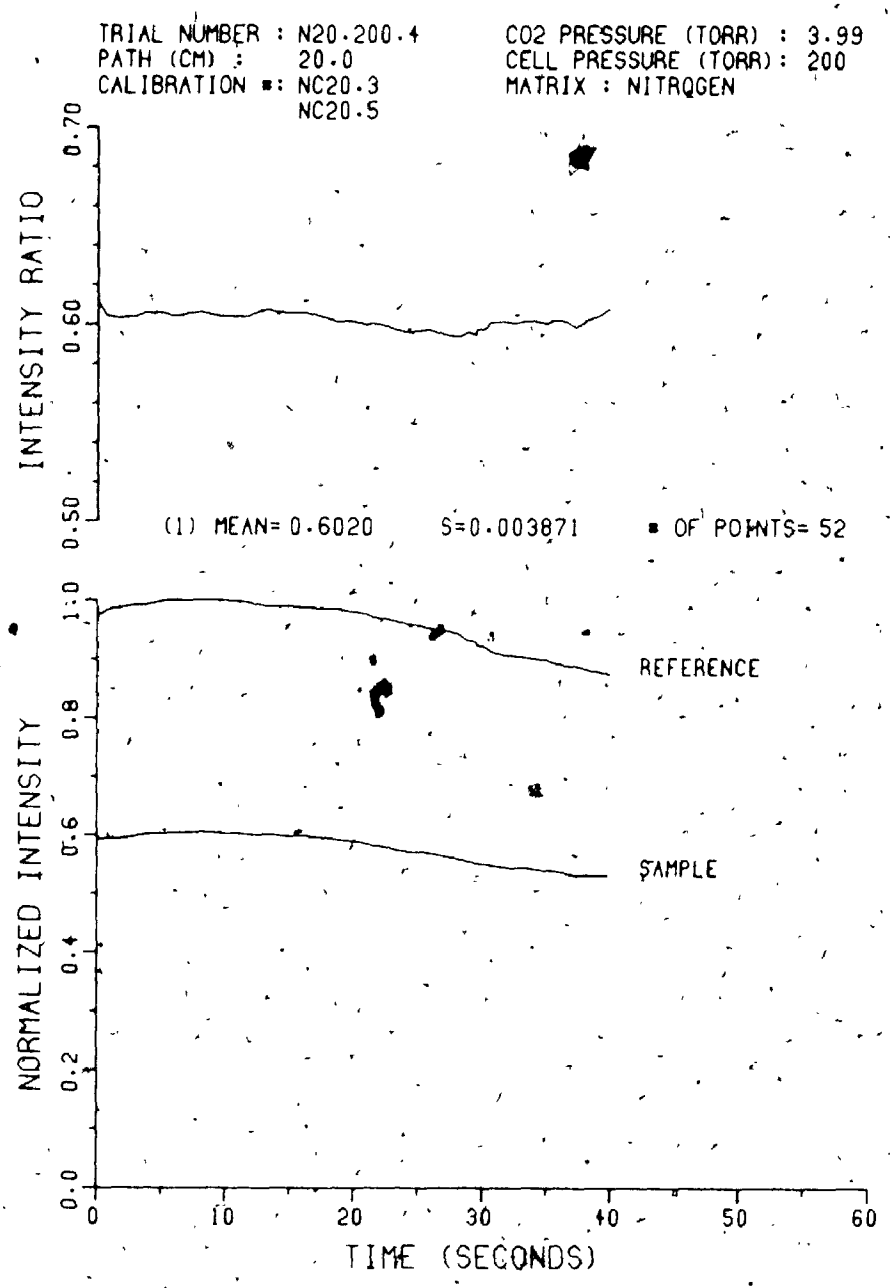
TRIAL NUMBER : N20.200.4
PATH (CM) : 20.0
CALIBRATION #: NC20.3
NC20.5
CO2 PRESSURE (TORR) : 3.99
CELL PRESSURE (TORR): 200
MATRIX : NITROGEN
INTENSITY RATIO
0.70
0.60
0.50
(1) MEAN= 0.6020 S=0.003871 # OF POINTS= 52
NORMALIZED INTENSITY
1.0
0.8
0.6
0.4
0.2
0.0
REFERENCE
SAMPLE
0
10
20
30
40
50
60
TIME (SECONDS)

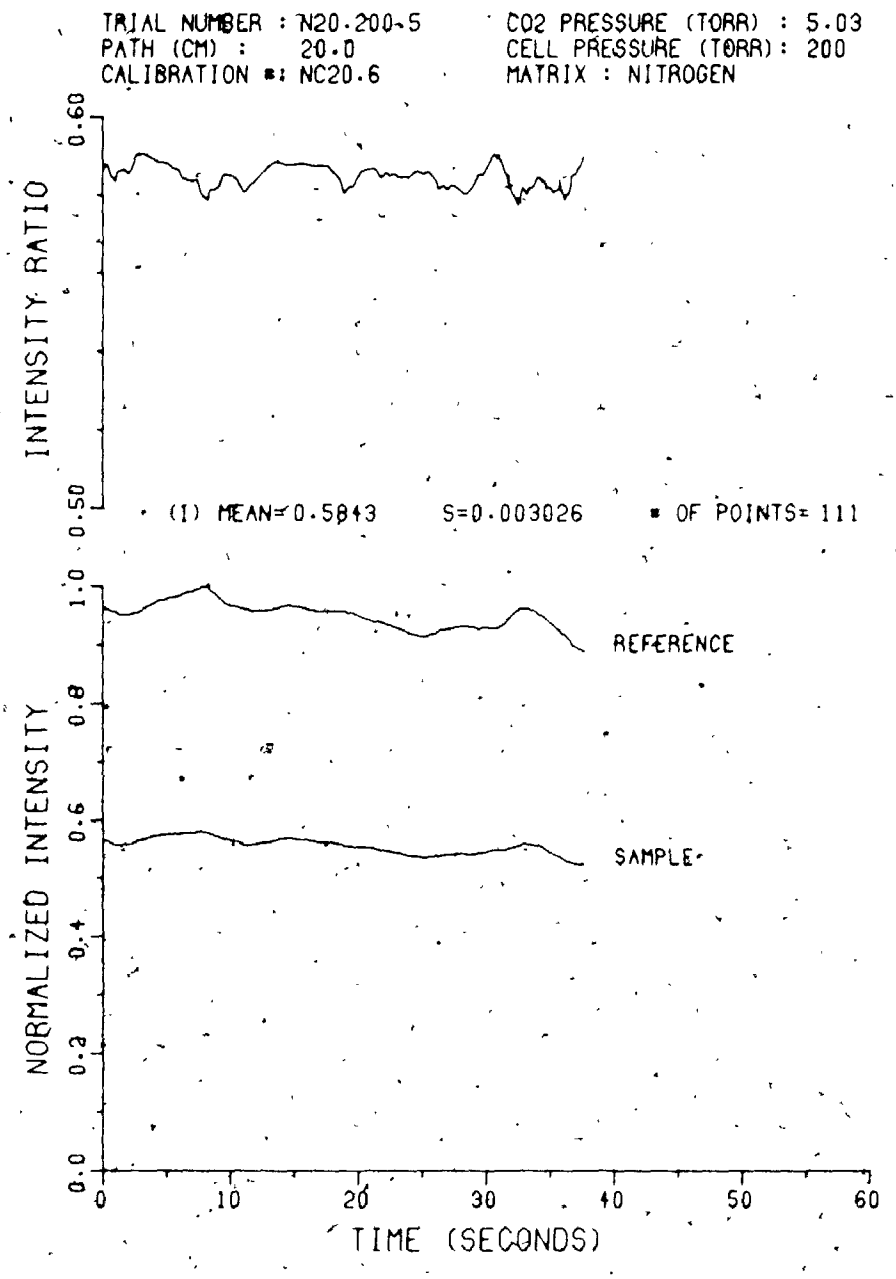
TRIAL NUMBER : N20.200-5
PATH (CM) : 20.0
CALIBRATION #: NC20.6
CO2 PRESSURE (TORR) : 5.03
CELL PRESSURE (TORR): 200
MATRIX : NITROGEN
INTENSITY RATIO
0.60
0.50
(I) MEAN=0.5843 S=0.003026 # OF POINTS= 111
NORMALIZED INTENSITY
1.0
0.8
0.6
0.4
0.2
0.0
REFERENCE
SAMPLE
0
10
20
30
40
50
60
TIME (SECONDS)

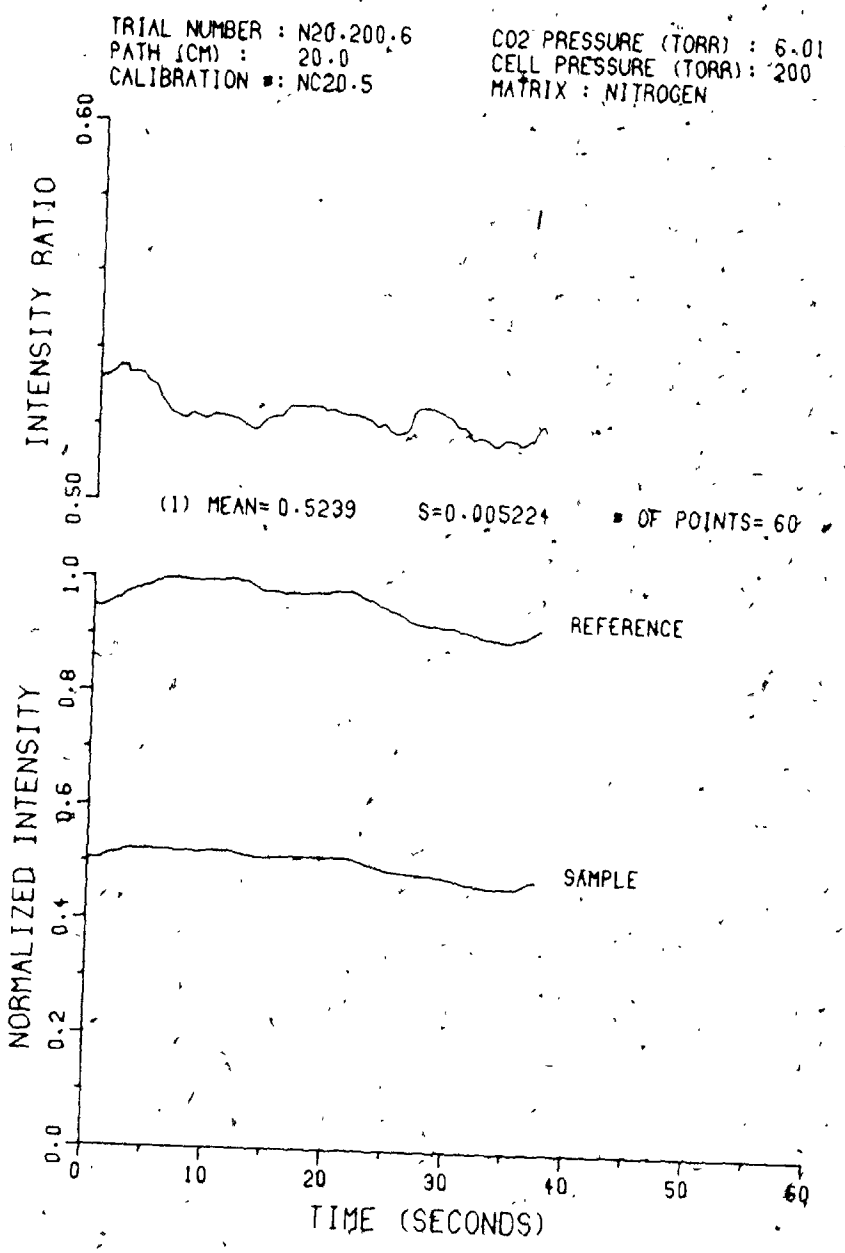
TRIAL NUMBER : N20.200.6
PATH (CM) : 20.0
CALIBRATION #: NC20.5
CO2 PRESSURE (TORR) : 6.01
CELL PRESSURE (TORR): 200
MATRIX : NITROGEN
INTENSITY RATIO
0.60
0.50
(1) MEAN= 0.5239 S=0.005224 # OF POINTS= 60
NORMALIZED INTENSITY
1.0
0.8
0.6
0.4
0.2
0.0
REFERENCE
SAMPLE
0
10
20
30
40
50
60
TIME (SECONDS)

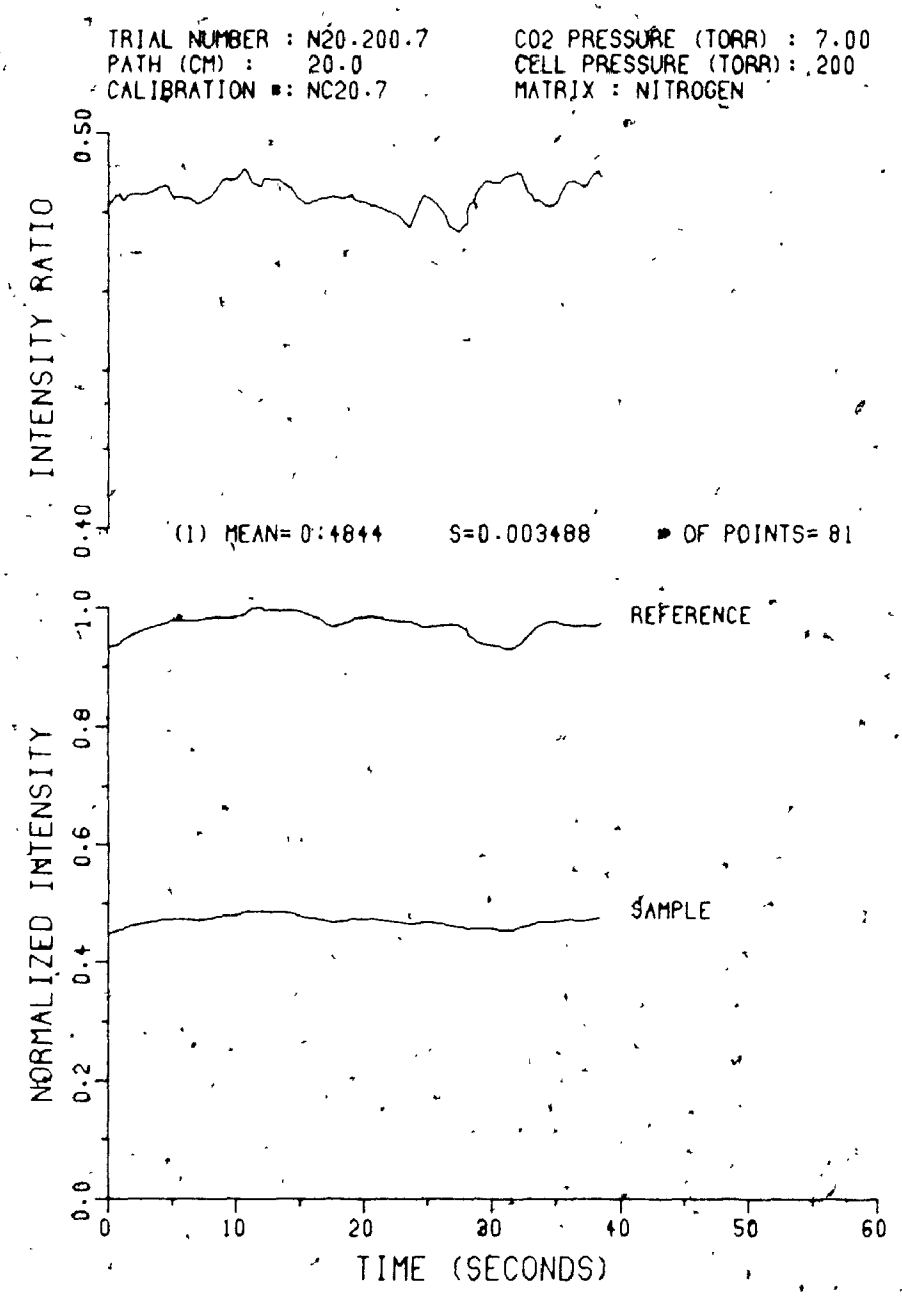
TRIAL NUMBER : N20.200.7
PATH (CM) : 20.0
CALIBRATION # : NC20.7
CO2 PRESSURE (TORR) : 7.00
CELL PRESSURE (TORR) : .200
MATRIX : NITROGEN
INTENSITY RATIO
0.50
0.40
(1) MEAN= 0.4844 S=0.003488 # OF POINTS= 81
NORMALIZED INTENSITY
1.0
0.8
0.6
0.4
0.2
0.0
REFERENCE
SAMPLE
0
10
20
30
40
50
60
TIME (SECONDS)

Data Files - Total Pressure: 300 Torr

Trial Numbers: N20.300.1-N20.300.8

Remote Gain: Sample.(G_s): 1 (V/V)

FSD_s: 2

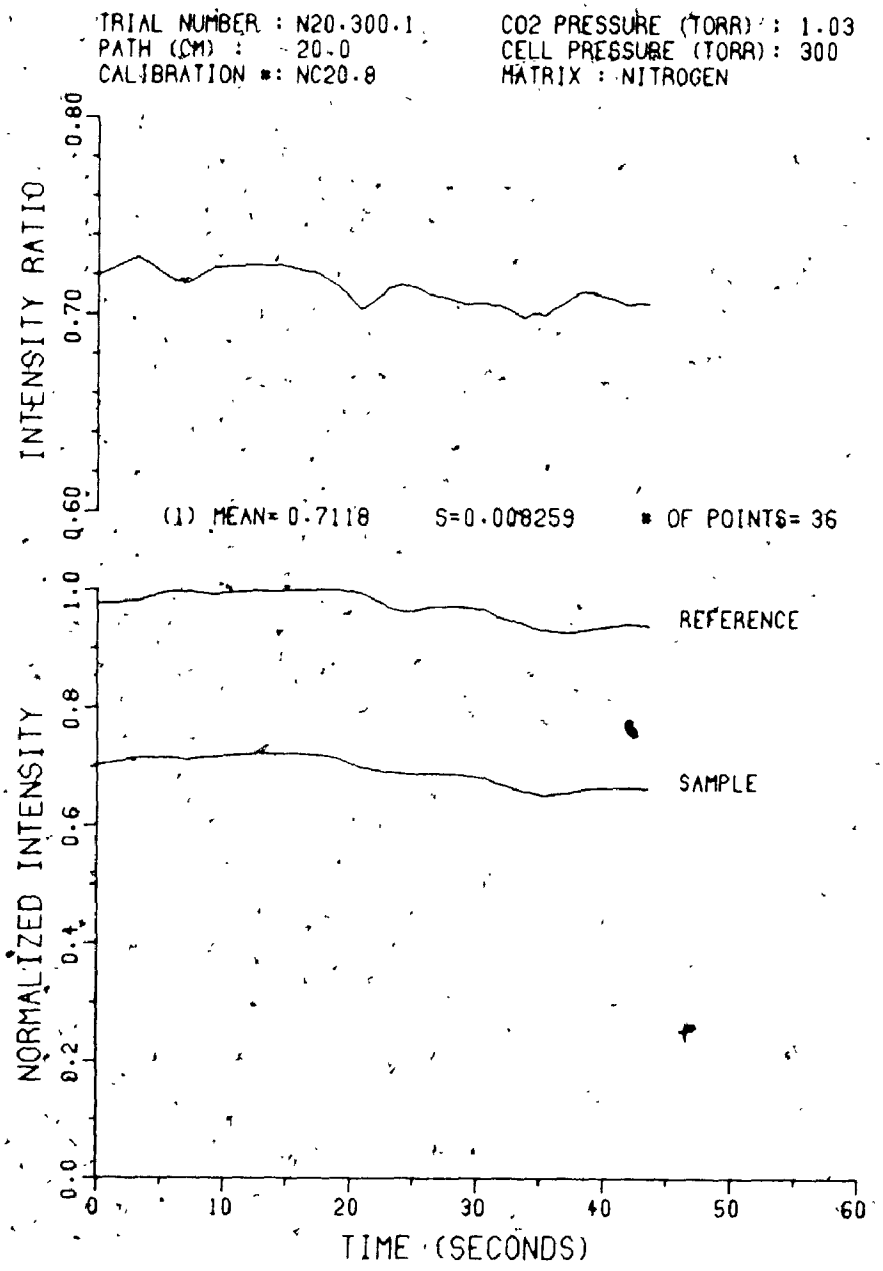

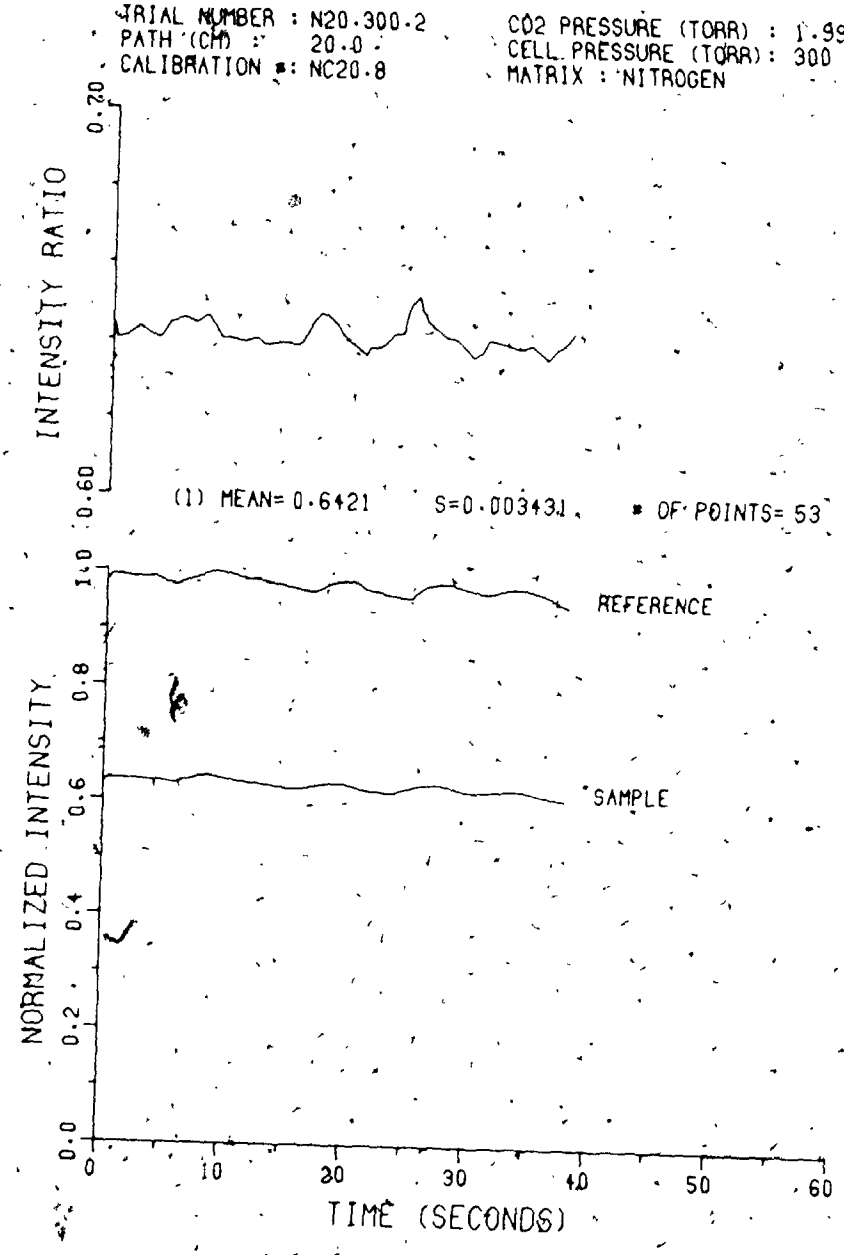
TRIAL NUMBER : N20.300.2
PATH (CM) : 20.0
CALIBRATION # : NC20.8
CO2 PRESSURE (TORR) : 1.99
CELL PRESSURE (TORR) : 300
MATRIX : NITROGEN
INTENSITY RATIO
0.20
0.60
(1) MEAN= 0.6421 S=0.003431 # OF POINTS= 53
NORMALIZED INTENSITY
1.0
0.8
0.6
0.4
0.2
0.0
REFERENCE
SAMPLE
0
10
20
30
40
50
60
TIME (SECONDS)

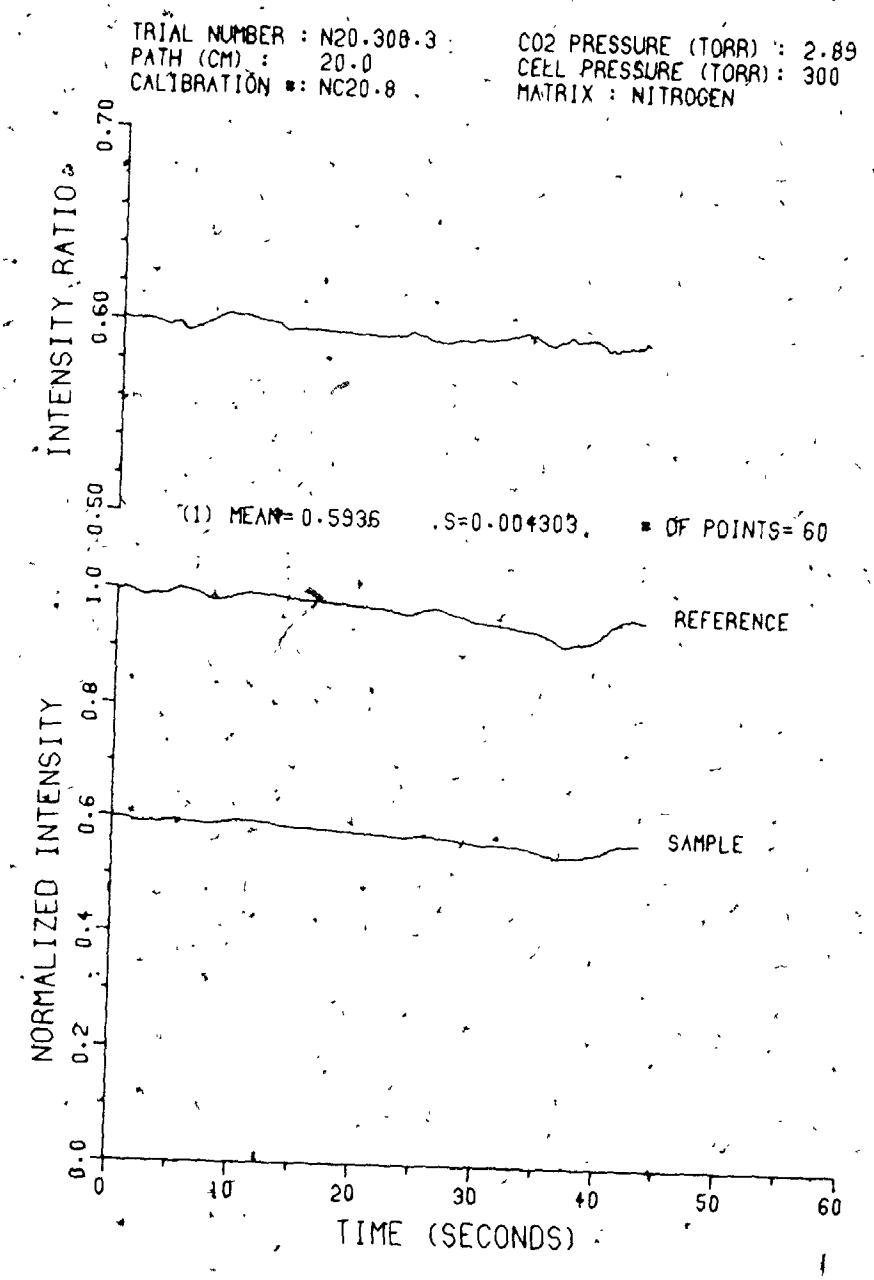
TRIAL NUMBER : N20.308.3
PATH (CM) : 20.0
CALIBRATION #: NC20.8
CO2 PRESSURE (TORR) : 2.89
CELL PRESSURE (TORR): 300
MATRIX : NITROGEN
INTENSITY RATIO
0.70
0.60
0.50
(1) MEAN= 0.5936 .S=0.004303. # OF POINTS= 60
NORMALIZED INTENSITY
1.0
0.8
0.6
0.4
0.2
0.0
REFERENCE
SAMPLE
0
10
20
30
40
50
60
TIME (SECONDS)

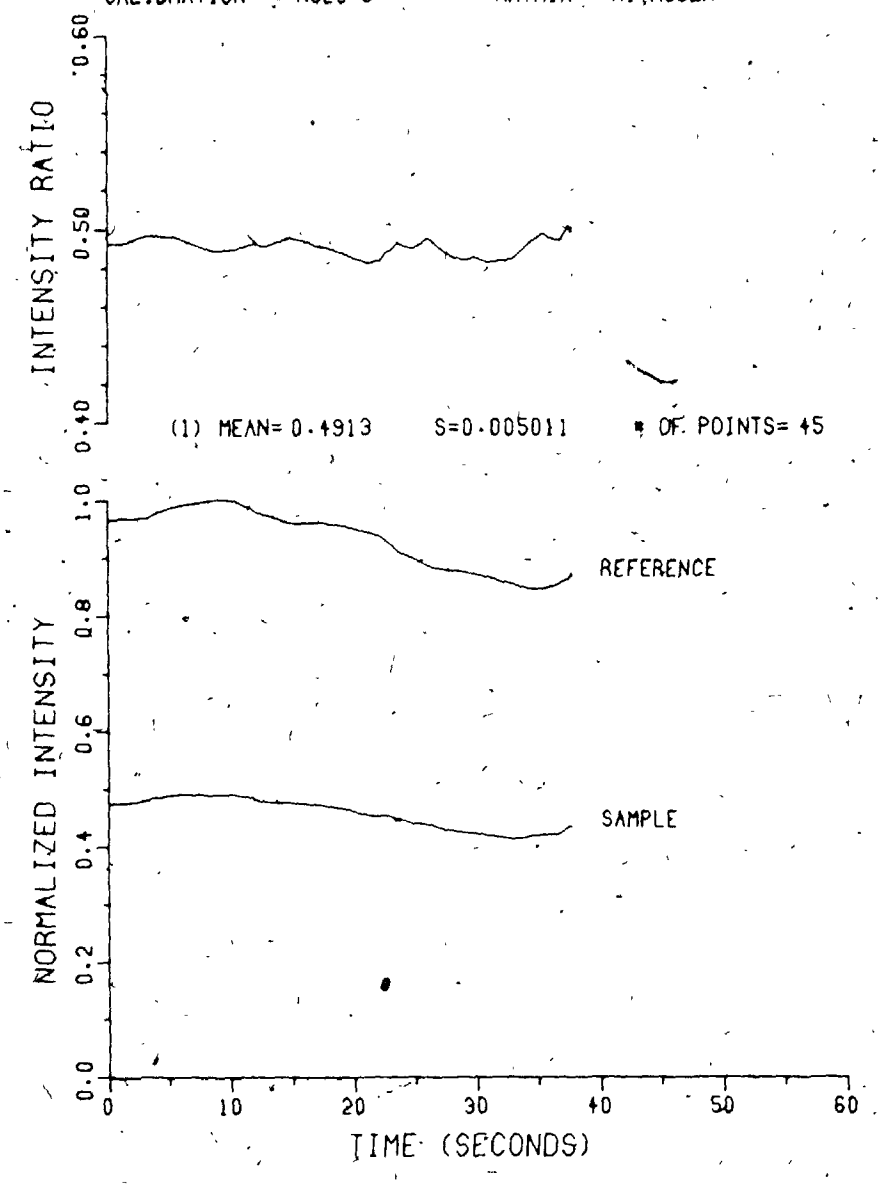
TRIAL NUMBER : N20.300.5
PATH (CM) : 20.0
CALIBRATION #: NC20.9
CO2 PRESSURE (TORR) : 5.03
CELL PRESSURE (TORR): 300
MATRIX : NITROGEN
INTENSITY RATIO
0.60
0.50
0.40
(1) MEAN= 0.4913 S=0.005011 # OF POINTS= 45
NORMALIZED INTENSITY
1.0
0.8
0.6
0.4
0.2
0.0
REFERENCE
SAMPLE
0
10
20
30
40
50
60
TIME (SECONDS)

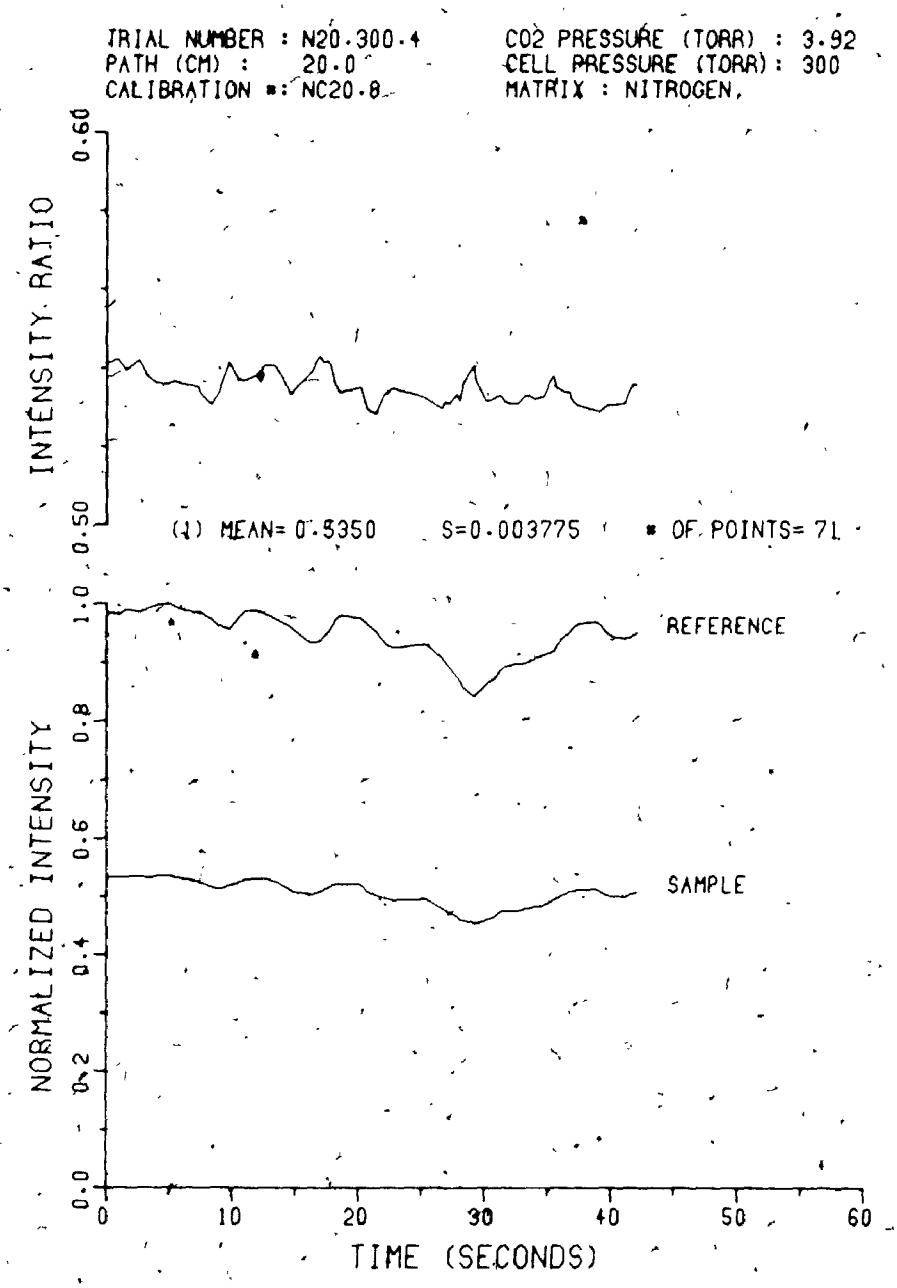
TRIAL NUMBER : N20.300.4
PATH (CM) : 20.0
CALIBRATION #: NC20.8
CO2 PRESSURE (TORR) : 3.92
CELL PRESSURE (TORR): 300
MATRIX : NITROGEN.
INTENSITY RATIO
0.60
0.50
(1) MEAN= 0.5350 S=0.003775 # OF POINTS= 71
NORMALIZED INTENSITY
1.0
0.8
0.6
0.4
0.2
0.0
REFERENCE
SAMPLE
0
10
20
30
40
50
60
TIME (SECONDS)

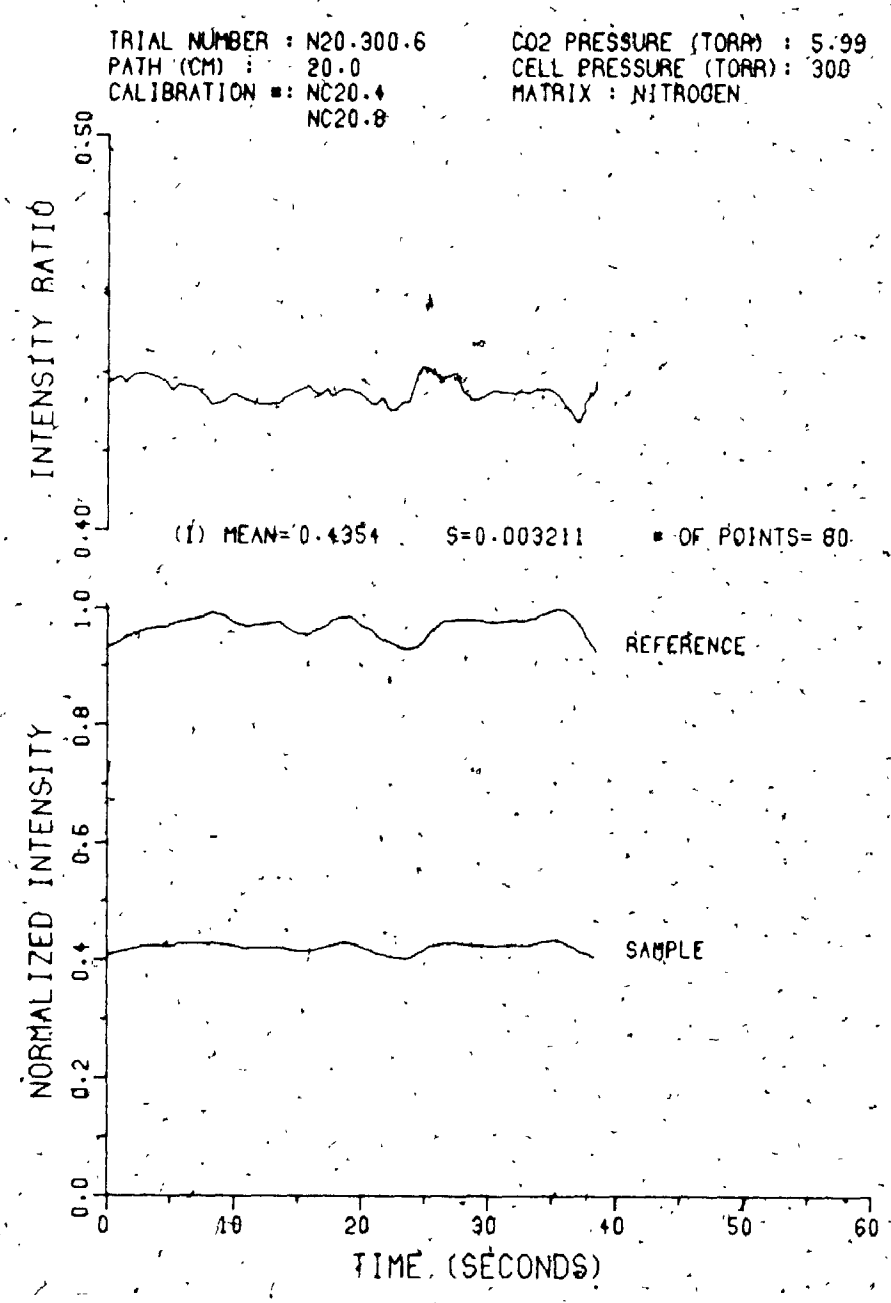
TRIAL NUMBER : N20.300.6
PATH (CM) : 20.0
CALIBRATION = : NC20.4
NC20.8
CO2 PRESSURE (TORR) : 5.99
CELL PRESSURE (TORR) : 300
MATRIX : NITROGEN
INTENSITY RATIO
0.50
0.40
(I) MEAN= 0.4354 S=0.003211 # OF POINTS= 80
NORMALIZED INTENSITY
1.0
0.8
0.6
0.4
0.2
0.0
REFERENCE
SAMPLE
0
10
20
30
40
50
60
TIME (SECONDS)

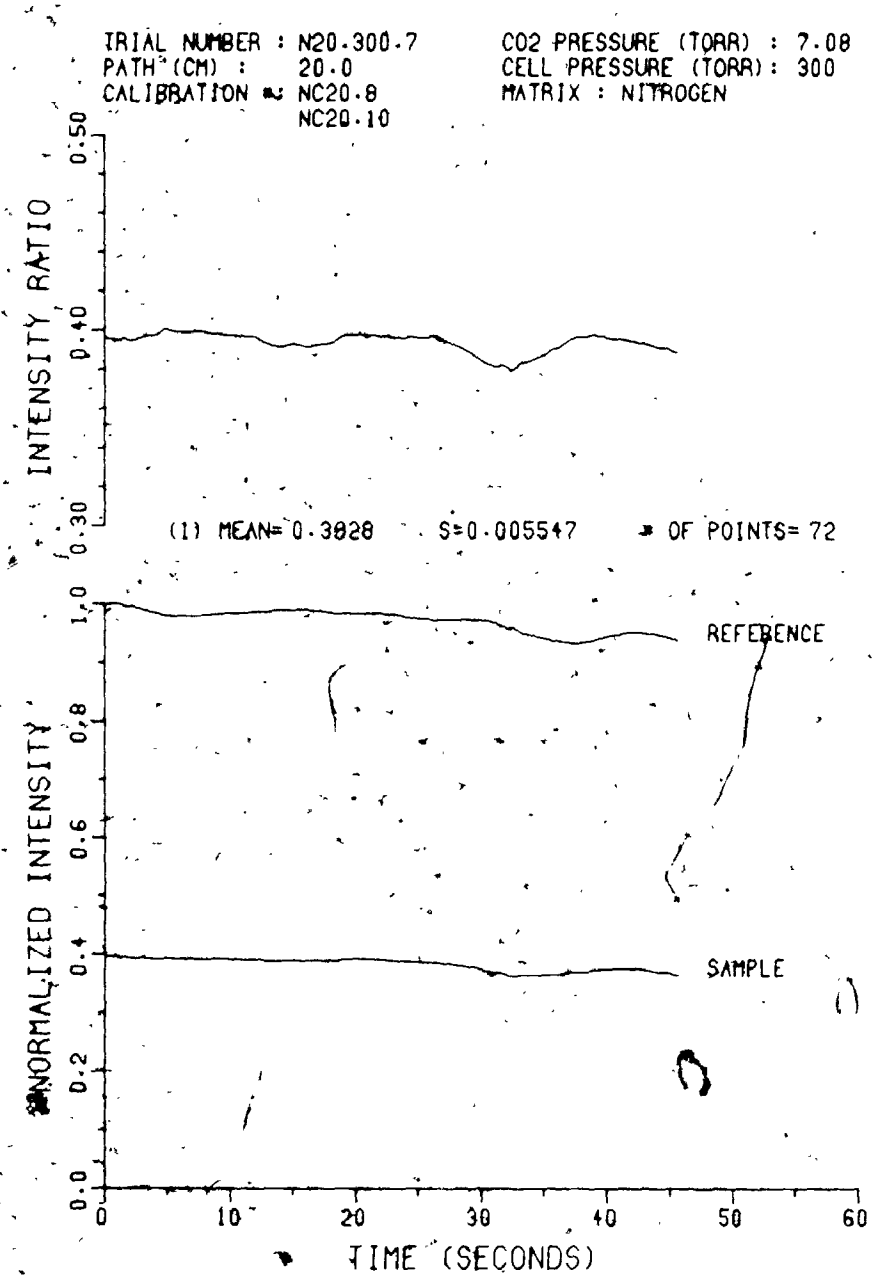
TRIAL NUMBER : N20.300.7
PATH (CM) : 20.0
CALIBRATION : NC20.8
NC20.10
CO2 PRESSURE (TORR) : 7.08
CELL PRESSURE (TORR) : 300
MATRIX : NITROGEN
INTENSITY RATIO
0.50
0.40
0.30
(1) MEAN= 0.3828 S=0.005547 # OF POINTS= 72
NORMALIZED INTENSITY
1.0
0.8
0.6
0.4
0.2
0.0
REFERENCE
SAMPLE
0
10
20
30
40
50
60
TIME (SECONDS)

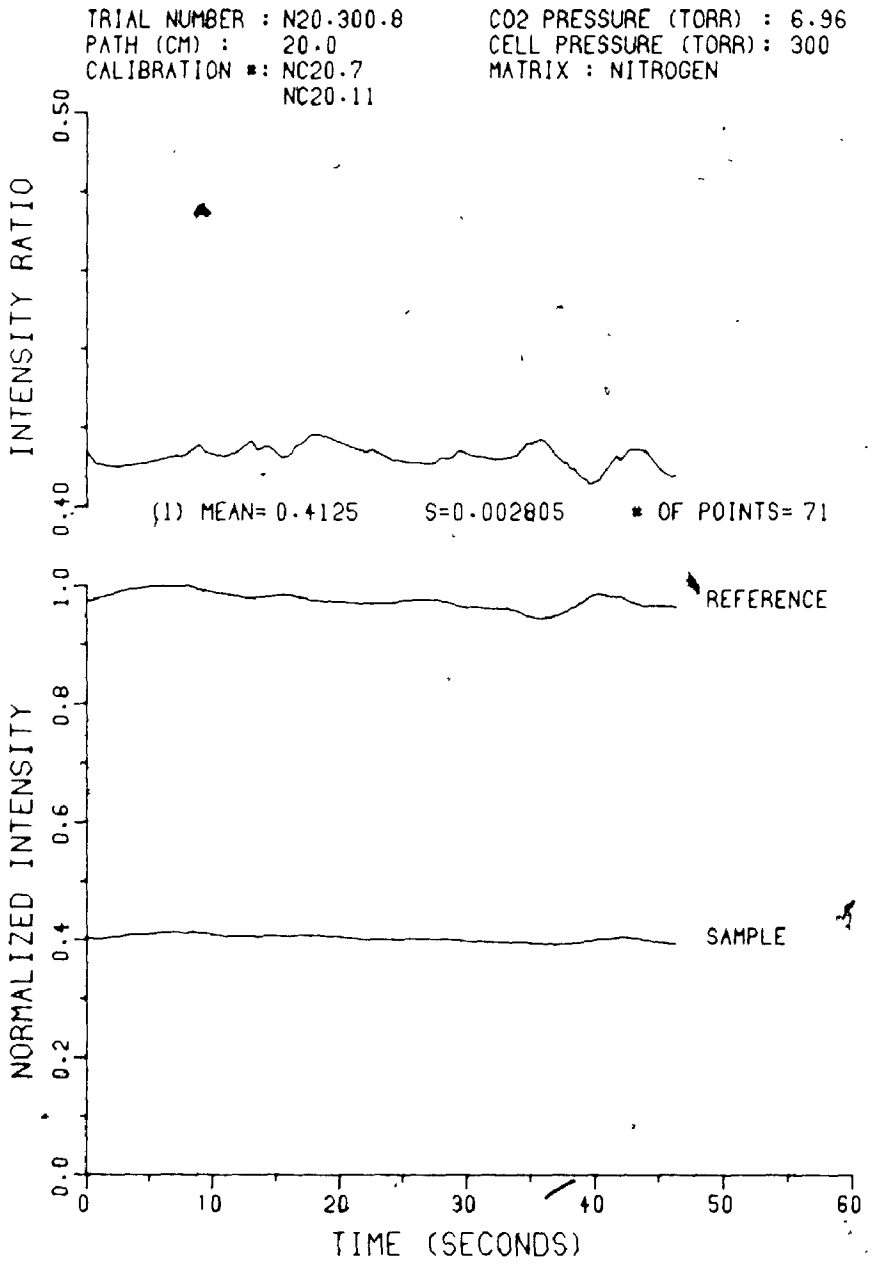
TRIAL NUMBER : N20.300.8
PATH (CM) : 20.0
CALIBRATION #: NC20.7
NC20.11
CO2 PRESSURE (TORR) : 6.96
CELL PRESSURE (TORR): 300
MATRIX : NITROGEN
INTENSITY RATIO
0.50
0.40
(1) MEAN= 0.4125 S=0.002805 # OF POINTS= 71
NORMALIZED INTENSITY
1.0
0.8
0.6
0.4
0.2
0.0
REFERENCE
SAMPLE
0
10
20
30
40
50
60
TIME (SECONDS)

Data Files - Total Pressure: 400 Torr

Trial Numbers: N20.400.1-N20.400.8

Remote Gain: Sample (G_S): 1 (V/V)

FSD_S: 2

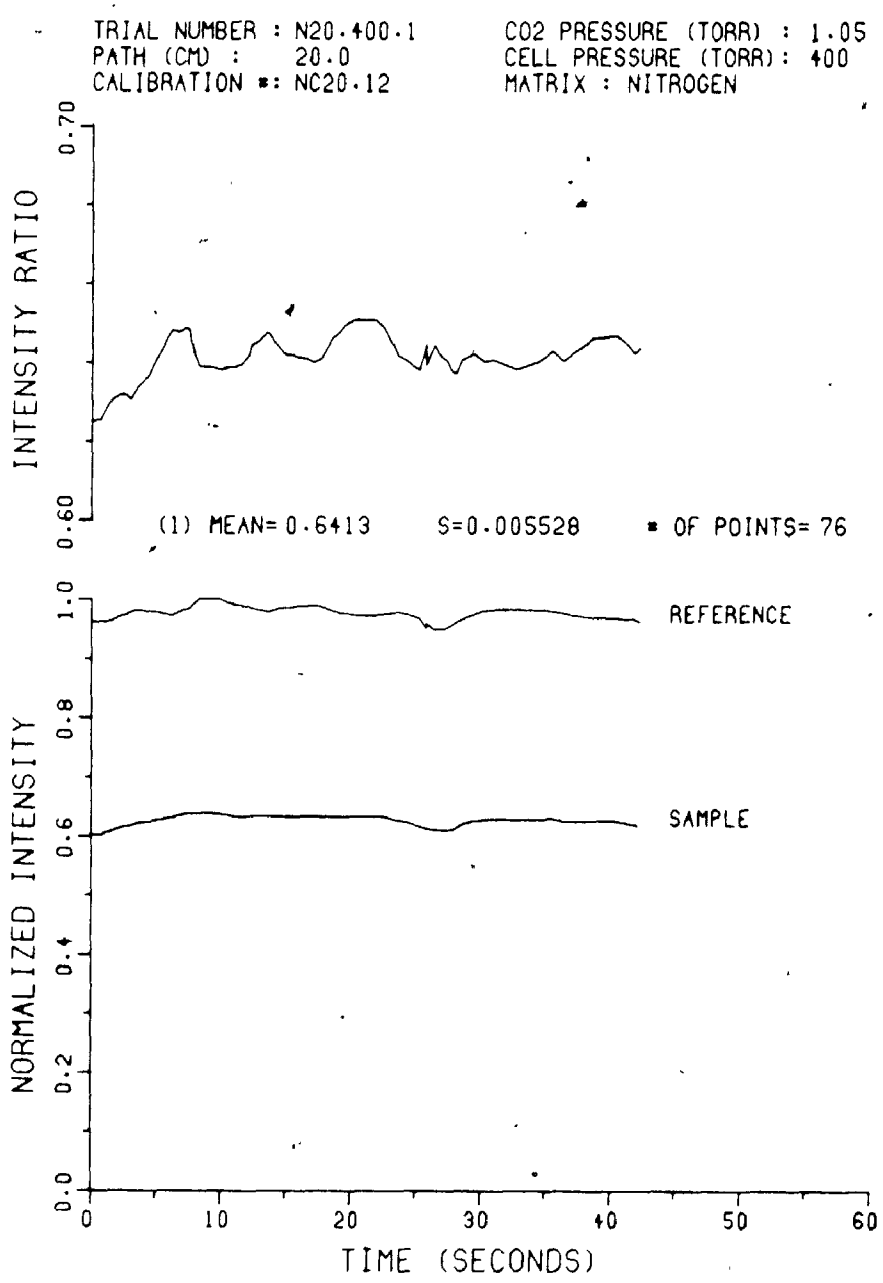

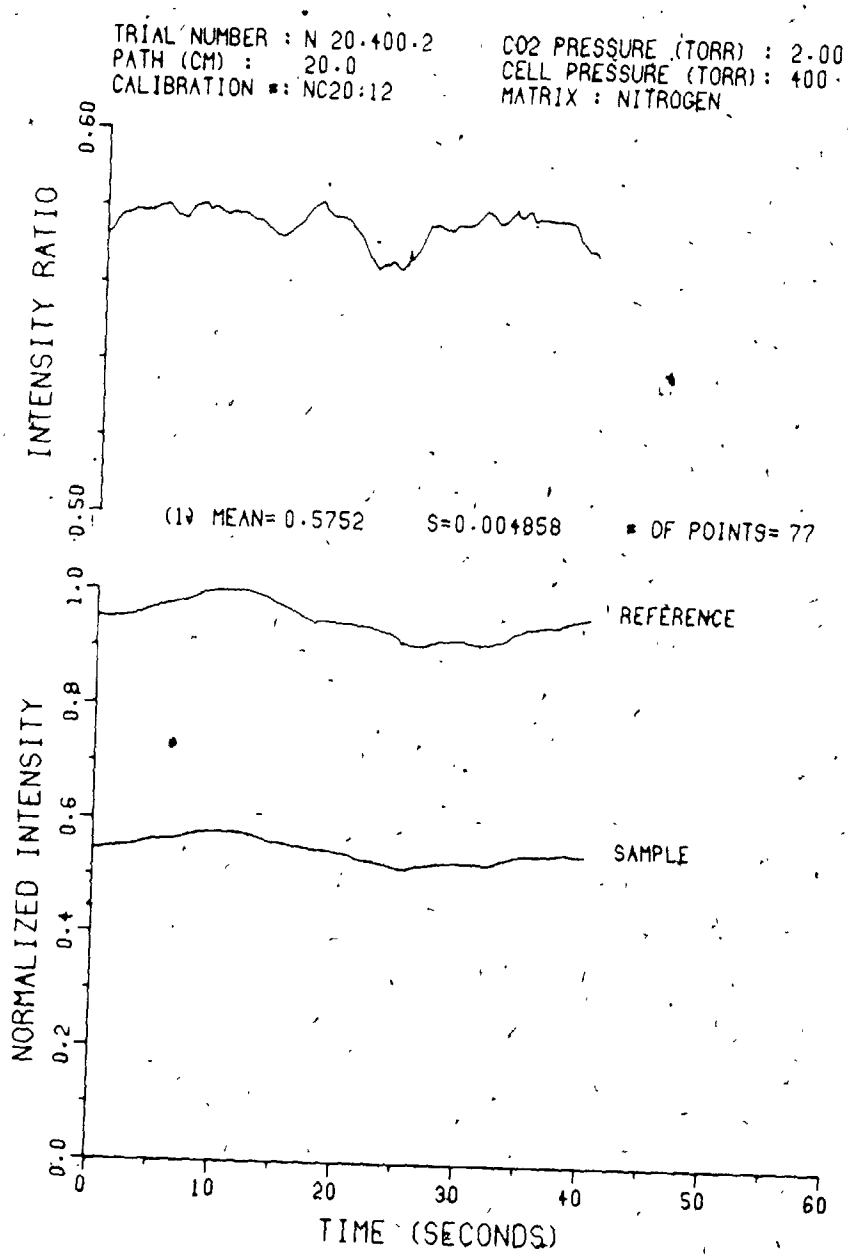
TRIAL NUMBER : N 20.400.2
PATH (CM) : 20.0
CALIBRATION #: NC20:12
CO2 PRESSURE (TORR) : 2.00
CELL PRESSURE (TORR): 400
MATRIX : NITROGEN
INTENSITY RATIO
0.60
0.50
(1σ MEAN= 0.5752 S=0.004858 # OF POINTS= 77
NORMALIZED INTENSITY
1.0
0.8
0.6
0.4
0.2
0.0
REFERENCE
SAMPLE
0
10
20
30
40
50
60
TIME (SECONDS)

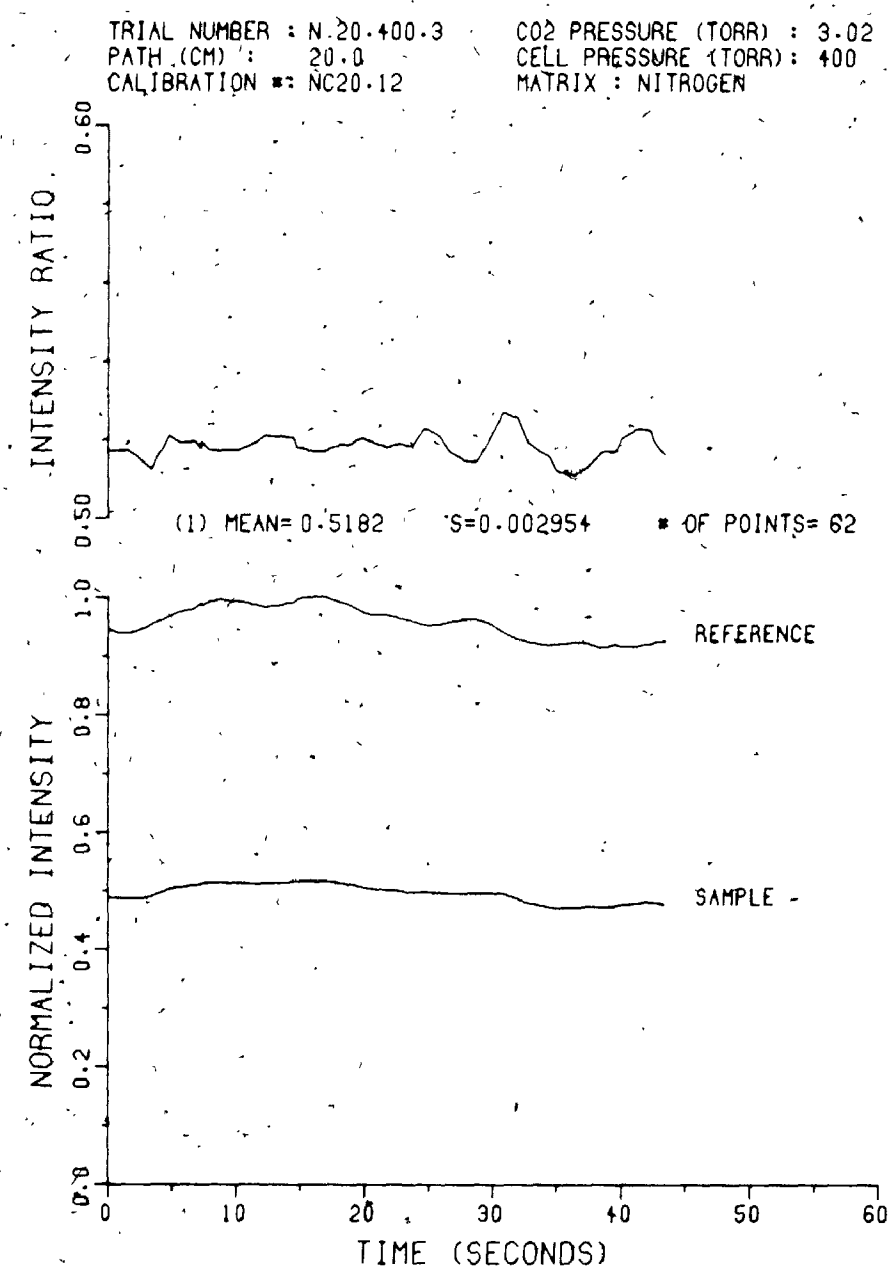
TRIAL NUMBER : N.20.400.3
PATH (CM) : 20.0
CALIBRATION #: NC20.12
CO2 PRESSURE (TORR) : 3.02
CELL PRESSURE (TORR): 400
MATRIX : NITROGEN
INTENSITY RATIO
0.60
0.50
(1) MEAN= 0.5182
S=0.002954
# OF POINTS= 62
NORMALIZED INTENSITY
1.0
0.8
0.6
0.4
0.2
0.0
REFERENCE
SAMPLE
0
10
20
30
40
50
60
TIME (SECONDS)

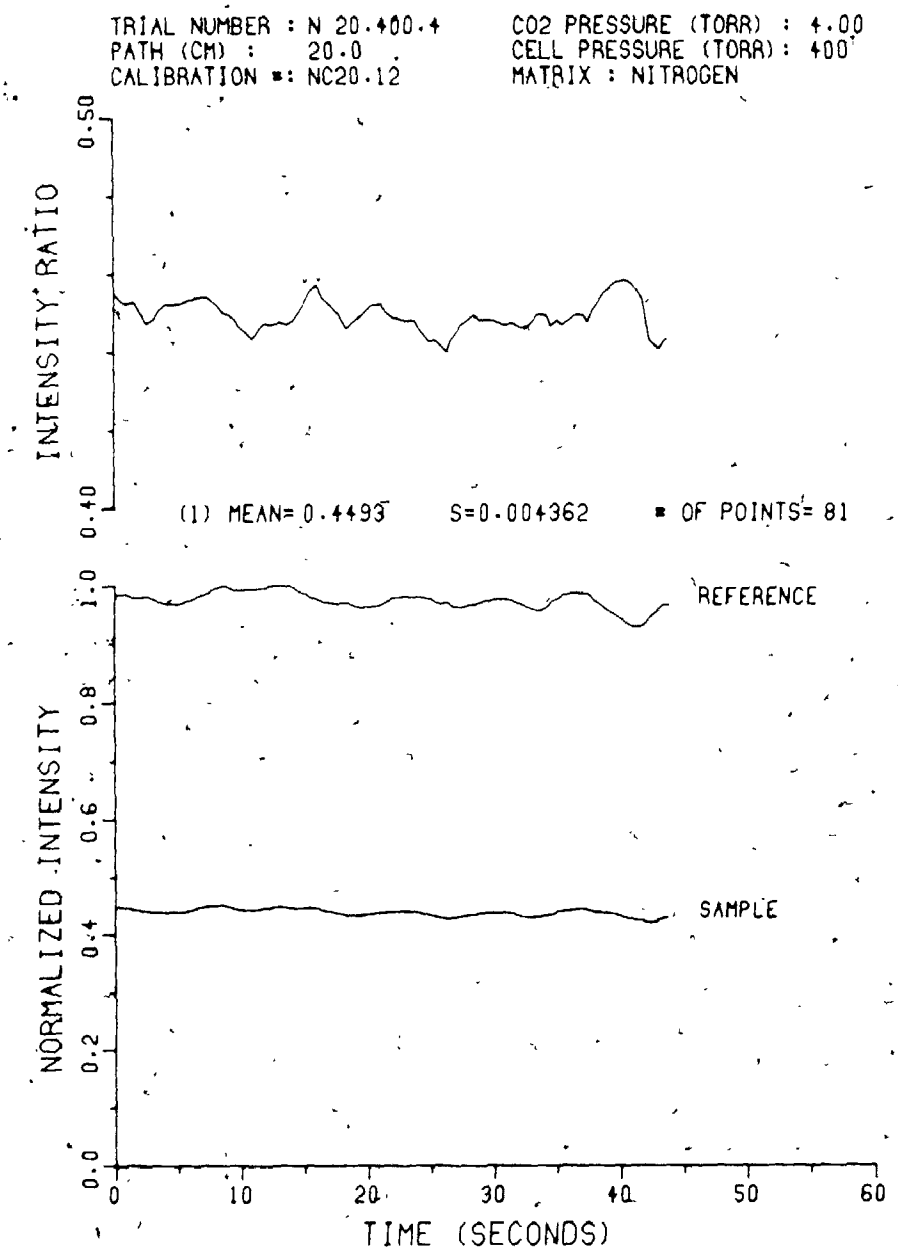
TRIAL NUMBER : N 20.400.4
PATH (CM) : 20.0
CALIBRATION #: NC20.12
CO2 PRESSURE (TORR) : 4.00
CELL PRESSURE (TORR): 400
MATRIX : NITROGEN
INTENSITY RATIO
0.50
0.40
(1) MEAN= 0.4493 S=0.004362 # OF POINTS= 81
REFERENCE
SAMPLE
NORMALIZED INTENSITY
1.0
0.8
0.6
0.4
0.2
0.0
0
10
20
30
40
50
60
TIME (SECONDS)

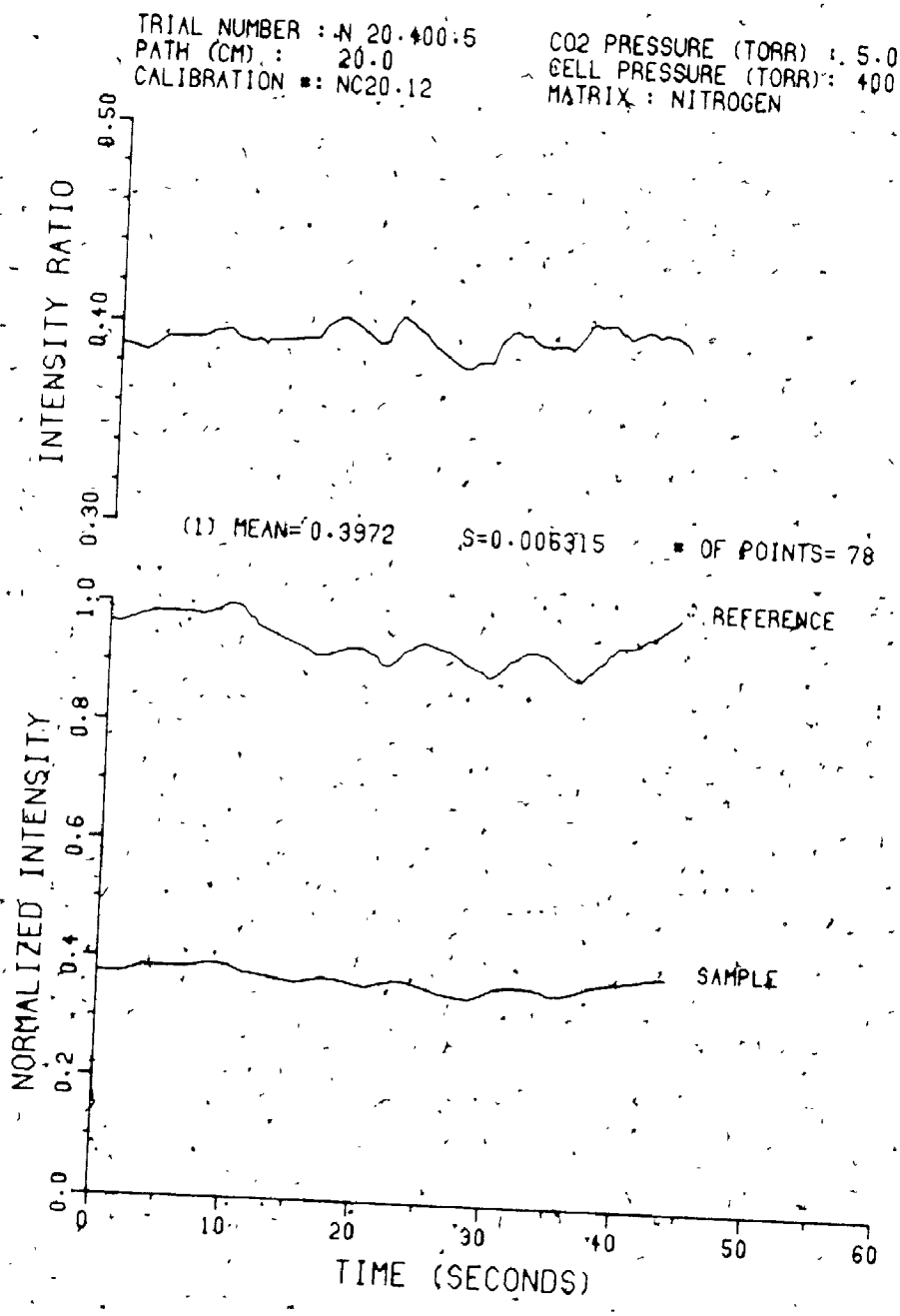
TRIAL NUMBER : N 20.400.5
PATH (CM) : 20.0
CALIBRATION #: NC20.12
CO2 PRESSURE (TORR) : 5.01
CELL PRESSURE (TORR): 400
MATRIX : NITROGEN
INTENSITY RATIO
0.50
0.40
0.30
(1) MEAN=0.3972
S=0.006315
# OF POINTS= 78
REFERENCE
SAMPLE
NORMALIZED INTENSITY
1.0
0.8
0.6
0.4
0.2
0.0
0
10
20
30
40
50
60
TIME (SECONDS)

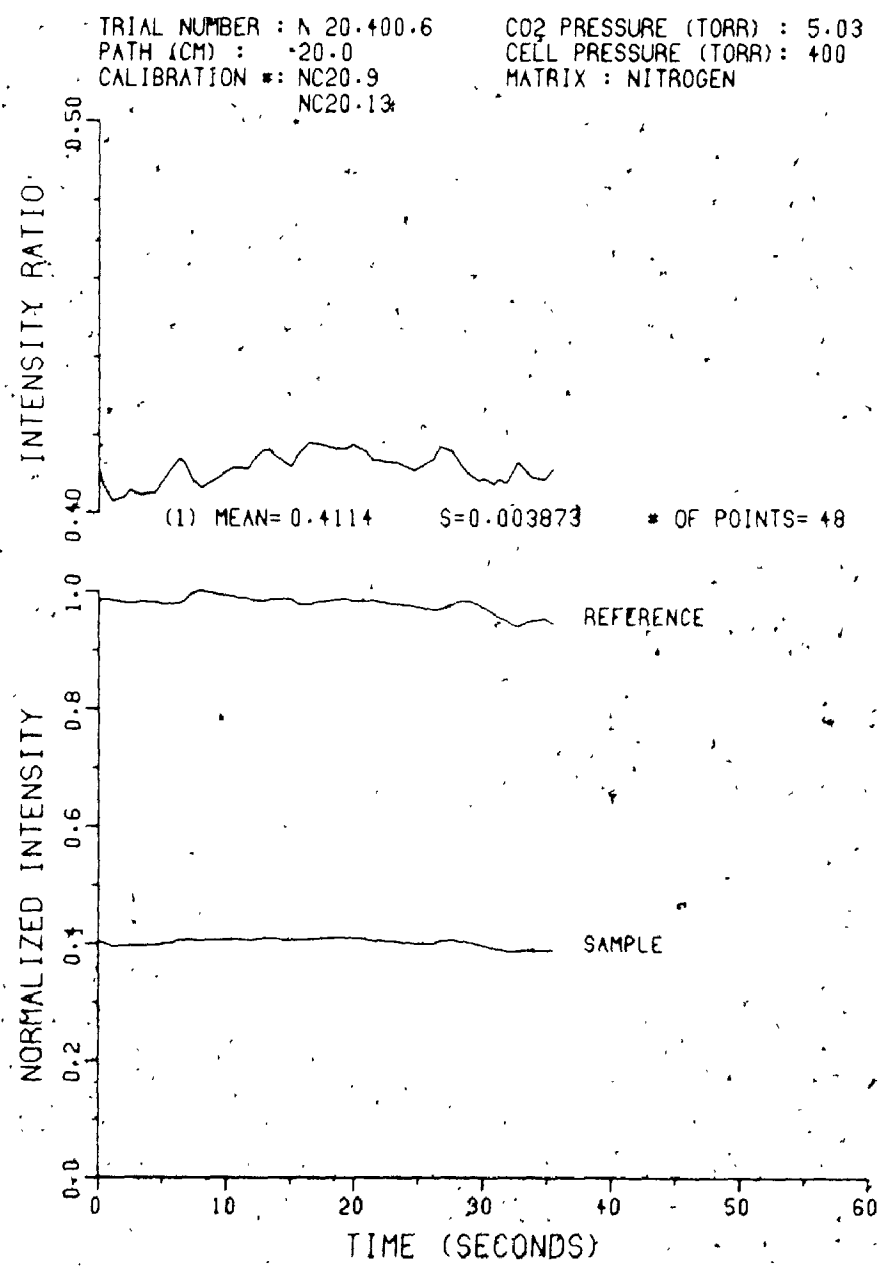
TRIAL NUMBER : N 20.400.6
PATH (CM) : 20.0
CALIBRATION #: NC20.9
NC20.13
CO2 PRESSURE (TORR) : 5.03
CELL PRESSURE (TORR): 400
MATRIX : NITROGEN
INTENSITY RATIO
0.50
0.40
(1) MEAN= 0.4114
S=0.003873
# OF POINTS= 48
NORMALIZED INTENSITY
1.0
0.8
0.6
0.4
0.2
0.0
REFERENCE
SAMPLE
0
10
20
30
40
50
60
TIME (SECONDS)

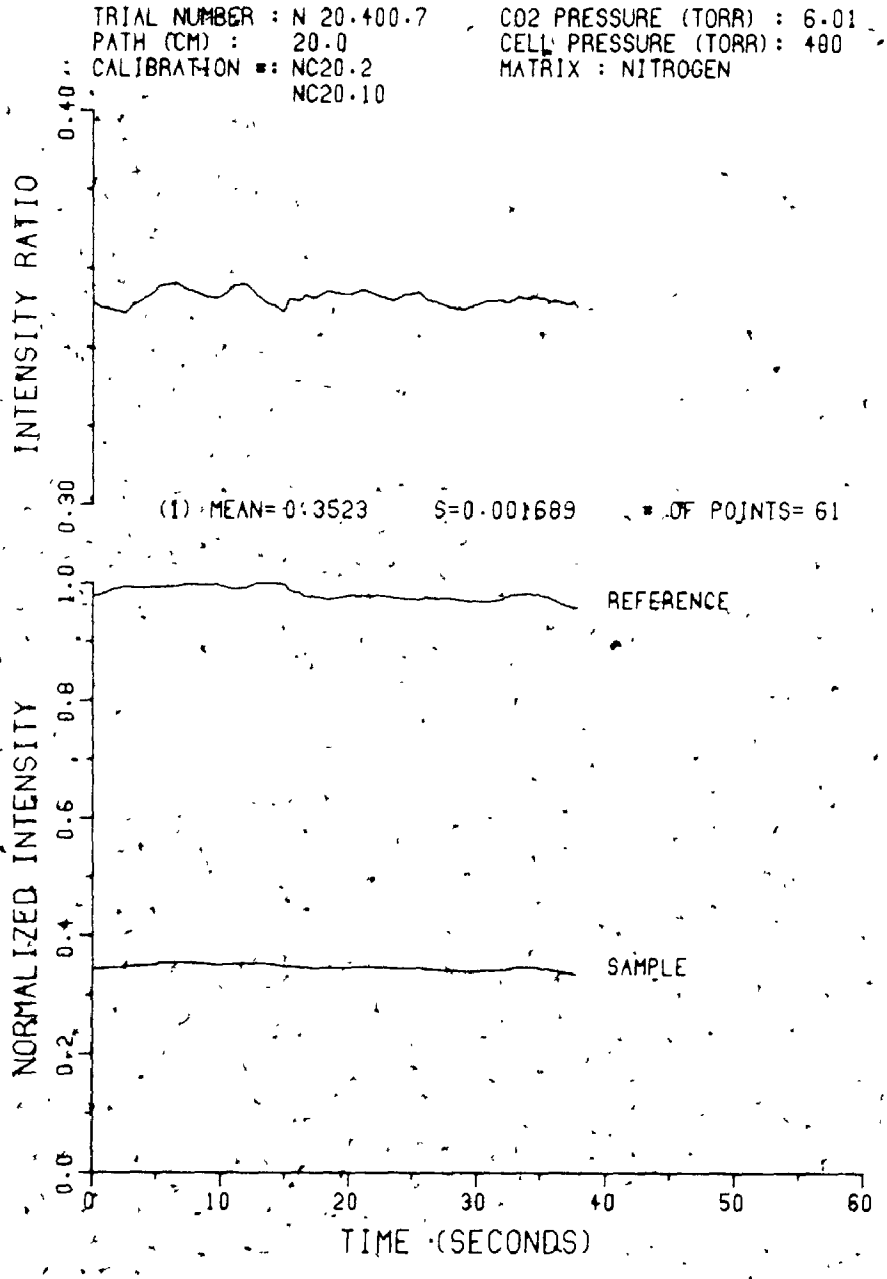
TRIAL NUMBER : N 20.400.7
PATH (CM) : 20.0
CALIBRATION = : NC20.2
NC20.10
CO2 PRESSURE (TORR) : 6.01
CELL PRESSURE (TORR): 400
MATRIX : NITROGEN
INTENSITY RATIO
0.40
0.30
(1) MEAN= 0.3523 S=0.001689 # OF POINTS= 61
NORMALIZED INTENSITY
1.0
0.8
0.6
0.4
0.2
0.0
REFERENCE
SAMPLE
0
10
20
30
40
50
60
TIME (SECONDS)

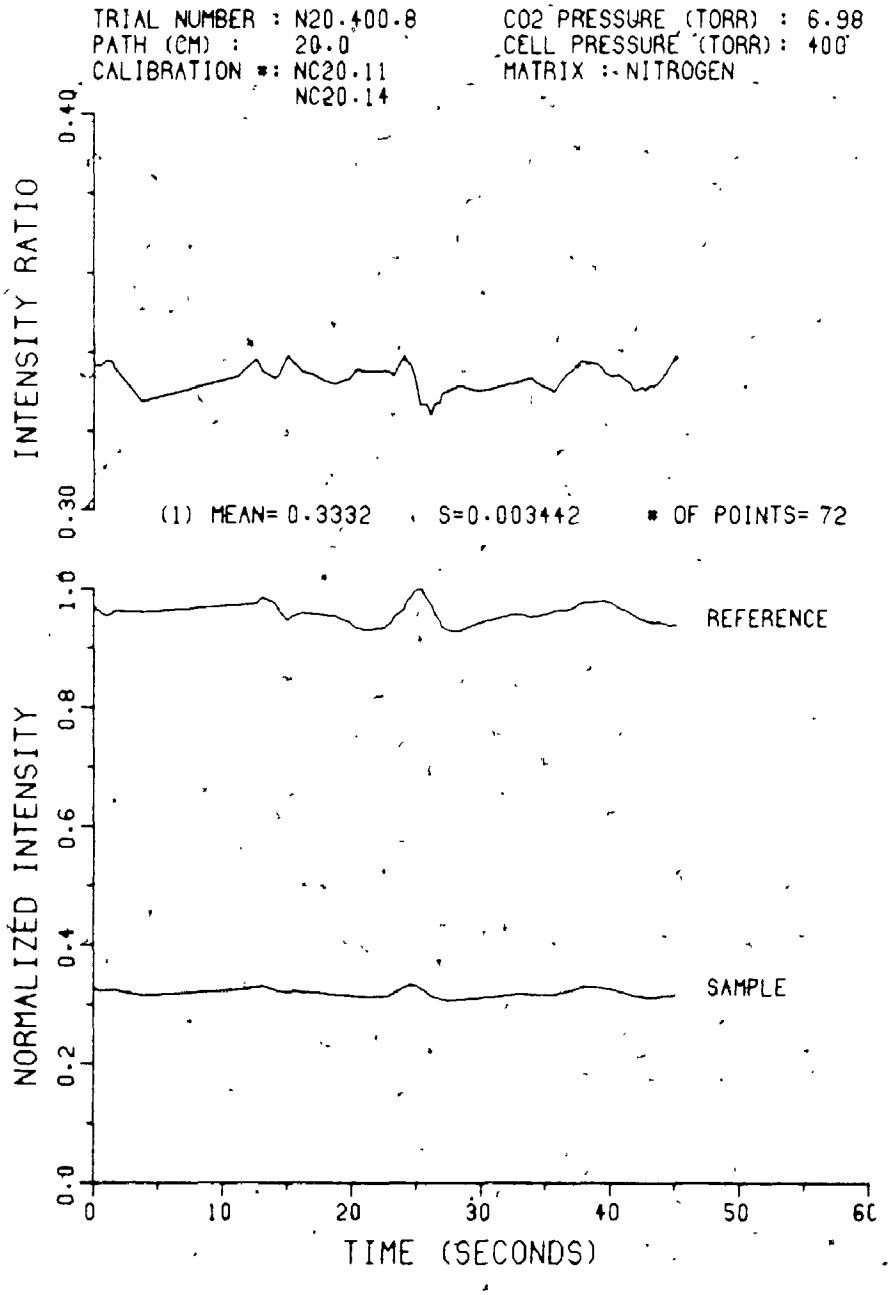
TRIAL NUMBER : N20.400.8
PATH (CM) : 20.0
CALIBRATION #: NC20.11
NC20.14
CO2 PRESSURE (TORR) : 6.98
CELL PRESSURE (TORR): 400
MATRIX : NITROGEN
INTENSITY RATIO
0.40
0.30
(1) MEAN= 0.3332 S=0.003442 # OF POINTS= 72
NORMALIZED INTENSITY
1.0
0.8
0.6
0.4
0.2
0.0
REFERENCE
SAMPLE
0
10
20
30
40
50
60
TIME (SECONDS)

Data Files - Total Pressure: 500 Torr

Trial Numbers: N20.500.1-N20.500.8

Remote Gain: Sample (G_S): 1 (V/V)

FSD_S: 2

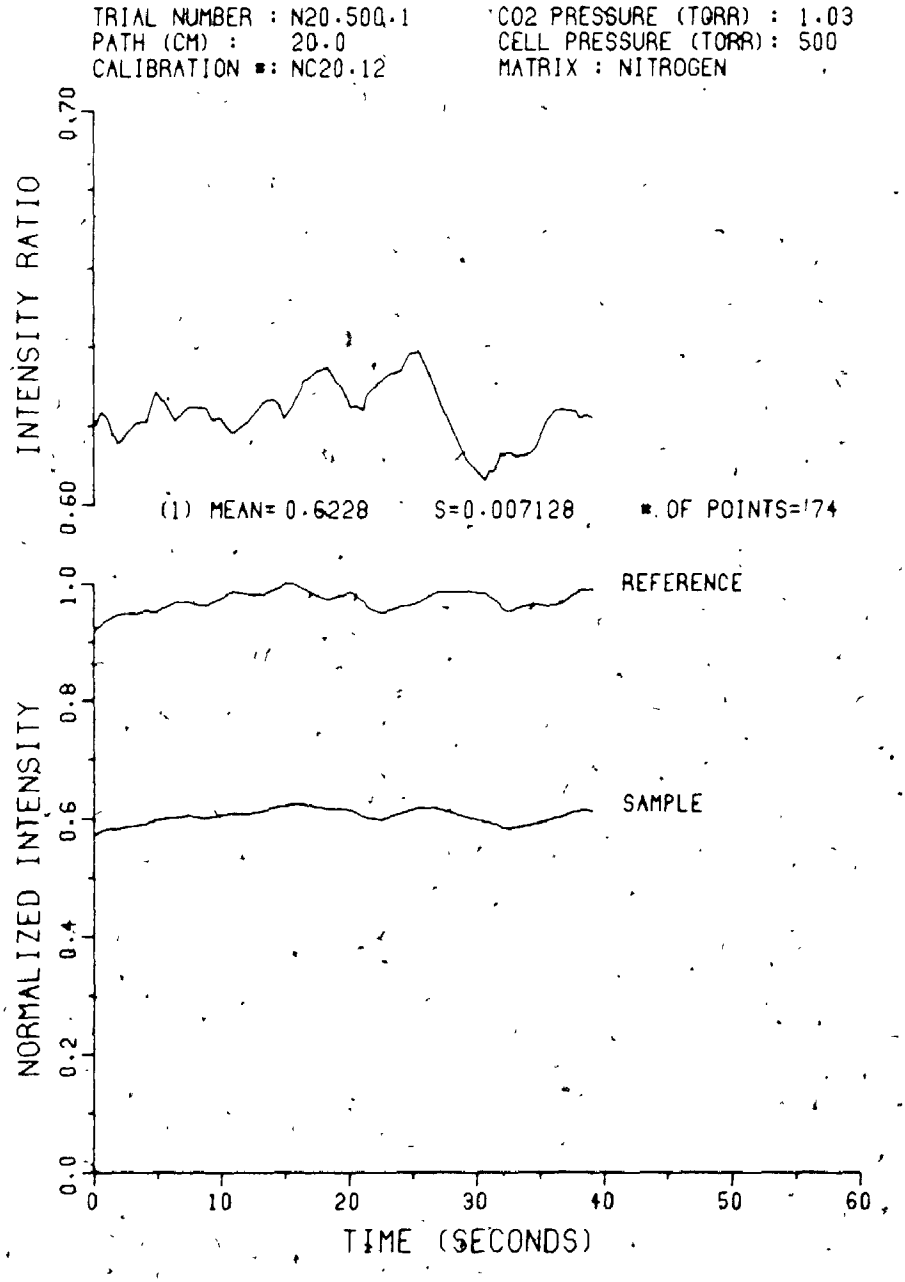

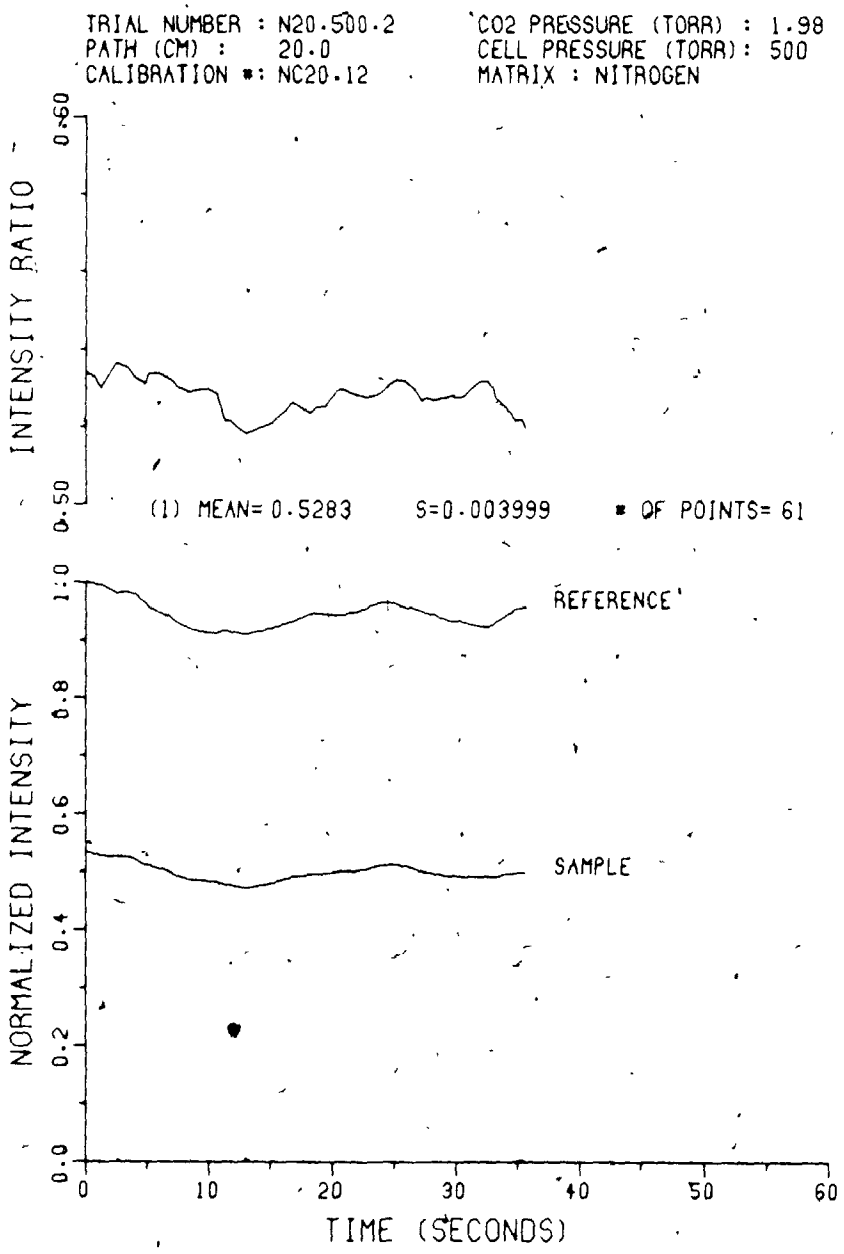
TRIAL NUMBER : N20.500.2
PATH (CM) : 20.0
CALIBRATION #: NC20.12
CO2 PRESSURE (TORR) : 1.98
CELL PRESSURE (TORR): 500
MATRIX : NITROGEN
INTENSITY RATIO
0.60
0.50
(1) MEAN= 0.5283 S=0.003999 # OF POINTS= 61
NORMALIZED INTENSITY
1.0
0.8
0.6
0.4
0.2
0.0
REFERENCE
SAMPLE
0
10
20
30
40
50
60
TIME (SECONDS)

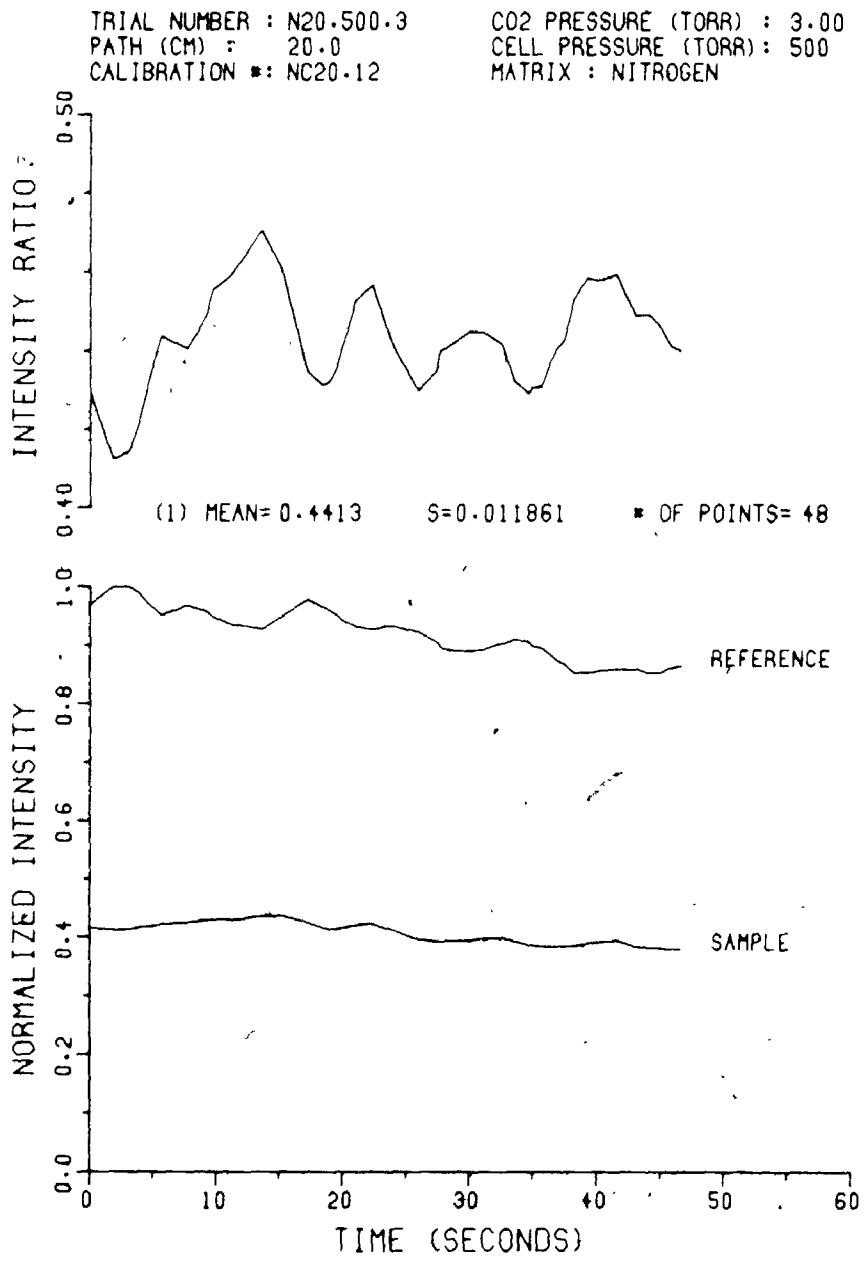
TRIAL NUMBER : N20.500.3
PATH (CM) : 20.0
CALIBRATION #: NC20.12
CO2 PRESSURE (TORR) : 3.00
CELL PRESSURE (TORR): 500
MATRIX : NITROGEN
INTENSITY RATIO
0.50
0.40
(1) MEAN= 0.4413 S=0.011861 # OF POINTS= 48
NORMALIZED INTENSITY
1.0
0.8
0.6
0.4
0.2
0.0
REFERENCE
SAMPLE
0
10
20
30
40
50
60
TIME (SECONDS)

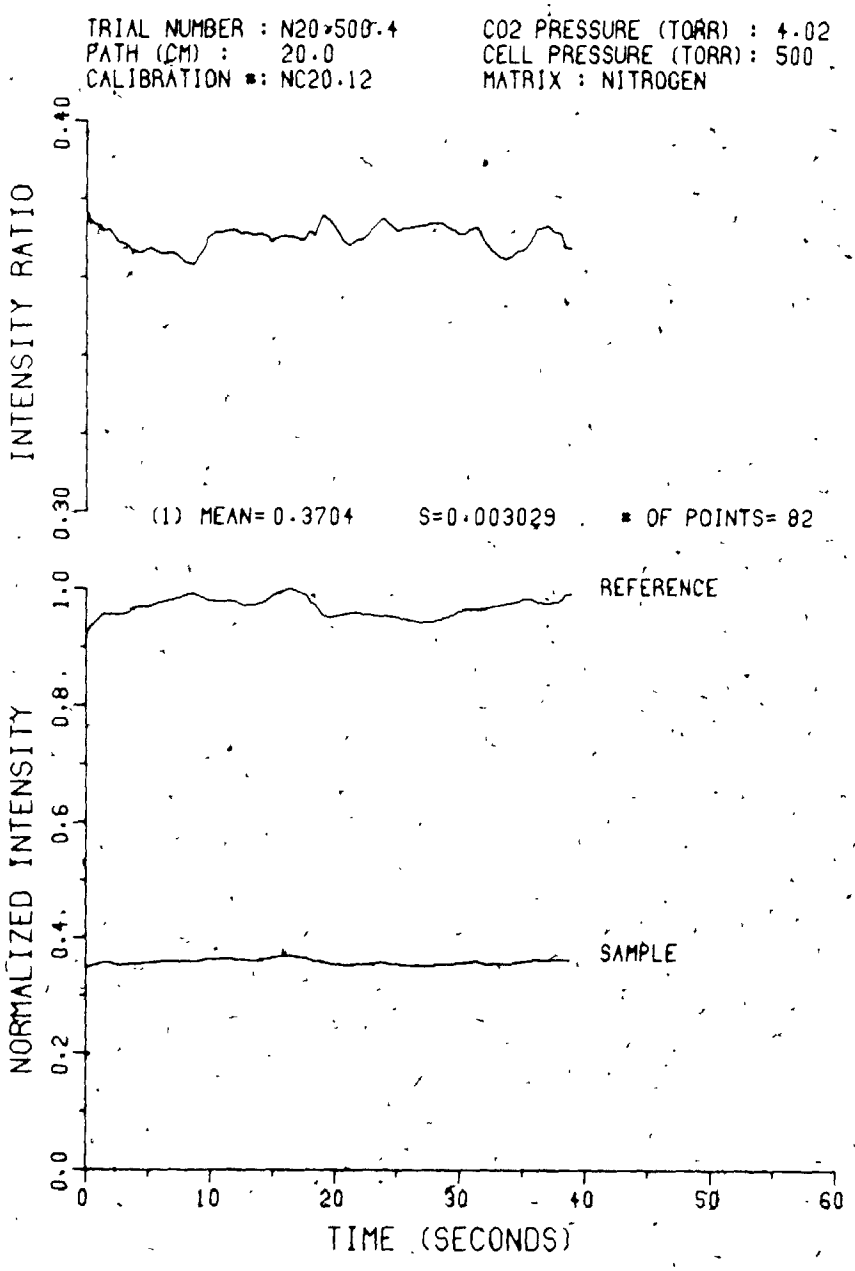
TRIAL NUMBER : N20-500-4
PATH (CM) : 20.0
CALIBRATION #: NC20.12
CO2 PRESSURE (TORR) : 4.02
CELL PRESSURE (TORR): 500
MATRIX : NITROGEN
INTENSITY RATIO
0.40
0.30
(1) MEAN= 0.3704
S=0.003029
# OF POINTS= 82
REFERENCE
SAMPLE
NORMALIZED INTENSITY
1.0
0.8
0.6
0.4
0.2
0.0
0
10
20
30
40
50
60
TIME (SECONDS)

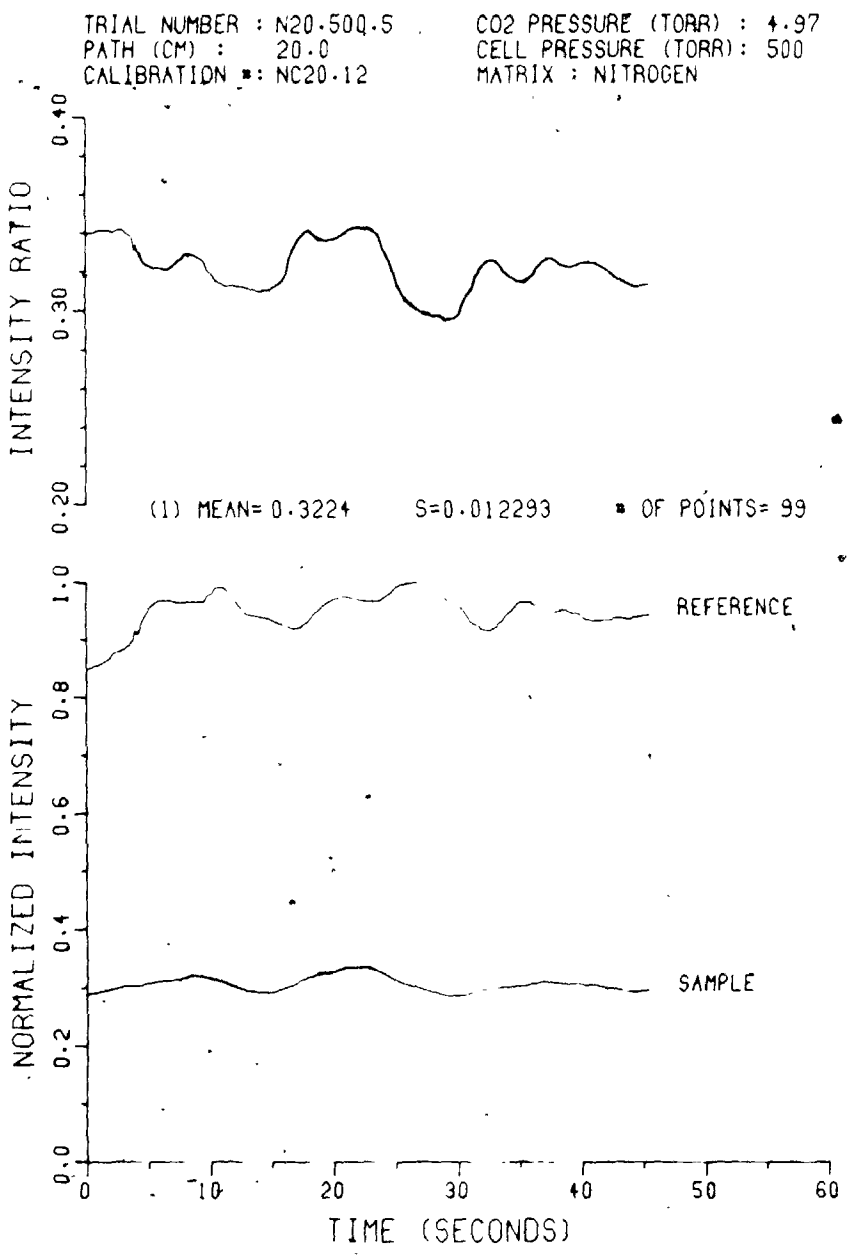
TRIAL NUMBER : N20.500.5
PATH (CM) : 20.0
CALIBRATION #: NC20.12
CO2 PRESSURE (TORR) : 4.97
CELL PRESSURE (TORR): 500
MATRIX : NITROGEN
INTENSITY RATIO
0.40
0.30
0.20
(1) MEAN= 0.3224 S=0.012293 # OF POINTS= 99
NORMALIZED INTENSITY
1.0
0.8
0.6
0.4
0.2
0.0
REFERENCE
SAMPLE
0
10
20
30
40
50
60
TIME (SECONDS)

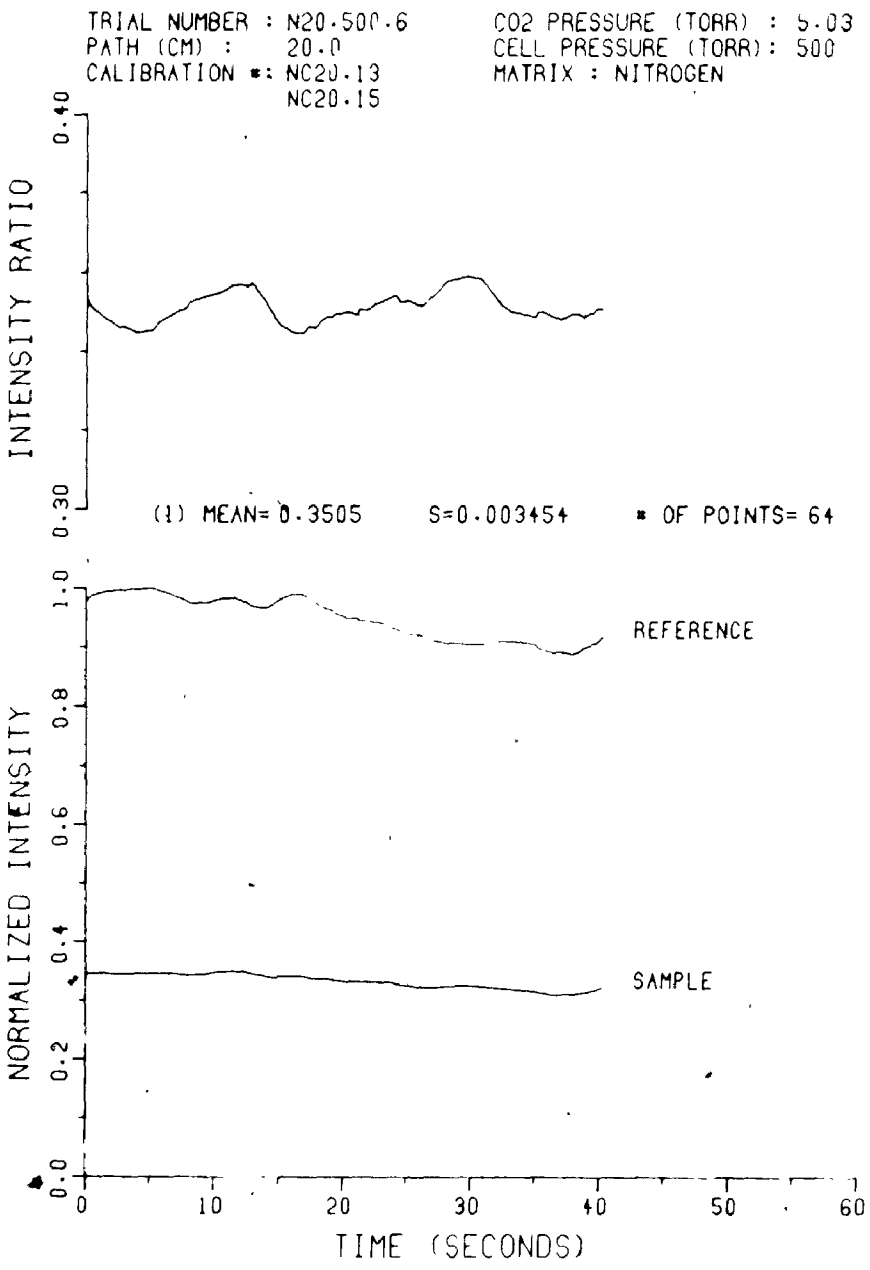
TRIAL NUMBER : N20.500.6
PATH (CM) : 20.0
CALIBRATION #: NC20.13
NC20.15
CO2 PRESSURE (TORR) : 5.03
CELL PRESSURE (TORR): 500
MATRIX : NITROGEN
INTENSITY RATIO
0.40
0.30
(1) MEAN= 0.3505 S=0.003454 # OF POINTS= 64
NORMALIZED INTENSITY
1.0
0.8
0.6
0.4
0.2
0.0
REFERENCE
SAMPLE
0
10
20
30
40
50
60
TIME (SECONDS)

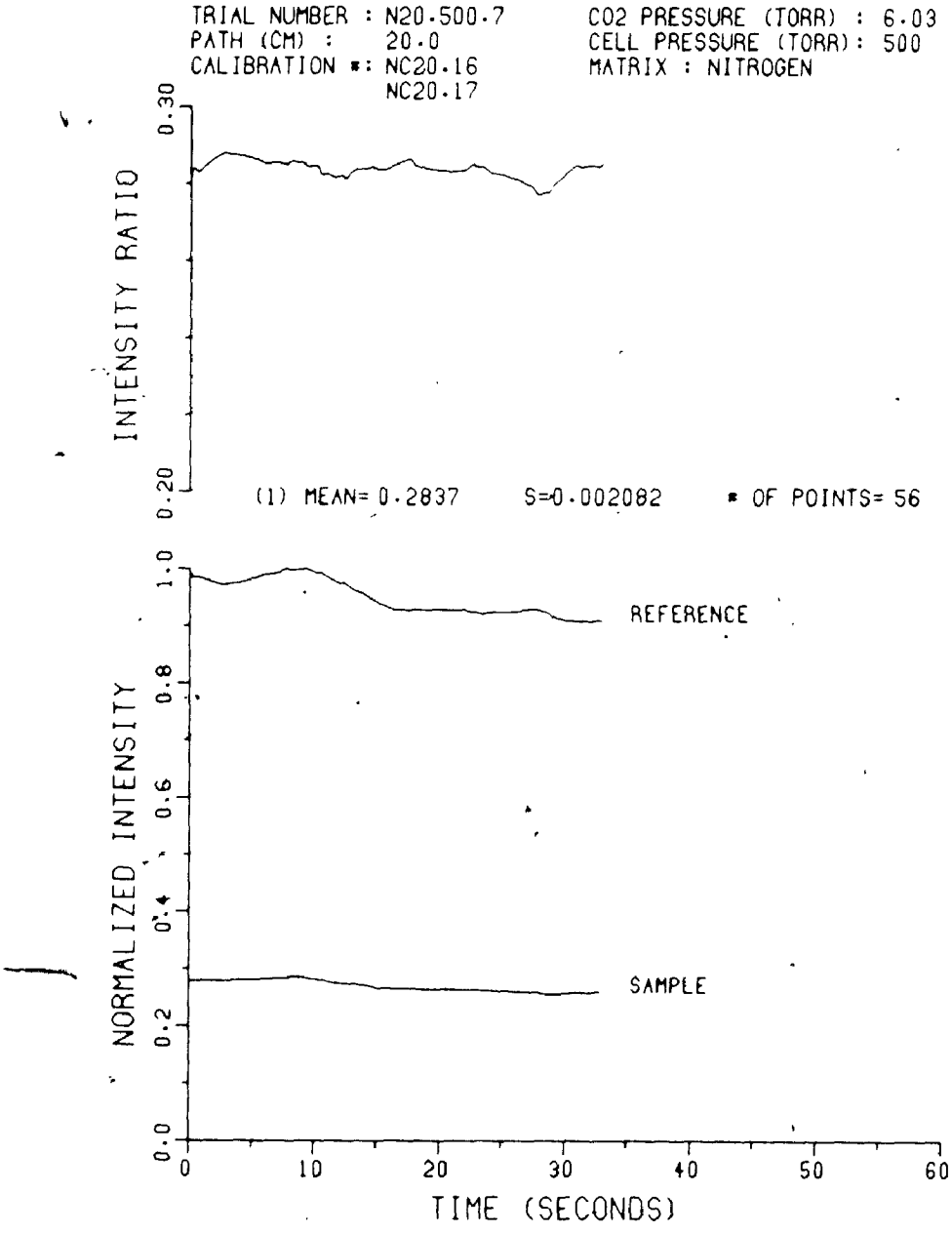
TRIAL NUMBER : N20.500.7
PATH (CM) : 20.0
CALIBRATION #: NC20.16
NC20.17
CO2 PRESSURE (TORR) : 6.03
CELL PRESSURE (TORR): 500
MATRIX : NITROGEN
INTENSITY RATIO
0.30
0.20
(1) MEAN= 0.2837 S=0.002082 # OF POINTS= 56
NORMALIZED INTENSITY
1.0
0.8
0.6
0.4
0.2
0.0
REFERENCE
SAMPLE
0
10
20
30
40
50
60
TIME (SECONDS)

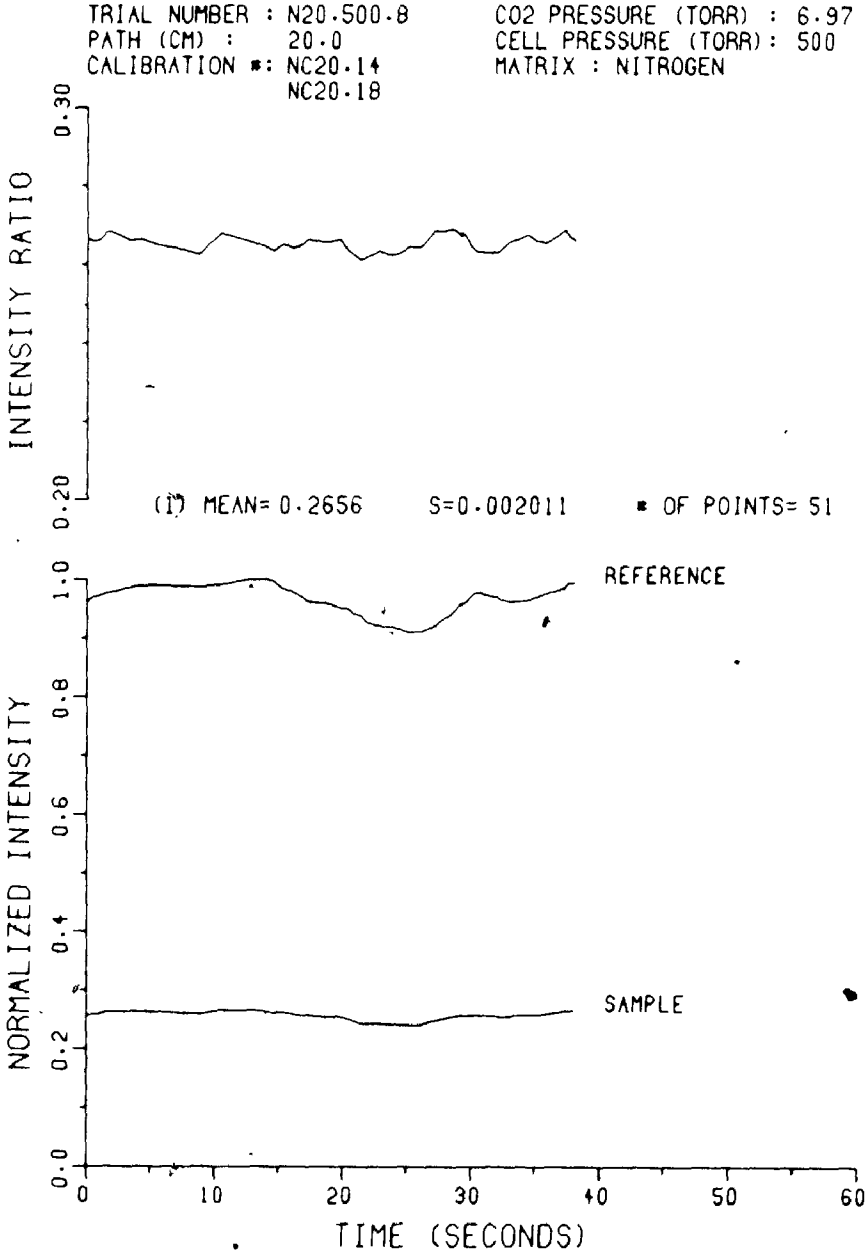
TRIAL NUMBER : N20.500.8
PATH (CM) : 20.0
CALIBRATION #: NC20.14
NC20.18
CO2 PRESSURE (TORR) : 6.97
CELL PRESSURE (TORR): 500
MATRIX : NITROGEN
INTENSITY RATIO
0.30
0.20
(1) MEAN= 0.2656 S=0.002011 # OF POINTS= 51
NORMALIZED INTENSITY
1.0
0.8
0.6
0.4
0.2
0.0
REFERENCE
SAMPLE
0
10
20
30
40
50
60
TIME (SECONDS)

Data Files - Total Pressure: 600 Torr

Trial Numbers: N20.600.1-N20.600.4

Remote Gain: Sample (G_S): 1 (V/V)

FSD_S: 2

Trial Numbers: N20.600.5-N20.600.8

Remote Gain: Sample (G_S): 1 (V/V)

FSD_S: 2

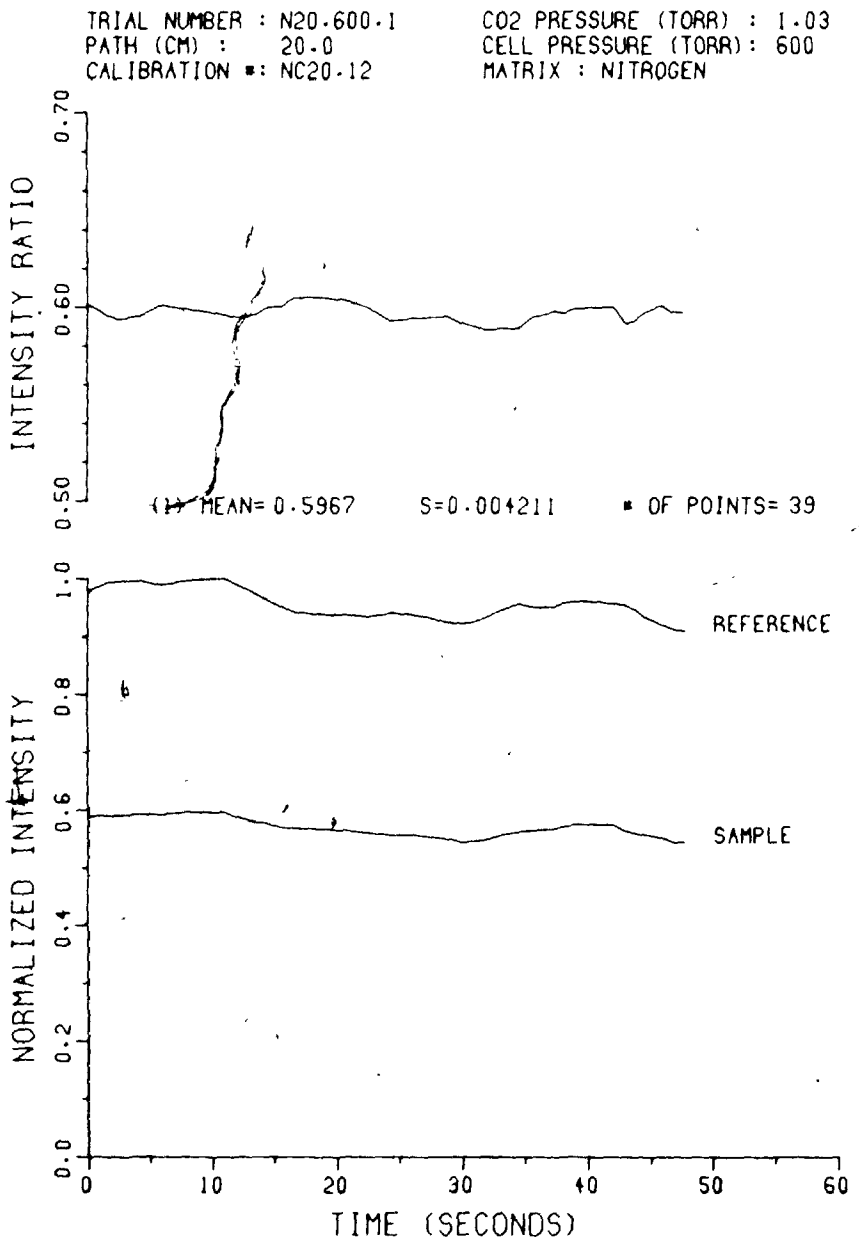
TRIAL NUMBER : N20.600.1
PATH (CM) : 20.0
CALIBRATION #: NC20.12
CO2 PRESSURE (TORR) : 1.03
CELL PRESSURE (TORR): 600
MATRIX : NITROGEN
INTENSITY RATIO
0.70
0.60
0.50
MEAN= 0.5967
S=0.004211
# OF POINTS= 39
NORMALIZED INTENSITY
1.0
0.8
0.6
0.4
0.2
0.0
REFERENCE
SAMPLE
0
10
20
30
40
50
60
TIME (SECONDS)

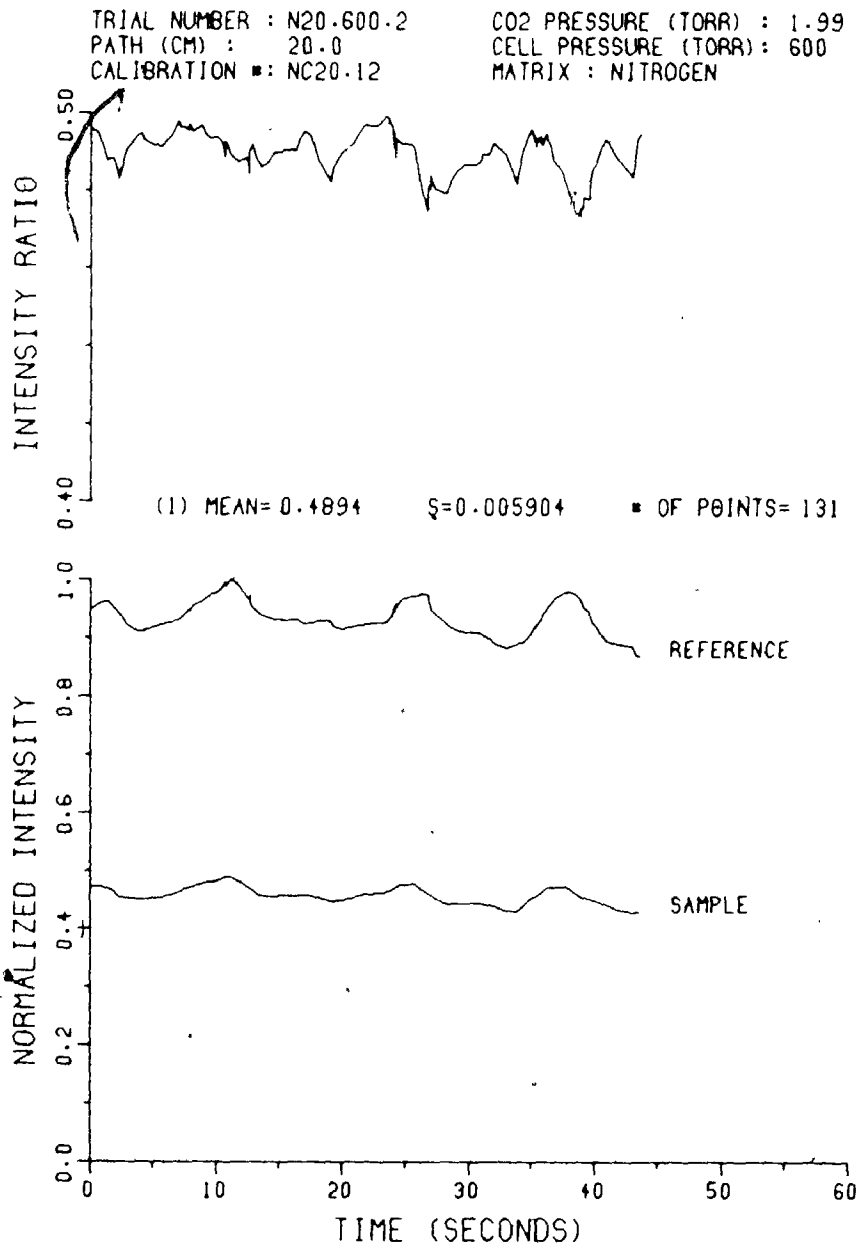
TRIAL NUMBER : N20.600.2
PATH (CM) : 20.0
CALIBRATION #: NC20.12
CO2 PRESSURE (TORR) : 1.99
CELL PRESSURE (TORR): 600
MATRIX : NITROGEN
INTENSITY RATIO
0.50
0.40
(1) MEAN= 0.4894 S=0.005904 # OF POINTS= 131
NORMALIZED INTENSITY
1.0
0.8
0.6
0.4
0.2
0.0
REFERENCE
SAMPLE
0
10
20
30
40
50
60
TIME (SECONDS)

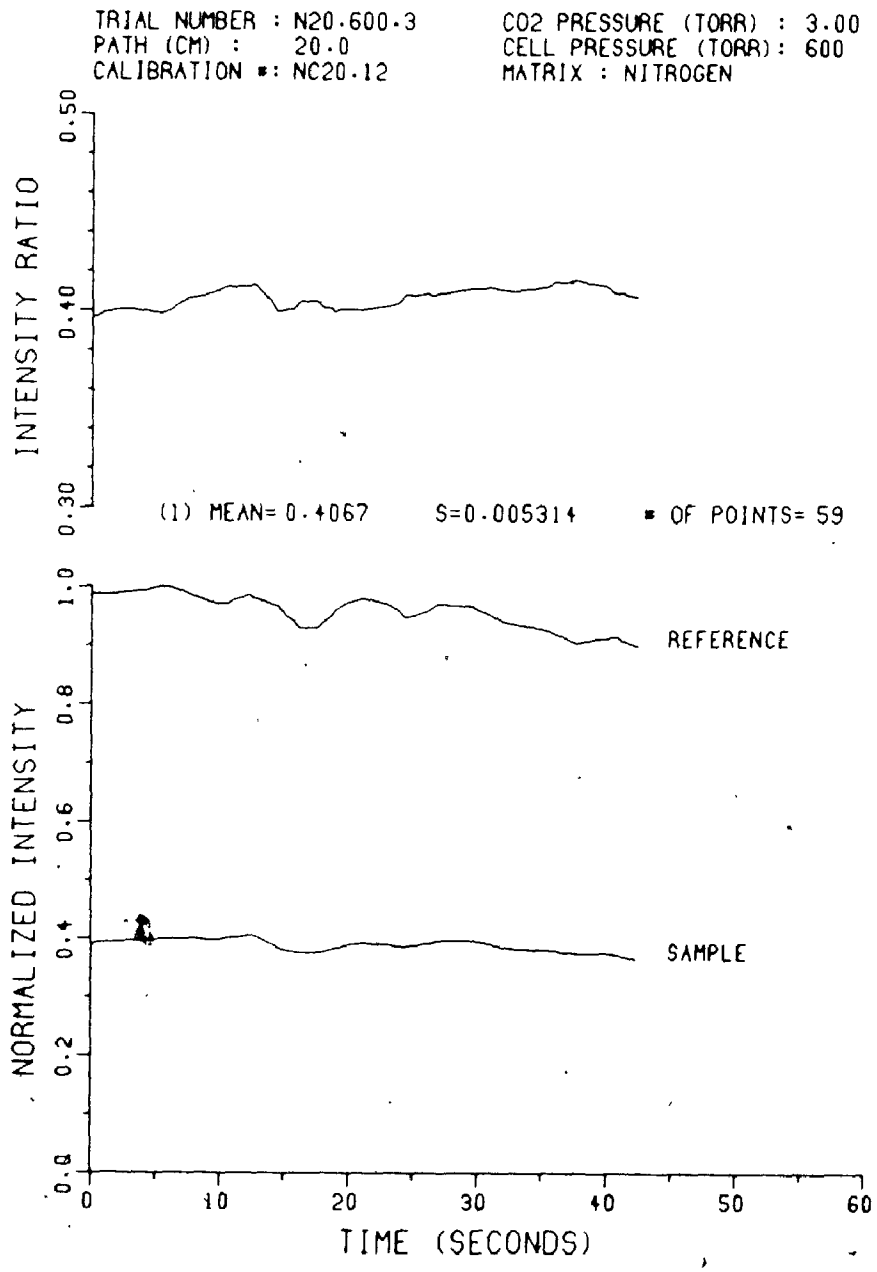
TRIAL NUMBER : N20.600.3
PATH (CM) : 20.0
CALIBRATION #: NC20.12
CO2 PRESSURE (TORR) : 3.00
CELL PRESSURE (TORR): 600
MATRIX : NITROGEN
INTENSITY RATIO
0.50
0.40
0.30
(1) MEAN= 0.4067
S=0.005314
# OF POINTS= 59
NORMALIZED INTENSITY
1.0
0.8
0.6
0.4
0.2
0.0
REFERENCE
SAMPLE
0
10
20
30
40
50
60
TIME (SECONDS)

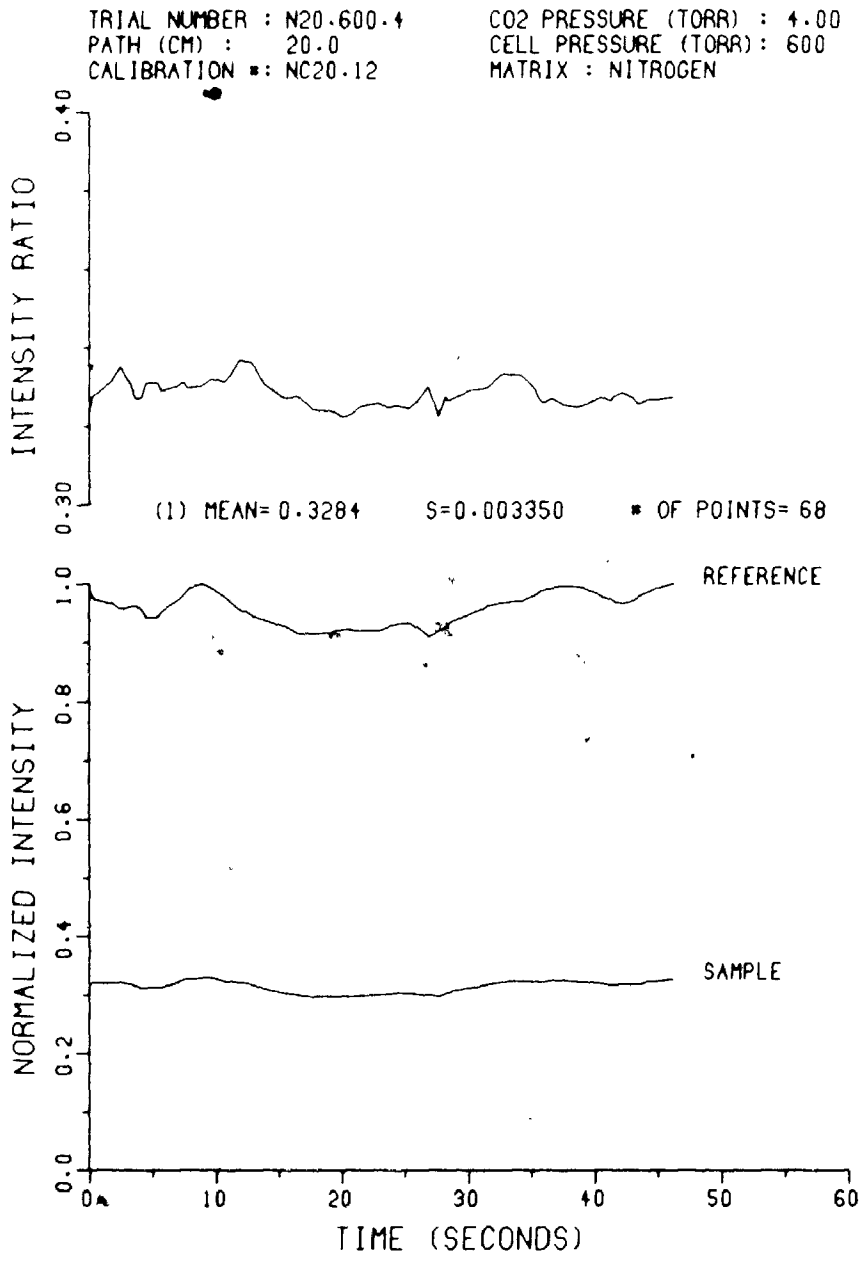
TRIAL NUMBER : N20.600.4
PATH (CM) : 20.0
CALIBRATION #: NC20.12
CO2 PRESSURE (TORR) : 4.00
CELL PRESSURE (TORR): 600
MATRIX : NITROGEN
INTENSITY RATIO
0.40
0.30
(1) MEAN= 0.3284 S=0.003350 # OF POINTS= 68
REFERENCE
SAMPLE
NORMALIZED INTENSITY
1.0
0.8
0.6
0.4
0.2
0.0
0
10
20
30
40
50
60
TIME (SECONDS)

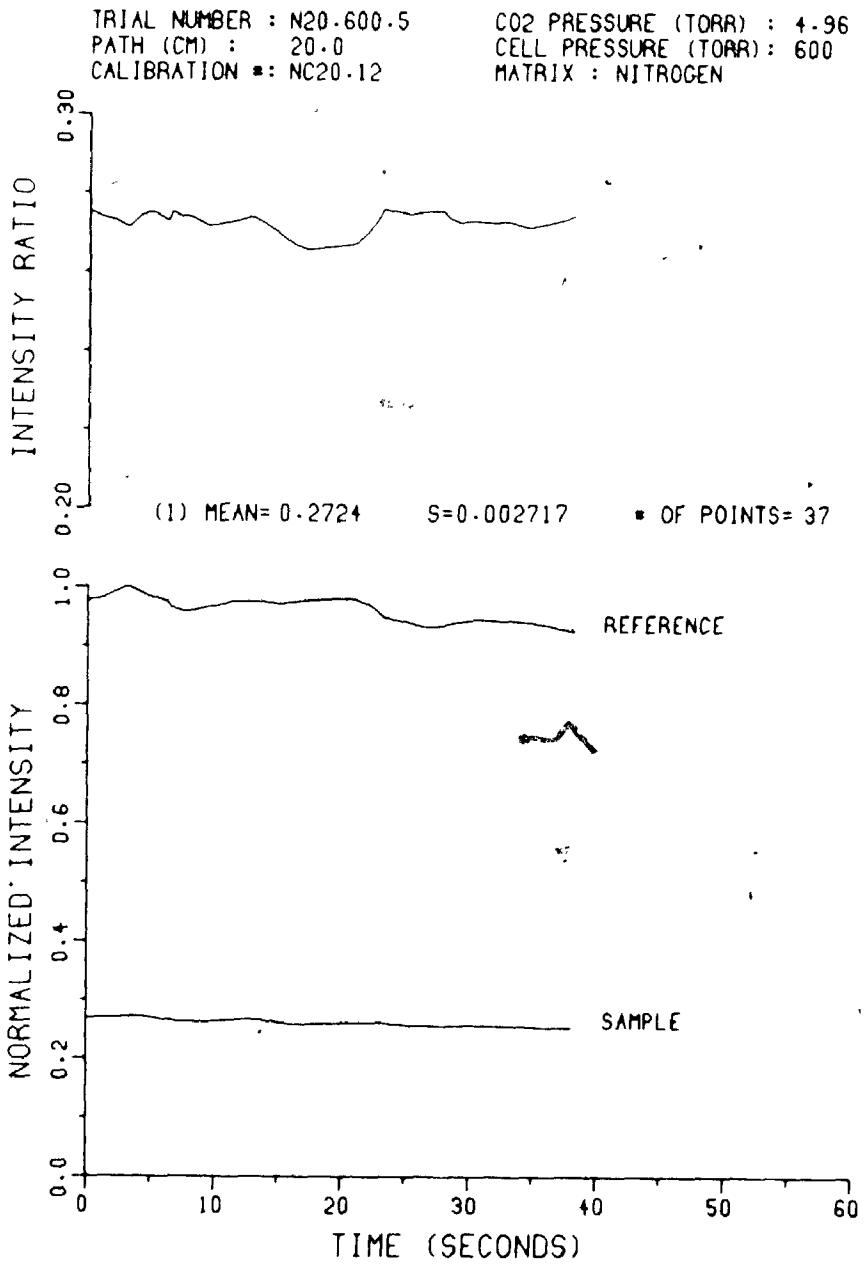
TRIAL NUMBER : N20.600.5
PATH (CM) : 20.0
CALIBRATION #: NC20.12
CO2 PRESSURE (TORR) : 4.96
CELL PRESSURE (TORR): 600
MATRIX : NITROGEN
INTENSITY RATIO
0.30
0.20
(1) MEAN= 0.2724 S=0.002717 # OF POINTS= 37
NORMALIZED INTENSITY
1.0
0.8
0.6
0.4
0.2
0.0
REFERENCE
SAMPLE
0
10
20
30
40
50
60
TIME (SECONDS)

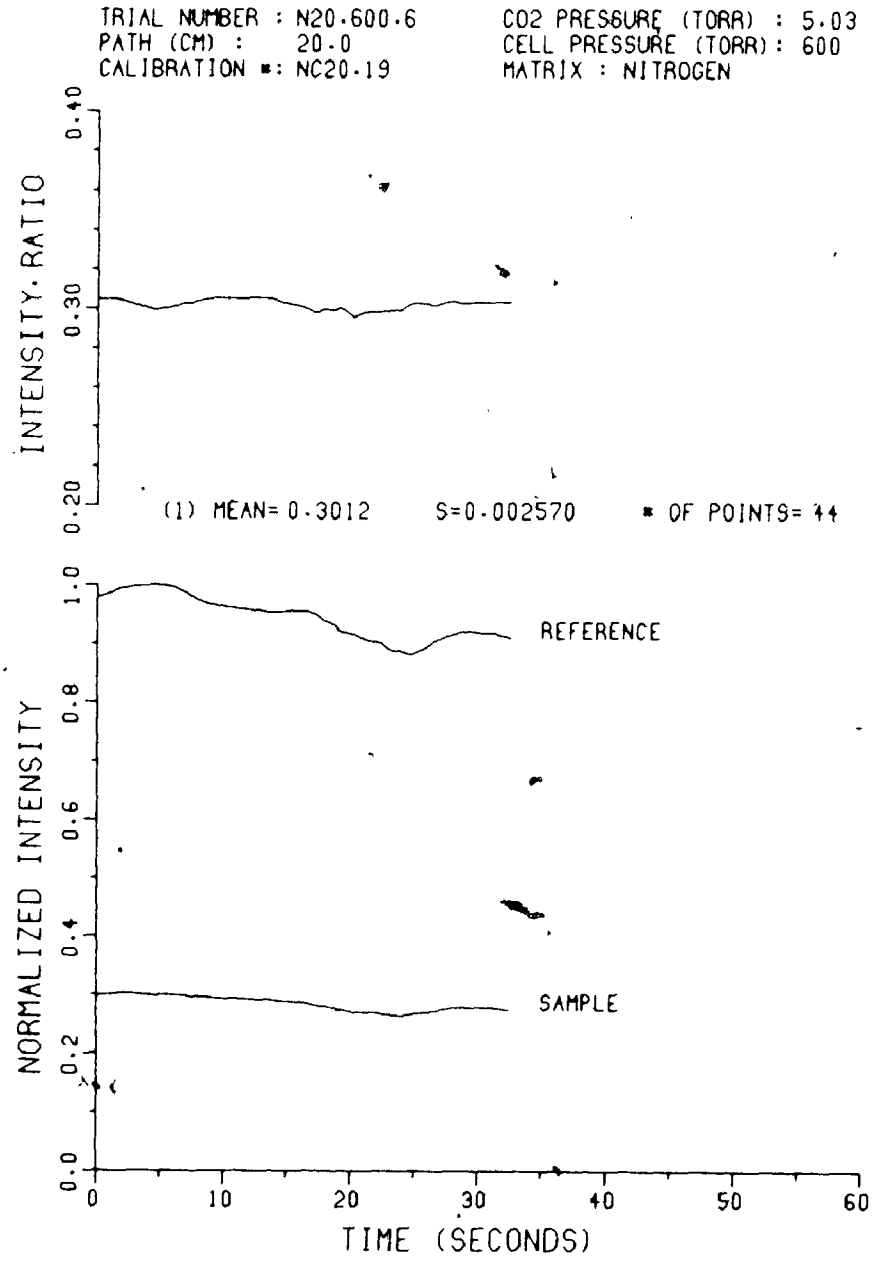
TRIAL NUMBER : N20.600.6
PATH (CM) : 20.0
CALIBRATION #: NC20.19
CO2 PRESSURE (TORR) : 5.03
CELL PRESSURE (TORR): 600
MATRIX : NITROGEN
INTENSITY RATIO
0.40
0.30
0.20
(1) MEAN= 0.3012 S=0.002570 # OF POINTS= 44
NORMALIZED INTENSITY
1.0
0.8
0.6
0.4
0.2
0.0
REFERENCE
SAMPLE
0
10
20
30
40
50
60
TIME (SECONDS)

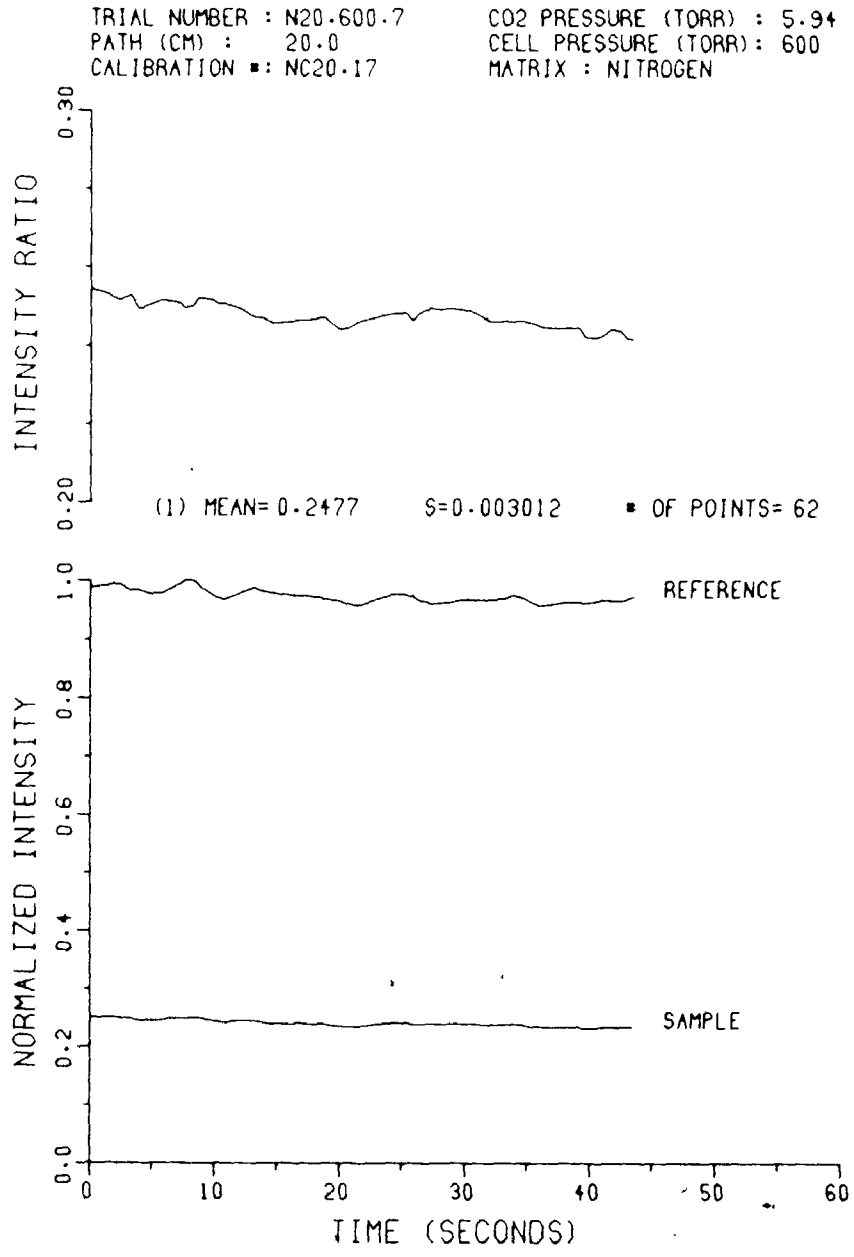
TRIAL NUMBER : N20.600.7
PATH (CM) : 20.0
CALIBRATION #: NC20.17
CO2 PRESSURE (TORR) : 5.94
CELL PRESSURE (TORR): 600
MATRIX : NITROGEN
INTENSITY RATIO
0.30
0.20
(1) MEAN= 0.2477 S=0.003012 # OF POINTS= 62
NORMALIZED INTENSITY
1.0
0.8
0.6
0.4
0.2
0.0
REFERENCE
SAMPLE
0
10
20
30
40
50
60
TIME (SECONDS)

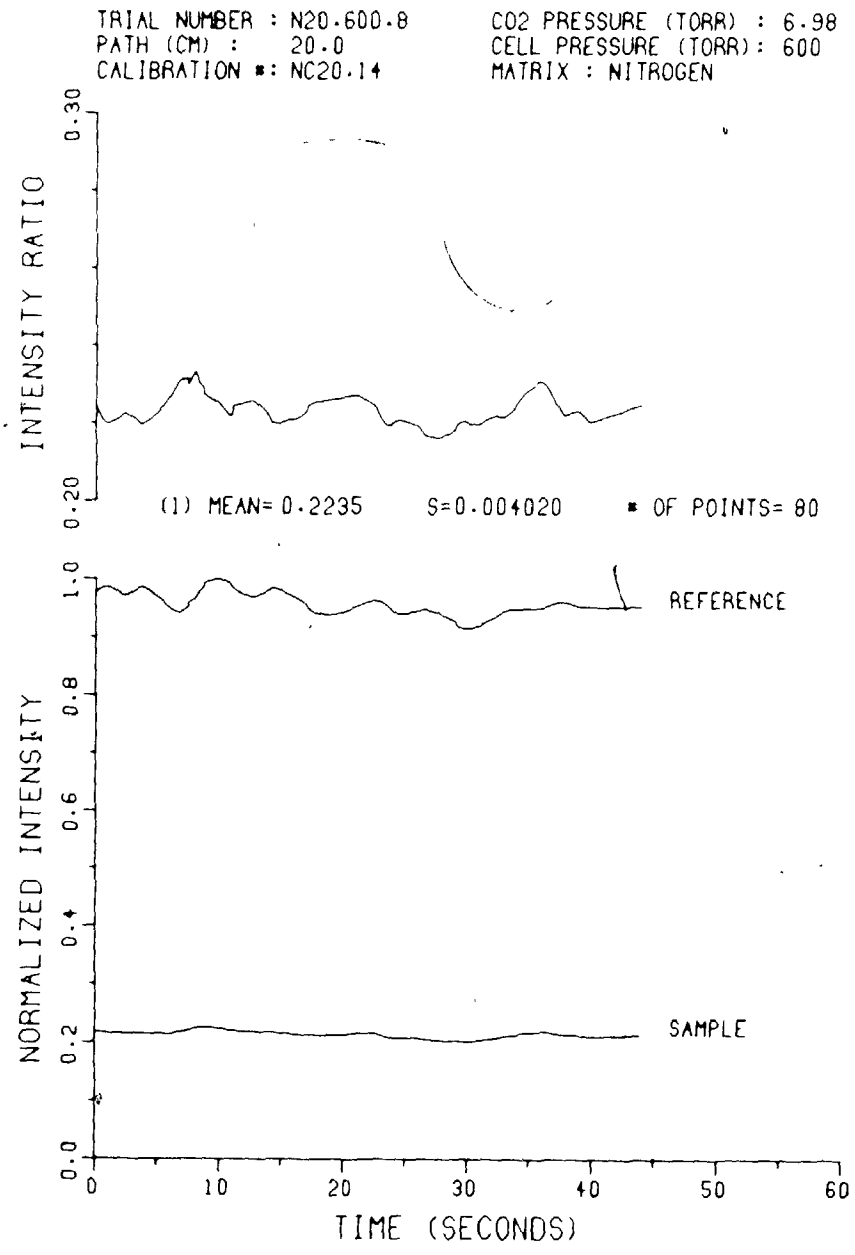
TRIAL NUMBER : N20.600.8
PATH (CM) : 20.0
CALIBRATION #: NC20.14
CO2 PRESSURE (TORR) : 6.98
CELL PRESSURE (TORR): 600
MATRIX : NITROGEN
INTENSITY RATIO
0.30
0.20
(1) MEAN= 0.2235 S=0.004020 # OF POINTS= 80
NORMALIZED INTENSITY
1.0
0.8
0.6
0.4
0.2
0.0
REFERENCE
SAMPLE
0
10
20
30
40
50
60
TIME (SECONDS)

Data Files - Total Pressure: 700 Torr

Trial Numbers: N20.700.1, N20.700.2, N20.700.5

Remote Gain: Sample (G_S): 1 (V/V)

FSD_S: 2

Trial Numbers: N20.700.3, N20.700.4

N20.700.6-N20.700.8

Remote Gain: Sample (G_S): 1 (V/V)

FSD_S: 1

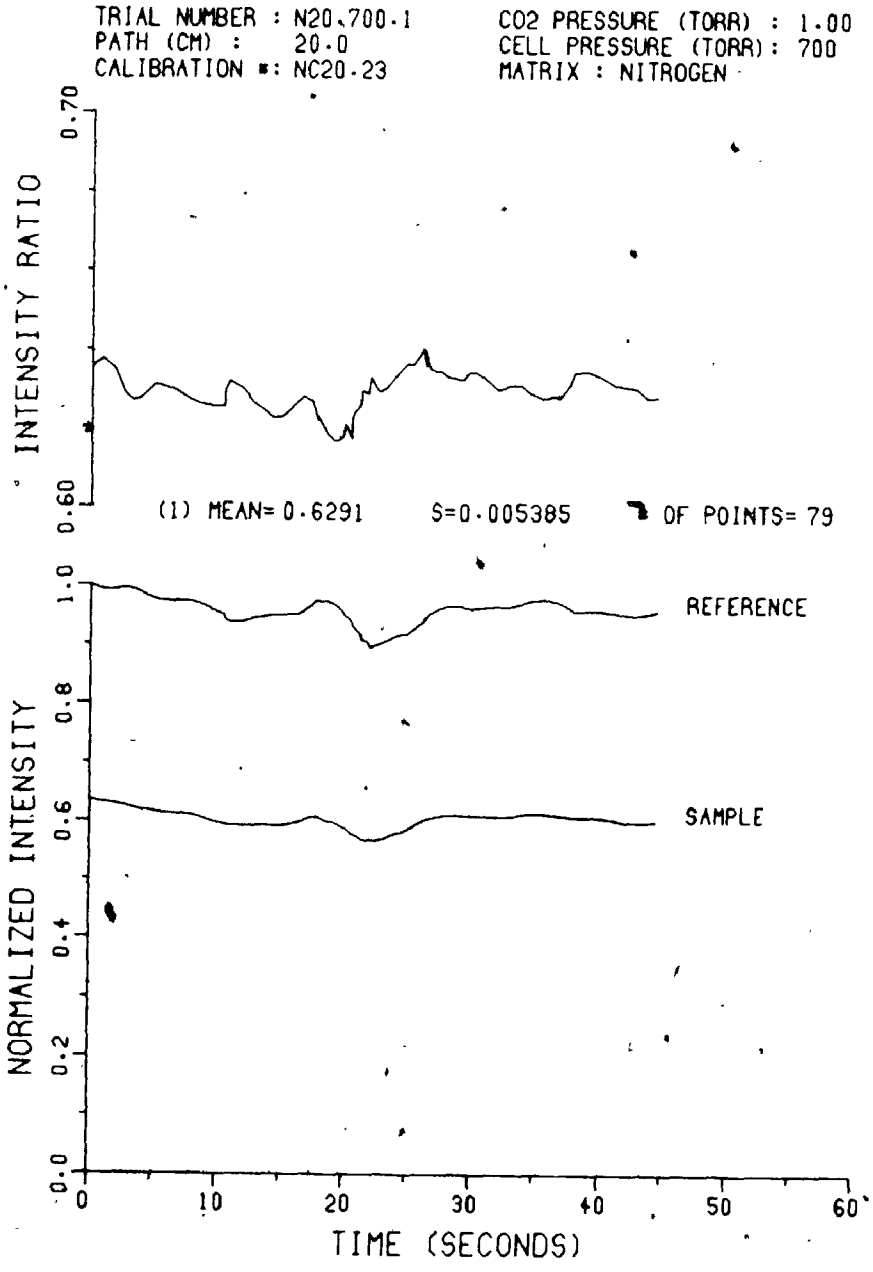
TRIAL NUMBER : N20.700.1
PATH (CM) : 20.0
CALIBRATION #: NC20.23
CO2 PRESSURE (TORR) : 1.00
CELL PRESSURE (TORR): 700
MATRIX : NITROGEN
INTENSITY RATIO
0.70
0.60
(1) MEAN= 0.6291
S=0.005385
OF POINTS= 79
NORMALIZED INTENSITY
1.0
0.8
0.6
0.4
0.2
0.0
REFERENCE
SAMPLE
0
10
20
30
40
50
60
TIME (SECONDS)

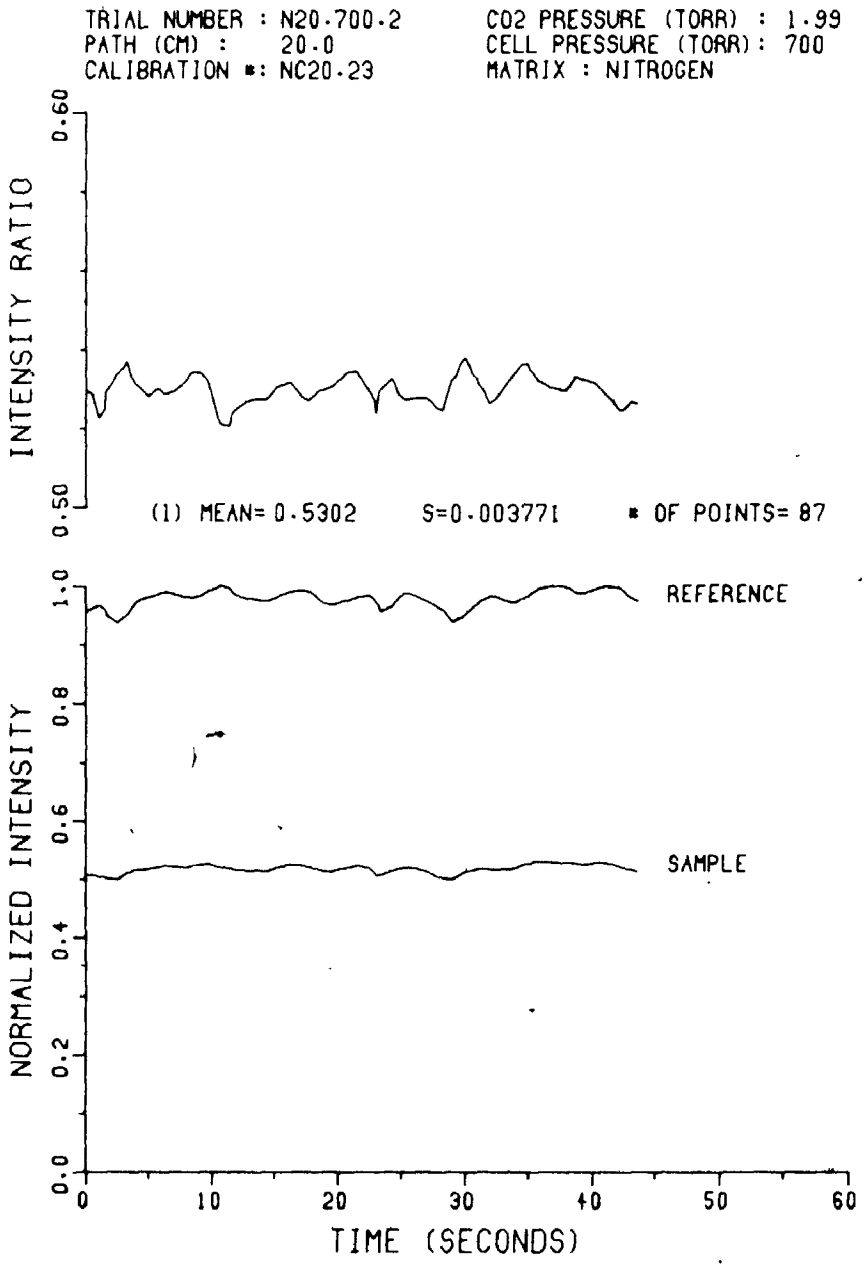
TRIAL NUMBER : N20.700.2
PATH (CM) : 20.0
CALIBRATION #: NC20.23
CO2 PRESSURE (TORR) : 1.99
CELL PRESSURE (TORR): 700
MATRIX : NITROGEN
INTENSITY RATIO
0.60
0.50
(1) MEAN= 0.5302 S=0.003771 # OF POINTS= 87
NORMALIZED INTENSITY
1.0
0.8
0.6
0.4
0.2
0.0
REFERENCE
SAMPLE
0
10
20
30
40
50
60
TIME (SECONDS)

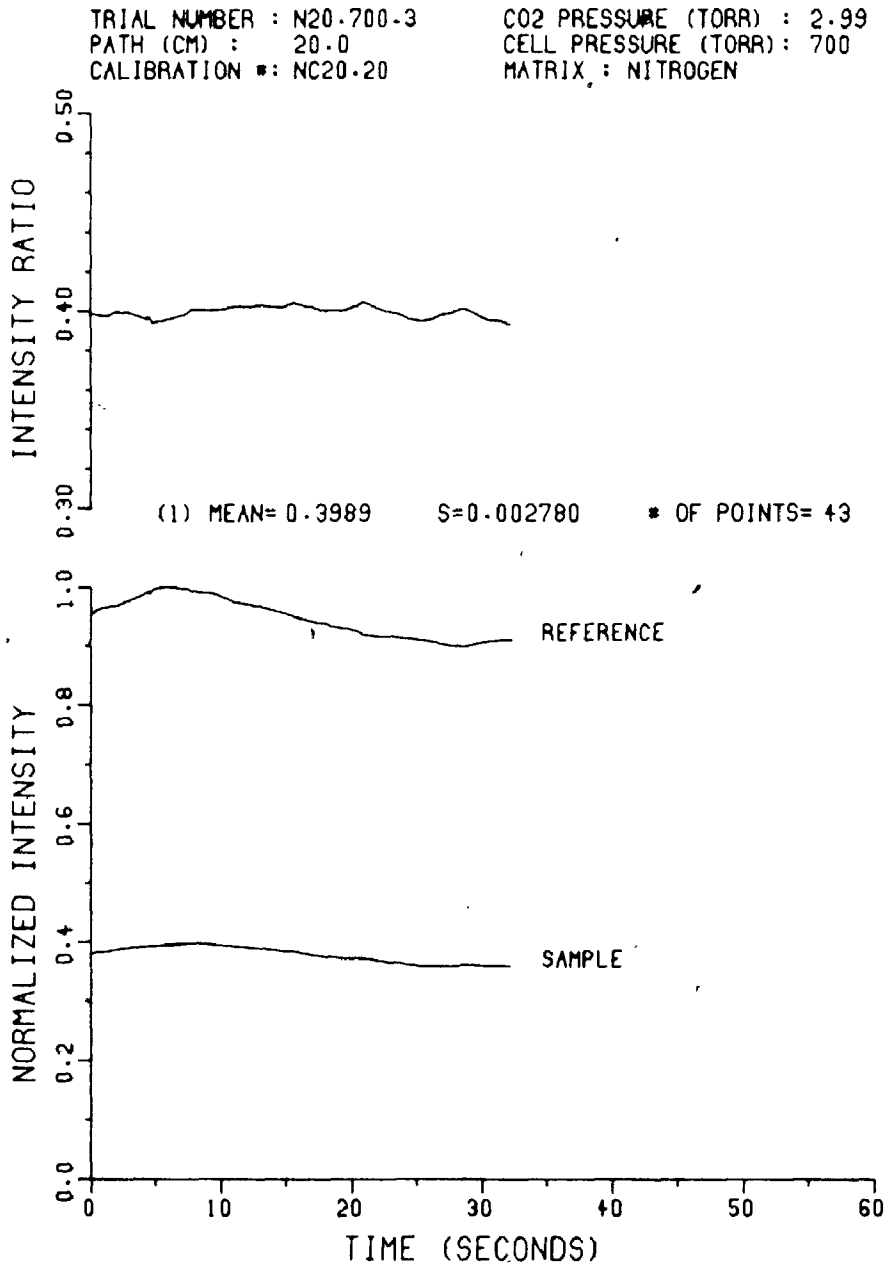
TRIAL NUMBER : N20.700-3
PATH (CM) : 20.0
CALIBRATION #: NC20.20
CO2 PRESSURE (TORR) : 2.99
CELL PRESSURE (TORR): 700
MATRIX : NITROGEN
INTENSITY RATIO
0.50
0.40
0.30
(1) MEAN= 0.3989 S=0.002780 # OF POINTS= 43
NORMALIZED INTENSITY
1.0
0.8
0.6
0.4
0.2
0.0
REFERENCE
SAMPLE
0
10
20
30
40
50
60
TIME (SECONDS)

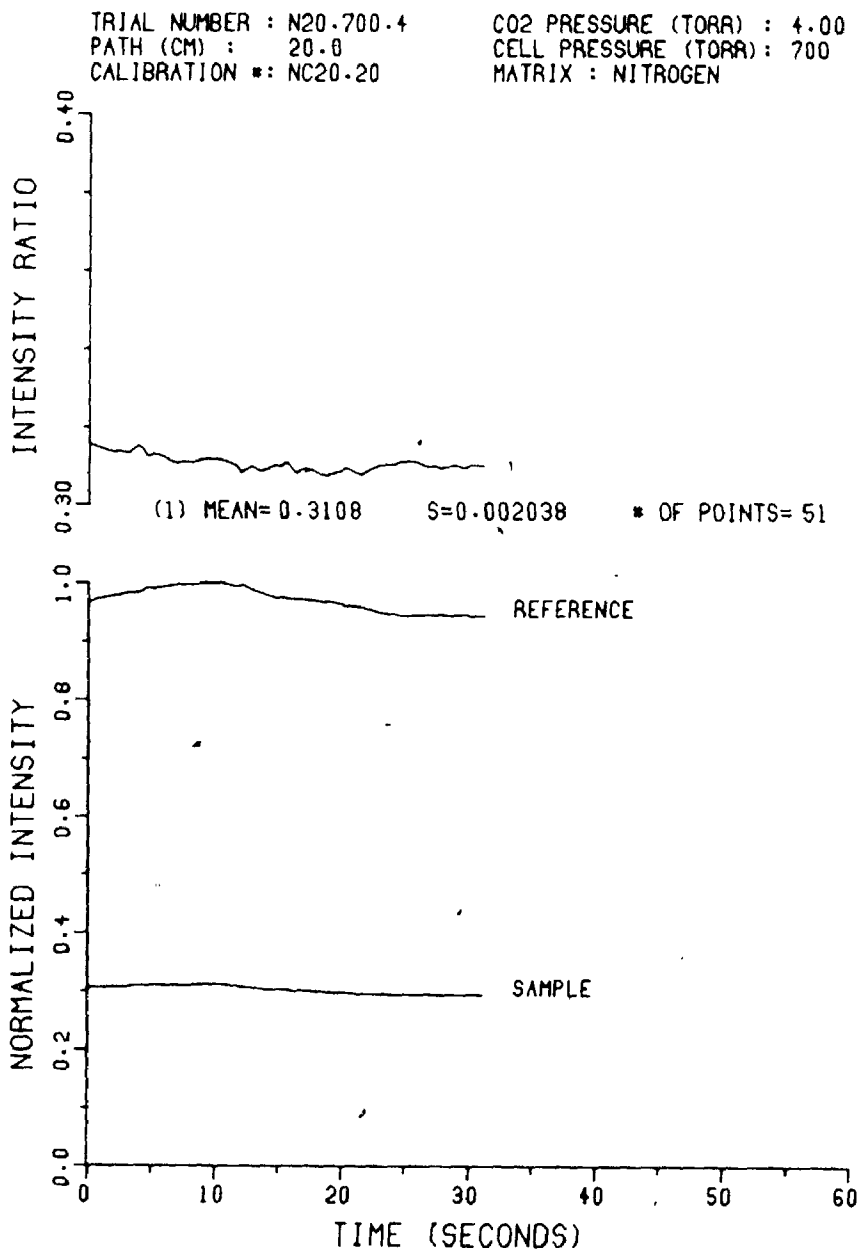
TRIAL NUMBER : N20.700.4
PATH (CM) : 20.8
CALIBRATION #: NC20.20
CO2 PRESSURE (TORR) : 4.00
CELL PRESSURE (TORR): 700
MATRIX : NITROGEN
INTENSITY RATIO
0.40
0.30
(1) MEAN= 0.3108 S=0.002038 # OF POINTS= 51
NORMALIZED INTENSITY
1.0
0.8
0.6
0.4
0.2
0.0
REFERENCE
SAMPLE
0
10
20
30
40
50
60
TIME (SECONDS)

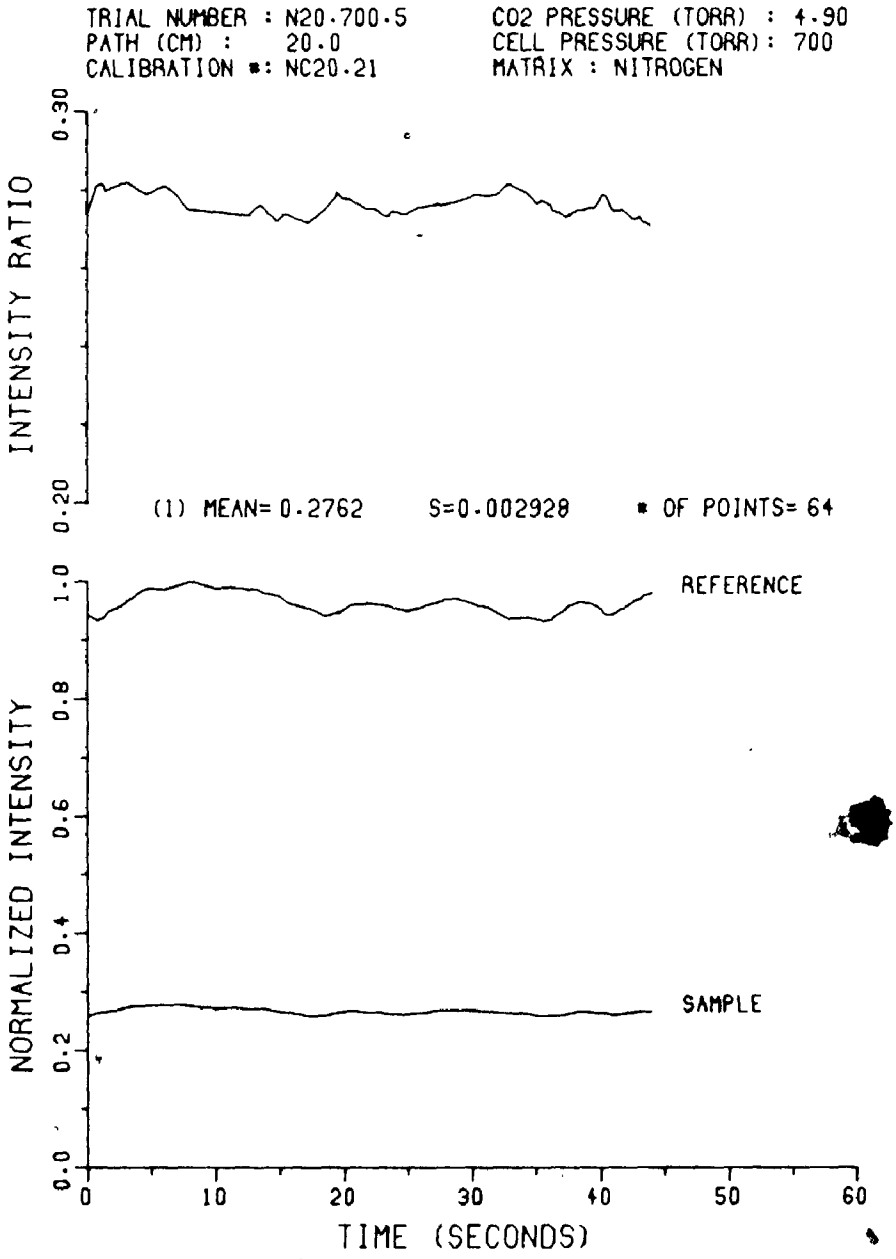
TRIAL NUMBER : N20.700.5
PATH (CM) : 20.0
CALIBRATION #: NC20.21
CO2 PRESSURE (TORR) : 4.90
CELL PRESSURE (TORR): 700
MATRIX : NITROGEN
INTENSITY RATIO
0.30
0.20
(1) MEAN= 0.2762 S=0.002928 # OF POINTS= 64
NORMALIZED INTENSITY
1.0
0.8
0.6
0.4
0.2
0.0
REFERENCE
SAMPLE
0
10
20
30
40
50
60
TIME (SECONDS)

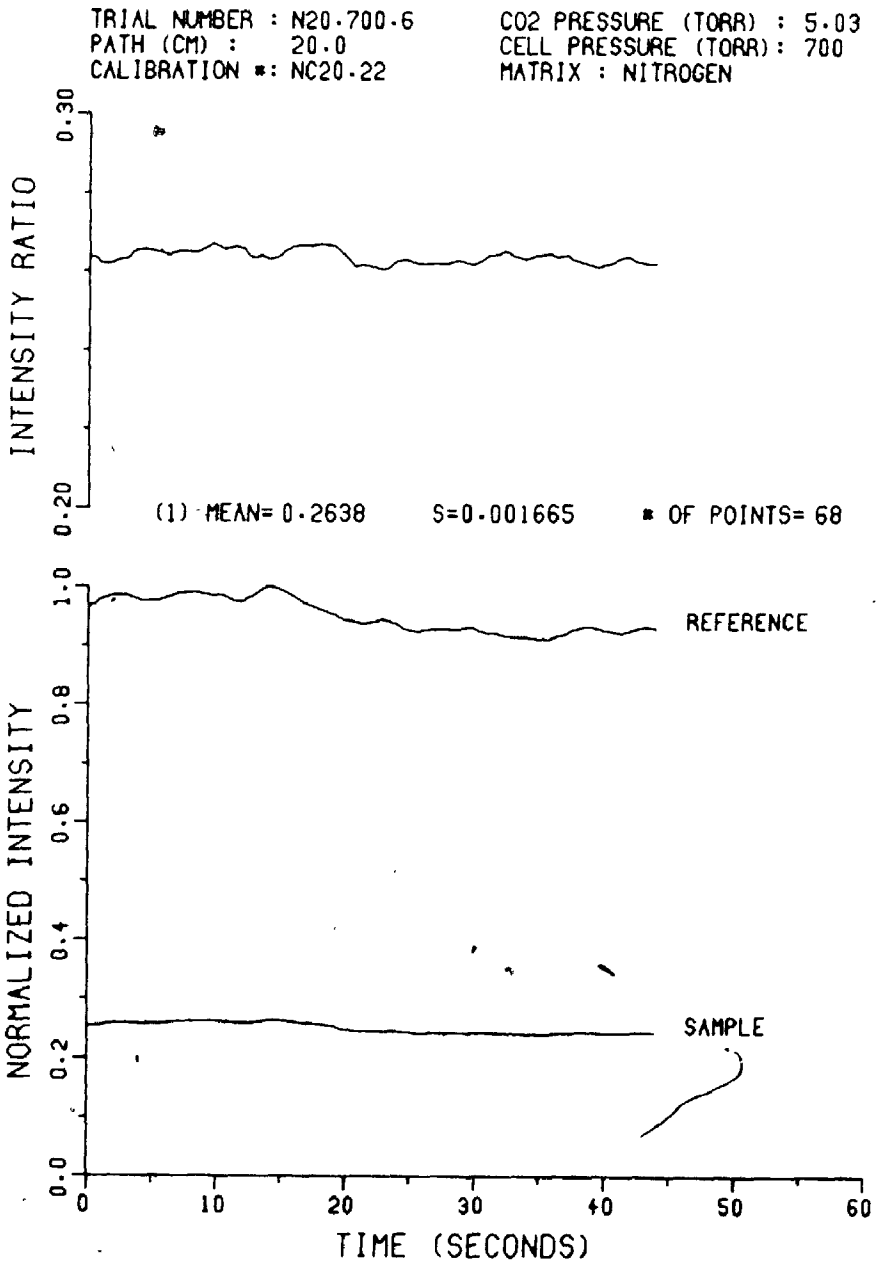
TRIAL NUMBER : N20.700.6
PATH (CM) : 20.0
CALIBRATION #: NC20.22
CO2 PRESSURE (TORR) : 5.03
CELL PRESSURE (TORR): 700
MATRIX : NITROGEN
INTENSITY RATIO
0.30
0.20
(1) MEAN= 0.2638
S=0.001665
# OF POINTS= 68
NORMALIZED INTENSITY
1.0
0.8
0.6
0.4
0.2
0.0
REFERENCE
SAMPLE
0
10
20
30
40
50
60
TIME (SECONDS)

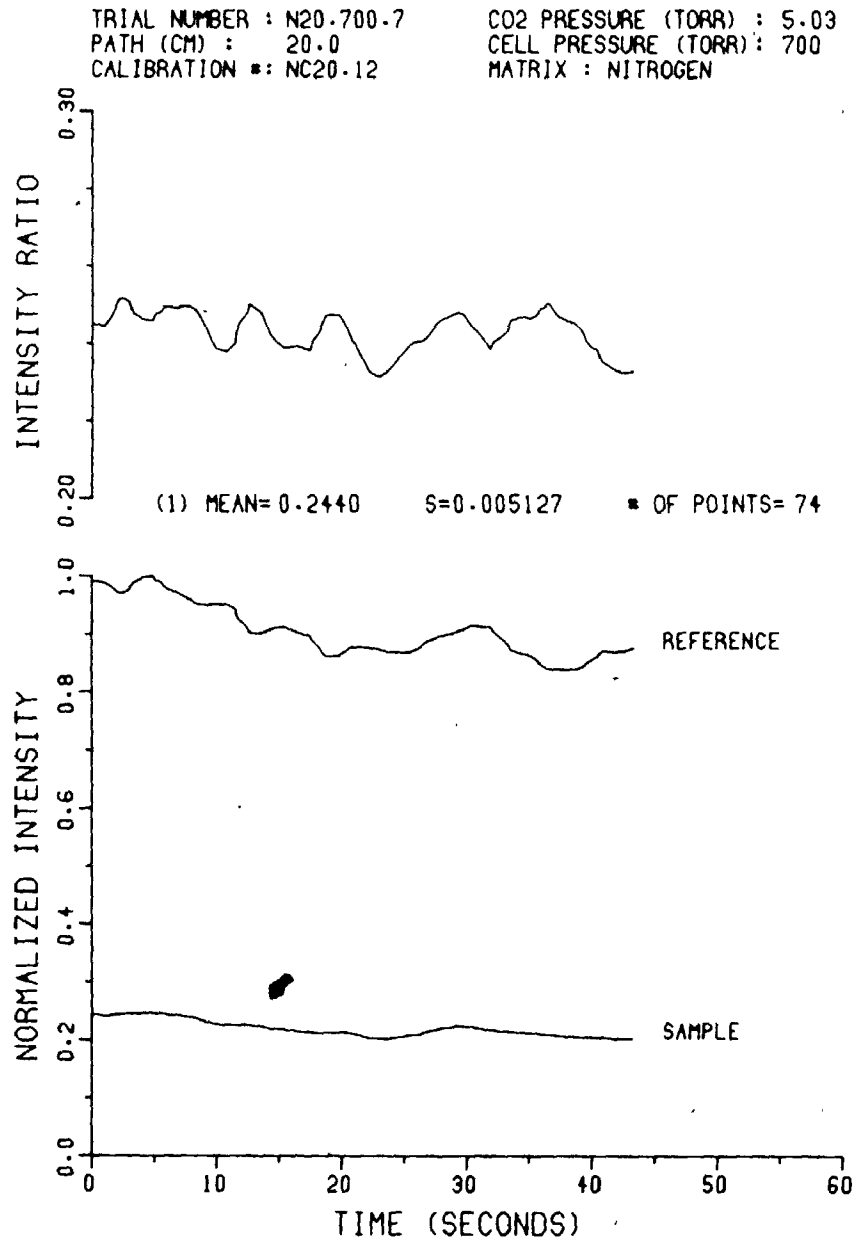
TRIAL NUMBER : N20.700.7
PATH (CM) : 20.0
CALIBRATION #: NC20.12
CO2 PRESSURE (TORR) : 5.03
CELL PRESSURE (TORR): 700
MATRIX : NITROGEN
INTENSITY RATIO
0.30
0.20
(1) MEAN= 0.2440 S=0.005127 # OF POINTS= 74
NORMALIZED INTENSITY
1.0
0.8
0.6
0.4
0.2
0.0
REFERENCE
SAMPLE
0
10
20
30
40
50
60
TIME (SECONDS)

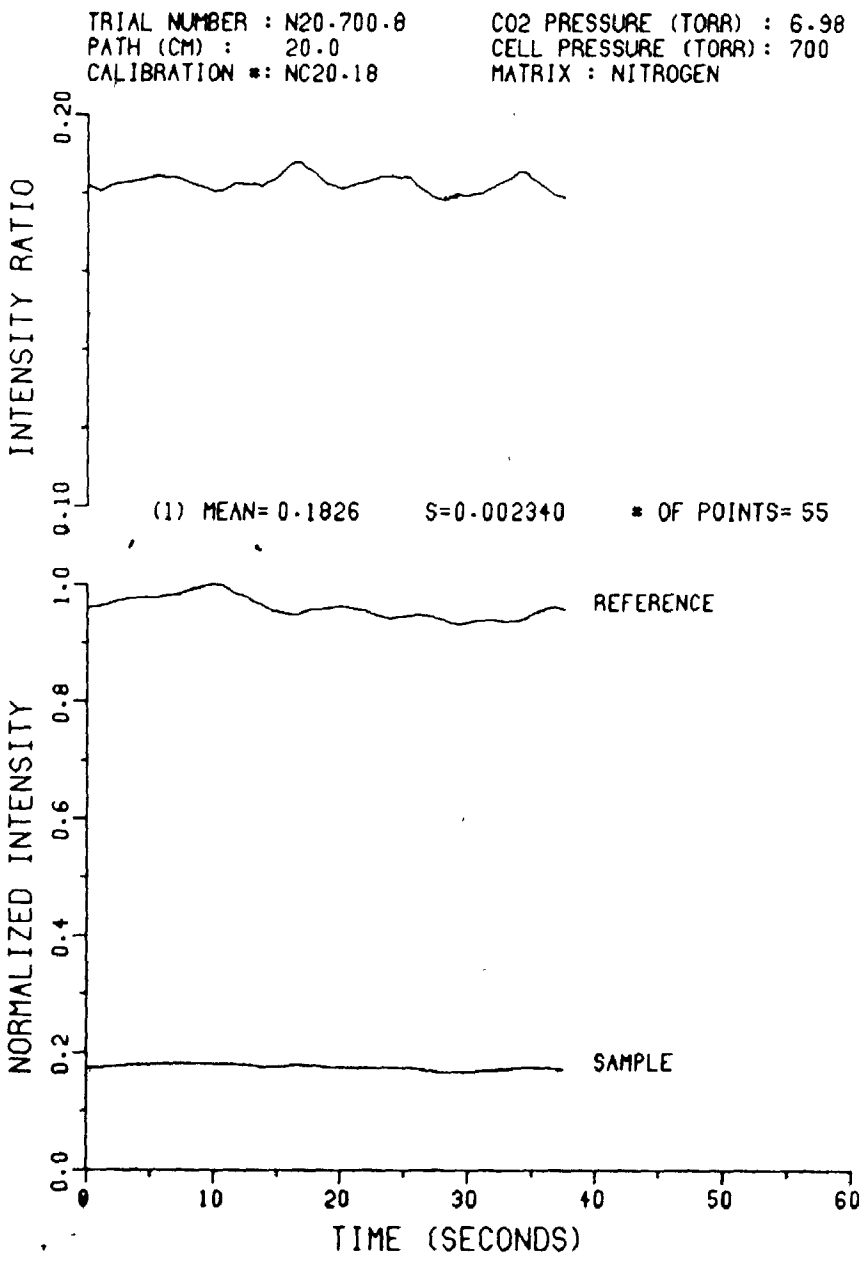
TRIAL NUMBER : N20-700-8
PATH (CM) : 20.0
CALIBRATION #: NC20-18
CO2 PRESSURE (TORR) : 6.98
CELL PRESSURE (TORR): 700
MATRIX : NITROGEN
INTENSITY RATIO
0.20
0.10
(1) MEAN= 0.1826 S=0.002340 # OF POINTS= 55
NORMALIZED INTENSITY
1.0
0.8
0.6
0.4
0.2
0.0
REFERENCE
SAMPLE
0
10
20
30
40
50
60
TIME (SECONDS)

Data Files - Total Pressure: 760 Torr

Trial Numbers: N20.760.1-N20.760.7

N20.760.5, N20.760.8

Remote Gain: Sample (G_S): 1 (V/V)

FSD_S: 2

Trial Numbers: N20.760.4, N20.760.6, N20.760.7

N20.760.9, N20.760.10

Remote Gain: Sample (G_S): 1 (V/V)

FSD_S: 1

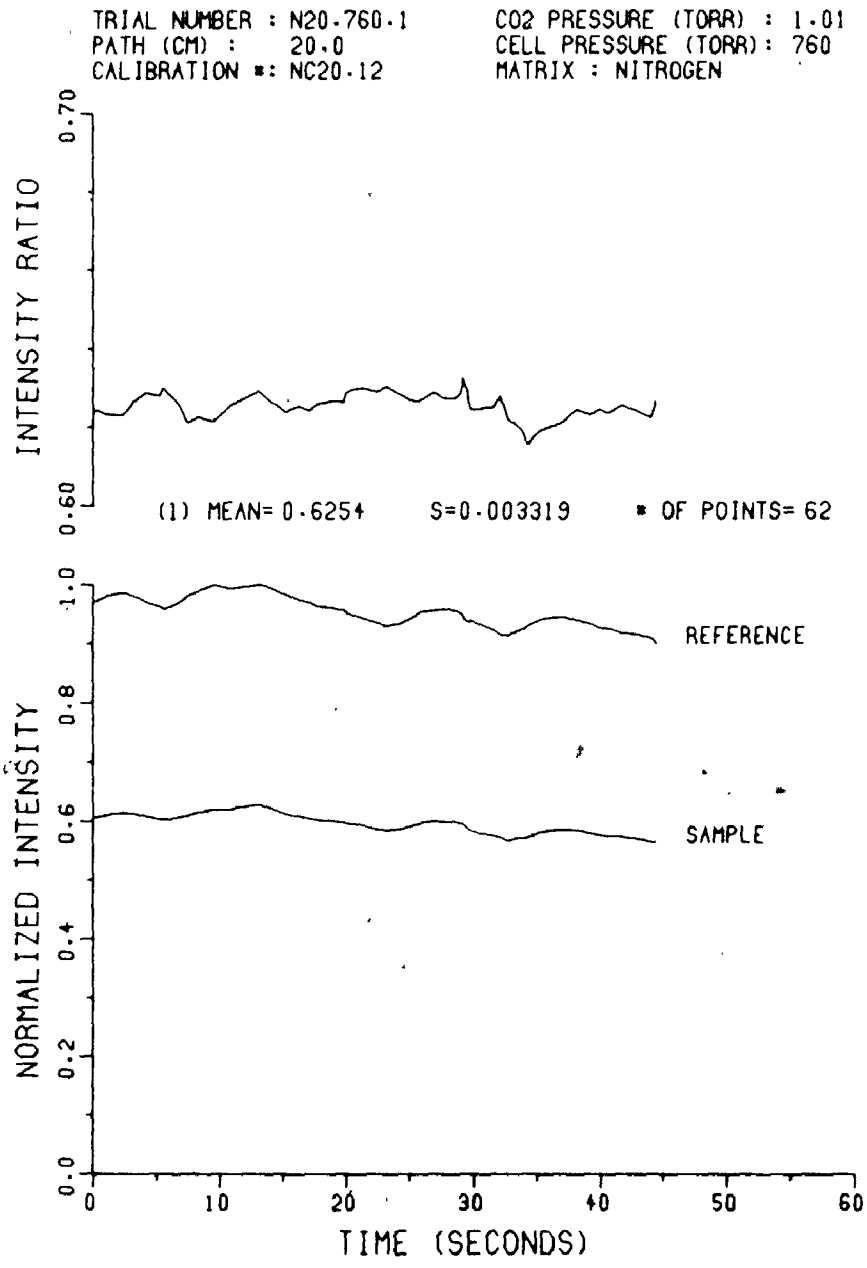
TRIAL NUMBER : N20-760-1
PATH (CM) : 20.0
CALIBRATION #: NC20-12
CO2 PRESSURE (TORR) : 1.01
CELL PRESSURE (TORR): 760
MATRIX : NITROGEN
INTENSITY RATIO
0.70
0.60
(1) MEAN= 0.6254 S=0.003319 # OF POINTS= 62
NORMALIZED INTENSITY
1.0
0.8
0.6
0.4
0.2
0.0
REFERENCE
SAMPLE
0
10
20
30
40
50
60
TIME (SECONDS)

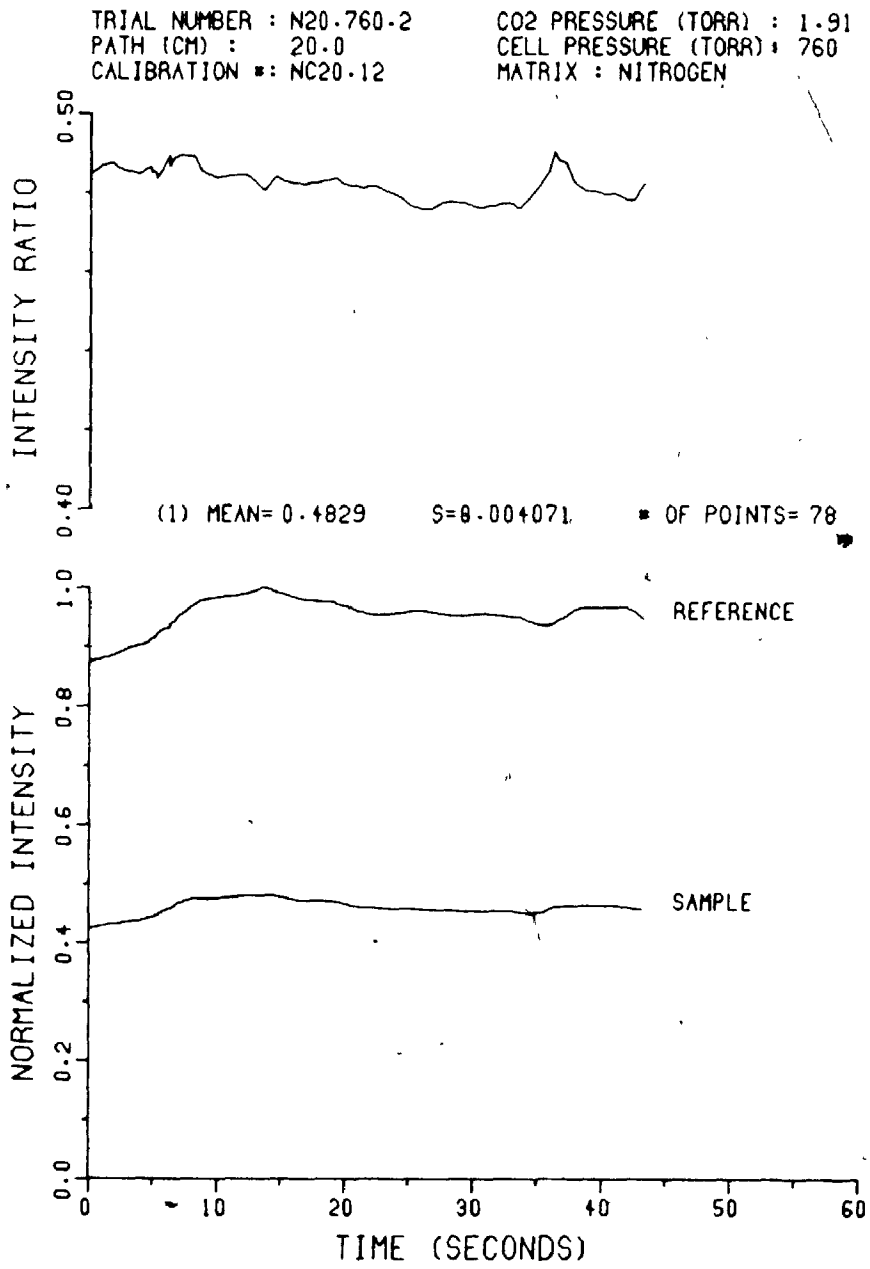
TRIAL NUMBER : N20.760-2
PATH (CM) : 20.0
CALIBRATION #: NC20.12
CO2 PRESSURE (TORR) : 1.91
CELL PRESSURE (TORR) : 760
MATRIX : NITROGEN
INTENSITY RATIO
0.50
0.40
(1) MEAN= 0.4829 S=0.004071 # OF POINTS= 78
NORMALIZED INTENSITY
1.0
0.8
0.6
0.4
0.2
0.0
REFERENCE
SAMPLE
0
10
20
30
40
50
60
TIME (SECONDS)

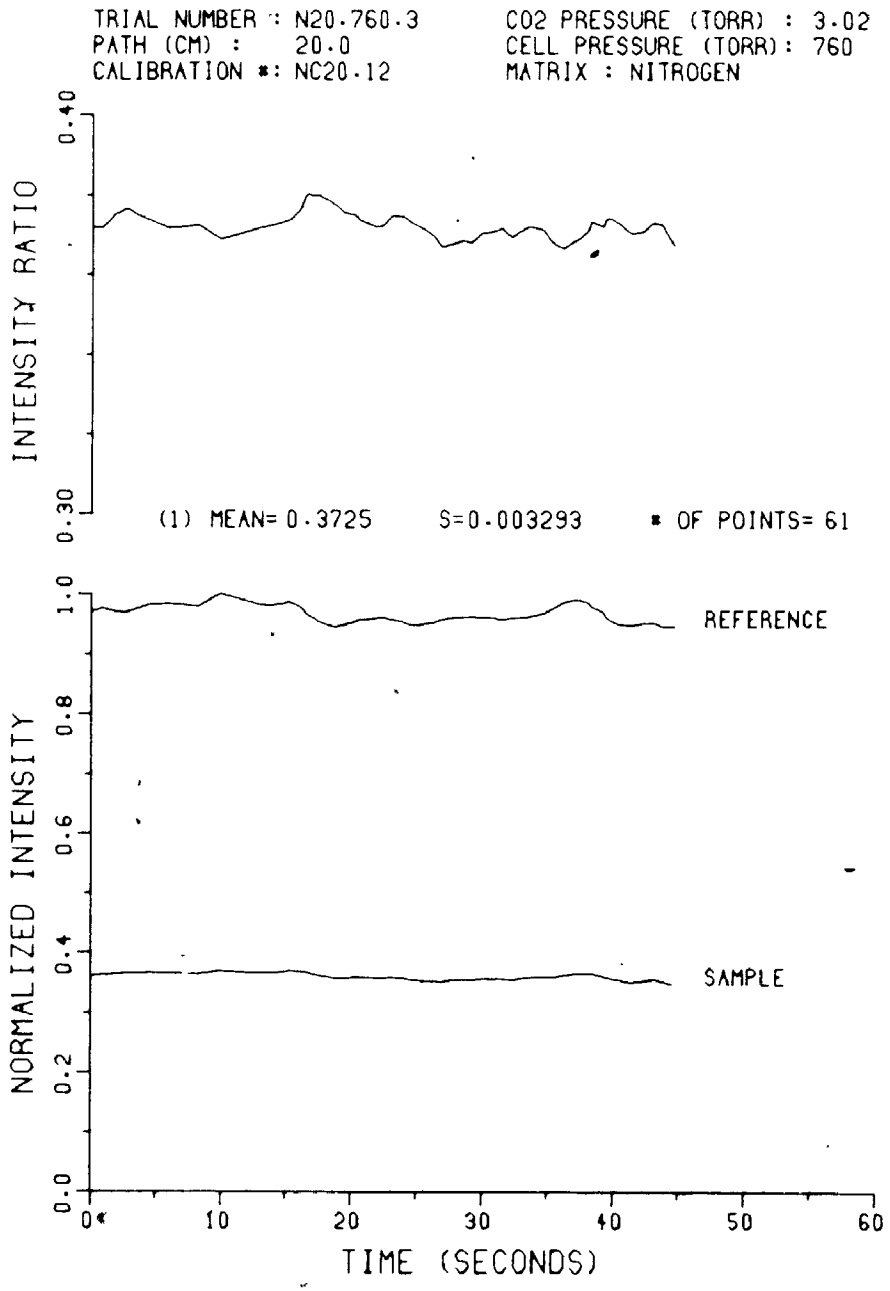
TRIAL NUMBER : N20.760.3
PATH (CM) : 20.0
CALIBRATION #: NC20.12
CO2 PRESSURE (TORR) : 3.02
CELL PRESSURE (TORR): 760
MATRIX : NITROGEN
INTENSITY RATIO
0.40
0.30
(1) MEAN= 0.3725 S=0.003293 # OF POINTS= 61
NORMALIZED INTENSITY
1.0
0.8
0.6
0.4
0.2
0.0
REFERENCE
SAMPLE
0
10
20
30
40
50
60
TIME (SECONDS)

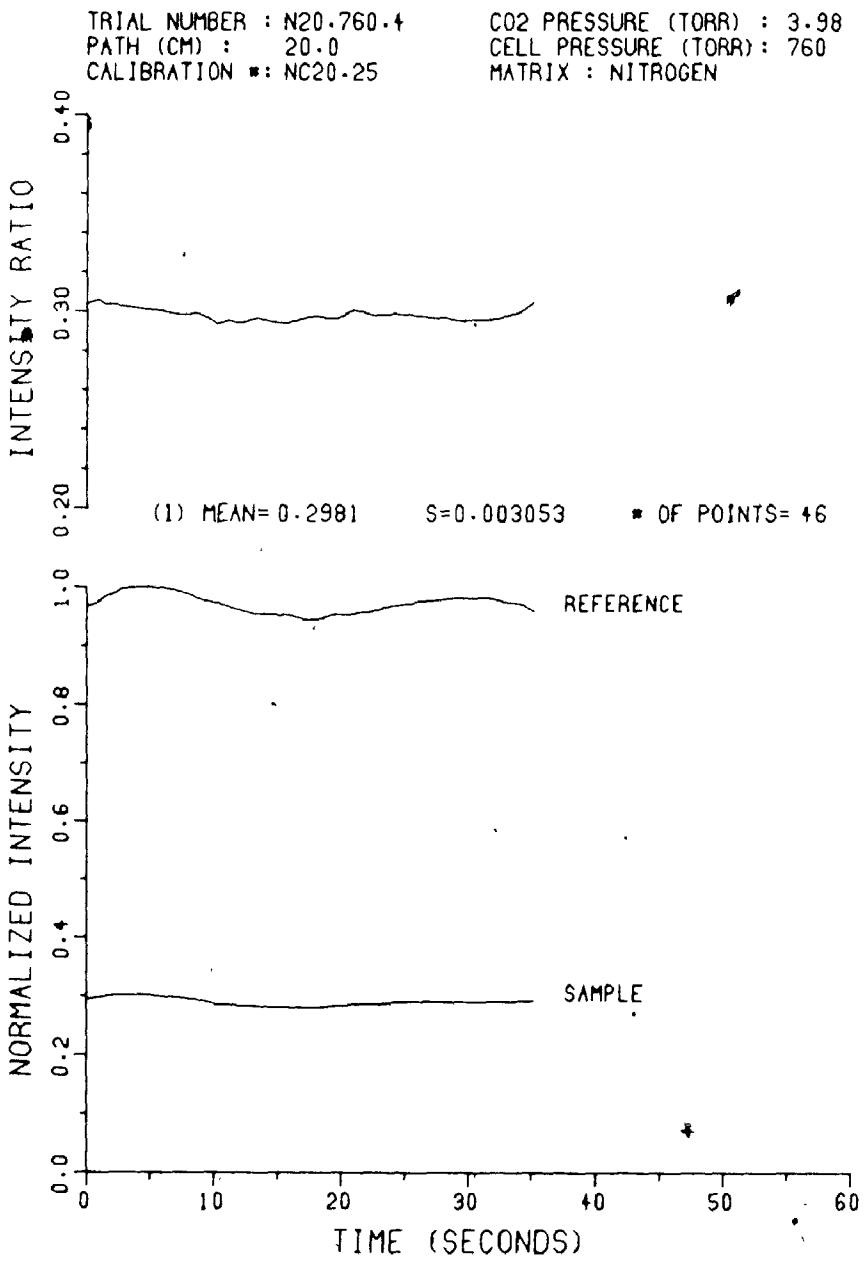
TRIAL NUMBER : N20.760.4
PATH (CM) : 20.0
CALIBRATION #: NC20.25
CO2 PRESSURE (TORR) : 3.98
CELL PRESSURE (TORR): 760
MATRIX : NITROGEN
INTENSITY RATIO
0.40
0.30
0.20
(1) MEAN= 0.2981
S=0.003053
# OF POINTS= 46
NORMALIZED INTENSITY
1.0
0.8
0.6
0.4
0.2
0.0
REFERENCE
SAMPLE
0
10
20
30
40
50
60
TIME (SECONDS)

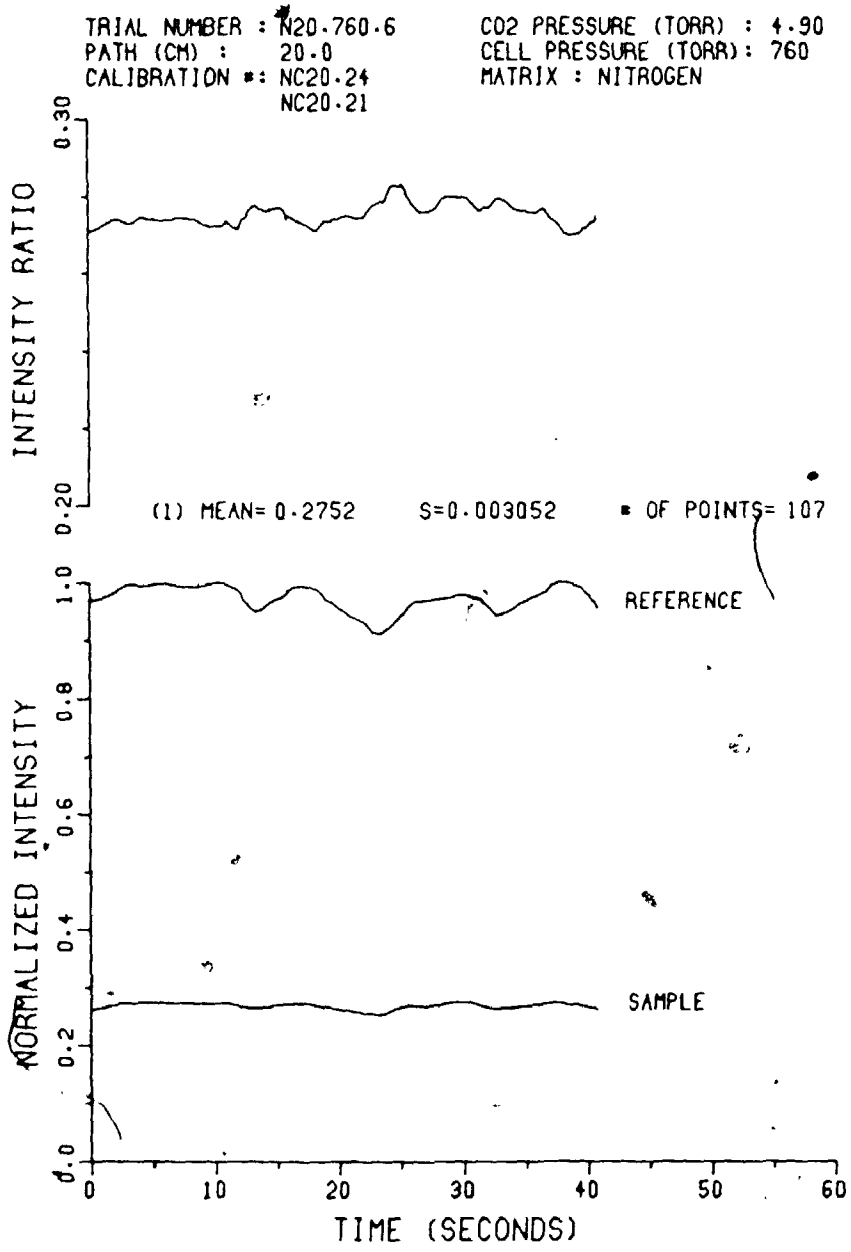
TRIAL NUMBER : N20.760.6
PATH (CM) : 20.0
CALIBRATION #: NC20.24
NC20.21
CO2 PRESSURE (TORR) : 4.90
CELL PRESSURE (TORR): 760
MATRIX : NITROGEN
INTENSITY RATIO
0.30
0.20
(1) MEAN= 0.2752 S=0.003052 # OF POINTS= 107
NORMALIZED INTENSITY
1.0
0.8
0.6
0.4
0.2
0.0
REFERENCE
SAMPLE
0
10
20
30
40
50
60
TIME (SECONDS)

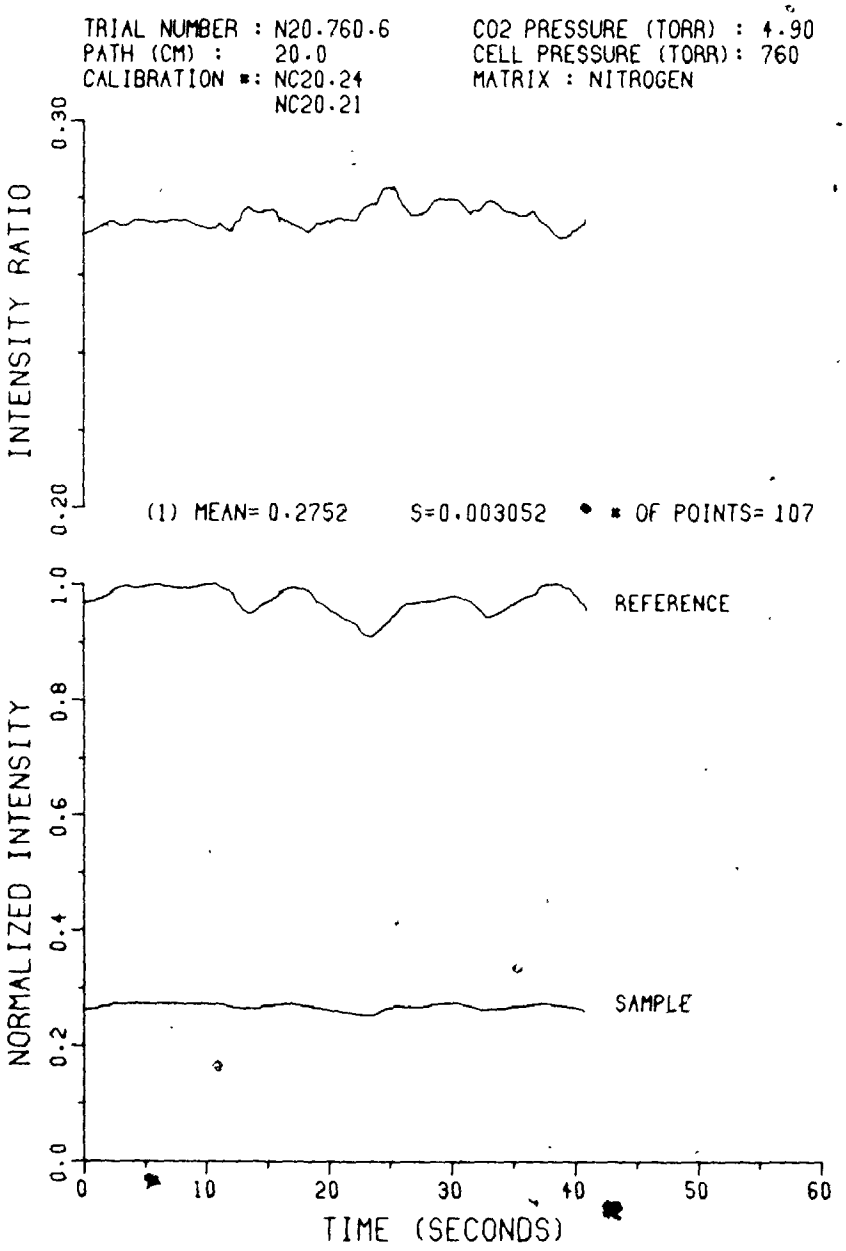
TRIAL NUMBER : N20.760.6
PATH (CM) : 20.0
CALIBRATION #: NC20.24
NC20.21
CO2 PRESSURE (TORR) : 4.90
CELL PRESSURE (TORR): 760
MATRIX : NITROGEN
INTENSITY RATIO
0.30
0.20
(1) MEAN= 0.2752 S=0.003052 # OF POINTS= 107
NORMALIZED INTENSITY
1.0
0.8
0.6
0.4
0.2
0.0
REFERENCE
SAMPLE
0
10
20
30
40
50
60
TIME (SECONDS)

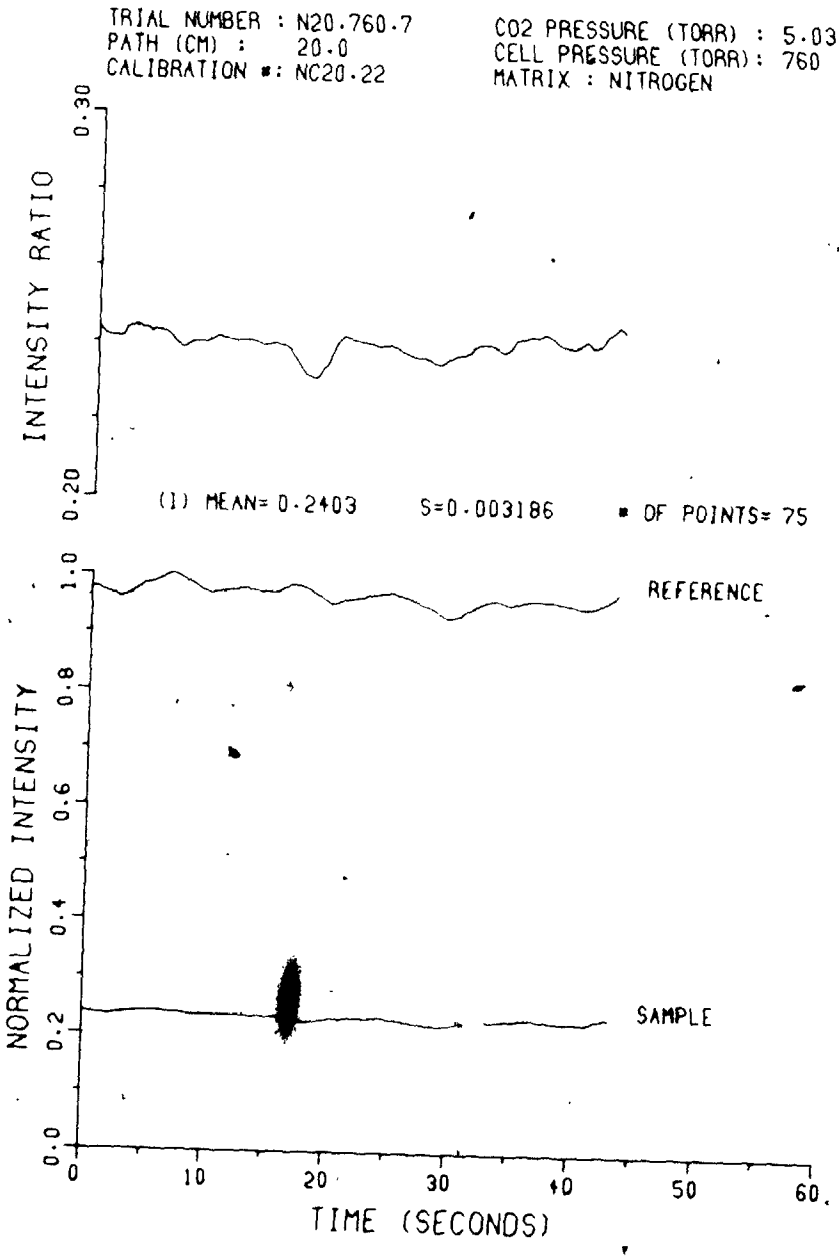
TRIAL NUMBER : N20.760.7
PATH (CM) : 20.0
CALIBRATION #: NC20.22
CO2 PRESSURE (TORR) : 5.03
CELL PRESSURE (TORR): 760
MATRIX : NITROGEN
INTENSITY RATIO
0.30
0.20
(1) MEAN= 0.2403 S=0.003186 # OF POINTS= 75
REFERENCE
SAMPLE
NORMALIZED INTENSITY
1.0
0.8
0.6
0.4
0.2
0.0
0
10
20
30
40
50
60
TIME (SECONDS)

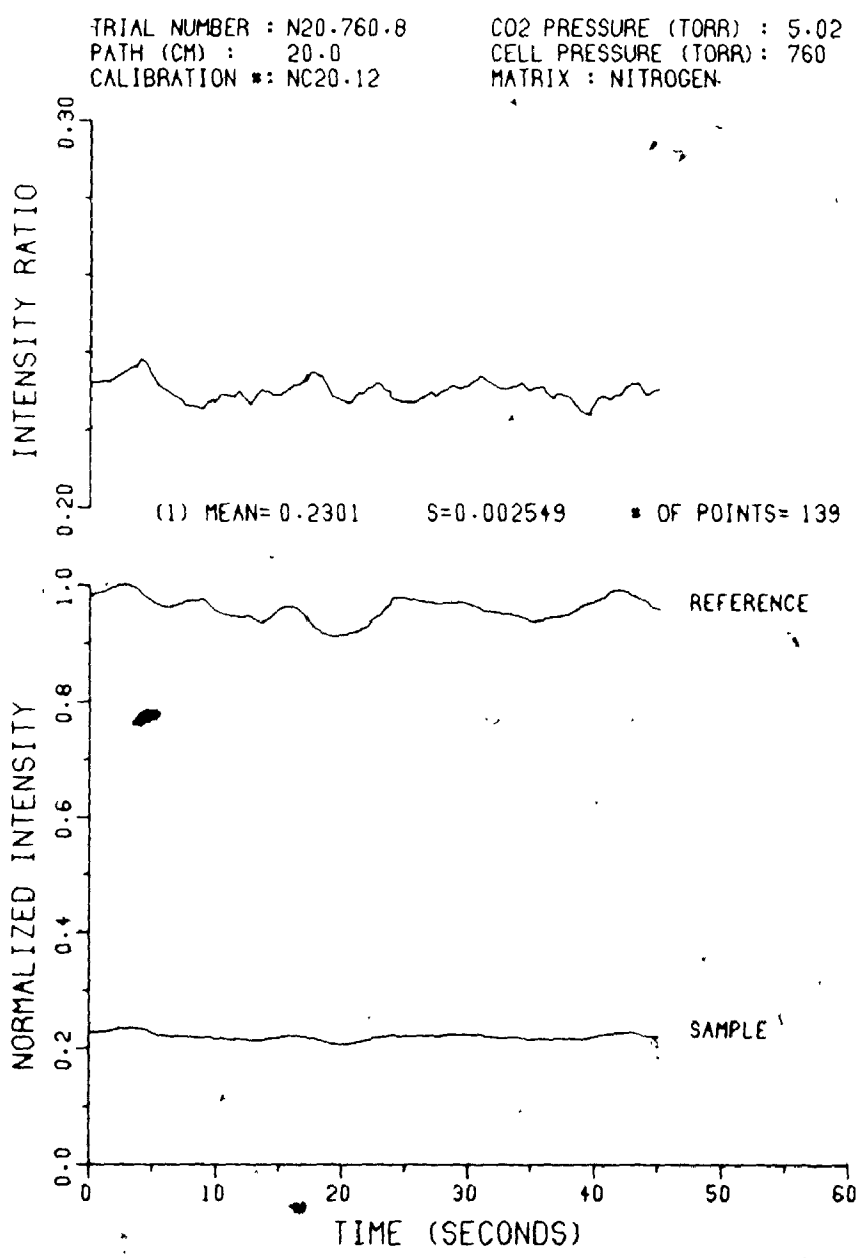
TRIAL NUMBER : N20.760.8
PATH (CM) : 20.0
CALIBRATION #: NC20.12
CO2 PRESSURE (TORR) : 5.02
CELL PRESSURE (TORR): 760
MATRIX : NITROGEN
INTENSITY RATIO
0.30
0.20
(1) MEAN= 0.2301 S=0.002549 # OF POINTS= 139
NORMALIZED INTENSITY
1.0
0.8
0.6
0.4
0.2
0.0
REFERENCE
SAMPLE
0
10
20
30
40
50
60
TIME (SECONDS)

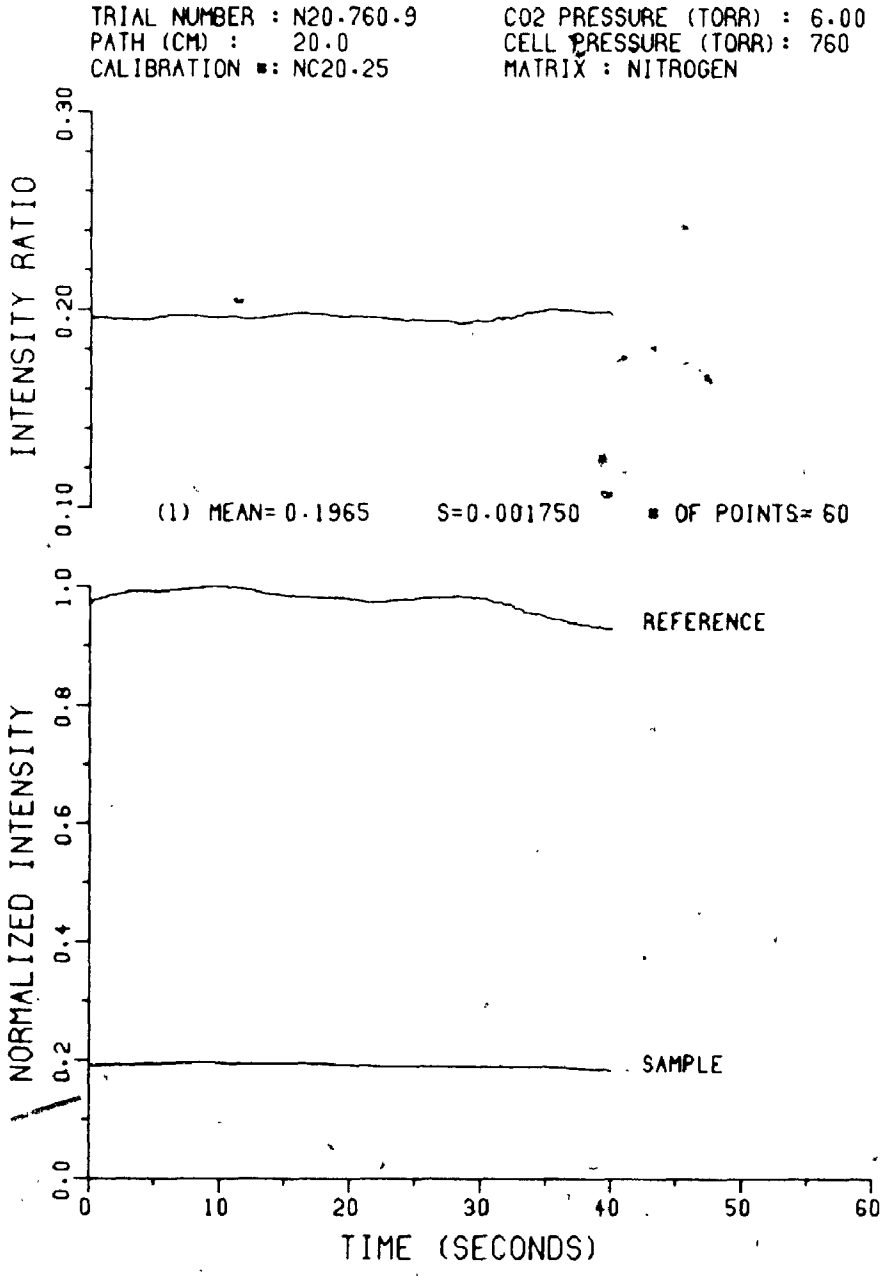
TRIAL NUMBER : N20.760.9
PATH (CM) : 20.0
CALIBRATION #: NC20.25
CO2 PRESSURE (TORR) : 6.00
CELL PRESSURE (TORR): 760
MATRIX : NITROGEN
INTENSITY RATIO
0.30
0.20
0.10
(1) MEAN= 0.1965 S=0.001750 # OF POINTS= 60
NORMALIZED INTENSITY
1.0
0.8
0.6
0.4
0.2
0.0
REFERENCE
SAMPLE
0
10
20
30
40
50
60
TIME (SECONDS)

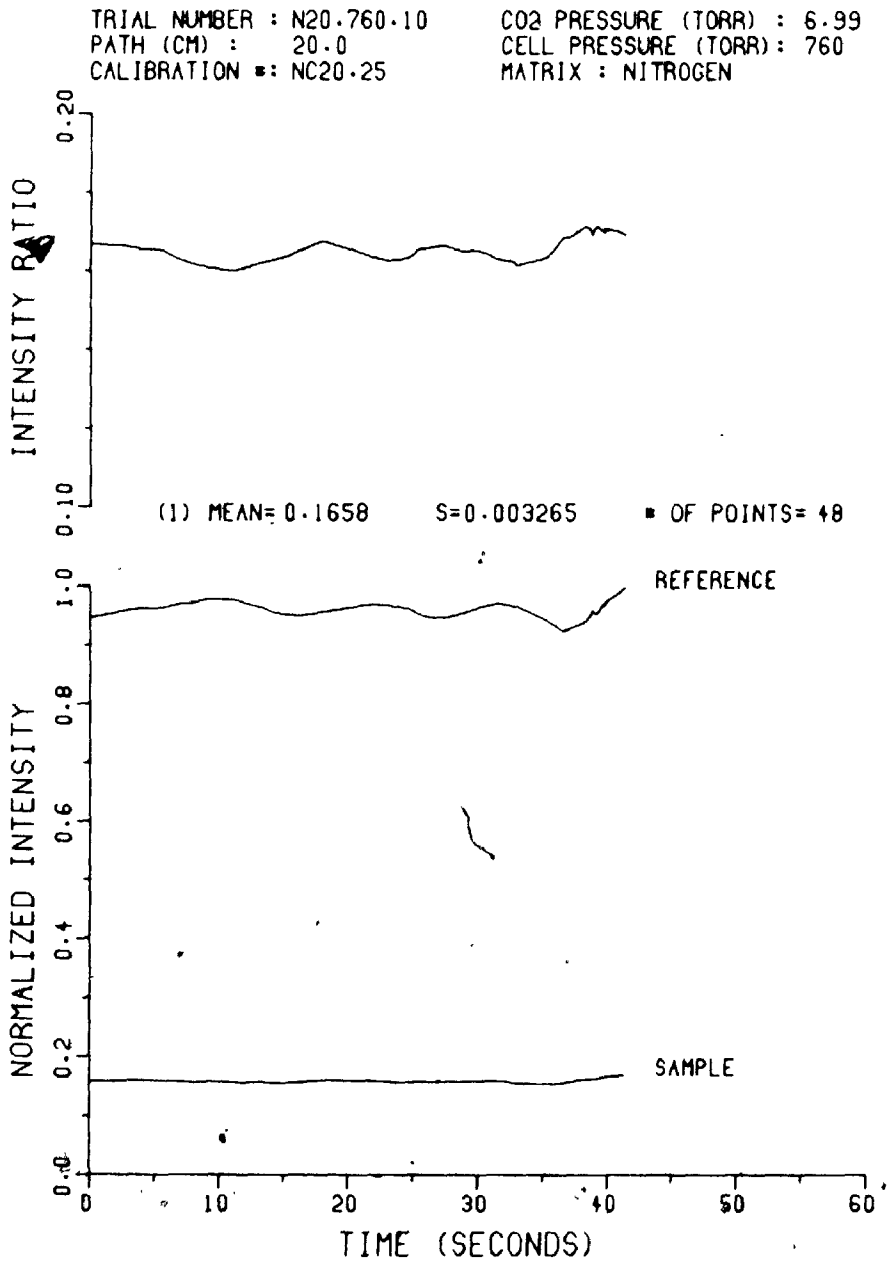
TRIAL NUMBER : N20.760.10
PATH (CM) : 20.0
CALIBRATION #: NC20.25
CO2 PRESSURE (TORR) : 6.99
CELL PRESSURE (TORR): 760
MATRIX : NITROGEN
INTENSITY RATIO
0.20
0.10
(1) MEAN= 0.1658 S=0.003265 # OF POINTS= 48
NORMALIZED INTENSITY
1.0
0.8
0.6
0.4
0.2
0.0
REFERENCE
SAMPLE
0
10
20
30
40
50
60
TIME (SECONDS)

Data Files - Total Pressure: 900 Torr

Trial Numbers: N20.900.1-N20.900.4

Remote Gain: Sample (G_S): 1 (V/V)

FSD_S: 1

Trial Numbers: N20.900.5-N20.900.7

Remote Gain: Sample (G_S): 2 (V/V)

FSD_S: 1

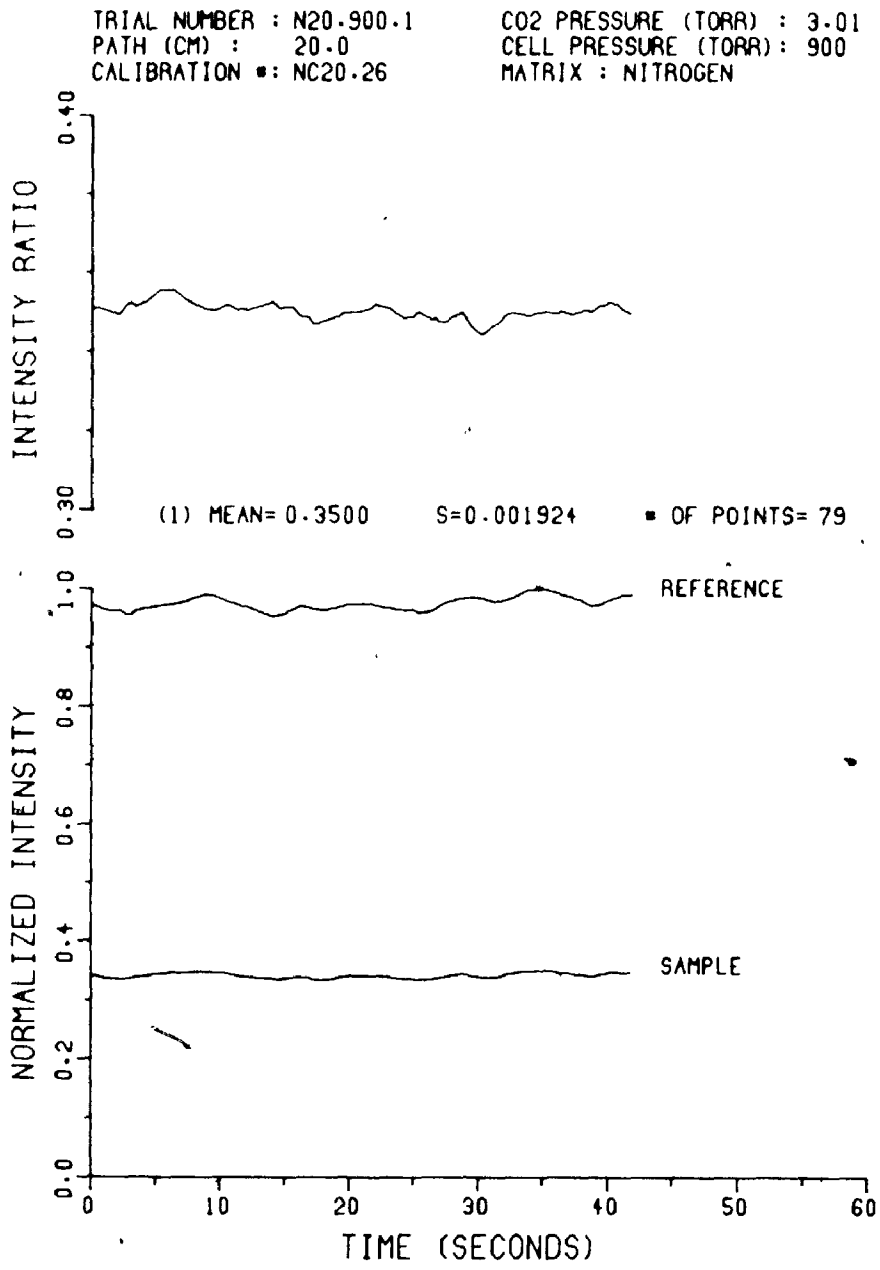
TRIAL NUMBER : N20.900.1
PATH (CM) : 20.0
CALIBRATION #: NC20.26
CO2 PRESSURE (TORR) : 3.01
CELL PRESSURE (TORR): 900
MATRIX : NITROGEN
INTENSITY RATIO
0.40
0.30
(1) MEAN= 0.3500 S=0.001924 # OF POINTS= 79
NORMALIZED INTENSITY
1.0
0.8
0.6
0.4
0.2
0.0
REFERENCE
SAMPLE
0
10
20
30
40
50
60
TIME (SECONDS)

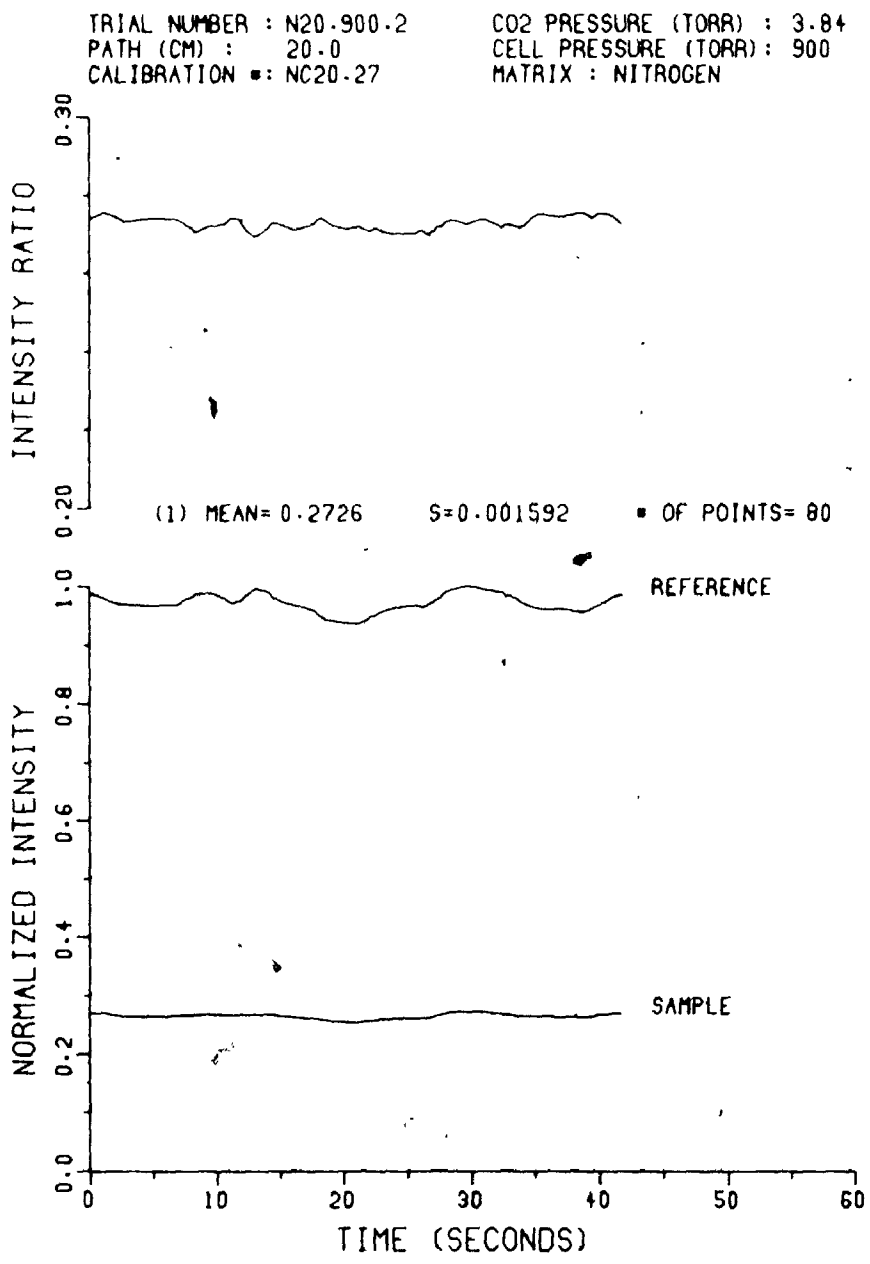
TRIAL NUMBER : N20.900.2
PATH (CM) : 20.0
CALIBRATION #: NC20.27
CO2 PRESSURE (TORR) : 3.84
CELL PRESSURE (TORR): 900
MATRIX : NITROGEN
INTENSITY RATIO
0.30
0.20
(1) MEAN= 0.2726 S=0.001592 # OF POINTS= 80
NORMALIZED INTENSITY
1.0
0.8
0.6
0.4
0.2
0.0
REFERENCE
SAMPLE
0
10
20
30
40
50
60
TIME (SECONDS)

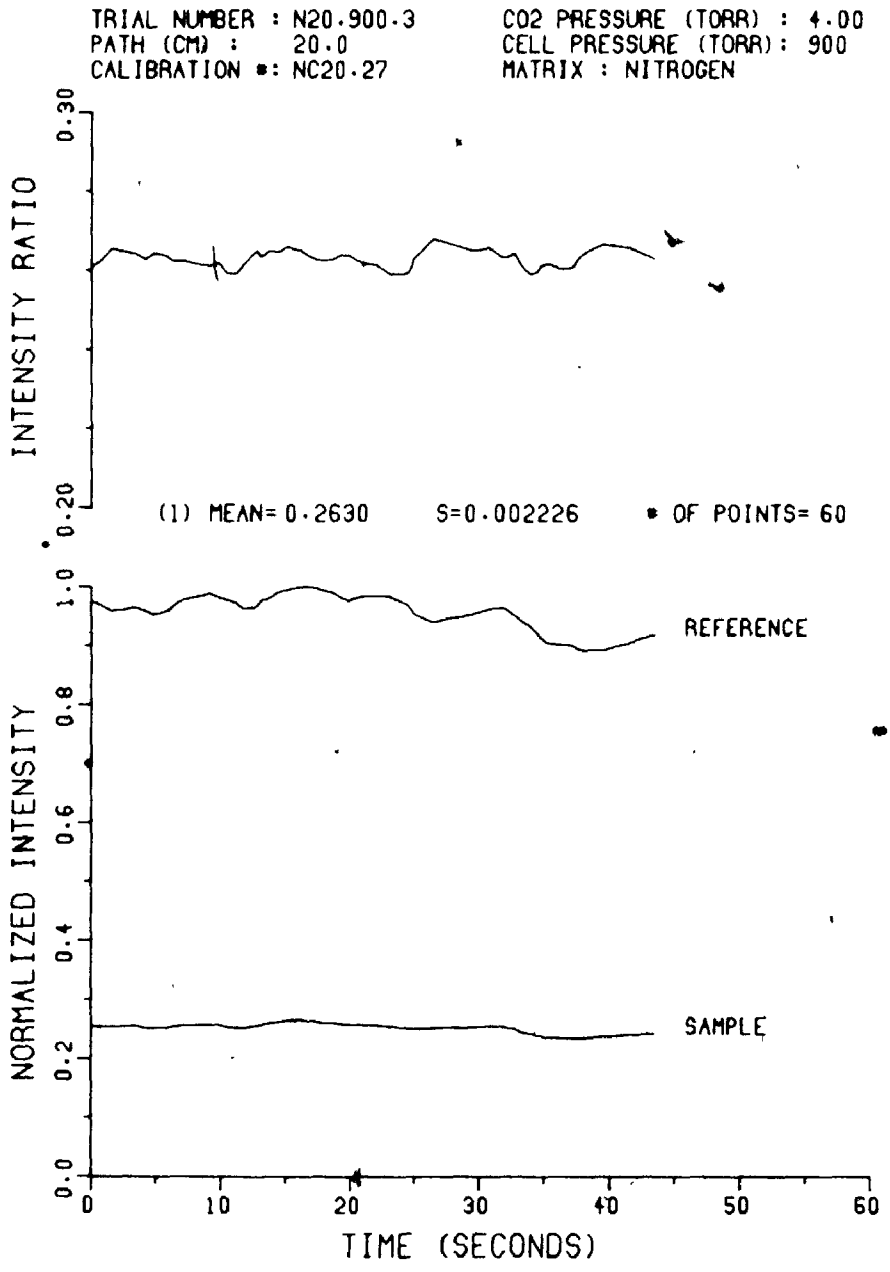
TRIAL NUMBER : N20.900.3
PATH (CM) : 20.0
CALIBRATION #: NC20.27
CO2 PRESSURE (TORR) : 4.00
CELL PRESSURE (TORR): 900
MATRIX : NITROGEN
INTENSITY RATIO
0.30
0.20
(1) MEAN= 0.2630 S=0.002226 # OF POINTS= 60
NORMALIZED INTENSITY
1.0
0.8
0.6
0.4
0.2
0.0
REFERENCE
SAMPLE
0
10
20
30
40
50
60
TIME (SECONDS)

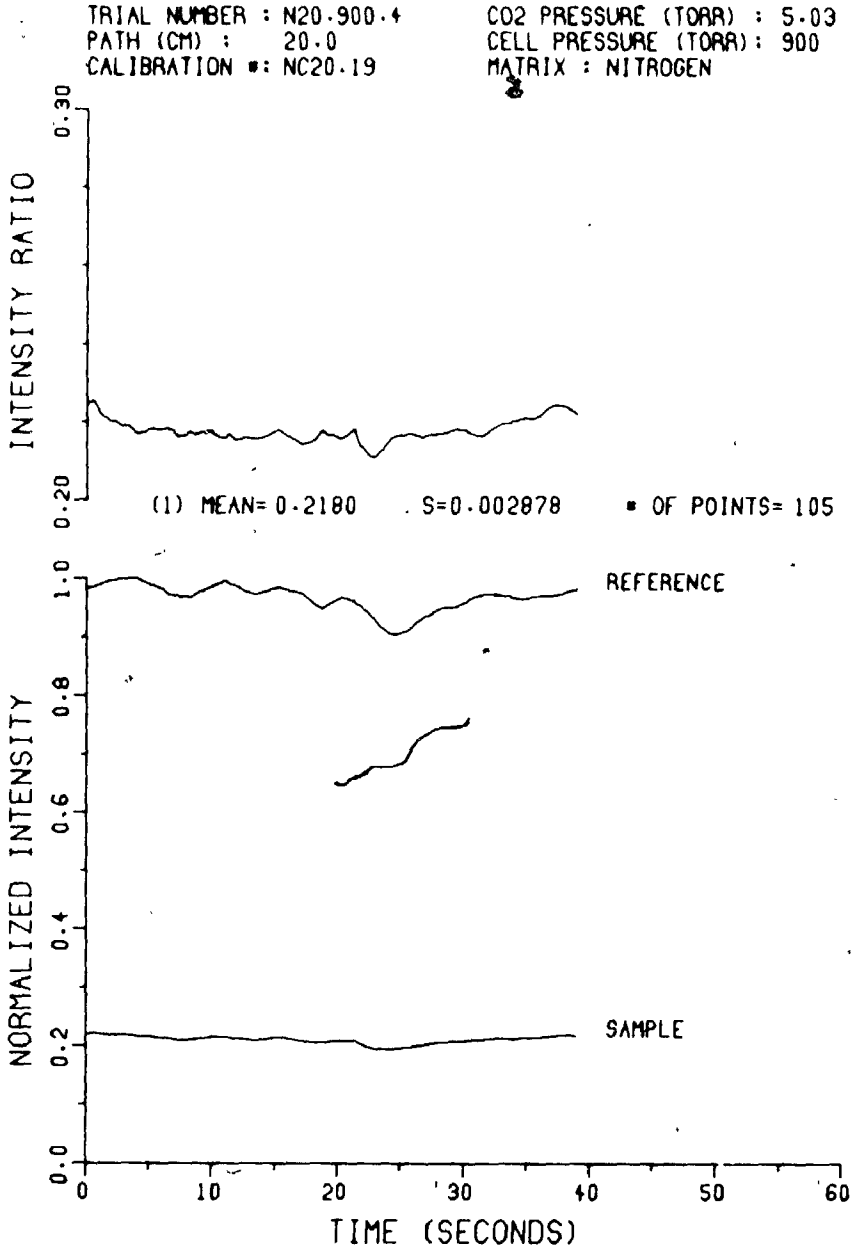
TRIAL NUMBER : N20.900.4
PATH (CM) : 20.0
CALIBRATION #: NC20.19
CO2 PRESSURE (TORR) : 5.03
CELL PRESSURE (TORR): 900
MATRIX : NITROGEN
INTENSITY RATIO
0.30
0.20
(1) MEAN= 0.2180 S=0.002878 # OF POINTS= 105
NORMALIZED INTENSITY
1.0
0.8
0.6
0.4
0.2
0.0
REFERENCE
SAMPLE
0
10
20
30
40
50
60
TIME (SECONDS)

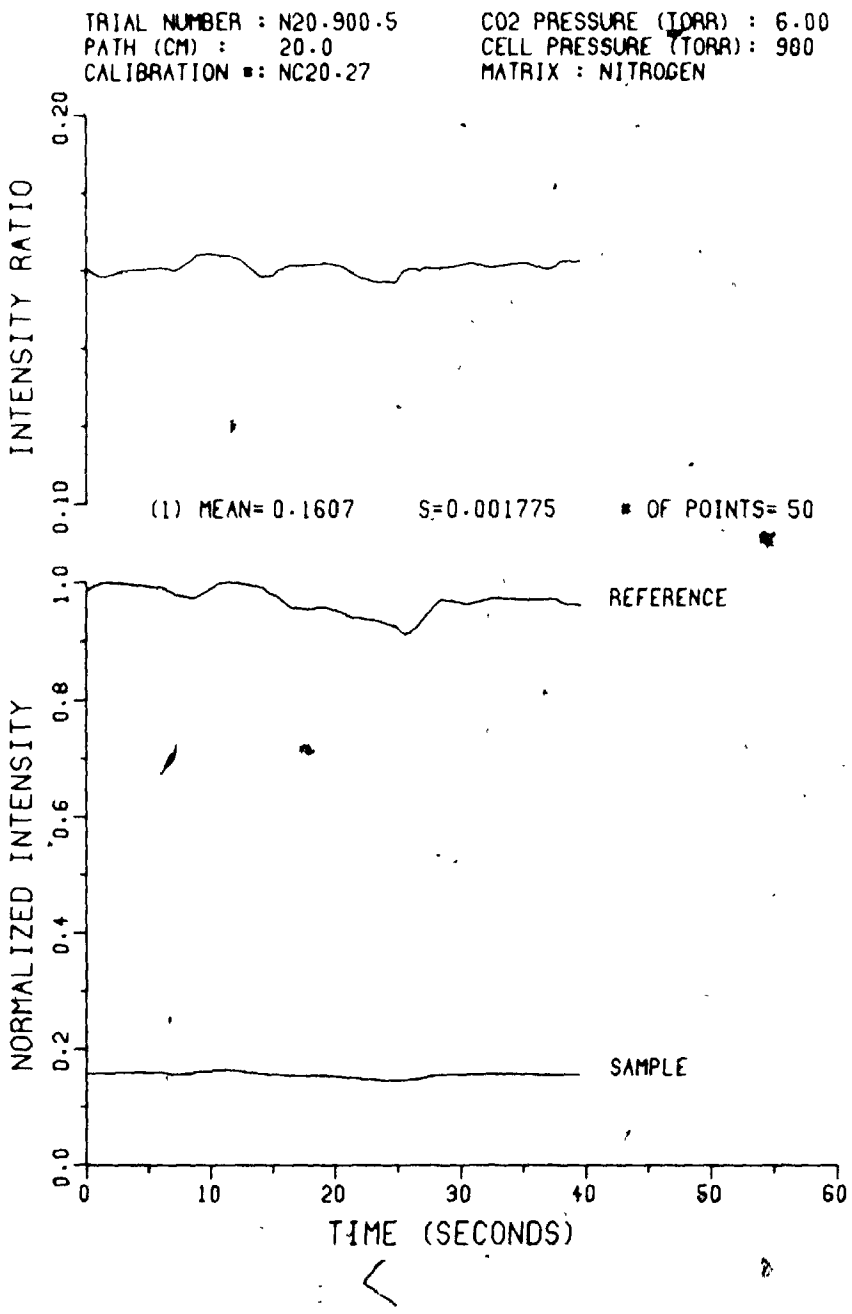
TRIAL NUMBER : N20.900.5
PATH (CM) : 20.0
CALIBRATION #: NC20.27
CO2 PRESSURE (TORR) : 6.00
CELL PRESSURE (TORR): 980
MATRIX : NITROGEN
INTENSITY RATIO
0.20
0.10
(1) MEAN= 0.1607 S=0.001775 # OF POINTS= 50
NORMALIZED INTENSITY
1.0
0.8
0.6
0.4
0.2
0.0
REFERENCE
SAMPLE
0
10
20
30
40
50
60
TIME (SECONDS)

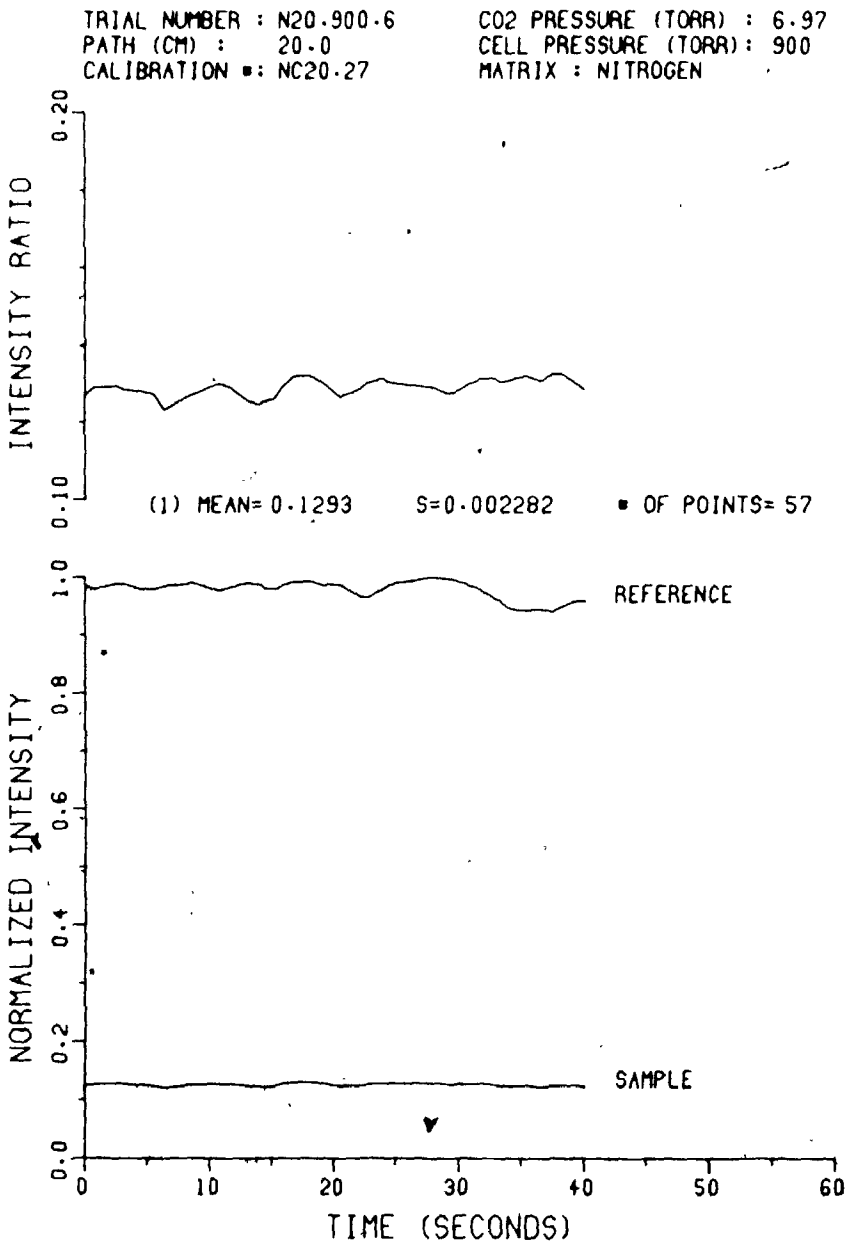
TRIAL NUMBER : N20.900.6
PATH (CM) : 20.0
CALIBRATION #: NC20.27
CO2 PRESSURE (TORR) : 6.97
CELL PRESSURE (TORR): 900
MATRIX : NITROGEN
INTENSITY RATIO
0.20
0.10
(1) MEAN= 0.1293 S=0.002282 # OF POINTS= 57
NORMALIZED INTENSITY
1.0
0.8
0.6
0.4
0.2
0.0
REFERENCE
SAMPLE
0
10
20
30
40
50
60
TIME (SECONDS)

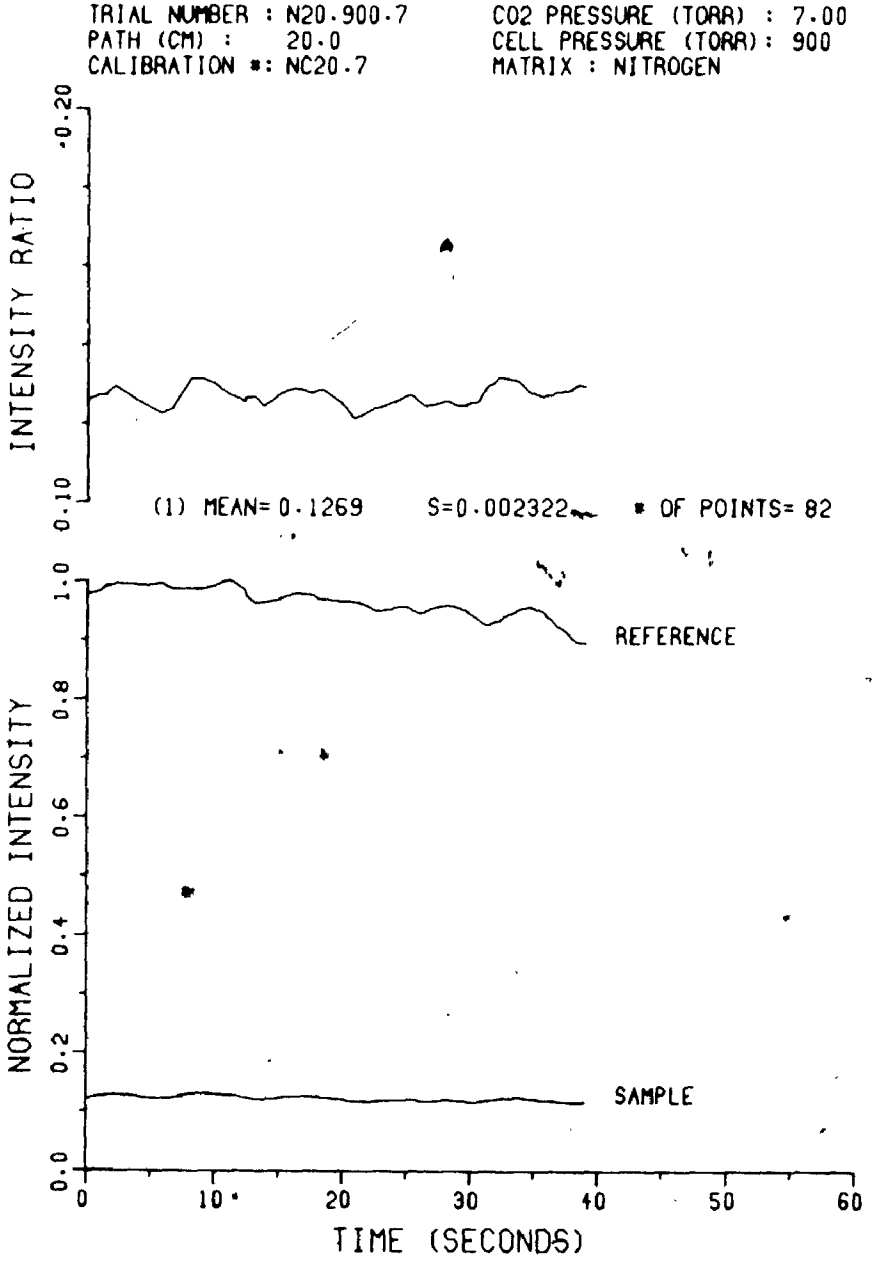
TRIAL NUMBER : N20.900.7
PATH (CM) : 20.0
CALIBRATION #: NC20.7
CO2 PRESSURE (TORR) : 7.00
CELL PRESSURE (TORR): 900
MATRIX : NITROGEN
INTENSITY RATIO
0.20
0.10
(1) MEAN= 0.1269
S=0.002322
# OF POINTS= 82
NORMALIZED INTENSITY
1.0
0.8
0.6
0.4
0.2
0.0
REFERENCE
SAMPLE
0
10
20
30
40
50
60
TIME (SECONDS)

G.3.2. Pathlength - 2.0 cm

Calibration Files

Trial Numbers: NC2.1-NC2.2

Remote Gain: Sample (G_S): 1 (V/V)

FSD_S: 2

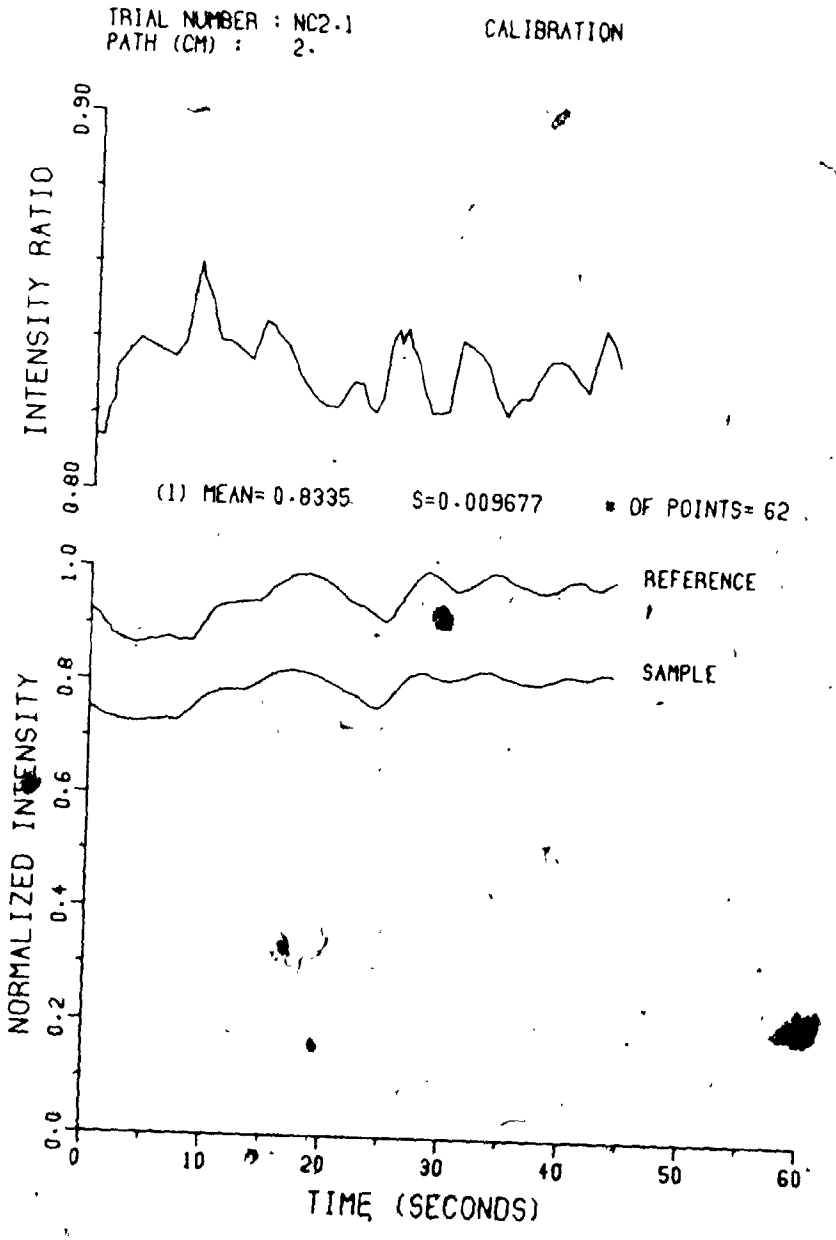

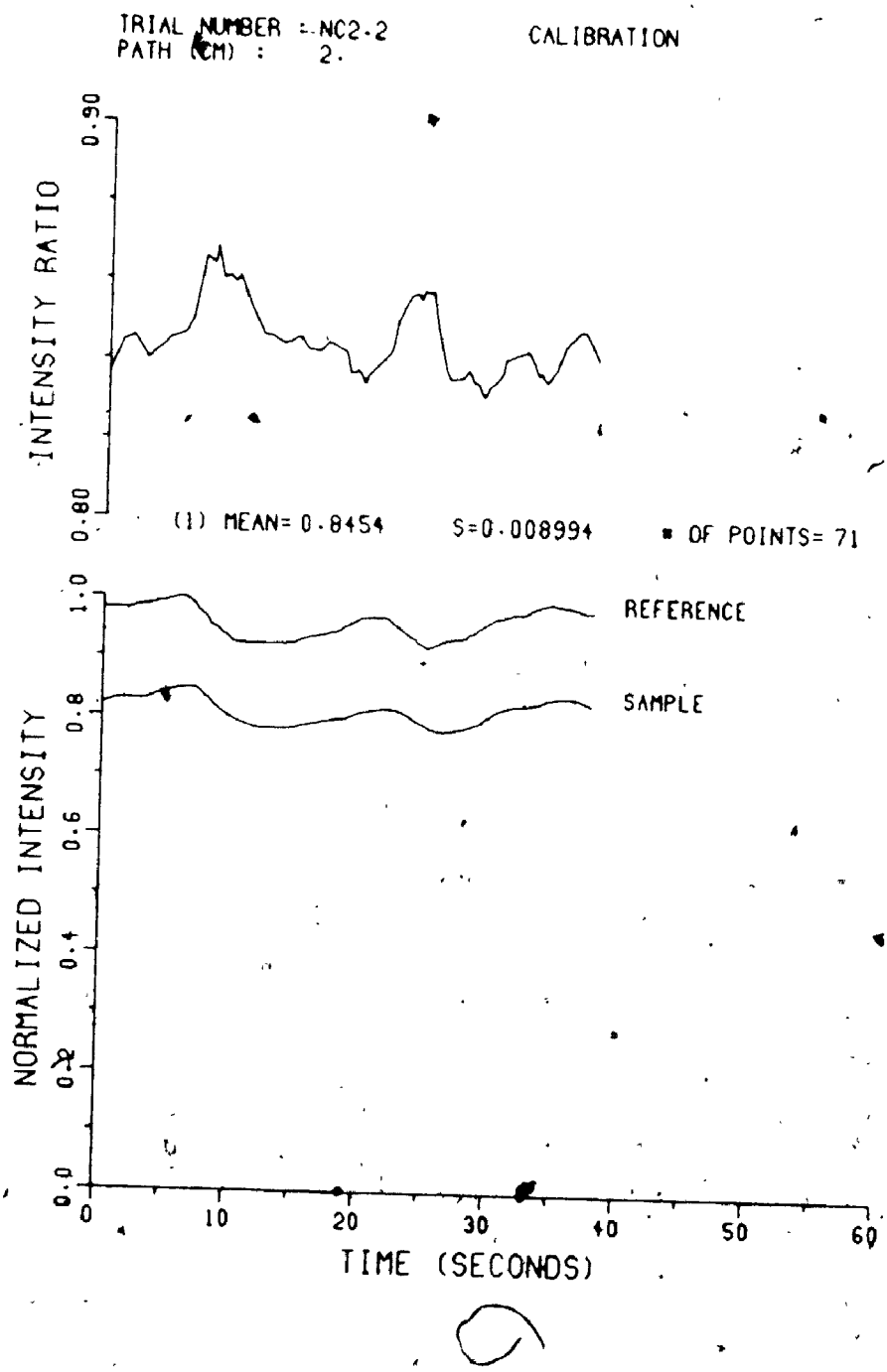
TRIAL NUMBER = NC2-2
PATH (CM) : 2.
CALIBRATION
INTENSITY RATIO
0.90
0.80
(1) MEAN= 0.8454
S=0.008994
# OF POINTS= 71
REFERENCE
SAMPLE
NORMALIZED INTENSITY
1.0
0.8
0.6
0.4
0.2
0.0
0
10
20
30
40
50
60
TIME (SECONDS)

Data Files - Total Pressure: 760 Torr

Trial Numbers: N2.760.1-N2.760.7

Remote Gain: Sample (G_s): 1 (V/V)

FSD_s: 2

Trial Numbers: N2.760.8-N2.760.10

Remote Gain: Sample (G_s): 1 (V/V)

FSD_s: 1

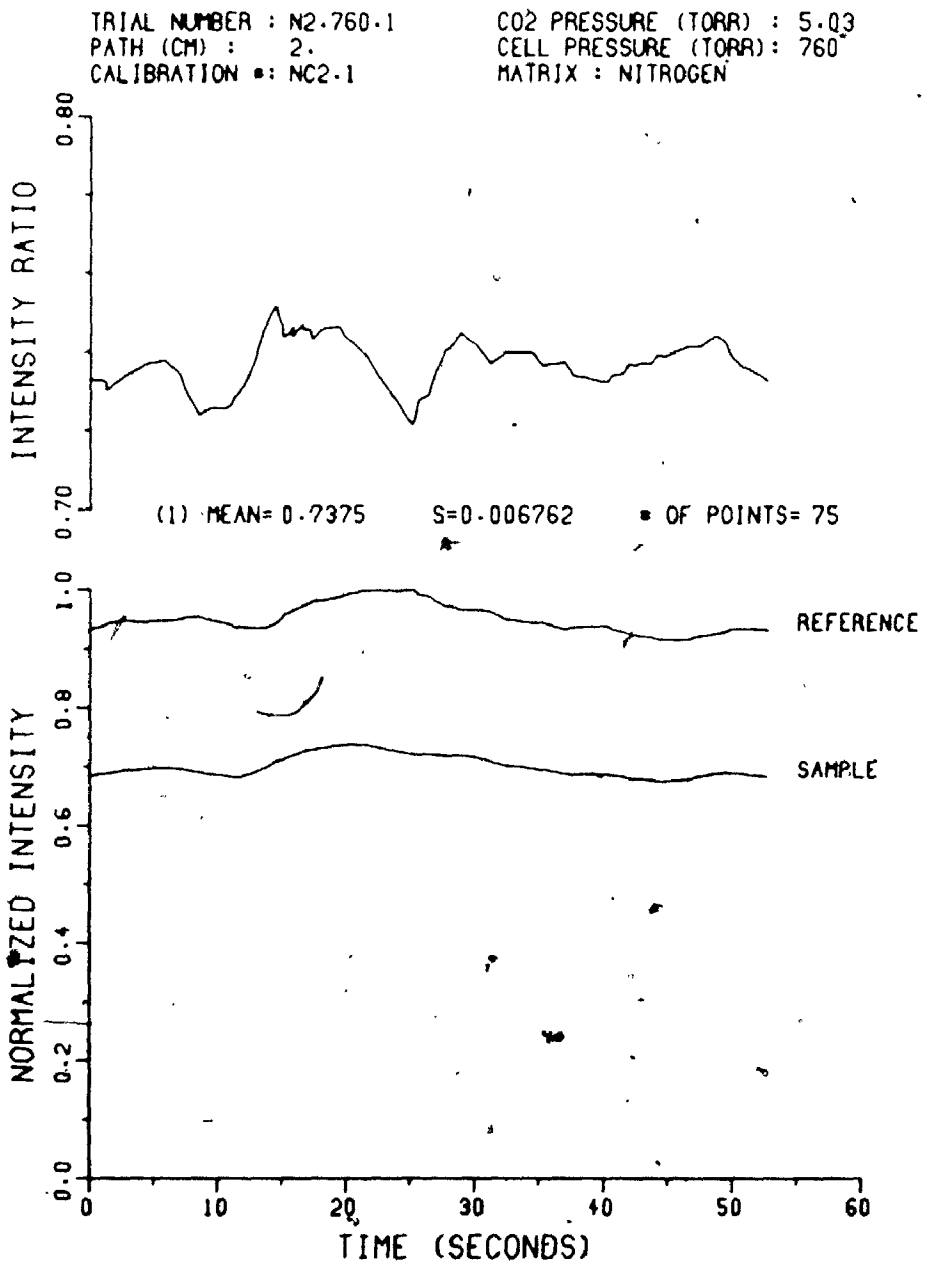
TRIAL NUMBER : N2·760·1
PATH (CM) : 2.
CALIBRATION #: NC2·1
CO2 PRESSURE (TORR) : 5.03
CELL PRESSURE (TORR): 760
MATRIX : NITROGEN
INTENSITY RATIO
0.80
0.70
(1) MEAN= 0·7375 S=0·006762 # OF POINTS= 75
NORMALIZED INTENSITY
1.0
0.8
0.6
0.4
0.2
0.0
REFERENCE
SAMPLE
0
10
20
30
40
50
60
TIME (SECONDS)

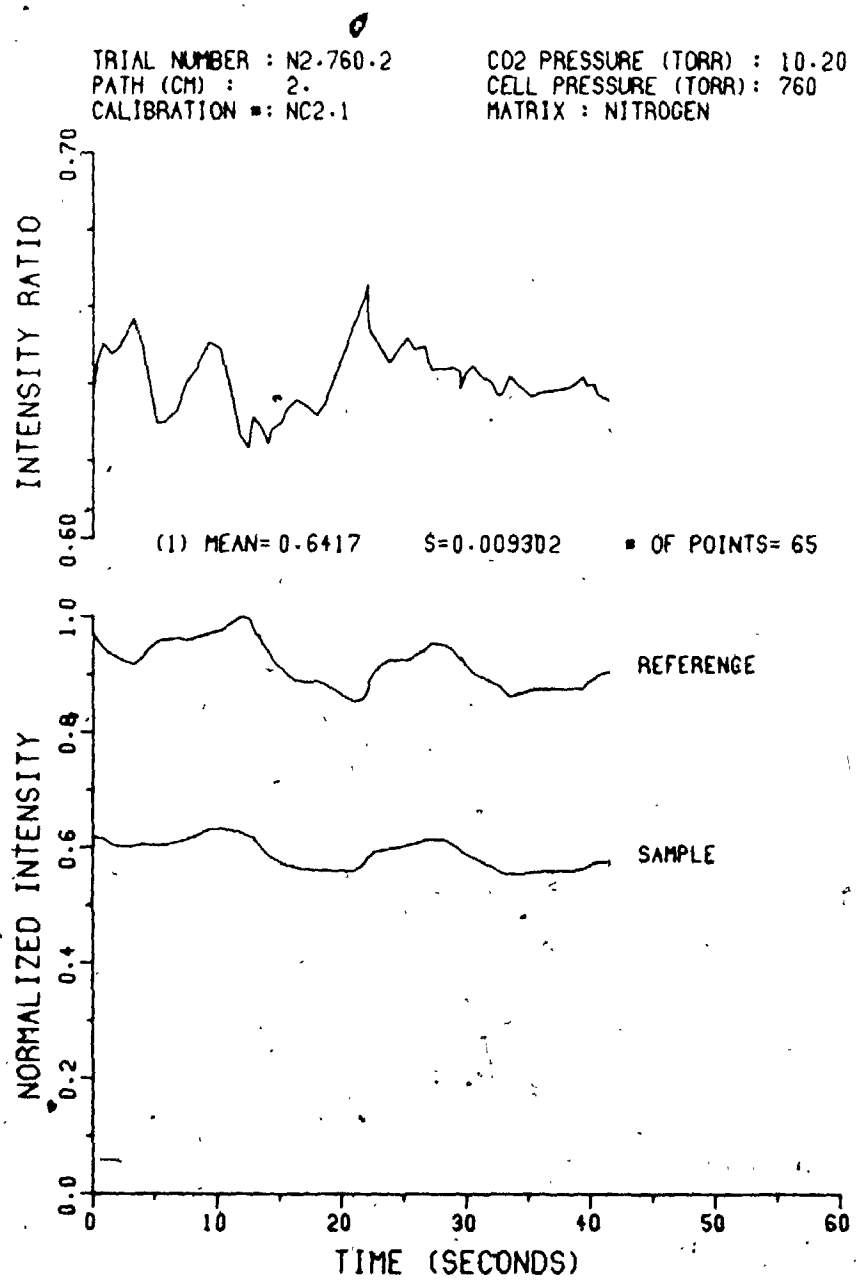
TRIAL NUMBER : N2·760·2
PATH (CM) : 2.
CALIBRATION #: NC2·1
CO2 PRESSURE (TORR) : 10·20
CELL PRESSURE (TORR): 760
MATRIX : NITROGEN
INTENSITY RATIO
0.70
0.60
(1) MEAN= 0.6417 S=0.009302 # OF POINTS= 65
NORMALIZED INTENSITY
1.0
0.8
0.6
0.4
0.2
0.0
REFERENCE
SAMPLE
0
10
20
30
40
50
60
TIME (SECONDS)

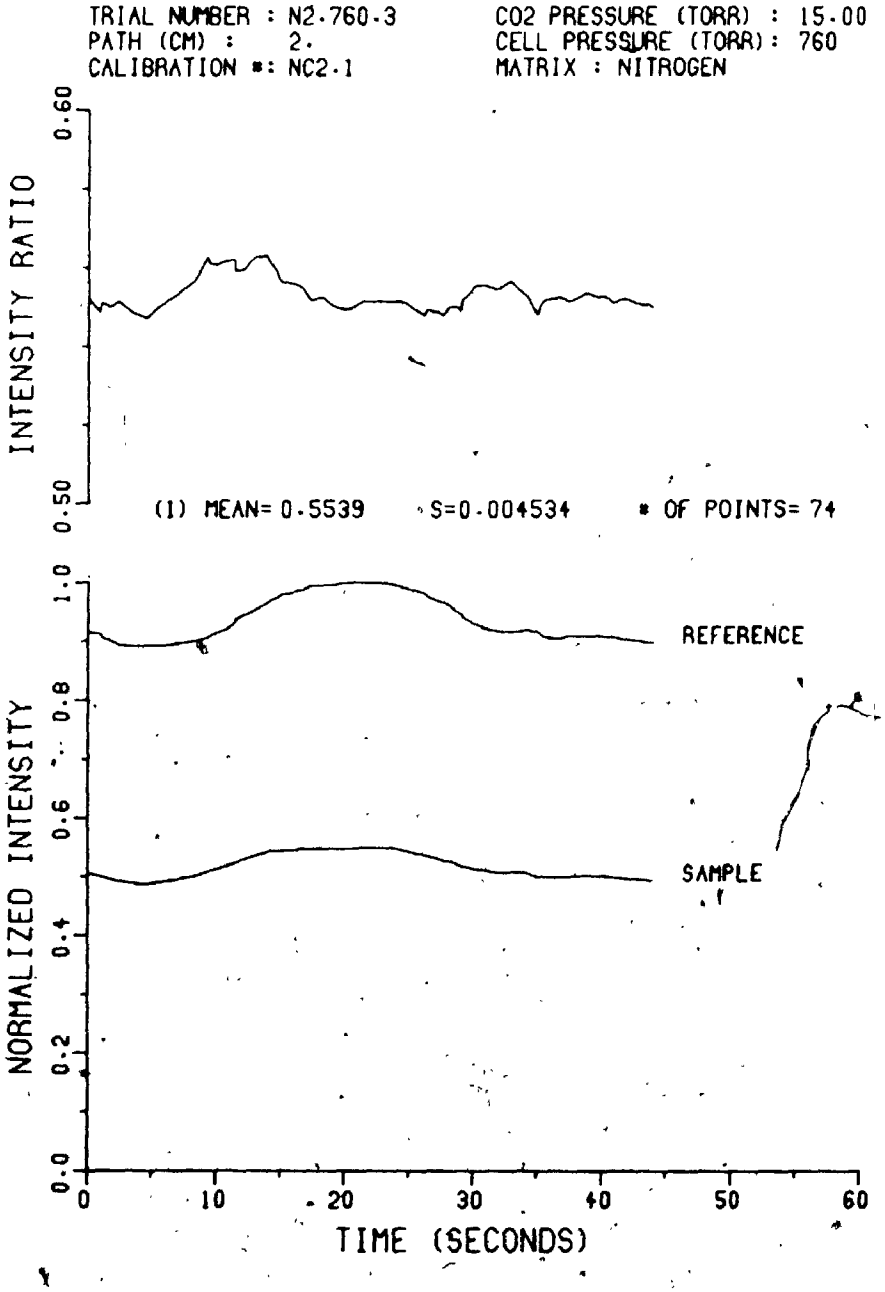
TRIAL NUMBER : N2.760-3
PATH (CM) : 2.
CALIBRATION #: NC2.1
CO2 PRESSURE (TORR) : 15.00
CELL PRESSURE (TORR): 760
MATRIX : NITROGEN
INTENSITY RATIO
0.60
0.50
(1) MEAN= 0.5539 S=0.004534 # OF POINTS= 74
NORMALIZED INTENSITY
1.0
0.8
0.6
0.4
0.2
0.0
REFERENCE
SAMPLE
0
10
20
30
40
50
60
TIME (SECONDS)

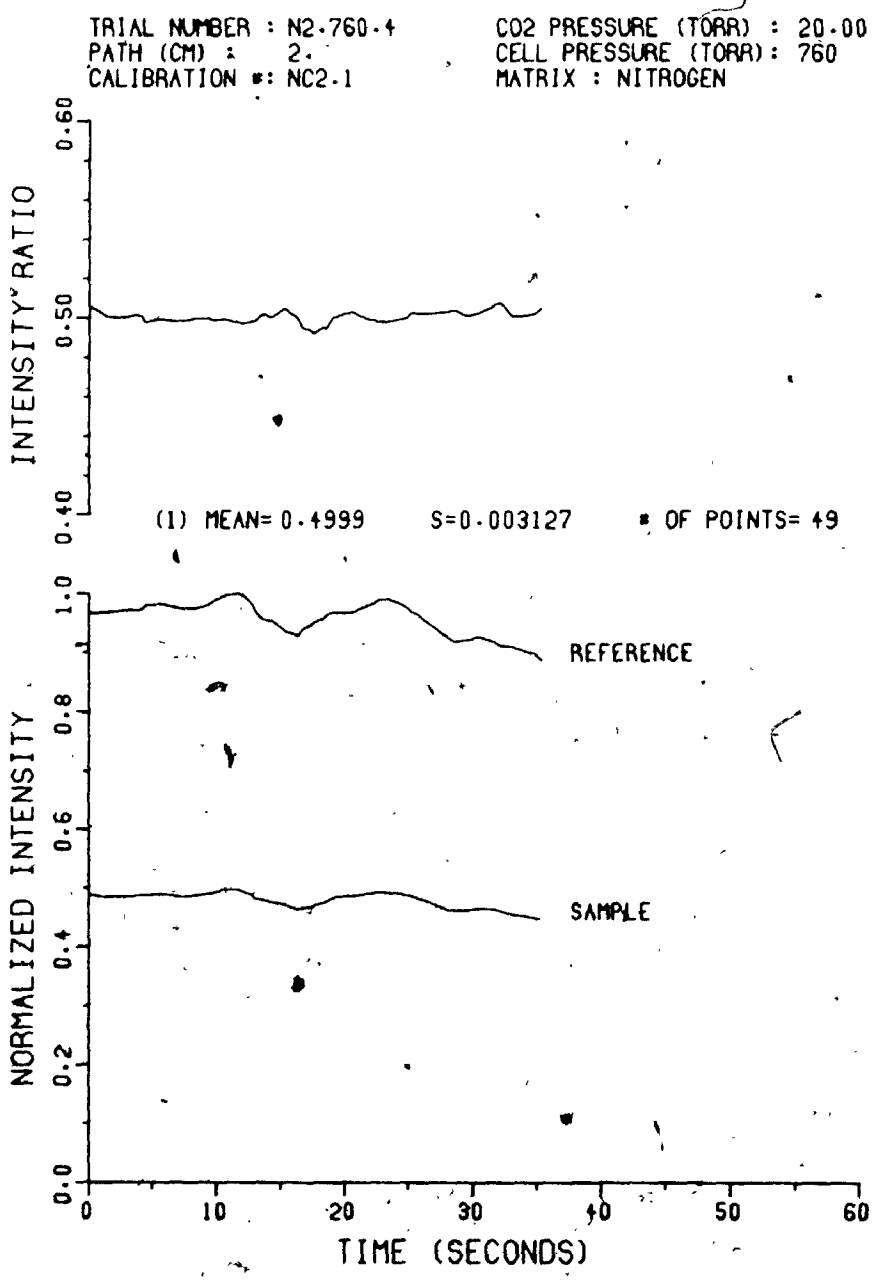
TRIAL NUMBER : N2-760-4
PATH (CM) : 2.
CALIBRATION #: NC2-1
CO2 PRESSURE (TORR) : 20.00
CELL PRESSURE (TORR): 760
MATRIX : NITROGEN
INTENSITY RATIO
0.60
0.50
0.40
(1) MEAN= 0.4999 S=0.003127 # OF POINTS= 49
NORMALIZED INTENSITY
1.0
0.8
0.6
0.4
0.2
0.0
REFERENCE
SAMPLE
0
10
20
30
40
50
60
TIME (SECONDS)

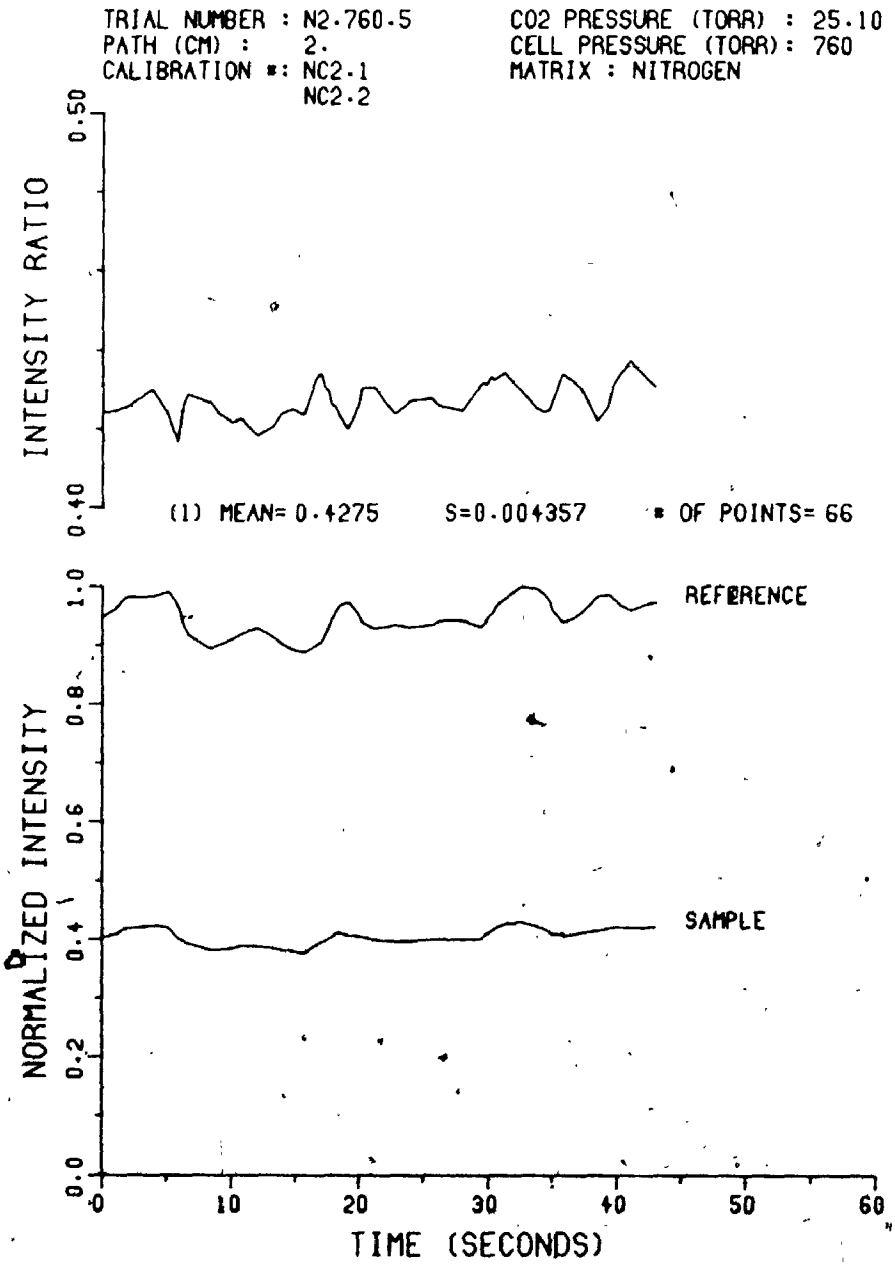
TRIAL NUMBER : N2.760.5
PATH (CM) : 2.
CALIBRATION #: NC2.1
NC2.2
CO2 PRESSURE (TORR) : 25.10
CELL PRESSURE (TORR): 760
MATRIX : NITROGEN
INTENSITY RATIO
0.50
0.40
(1) MEAN= 0.4275 S=0.004357 # OF POINTS= 66
NORMALIZED INTENSITY
1.0
0.8
0.6
0.4
0.2
0.0
REFERENCE
SAMPLE
0
10
20
30
40
50
60
TIME (SECONDS)

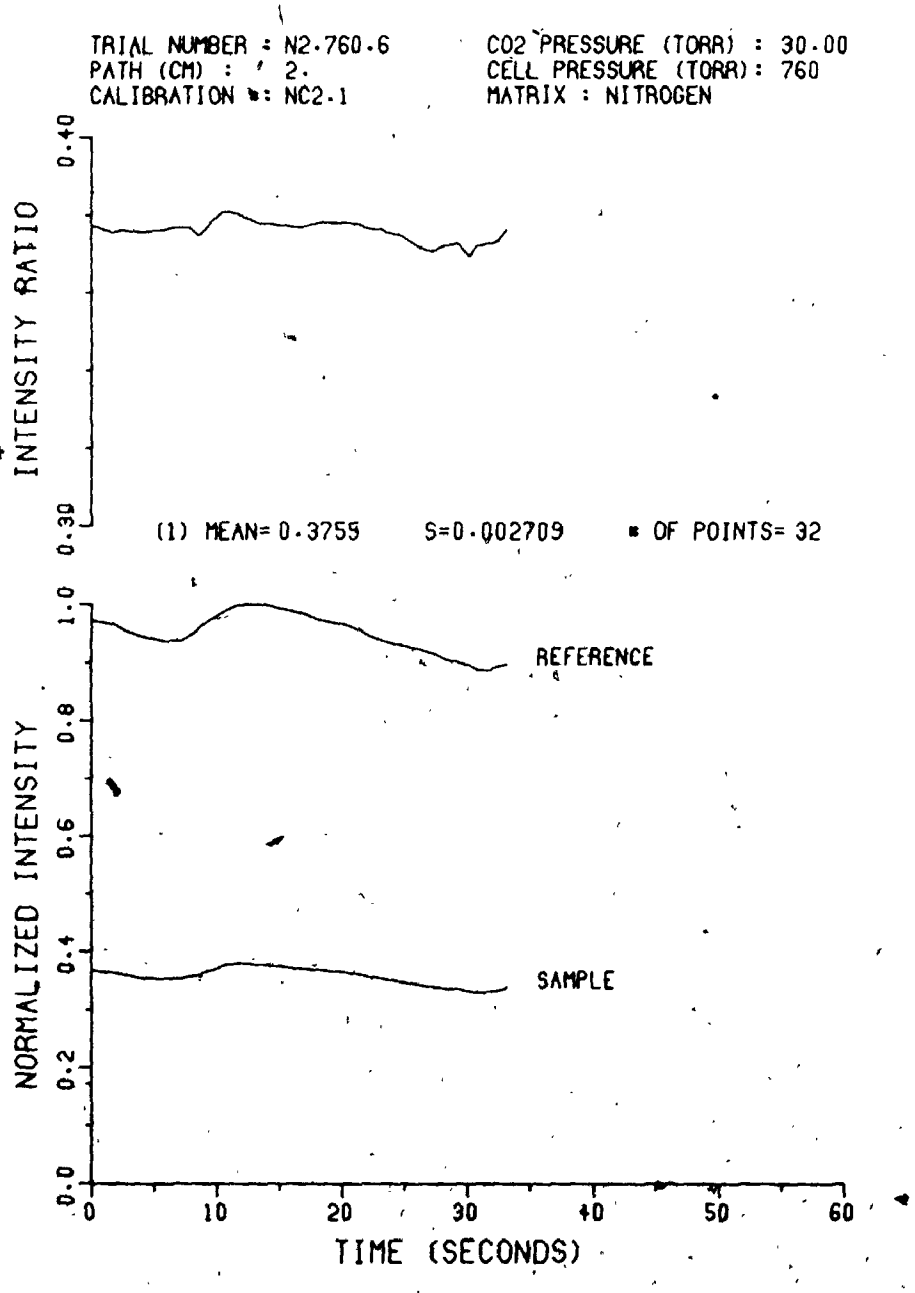
TRIAL NUMBER : N2.760.6
PATH (CM) : 2.
CALIBRATION : NC2.1
CO2 PRESSURE (TORR) : 30.00
CELL PRESSURE (TORR): 760
MATRIX : NITROGEN
INTENSITY RATIO
0.40
0.30
(1) MEAN= 0.3755 S=0.002709 # OF POINTS= 32
NORMALIZED INTENSITY
1.0
0.8
0.6
0.4
0.2
0.0
REFERENCE
SAMPLE
0
10
20
30
40
50
60
TIME (SECONDS)

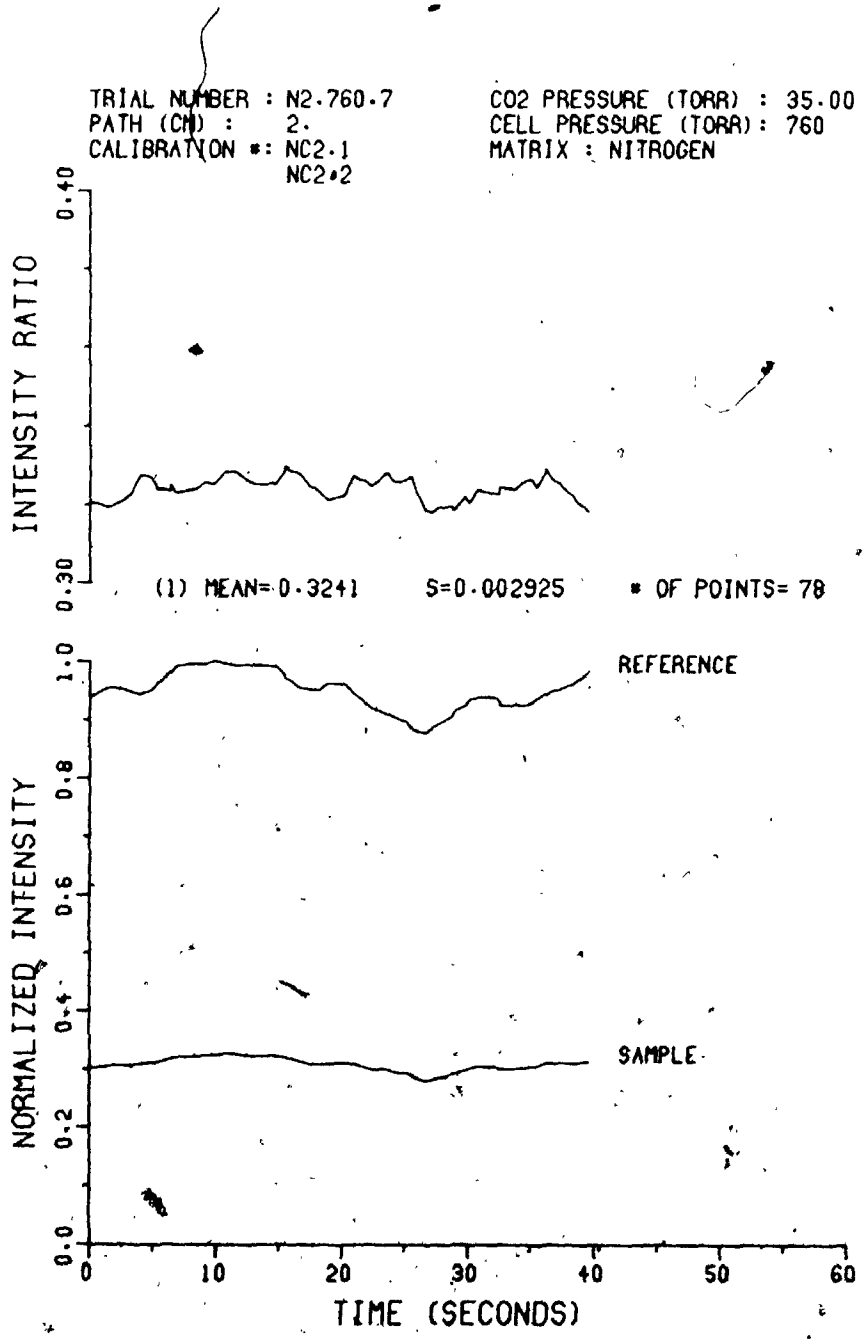
TRIAL NUMBER : N2.760.7
PATH (CM) : 2.
CALIBRATION #: NC2.1
NC2.2
CO2 PRESSURE (TORR) : 35.00
CELL PRESSURE (TORR): 760
MATRIX : NITROGEN
INTENSITY RATIO
0.40
0.30
(1) MEAN=0.3241 S=0.002925 # OF POINTS= 78
NORMALIZED INTENSITY
1.0
0.8
0.6
0.4
0.2
0.0
REFERENCE
SAMPLE
0
10
20
30
40
50
60
TIME (SECONDS)

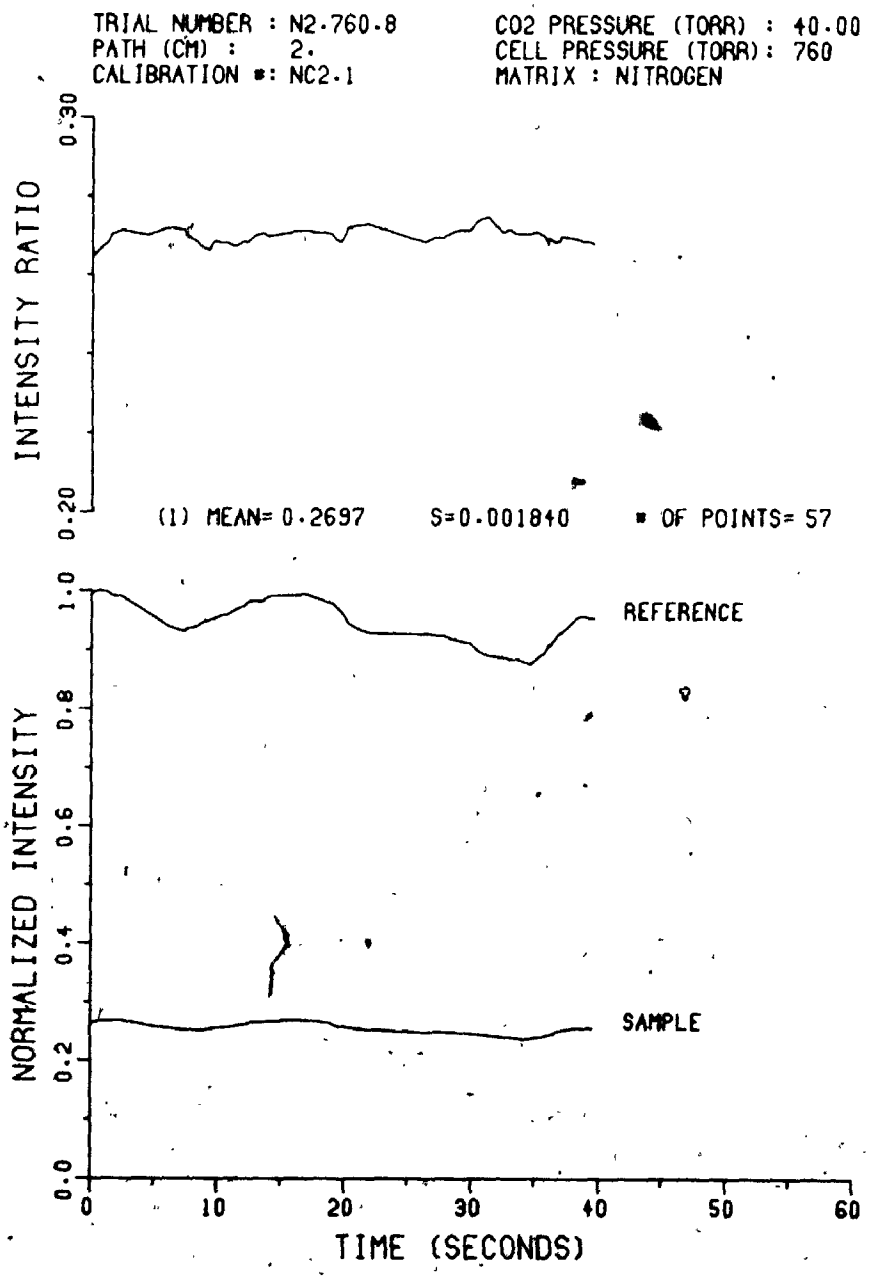
TRIAL NUMBER : N2-760-8
PATH (CM) : 2.
CALIBRATION #: NC2-1
CO2 PRESSURE (TORR) : 40.00
CELL PRESSURE (TORR): 760
MATRIX : NITROGEN
INTENSITY RATIO
0.30
0.20
(1) MEAN= 0.2697 S=0.001840 # OF POINTS= 57
NORMALIZED INTENSITY
1.0
0.8
0.6
0.4
0.2
0.0
REFERENCE
SAMPLE
0
10
20
30
40
50
60
TIME (SECONDS)

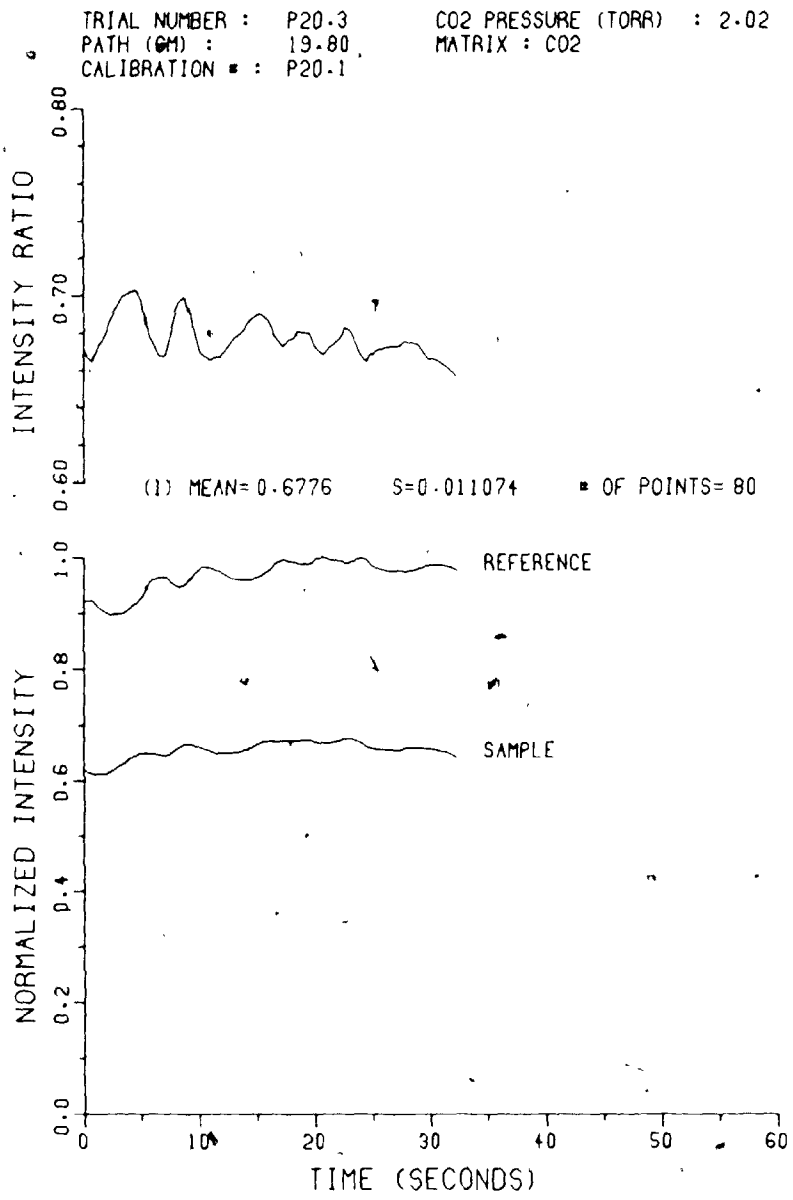
TRIAL NUMBER : P20.3
PATH (CM) : 19.80
CALIBRATION # : P20.1
CO2 PRESSURE (TORR) : 2.02
MATRIX : CO2
INTENSITY RATIO
0.80
0.70
0.60
(1) MEAN= 0.6776 S=0.011074 # OF POINTS= 80
NORMALIZED INTENSITY
1.0
0.8
0.6
0.4
0.2
0.0
REFERENCE
SAMPLE
0
10
20
30
40
50
60
TIME (SECONDS)

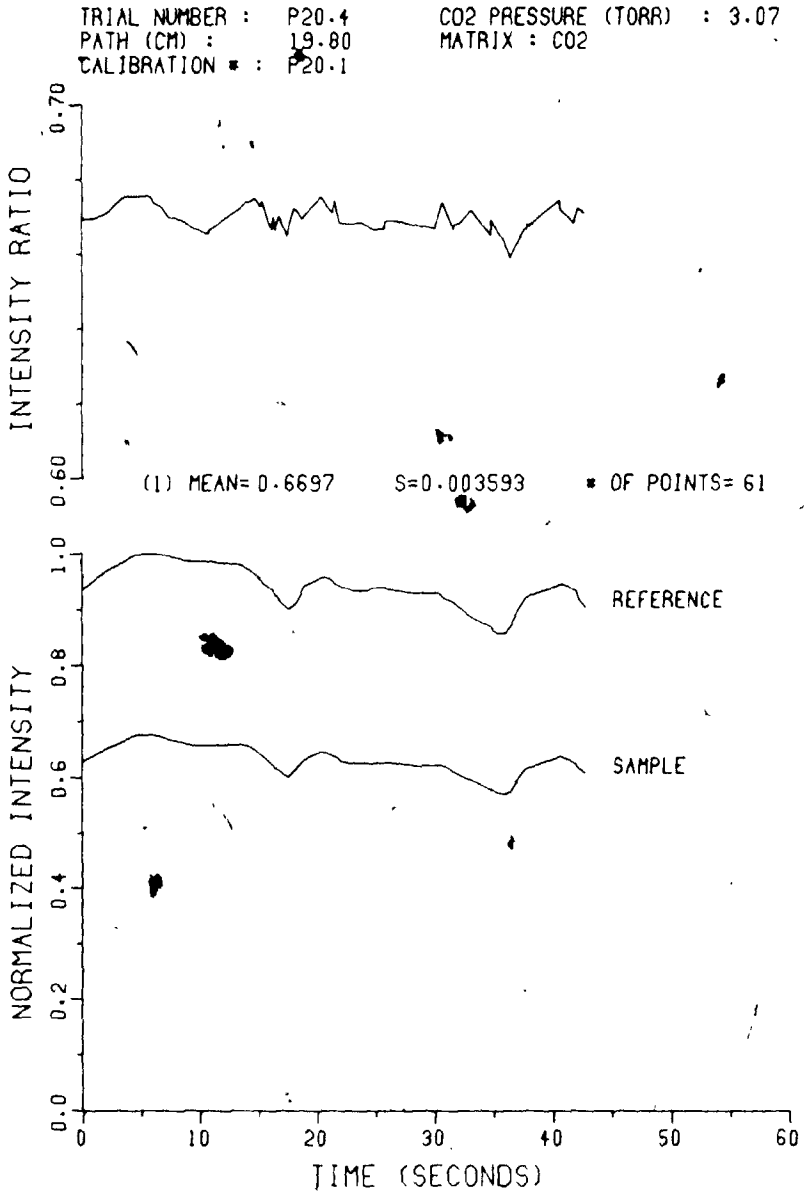
TRIAL NUMBER : P20.4
PATH (CM) : 19.80
CALIBRATION # : P20.1
CO2 PRESSURE (TORR) : 3.07
MATRIX : CO2
INTENSITY RATIO
0.70
0.60
(1) MEAN= 0.6697 S=0.003593 # OF POINTS= 61
NORMALIZED INTENSITY
1.0
0.8
0.6
0.4
0.2
0.0
REFERENCE
SAMPLE
0
10
20
30
40
50
60
TIME (SECONDS)

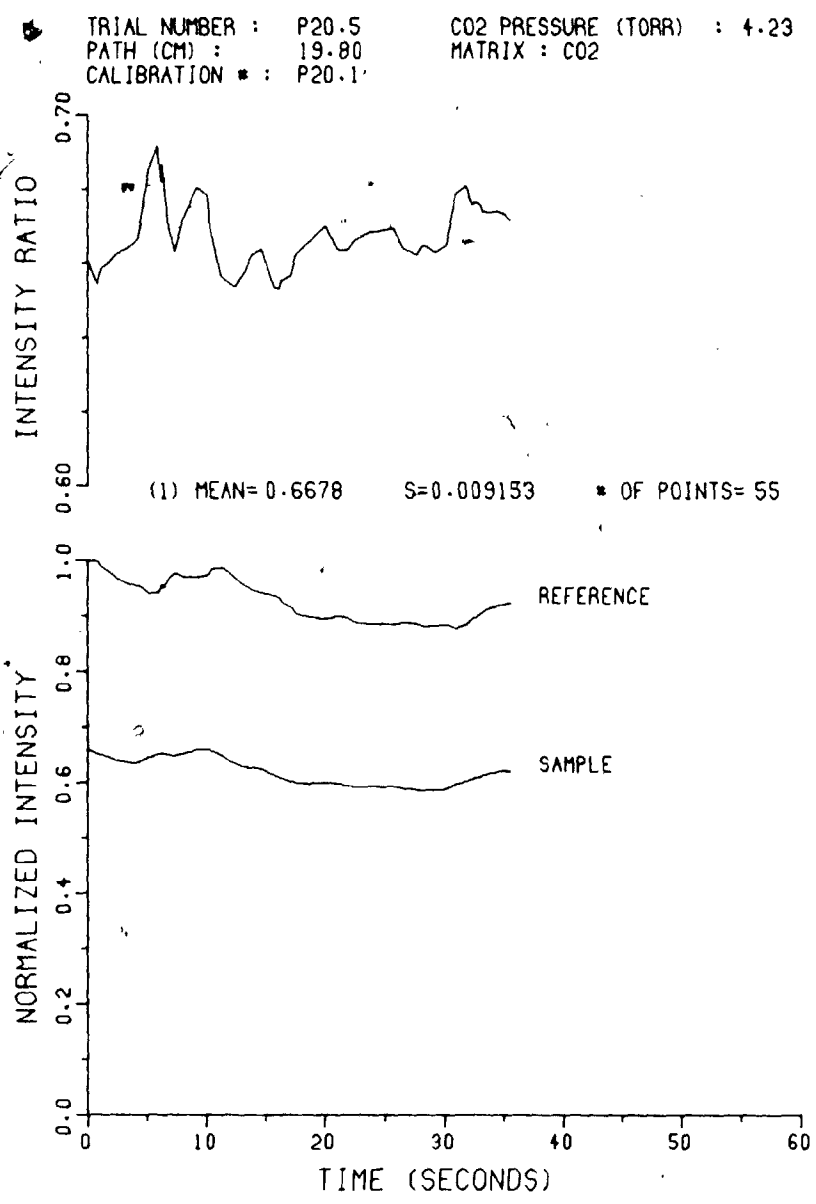
TRIAL NUMBER : P20.5
PATH (CM) : 19.80
CALIBRATION # : P20.1
CO2 PRESSURE (TORR) : 4.23
MATRIX : CO2
INTENSITY RATIO
0.70
0.60
(1) MEAN= 0.6678 S=0.009153 # OF POINTS= 55
NORMALIZED INTENSITY
1.0
0.8
0.6
0.4
0.2
0.0
REFERENCE
SAMPLE
0
10
20
30
40
50
60
TIME (SECONDS)

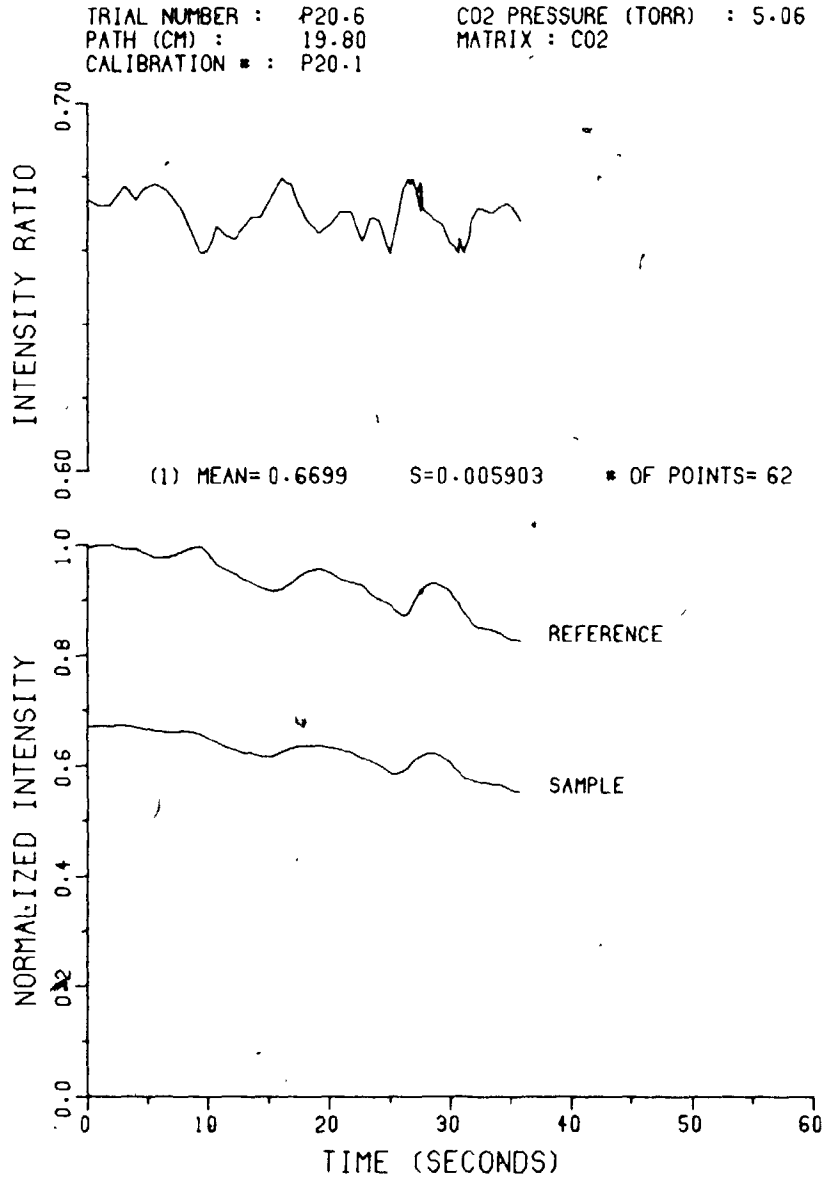
TRIAL NUMBER : P20-6
PATH (CM) : 19.80
CALIBRATION # : P20-1
CO2 PRESSURE (TORR) : 5.06
MATRIX : CO2
INTENSITY RATIO
0.70
0.60
(1) MEAN= 0.6699 S=0.005903 # OF POINTS= 62
NORMALIZED INTENSITY
1.0
0.8
0.6
0.4
0.2
0.0
REFERENCE
SAMPLE
0
10
20
30
40
50
60
TIME (SECONDS)

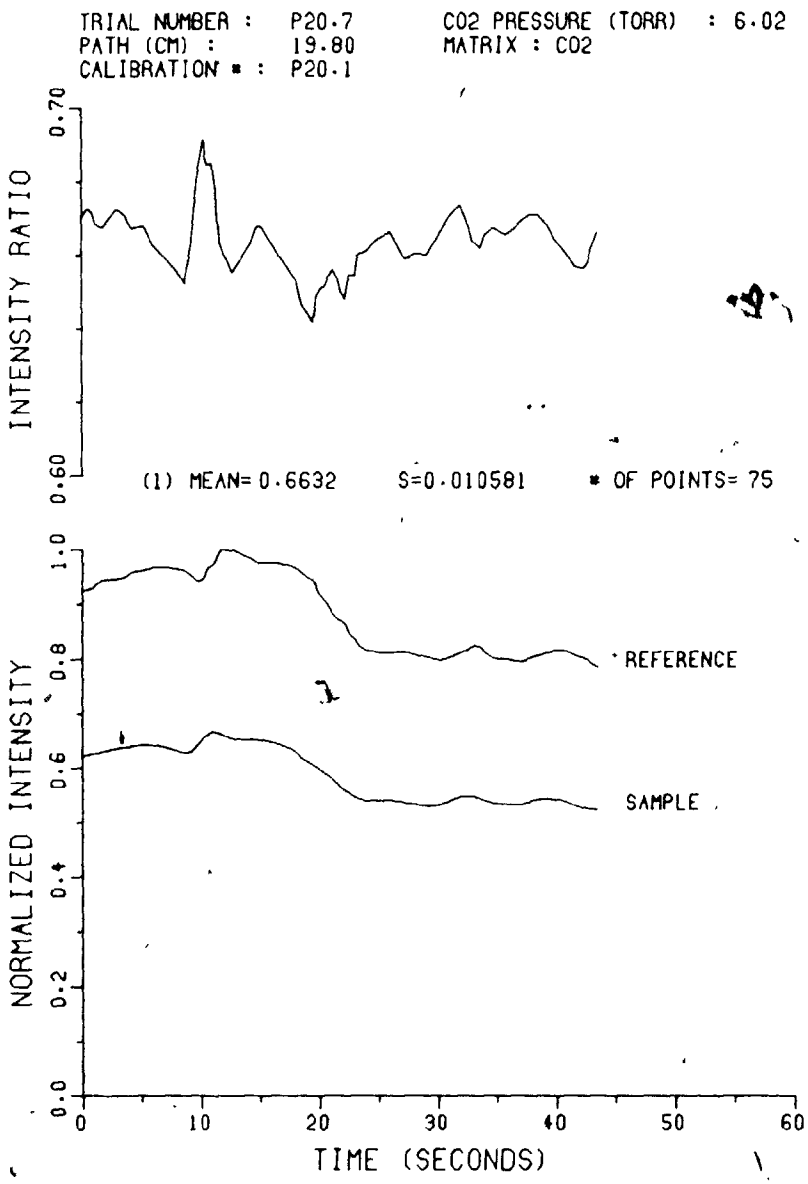
TRIAL NUMBER : P20.7
PATH (CM) : 19.80
CALIBRATION # : P20.1
CO2 PRESSURE (TORR) : 6.02
MATRIX : CO2
INTENSITY RATIO
0.70
0.60
(1) MEAN= 0.6632 S=0.010581 # OF POINTS= 75
NORMALIZED INTENSITY
1.0
0.8
0.6
0.4
0.2
0.0
REFERENCE
SAMPLE
0
10
20
30
40
50
60
TIME (SECONDS)

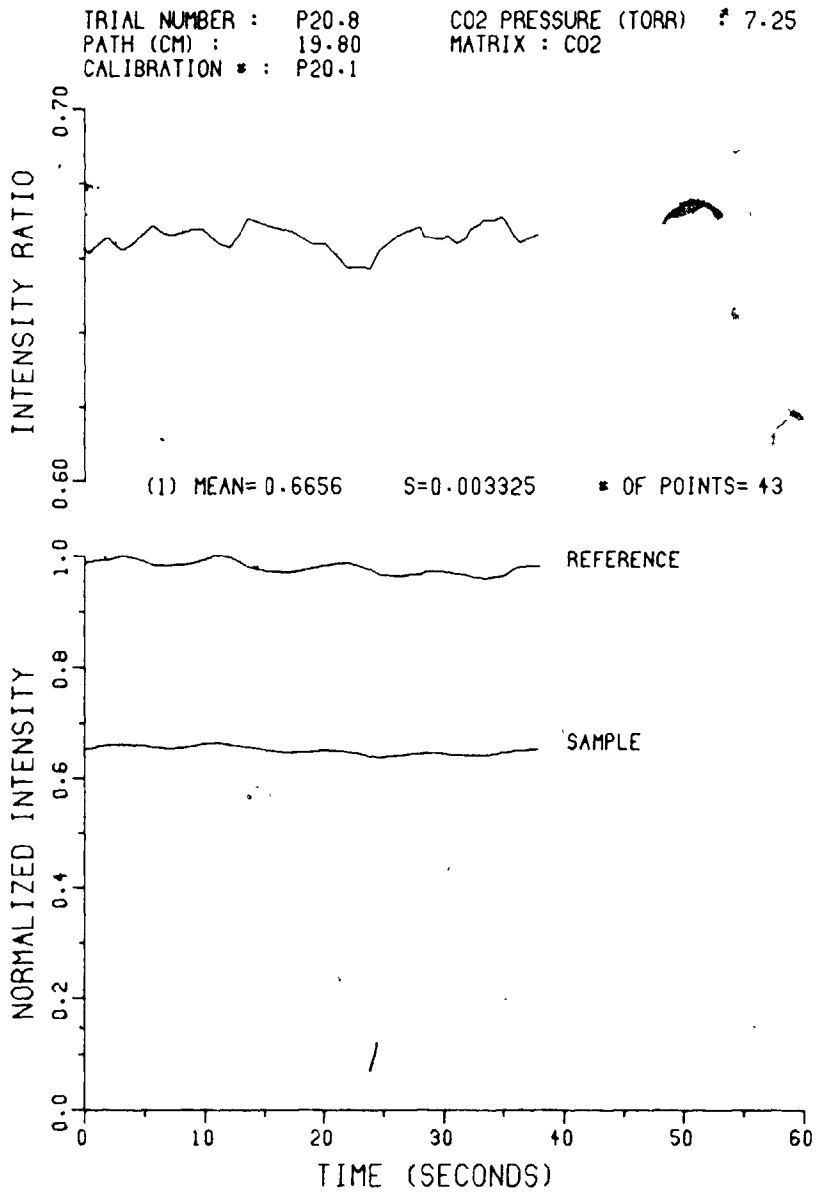
TRIAL NUMBER : P20-8
PATH (CM) : 19.80
CALIBRATION # : P20-1
CO2 PRESSURE (TORR) = 7.25
MATRIX : CO2
INTENSITY RATIO
0.70
0.60
(1) MEAN= 0.6656 S=0.003325 # OF POINTS= 43
REFERENCE
SAMPLE
NORMALIZED INTENSITY
1.0
0.8
0.6
0.4
0.2
0.0
0
10
20
30
40
50
60
TIME (SECONDS)

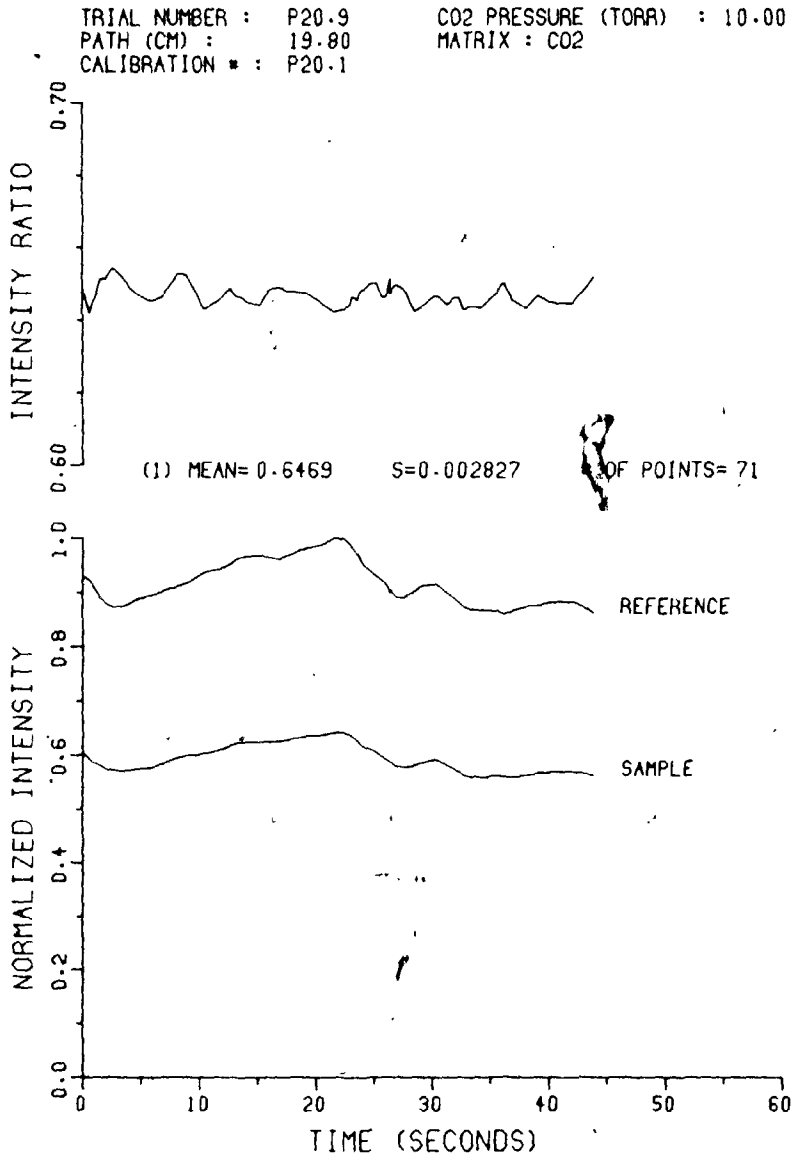
TRIAL NUMBER : P20.9
PATH (CM) : 19.80
CALIBRATION # : P20.1
CO2 PRESSURE (TORR) : 10.00
MATRIX : CO2
INTENSITY RATIO
0.70
0.60
(1) MEAN= 0.6469 S=0.002827 # OF POINTS= 71
NORMALIZED INTENSITY
1.0
0.8
0.6
0.4
0.2
0.0
REFERENCE
SAMPLE
0
10
20
30
40
50
60
TIME (SECONDS)

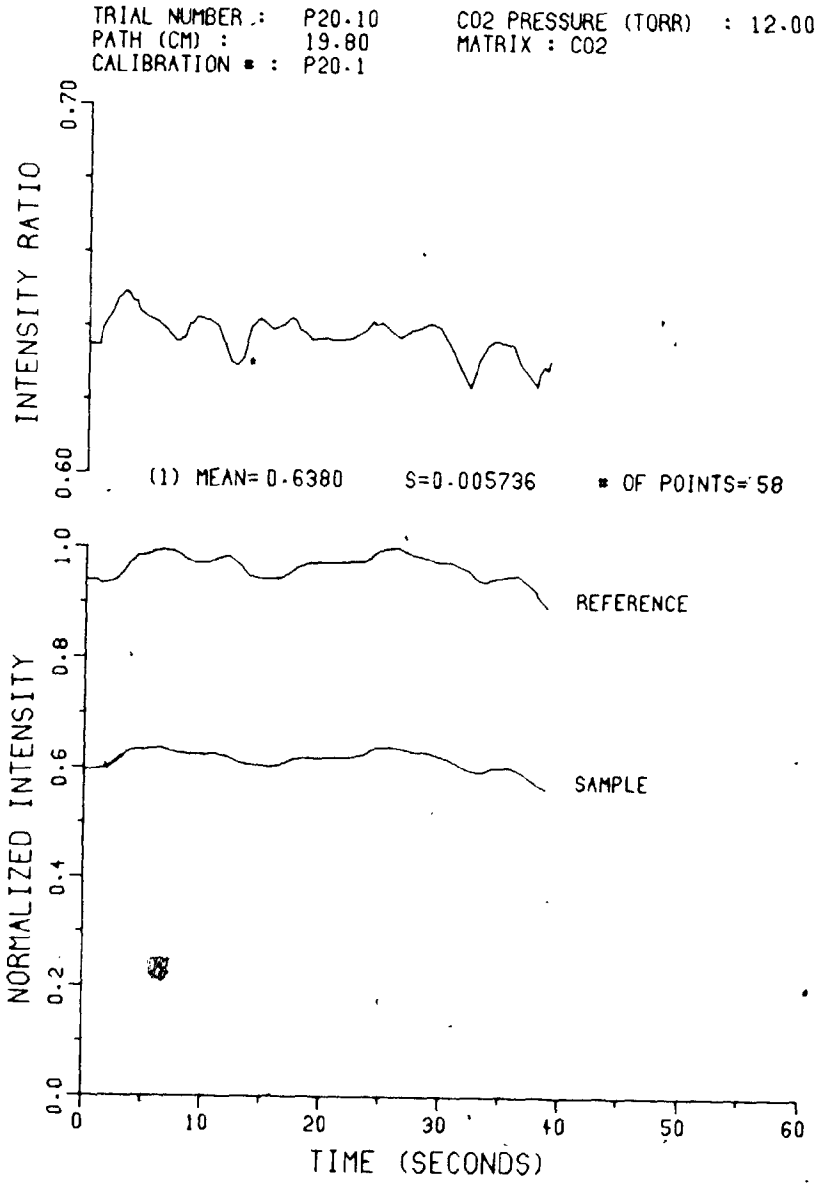
TRIAL NUMBER : P20.10
PATH (CM) : 19.80
CALIBRATION # : P20.1
CO2 PRESSURE (TORR) : 12.00
MATRIX : CO2
INTENSITY RATIO
0.70
0.60
(1) MEAN= 0.6380 S=0.005736 # OF POINTS= 58
NORMALIZED INTENSITY
1.0
0.8
0.6
0.4
0.2
0.0
REFERENCE
SAMPLE
0
10
20
30
40
50
60
TIME (SECONDS)

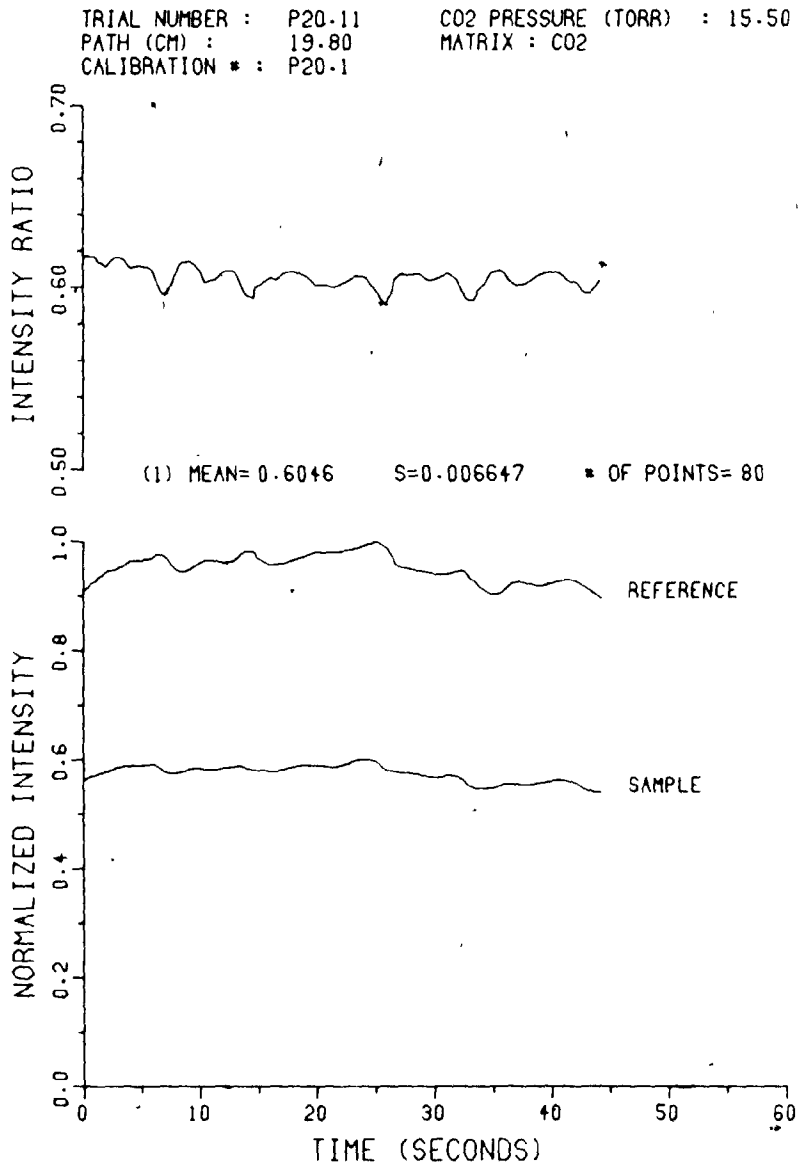
TRIAL NUMBER : P20-11
PATH (CM) : 19.80
CALIBRATION # : P20-1
CO2 PRESSURE (TORR) : 15.50
MATRIX : CO2
INTENSITY RATIO
0.70
0.60
0.50
(1) MEAN= 0.6046 S=0.006647 # OF POINTS= 80
NORMALIZED INTENSITY
1.0
0.8
0.6
0.4
0.2
0.0
REFERENCE
SAMPLE
0
10
20
30
40
50
60
TIME (SECONDS)

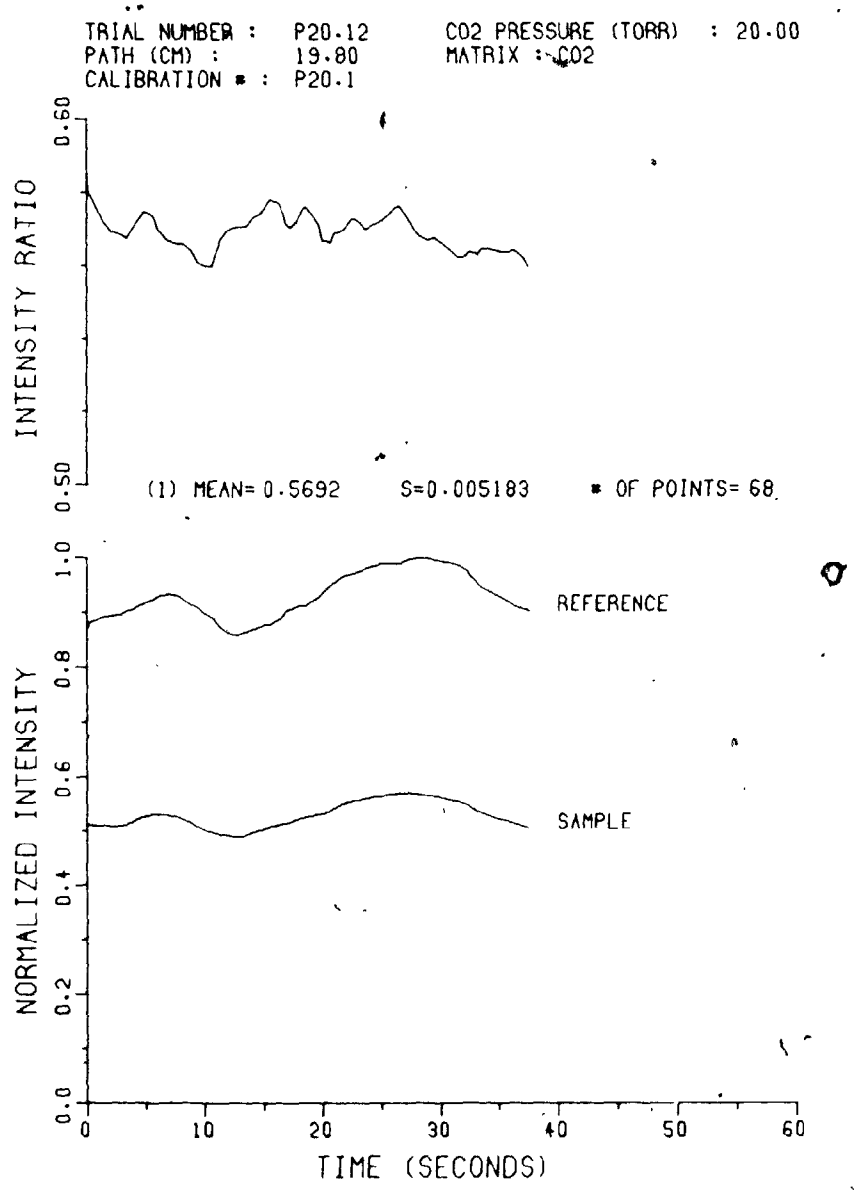
TRIAL NUMBER : P20.12
CO2 PRESSURE (TORR) : 20.00
PATH (CM) : 19.80
MATRIX : CO2
CALIBRATION # : P20.1
INTENSITY RATIO
0.60
0.50
(1) MEAN= 0.5692 S=0.005183 # OF POINTS= 68
NORMALIZED INTENSITY
1.0
0.8
0.6
0.4
0.2
0.0
REFERENCE
SAMPLE
0
10
20
30
40
50
60
TIME (SECONDS)

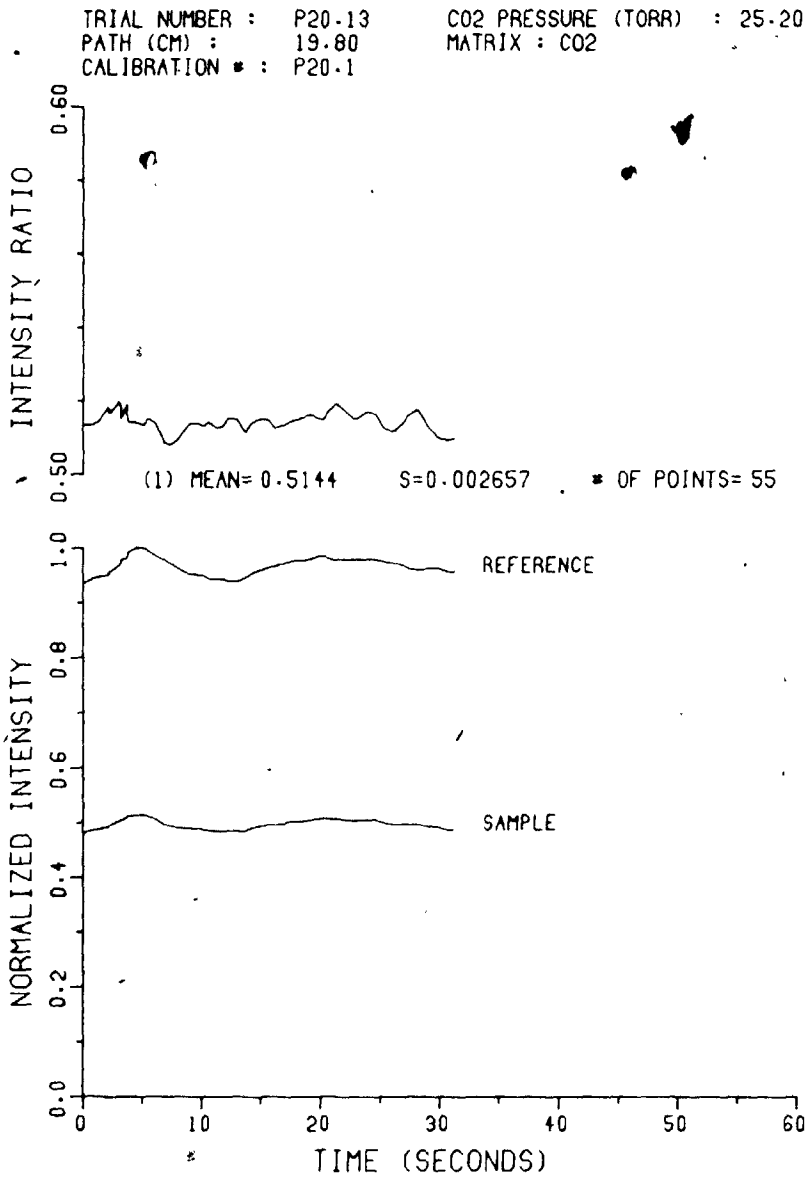
TRIAL NUMBER : P20-13
PATH (CM) : 19.80
CALIBRATION # : P20-1
CO2 PRESSURE (TORR) : 25.20
MATRIX : CO2
INTENSITY RATIO
0.60
0.50
(1) MEAN= 0.5144 S=0.002657 # OF POINTS= 55
NORMALIZED INTENSITY
1.0
0.8
0.6
0.4
0.2
0.0
REFERENCE
SAMPLE
0
10
20
30
40
50
60
TIME (SECONDS)

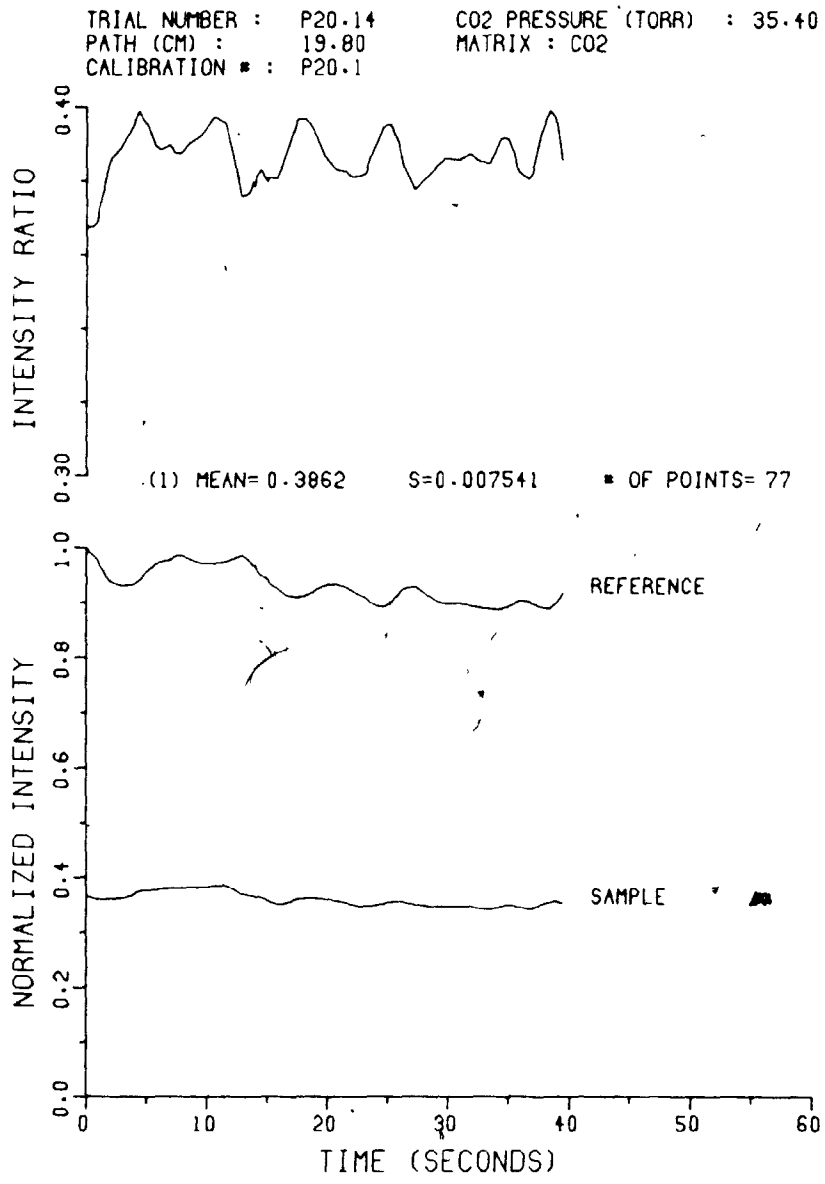
TRIAL NUMBER : P20.14
PATH (CM) : 19.80
CALIBRATION # : P20.1
CO2 PRESSURE (TORR) : 35.40
MATRIX : CO2
INTENSITY RATIO
0.40
0.30
(1) MEAN= 0.3862 S=0.007541 # OF POINTS= 77
NORMALIZED INTENSITY
1.0
0.8
0.6
0.4
0.2
0.0
REFERENCE
SAMPLE
0
10
20
30
40
50
60
TIME (SECONDS)

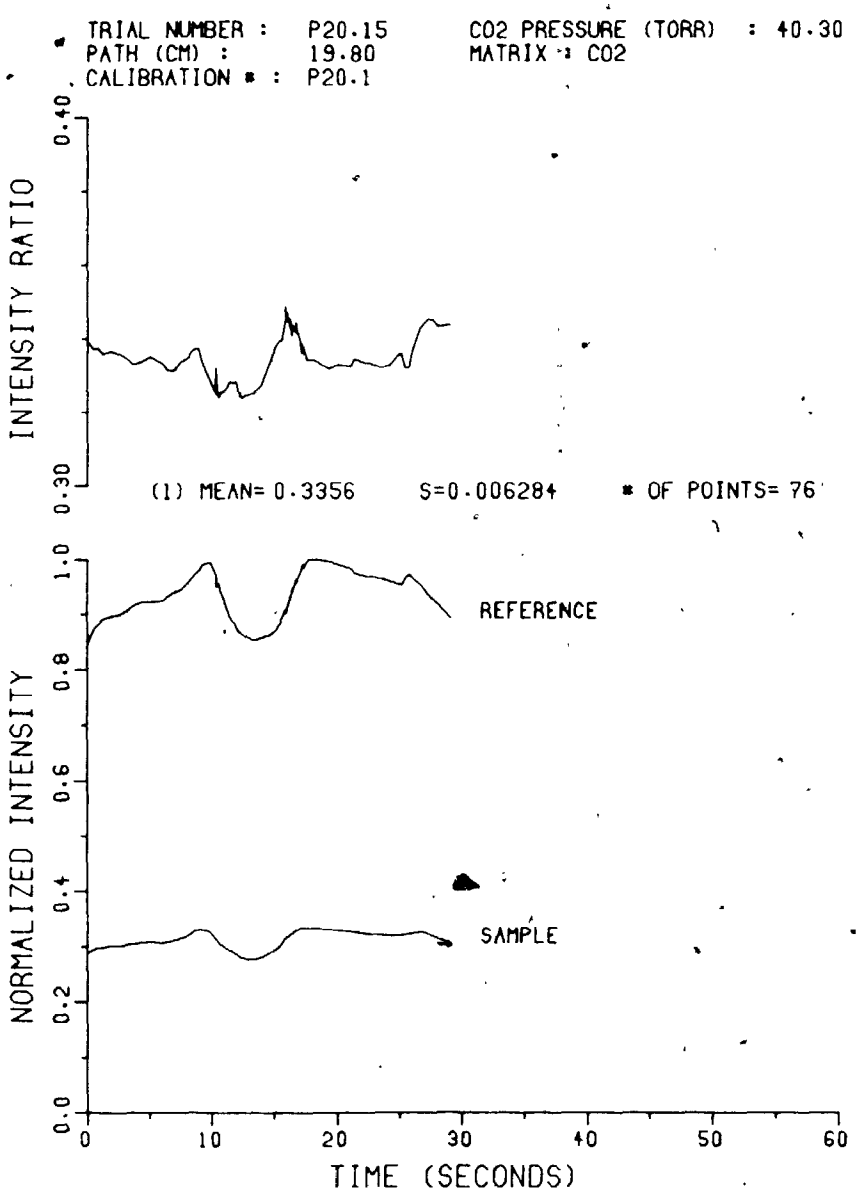
TRIAL NUMBER : P20.15
PATH (CM) : 19.80
CALIBRATION # : P20.1
CO2 PRESSURE (TORR) : 40.30
MATRIX : CO2
INTENSITY RATIO
0.40
0.30
(1) MEAN= 0.3356 S=0.006284 # OF POINTS= 76
NORMALIZED INTENSITY
1.0
0.8
0.6
0.4
0.2
0.0
REFERENCE
SAMPLE
0
10
20
30
40
50
60
TIME (SECONDS)

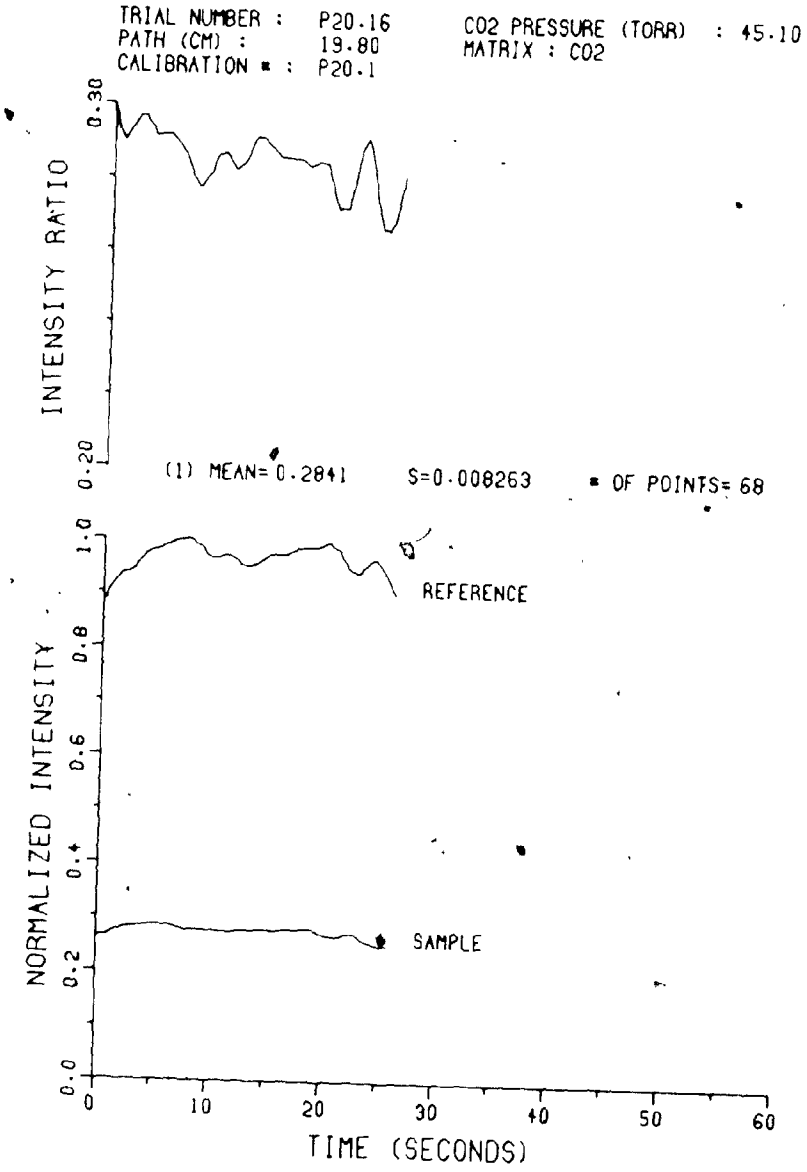
TRIAL NUMBER : P20.16
PATH (CM) : 19.80
CALIBRATION # : P20.1
CO2 PRESSURE (TORR) : 45.10
MATRIX : CO2
INTENSITY RATIO
0.30
0.20
(1) MEAN= 0.2841 S=0.008263 # OF POINTS= 68
NORMALIZED INTENSITY
1.0
0.8
0.6
0.4
0.2
0.0
REFERENCE
SAMPLE
0
10
20
30
40
50
60
TIME (SECONDS)

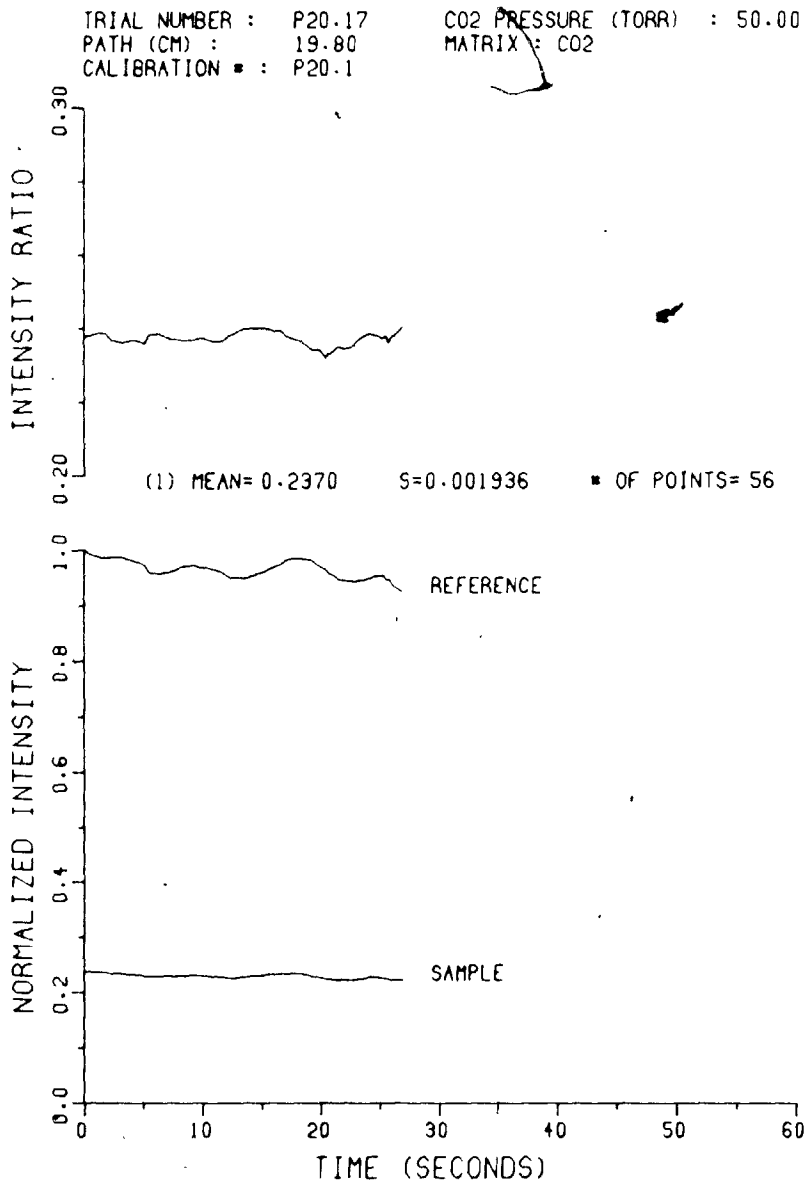
TRIAL NUMBER : P20.17
PATH (CM) : 19.80
CALIBRATION # : P20.1
CO2 PRESSURE (TORR) : 50.00
MATRIX : CO2
INTENSITY RATIO
0.30
0.20
(1) MEAN= 0.2370 S=0.001936 # OF POINTS= 56
NORMALIZED INTENSITY
1.0
0.8
0.6
0.4
0.2
0.0
REFERENCE
SAMPLE
0
10
20
30
40
50
60
TIME (SECONDS)

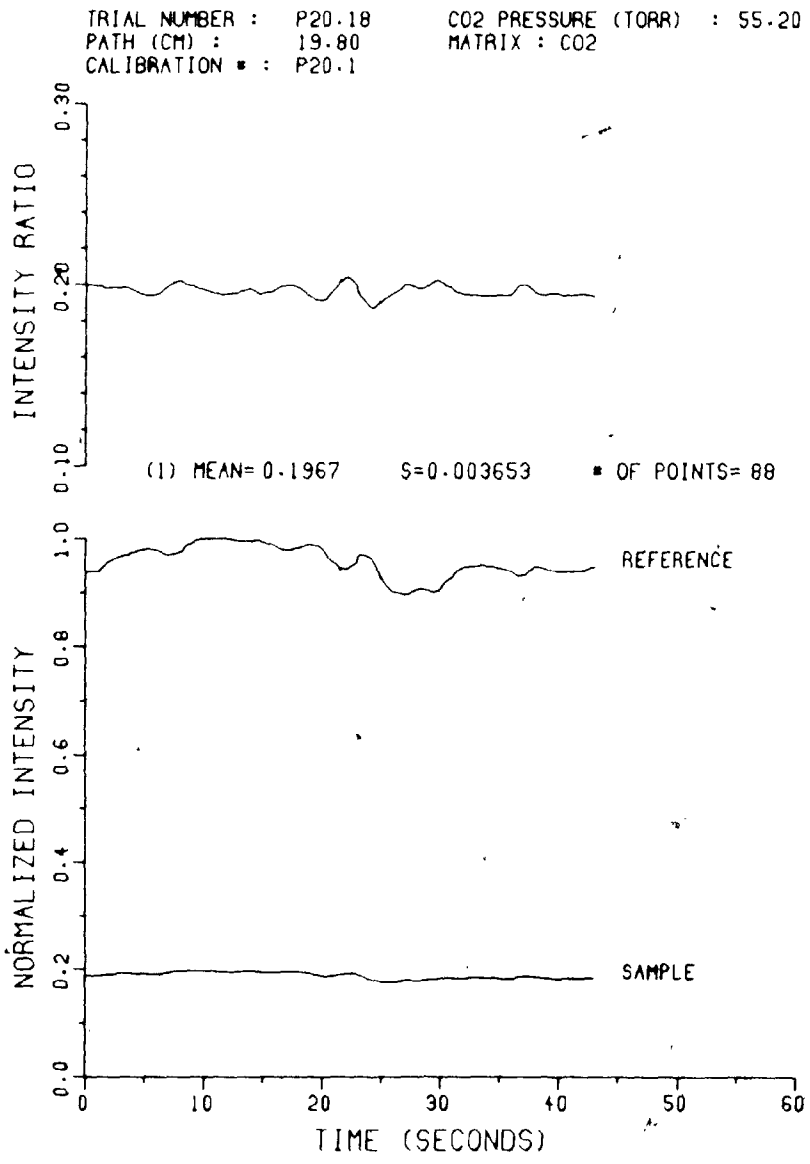
TRIAL NUMBER : P20.18
PATH (CM) : 19.80
CALIBRATION # : P20.1
CO2 PRESSURE (TORR) : 55.20
MATRIX : CO2
INTENSITY RATIO
0.30
0.20
0.10
(1) MEAN= 0.1967 S=0.003653 # OF POINTS= 88
NORMALIZED INTENSITY
1.0
0.8
0.6
0.4
0.2
0.0
REFERENCE
SAMPLE
0
10
20
30
40
50
60
TIME (SECONDS)

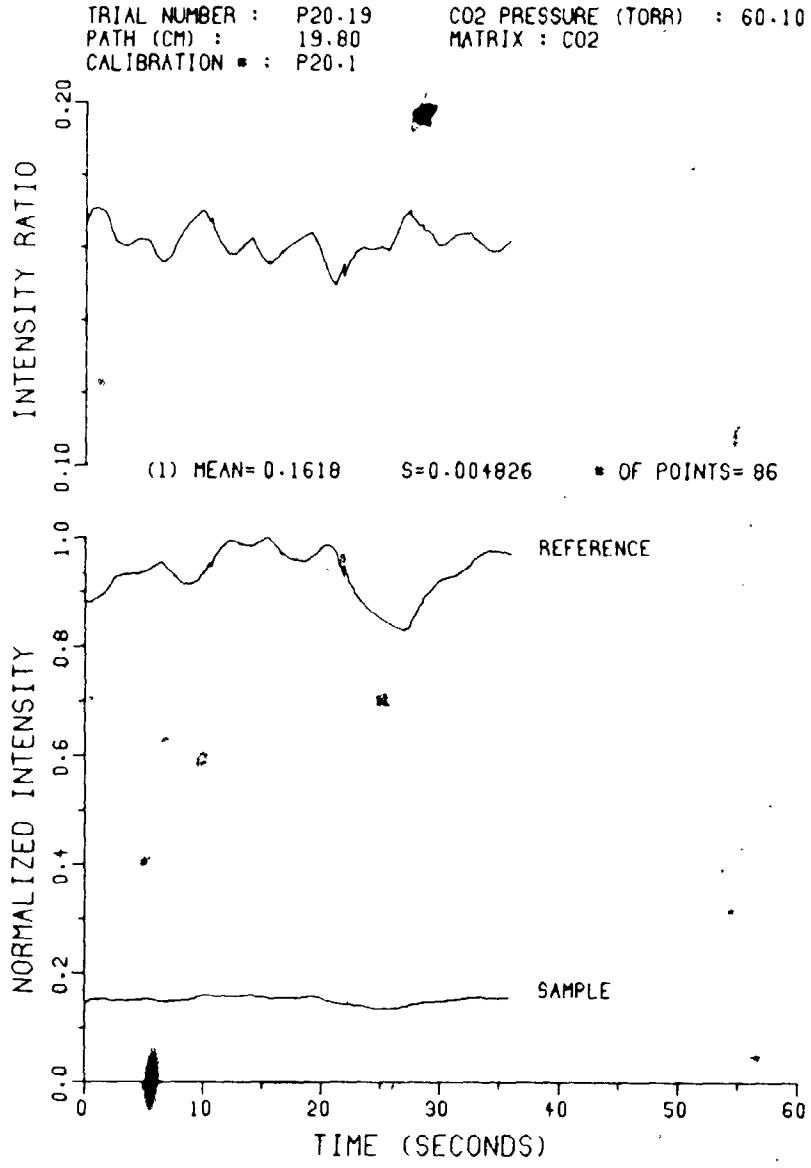
TRIAL NUMBER : P20.19
PATH (CM) : 19.80
CALIBRATION # : P20.1
CO2 PRESSURE (TORR) : 60.10
MATRIX : CO2
INTENSITY RATIO
0.20
0.10
(1) MEAN= 0.1618 S=0.004826 # OF POINTS= 86
NORMALIZED INTENSITY
1.0
0.8
0.6
0.4
0.2
0.0
REFERENCE
SAMPLE
0
10
20
30
40
50
60
TIME (SECONDS)

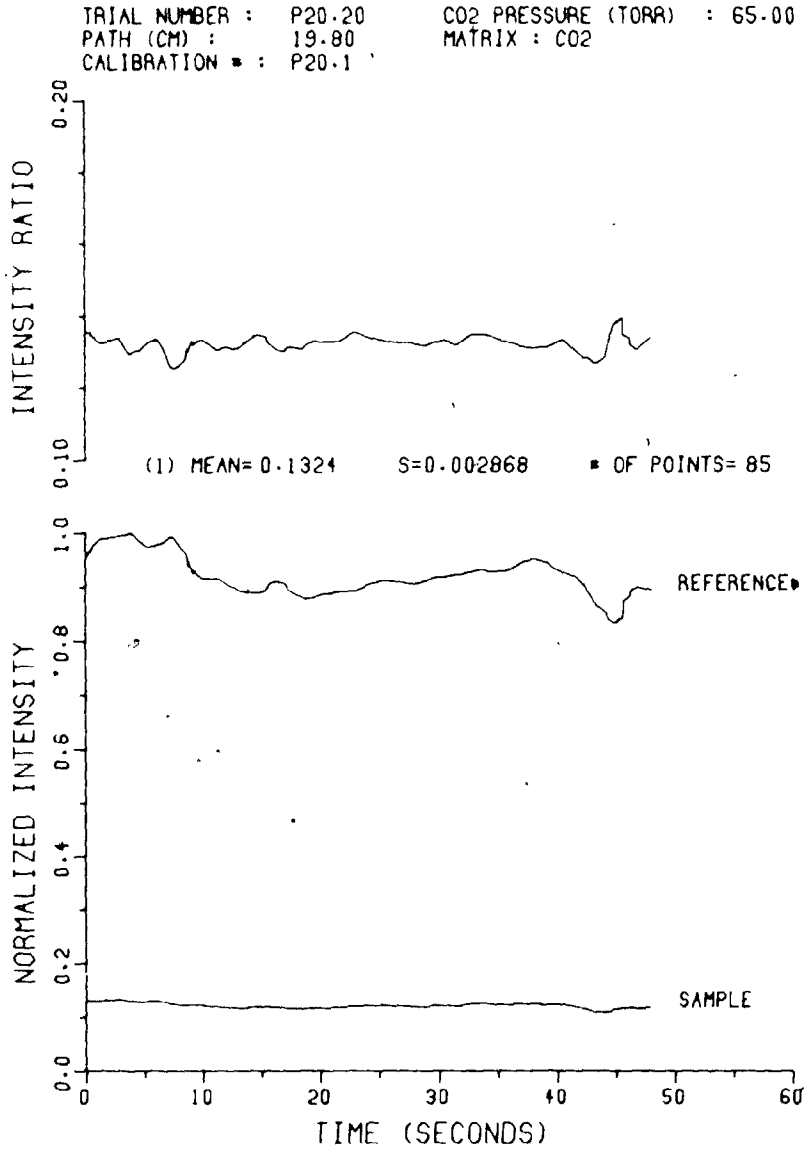
TRIAL NUMBER : P20.20
PATH (CM) : 19.80
CALIBRATION # : P20.1
CO2 PRESSURE (TORR) : 65.00
MATRIX : CO2
INTENSITY RATIO
0.20
0.10
(1) MEAN= 0.1324 S=0.002868 # OF POINTS= 85
NORMALIZED INTENSITY
1.0
0.8
0.6
0.4
0.2
0.0
REFERENCE
SAMPLE
0
10
20
30
40
50
60
TIME (SECONDS)

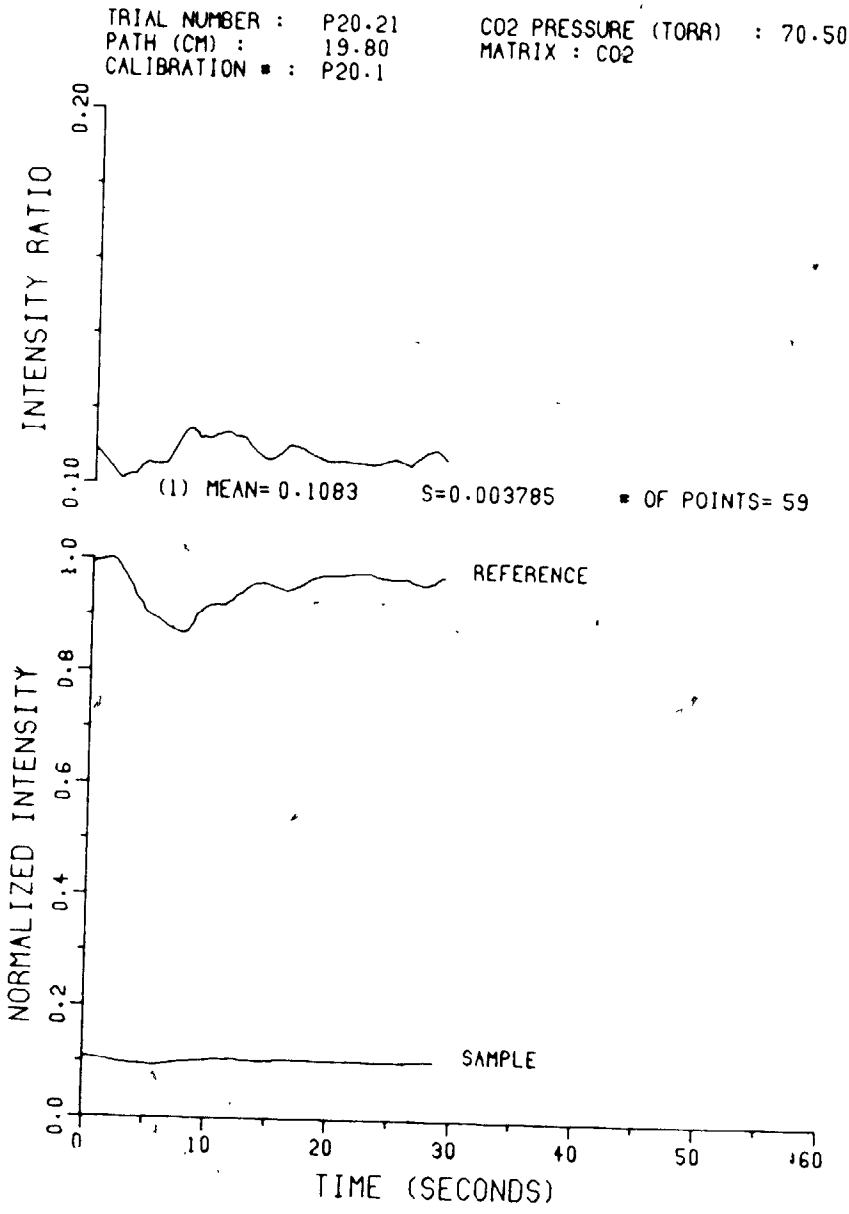
TRIAL NUMBER : P20.21
PATH (CM) : 19.80
CALIBRATION # : P20.1
CO2 PRESSURE (TORR) : 70.50
MATRIX : CO2
INTENSITY RATIO
0.20
0.10
(1) MEAN= 0.1083
S=0.003785
# OF POINTS= 59
NORMALIZED INTENSITY
1.0
0.8
0.6
0.4
0.2
0.0
REFERENCE
SAMPLE
0
10
20
30
40
50
60
TIME (SECONDS)

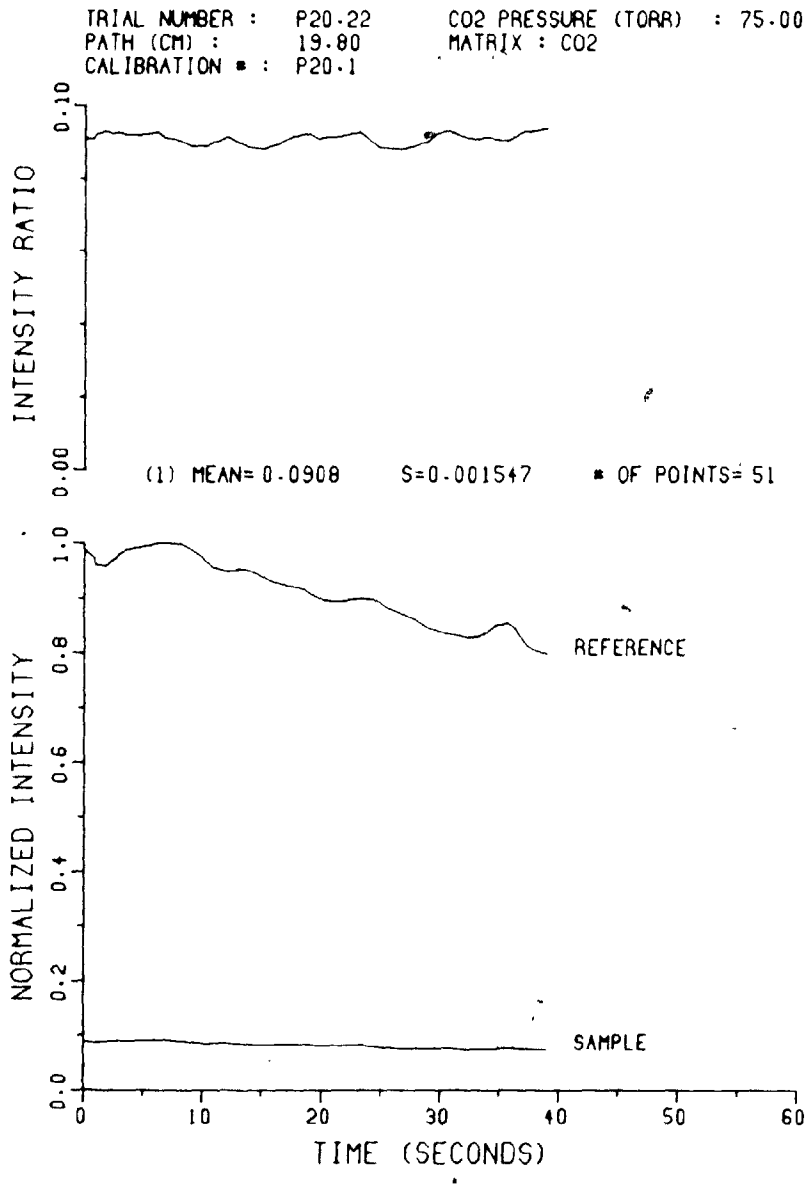
TRIAL NUMBER : P20.22
PATH (CM) : 19.80
CALIBRATION # : P20.1
CO2 PRESSURE (TORR) : 75.00
MATRIX : CO2
INTENSITY RATIO
0.10
0.00
(1) MEAN= 0.0908 S=0.001547 # OF POINTS= 51
NORMALIZED INTENSITY
1.0
0.8
0.6
0.4
0.2
0.0
REFERENCE
SAMPLE
0
10
20
30
40
50
60
TIME (SECONDS)

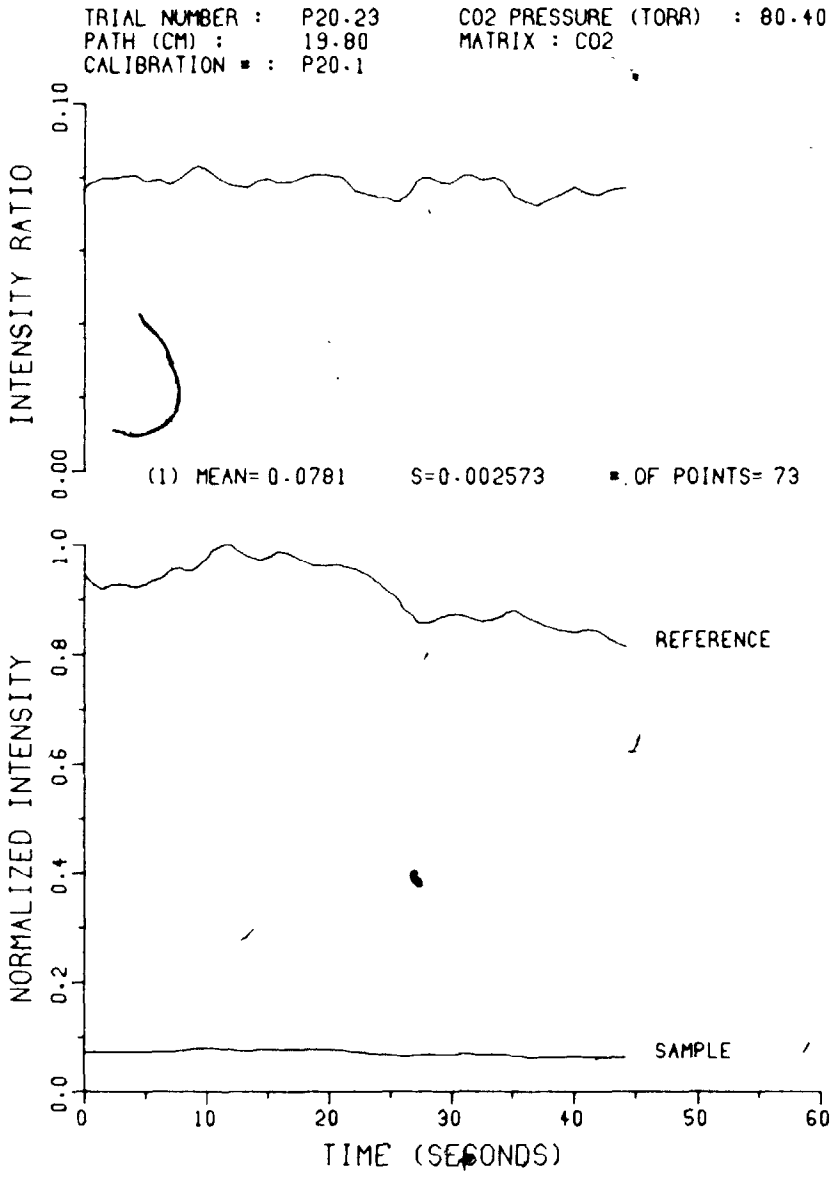
TRIAL NUMBER : P20.23
PATH (CM) : 19.80
CALIBRATION # : P20.1
CO2 PRESSURE (TORR) : 80.40
MATRIX : CO2
INTENSITY RATIO
0.10
0.00
(1) MEAN= 0.0781 S=0.002573 # OF POINTS= 73
NORMALIZED INTENSITY
1.0
0.8
0.6
0.4
0.2
0.0
REFERENCE
SAMPLE
0
10
20
30
40
50
60
TIME (SECONDS)

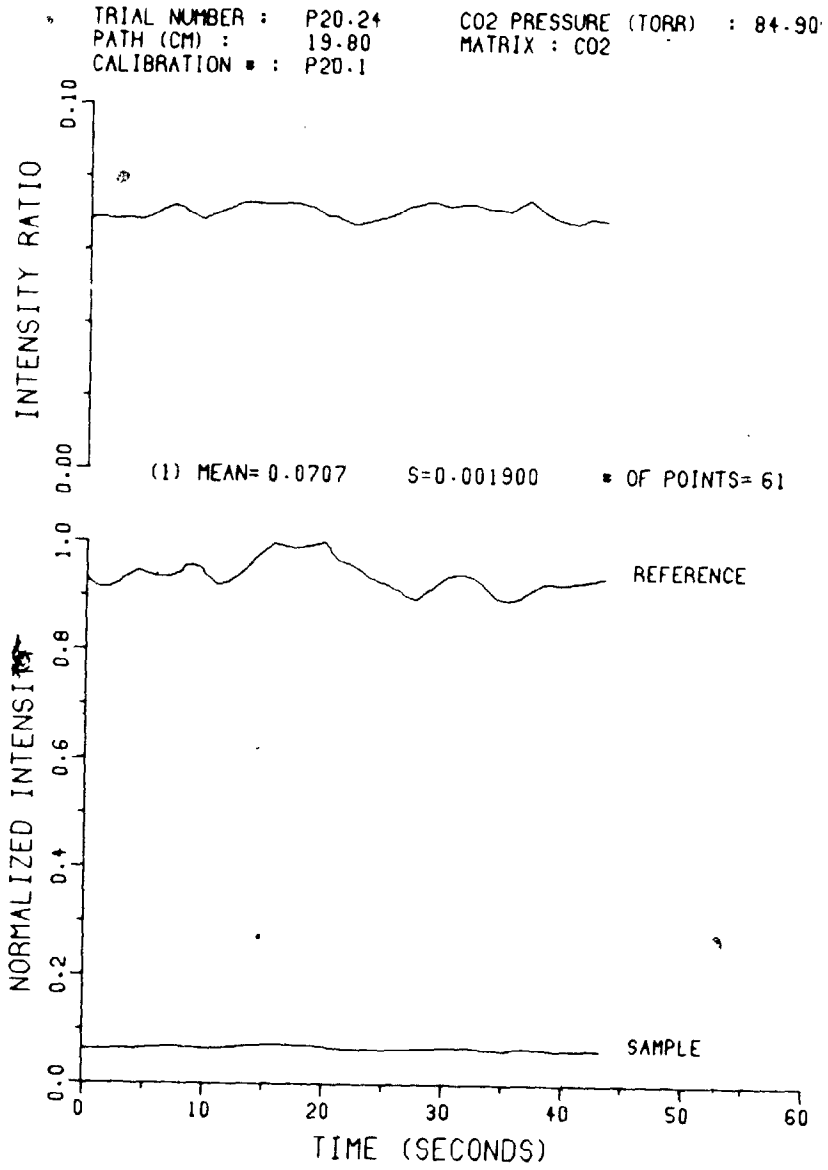
TRIAL NUMBER : P20.24
PATH (CM) : 19.80
CALIBRATION # : P20.1
CO2 PRESSURE (TORR) : 84.90
MATRIX : CO2
INTENSITY RATIO
0.10
0.00
(1) MEAN= 0.0707 S=0.001900 # OF POINTS= 61
NORMALIZED INTENSITY
1.0
0.8
0.6
0.4
0.2
0.0
REFERENCE
SAMPLE
0
10
20
30
40
50
60
TIME (SECONDS)

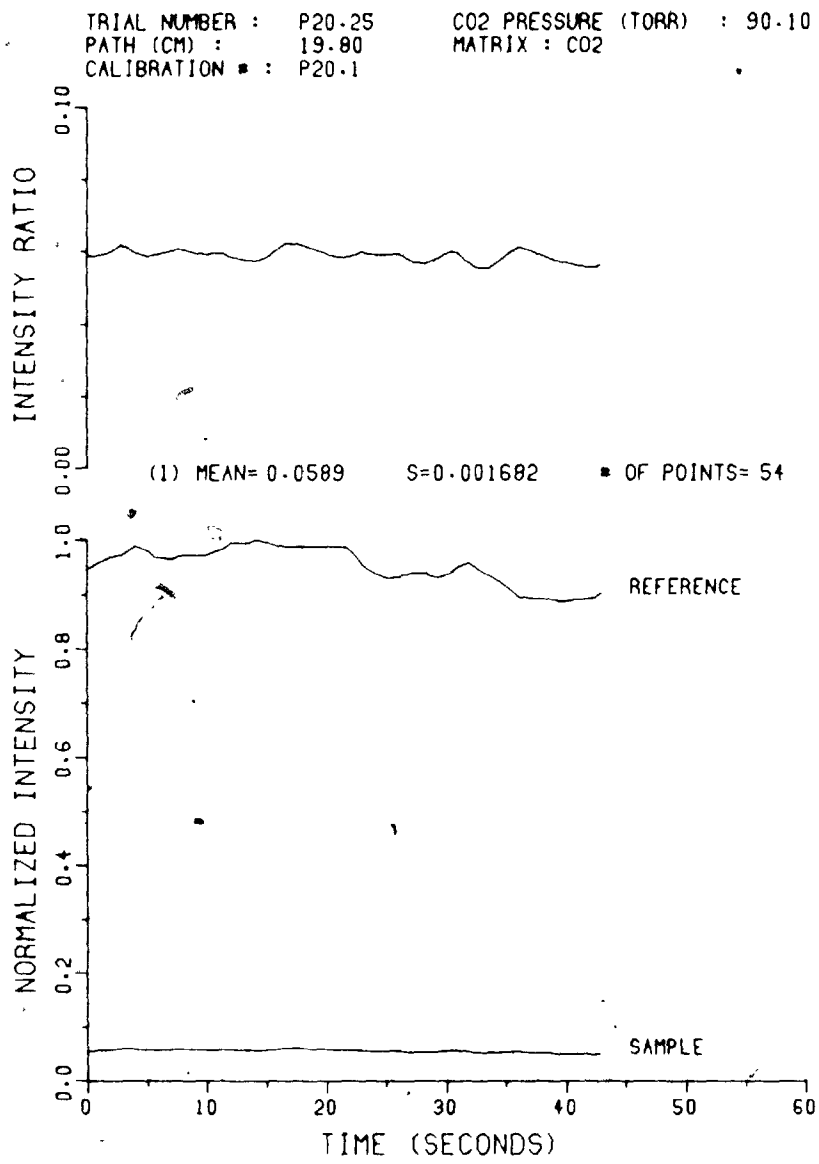
TRIAL NUMBER : P20.25
CO2 PRESSURE (TORR) : 90.10
PATH (CM) : 19.80
MATRIX : CO2
CALIBRATION # : P20.1
INTENSITY RATIO
0.10
0.00
(1) MEAN= 0.0589 S=0.001682 # OF POINTS= 54
NORMALIZED INTENSITY
1.0
0.8
0.6
0.4
0.2
0.0
REFERENCE
SAMPLE
0
10
20
30
40
50
60
TIME (SECONDS)

G.4.2. Pathlength - 2.0 cm

Calibration Files

Trial Numbers: PC2.1-PC2.4

Remote Gain: Sample (G_S): 1 (V/V)

FSD_S: 2 V

FILE	T_L
.1	0.864
.2	.855
.3	.868
.4	.860

Data Files

Trial Numbers: P2.1-P2.11

Remote Gain: Sample (G_S): 1 (V/V)

FSD_S: 2 V

Trial Numbers: P2.12-P2.14

Remote Gain: Sample (G_S): 1 (V/V)

FSD_S: 1 V

Trial Numbers: P2.15-P2.18

Remote Gain: Sample (G_S): 1 (V/V)

FSD_S: 500 mV

Trial Numbers: P2.17-P2.19

Remote Gain: Sample (G_S): 2 (V/V)

FSD_S: 500 mV

FILE	P_{CO_2} (Torr)	T(v)	T_L FILE
P2.1	25.0	0.955	PC.1
.2	37.5	.921	
.3	50.0	.882	
.4	62.5	.830	
.5	75.0	.744	
.6	87.5	.682	
.7	100.	.607	PC 2
.8	113.	.538	
.9	125.	.457	
.10	138.	.392	
.11	150.	.329	
.12	163.	.274	

FILE	P_{CO_2} (Torr)	T(v)	T_L FILE
P2.13	175.	0.222	PC.3
.14	188.	.175	
.15	200.	.144	
.16	213.	.121	
.17	225.	.096	PC.4
.18	238.	.073	
.19	250.	.057	

Appendix H
Linear Regression Results

H.1. Pathlength - 20.0 cm

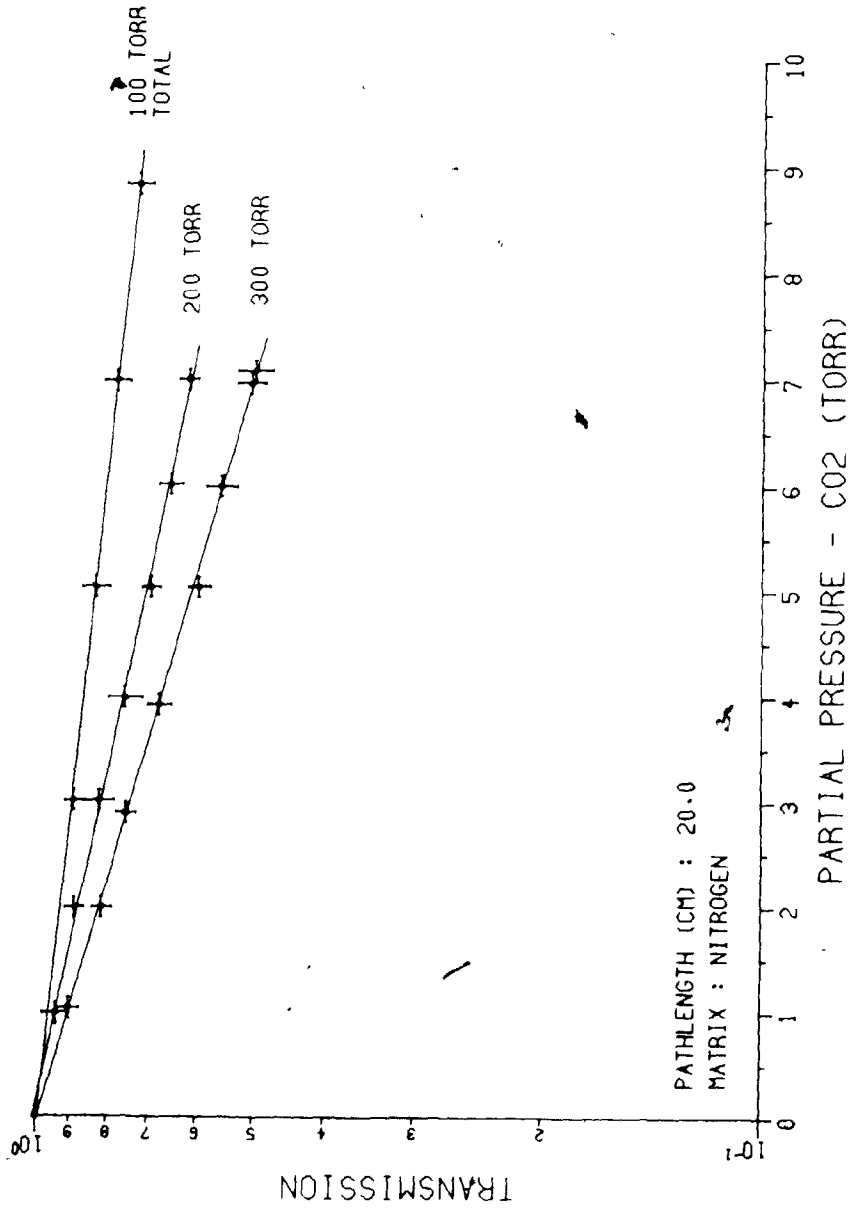

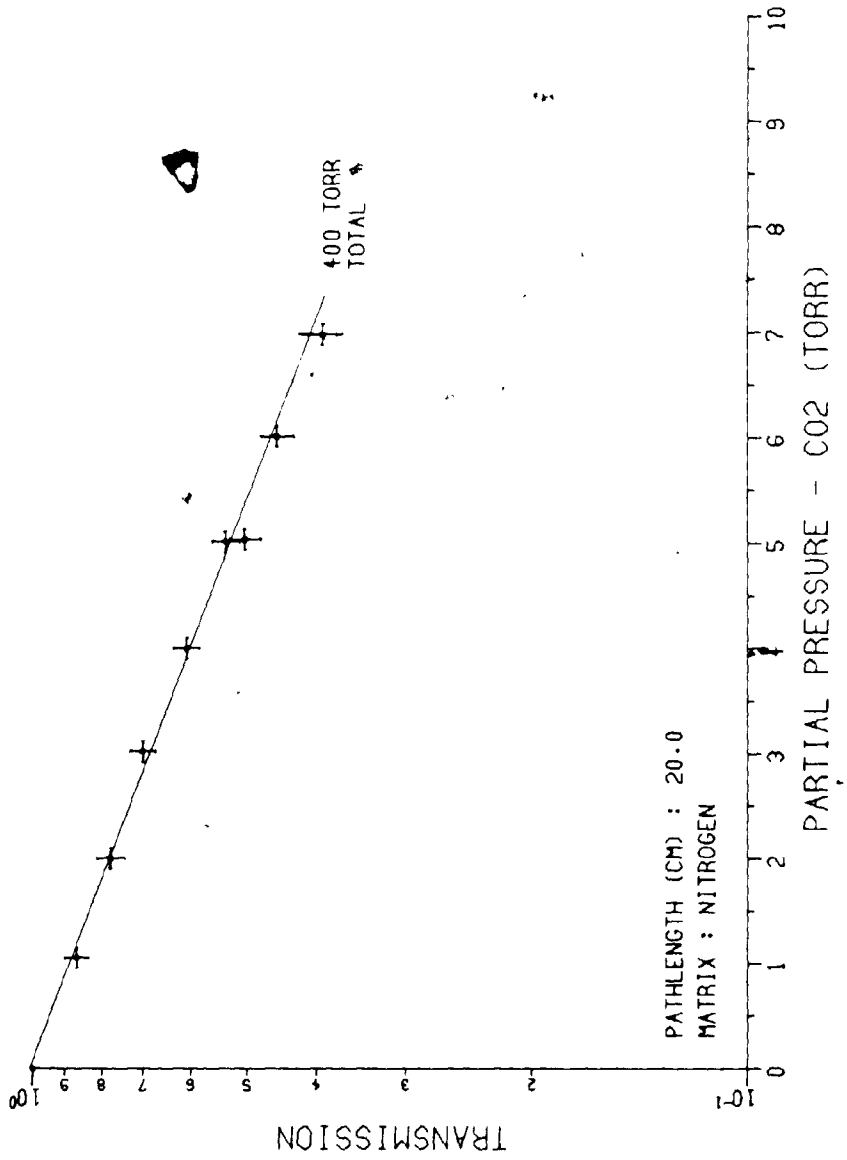
400 TORR
TOTAL
PATHLENGTH (CM) : 20.0
MATRIX : NITROGEN
PARTIAL PRESSURE - CO2 (TORR)
TRANSMISSION
0
1
2
3
4
5
6
7
8
9
10
10⁻¹
100

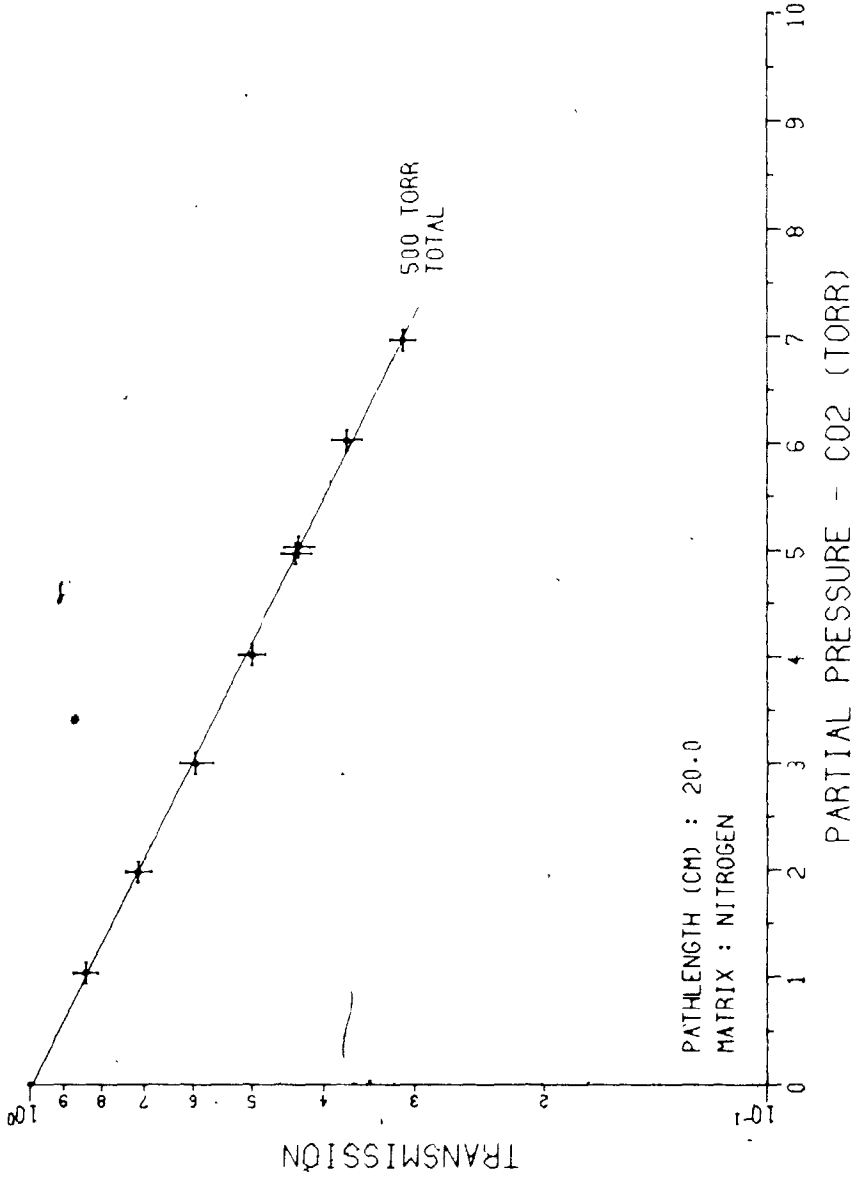
500 TORR
TOTAL
PATHLENGTH (CM) : 20.0
MATRIX : NITROGEN
PARTIAL PRESSURE - CO2 (TORR)
TRANSMISSION
10-1
100
0
1
2
3
4
5
6
7
8
9
10

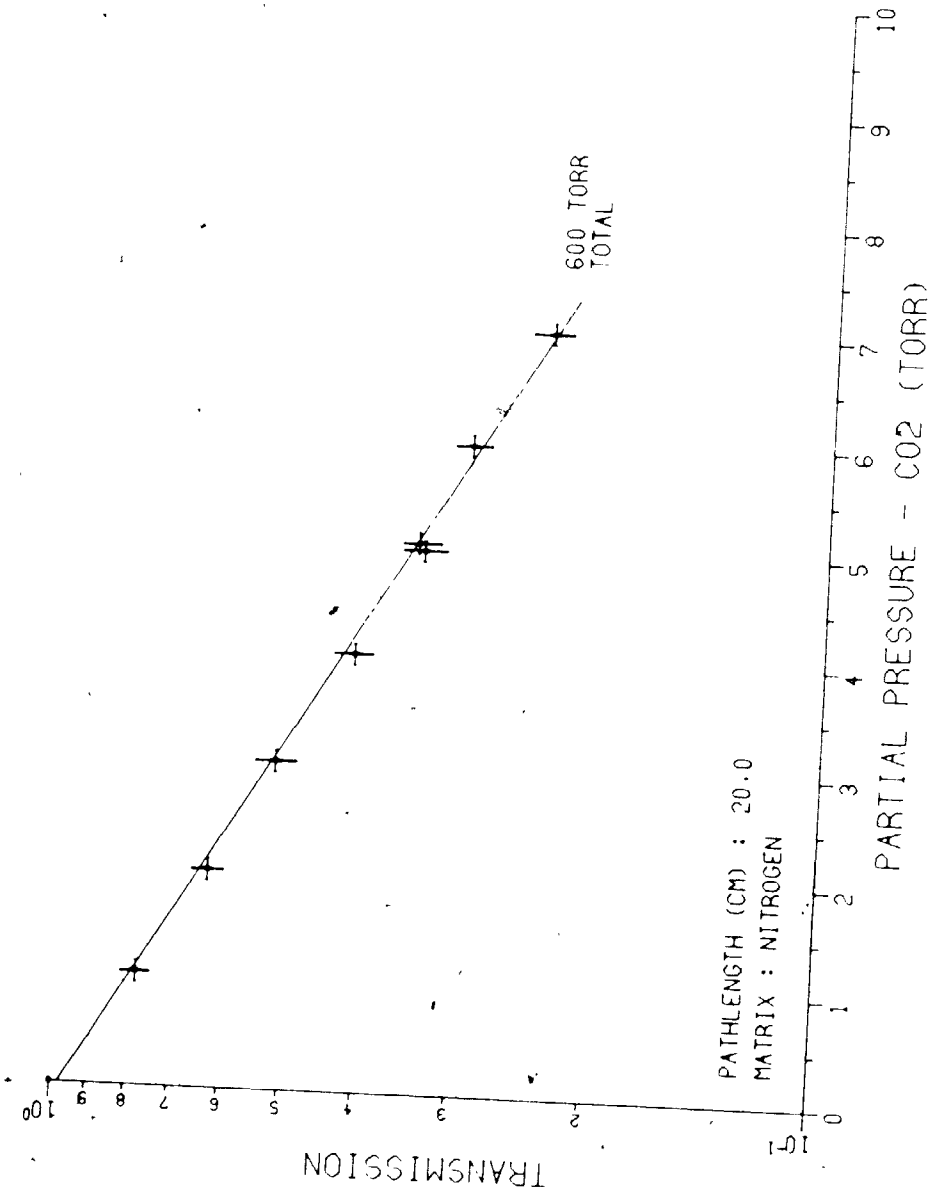
600 TORR
TOTAL
PATHLENGTH (CM) : 20.0
MATRIX : NITROGEN
PARTIAL PRESSURE - CO2 (TORR)
TRANSMISSION
0
1
2
3
4
5
6
7
8
9
10
100
9
8
7
6
5
4
3
2
1
0

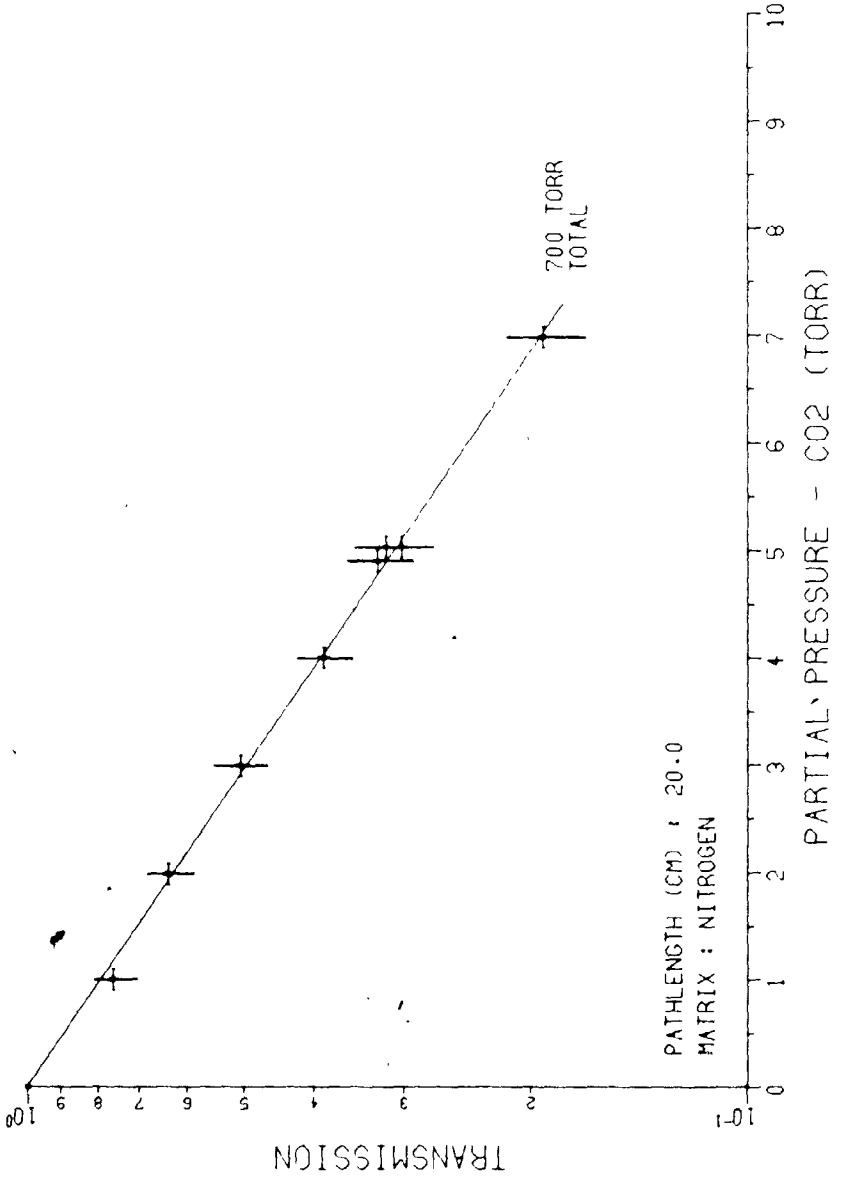
700 TORR
TOTAL
PATHLENGTH (CM) : 20.0
MATRIX : NITROGEN
PARTIAL PRESSURE - CO2 (TORR)
TRANSMISSION
0
1
2
3
4
5
6
7
8
9
10
10-1
2
3
4
5
6
7
8
9
100

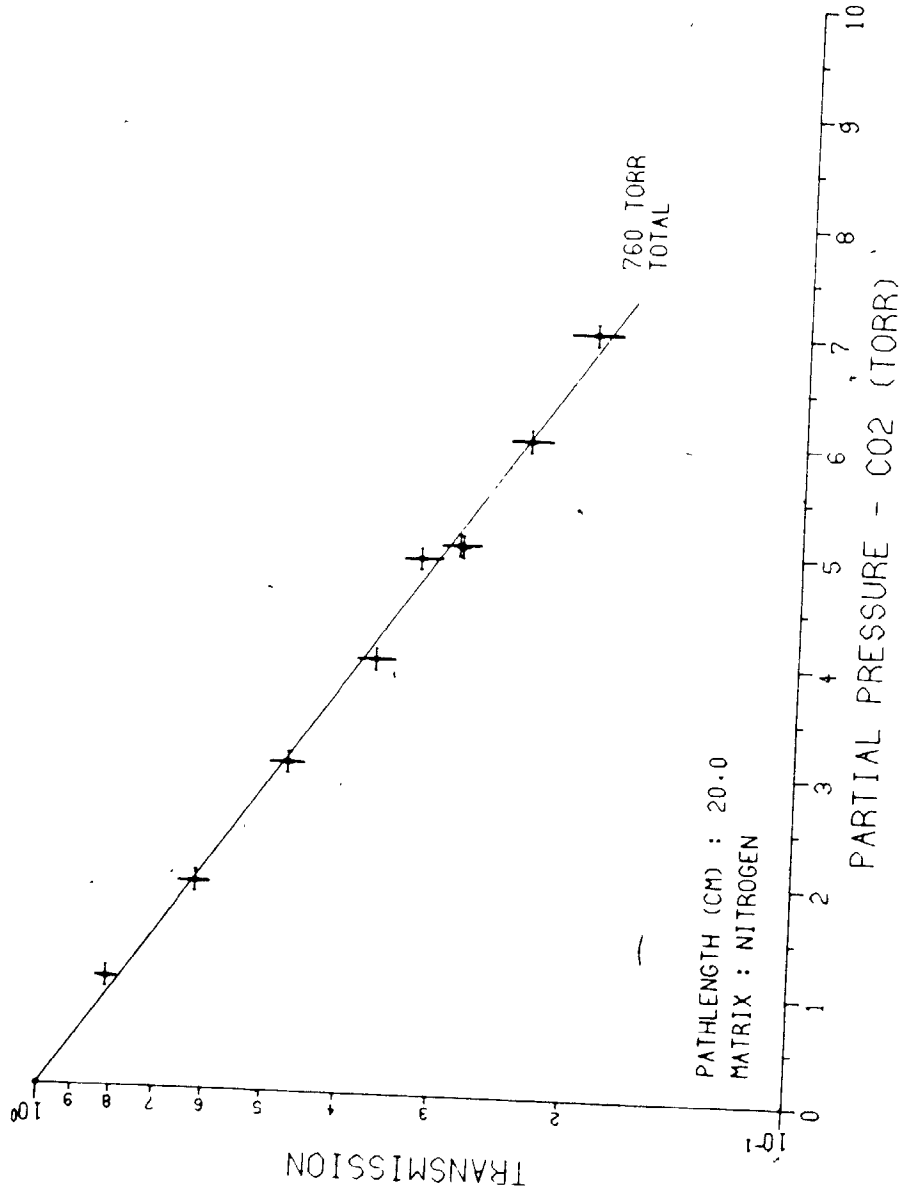
760 TORR
TOTAL
PATHLENGTH (CM) : 20.0
MATRIX : NITROGEN
PARTIAL PRESSURE - CO2 (TORR)
TRANSMISSION
0
1
2
3
4
5
6
7
8
9
10
10-1
100

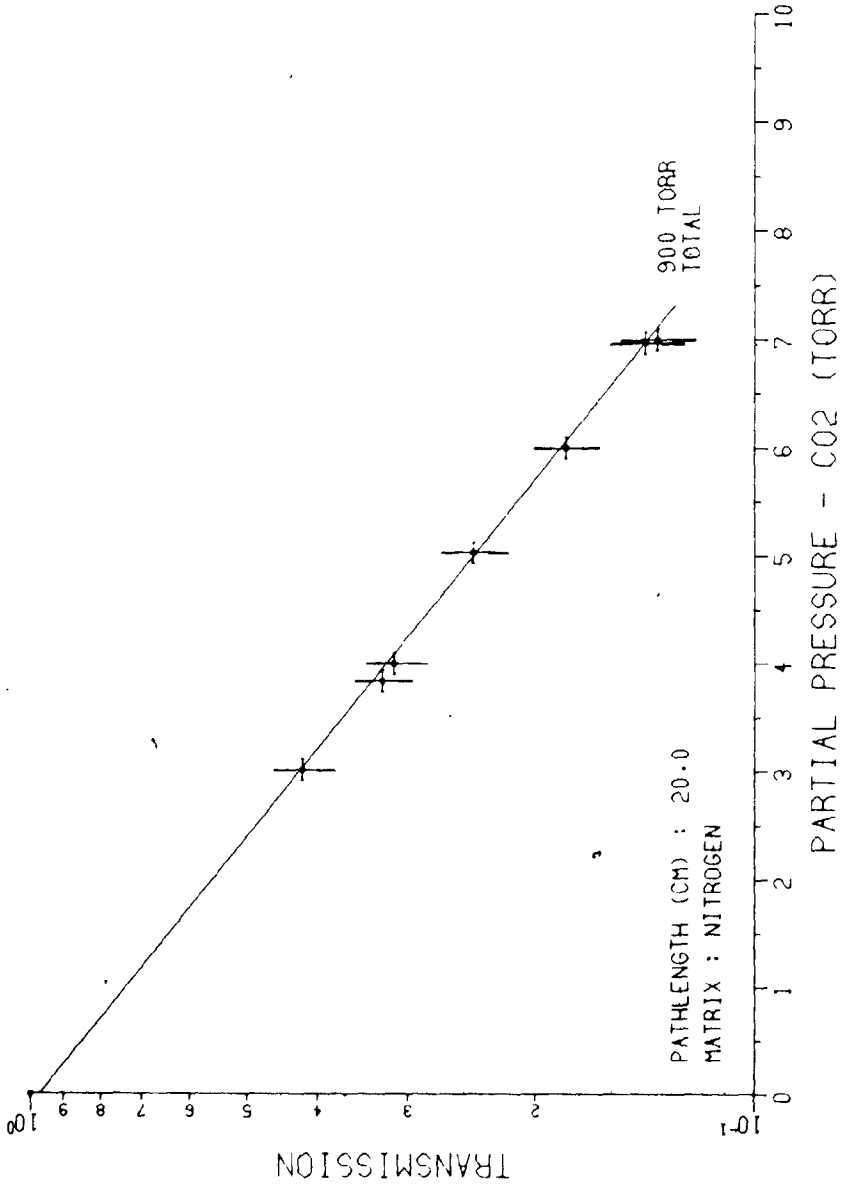
TRANSMISSION
PARTIAL PRESSURE - CO2 (TORR)
900 TORR TOTAL
PATHLENGTH (CM) : 20.0
MATRIX : NITROGEN

H.2. Pathlength - 2.0 cm

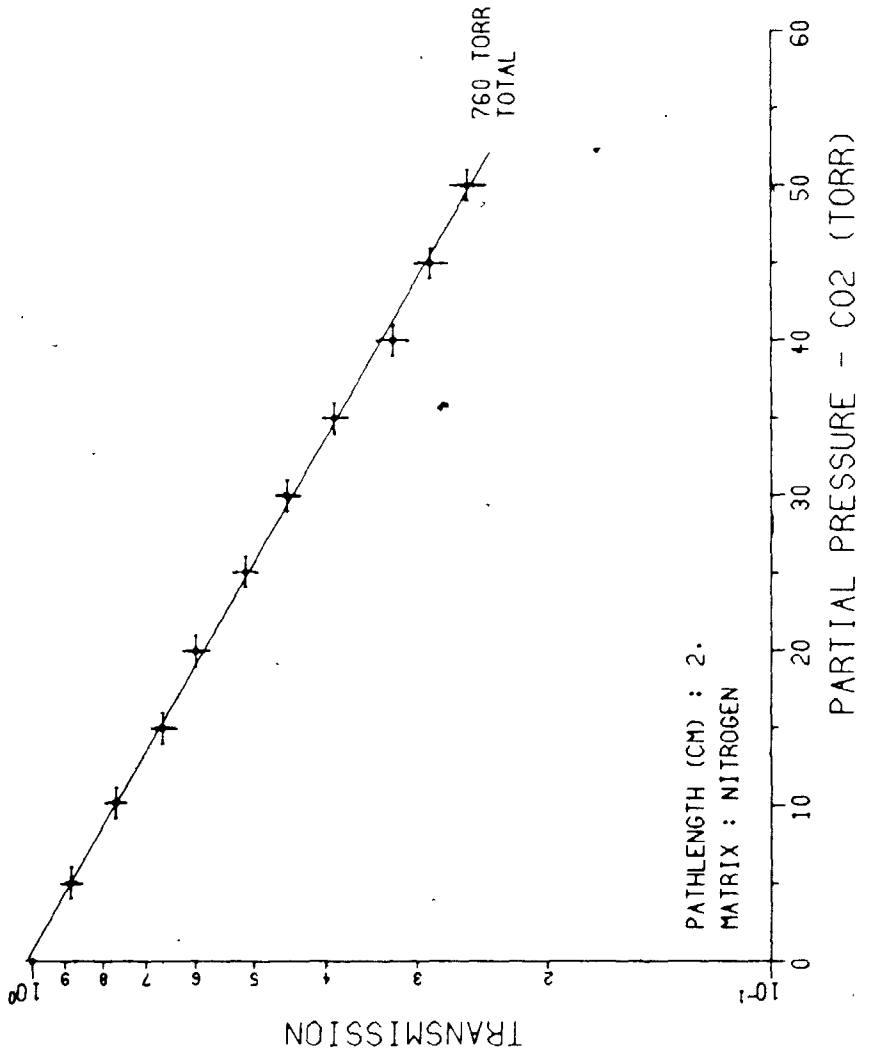

References

1. Schneider, C. W. , *A Long Path Resonance Absorption Spectrometer*, Masters Thesis, University of Western Ontario, London, Ontario (1981)

2. Kidal, H. ,Byer, R. L., *Proc. IEEE* **59**, 1644 (1971)

3. Cameron, D. M. , Nellson, H. H. , *Phys. Rev.* **53**, 246-247 (1938)

4. Dennison, D. M. , *Rev. Mod. Phys.* **12**, 175-213 (1940)

5. Herzberg, G. , *Rev. Mod. Phys.* **14**, 219-223 (1942)

6. Weber, D. , Holm, R. J. , Penner, S. S. , *J. Chem. Phys.* **20**, 1820 (1952)

7. Plyler, E. K. , Blaine L. R. , Tidwell E. D. , *J. Res. Nat. Bur. Stand.* **55**, 183-189 (1955)

8. Plyler, E. K. , Dantl, A. , Blaine L. R. , Tidwell E. D. , *J. Res. Nat. Bur. Stand. - A: Phys. Chem.* **64**, 29-48 (1960)

9. Roney, P. L. , Findley, F. D. , Buijs H. L. , Cann M. W. P2., Nicholls, R. W. , *App. Opt.* **17**, 2599-2604 (1978)

10. Rothman, L. S. , Benedict, W. S. , *App. Opt.* **17**, 2605-2611 (1978)

11. Herzberg, G. , *Molecular Spectra and Molecular Structure II, Infrared and Raman Spectra of Polyatomic Molecules*, pub. Van Nostrand (New York), pp. 272 (1945)

12. Mulliken, R. ,S. , *J. Phys. Chem.* **41**, 159-173 (1937)

13. Herzberg, G. , *Molecular Spectra and Molecular Structure II, Infrared and Raman Spectra of Polyatomic Molecules*, pub. Van Nostrand (New York), pp. 21 (1945)

14. Benedict, W. S. , Herman, R. , Moore, G. E. , Silverman, S. , *Can. J. Phys.* **34**, 830-849 (1956)

15. Burch, D. E. , Gryvnak, D. A. , Patty, R. R. , Bartky, C. E. , *J. Opt. Soc. Am.* **59**, 267-280 (1969)

16. Gray, L. D. , *J. Quant. Spectros. Radiat Transfer.* **5**, 298-301 (1965)

17. Penner, S. S. , *Quantitative Molecular Spectroscopy and Gas Emissivities*, Addison Wesley (Reading), pp. 158 (1959)

18. Werthelm, G. K. , Butler, M. A. , West, K. W. , Buchanan, D. N. E. , *Rev. Sci. Instrum.* **45**, 1369-1371 (1974)

19. Farach, H. A. , Teltelbaum, H. , *Can. J. Phys* **45**, 2913-2921 (1967)

20. Michelson, A. A. , *Phil. Mag.* **34**, 280 (1892)

21. van Trigt, C. , *Physica* **32**, 571-575 (1966)

22. Anderson, P. W. , *Phys. Rev.* **76**, 647-661 (1949)

23. Dicke, R. H. , *Phys. Rev.* **89**, 472-473 (1953)

24. Gordon, R. G. , *J. Chem. Phys.* **44**, 3083-3089 (1966)

25. Gordon, R. G. , *J. Chem. Phys.* **45**, 1649-1655 (1966)

26. Gordon, R. G. , McGinnis, R. P. , *J. Chem. Phys.* **55**, 4898-4906 (1971)

27. Fano, U. , *Phys. Rev.* **131**, 259-268 (1963)

28. Breene, R. G. , *The Shift and Shape of Spectral Lines*, pub. Pergamon Press (Oxford) (1961)

29. Hindmarsh, W. R. , Farr, J. M. , *Collision Broadening of Spectral Lines by Neutral Atoms*, In *Progress in Quantum Electronics*, Vol. 2, Part 3, ed. J. H. Sanders and S. Stenholm, pub. Pergamon Press (Oxford) (1972)

30. Ben-Reuven, A. , *The Meaning of Collision Broadening of Spectral Lines: The Classical Oscillator Analog*, In *Advances in*

Atomic and Molecular Physics, Vol. 5, ed. D. R. Bates and I. Estermann, pub. Academic Press (New York), pp. 201-235 (1969)

31. May, A. D. , *App. Opt.* **12**, 1102-1103 (1973)

32. Bracewell, R. N. , *The Fourier Transform and Its Applications*, 2nd, ed. , pub. McGraw Hill Book Co. (New York), pp. 115 (1978)

33. Demtroder, W. , *Laser Spectroscopy - Basic Concepts and Instrumentation*, in *Springer Series in Chemical Physics*, Vol. 5, pub. Springer-Verlag (Berlin), pp. 89-97 (1981)

34. Tsao, C. J. , Curnutte, B. , *J. Quant. Spectros. Radiat. Transfer* **2**, 41-91 (1962)

35. Bulanin, M. O. , Bulychev. , V. P. , Khodos, E. B. , *Opt. Spectrosc. (USSR)* **48**, 486-489 (1980)

36. Van Vleck, J. H. , Weisskopf, V. F. , *Rev. Mod. Phys.* **17**, 227-236 (1945)

37. Herzberg, G. , *Molecular Spectra and Molecular Structure I, Spectra of Diatomic Molecules*, pub. Van Nostrand (New York), p. 17 (1945)

38. Rank, D. H. , Birtley, W. B. , Eastman, D. P. , Wiggens, T. A. , *J. Chem. Phys.* **32**, 296-297 (1960)

39. Hirshfeld, M. A. , Jaffe, J. H. , Kimel, S. , *J. Chem. Phys.* **32**, 297-298 (1960)

40. Rank, D. H. , Birtley, W. B. , Eastman, D. P. , Wiggens, T. A. , *J. Chem. Phys.* **32**, 298-299 (1960)

41. Kimel, S. , Hirshfeld, M. A. , Jaffe, J. H. , *J. Chem. Phys.* **31**, 81-84 (1959)

42. Rank, D. H. , Eastman, D. P. , Birtley, W. B. , Wiggens, T. A. , *J. Chem. Phys.* **33**, 327-328 (1960)

43. Dokuchaev, A. B. , Tonkov, M. V. , *Opt. Spectrosc. (USSR)* **48**, 407-419 (1980)

44. Anderson, A. , Chal, A. , Williams, D. , *J. Opt. Soc. Am.* **57**, 240-246 (1967)

45. Eng, R. S. , Calawa, A. R. , Harman, T. C. , Kelley, P. L. , Javan, A. , *App. Phys. Lett.* **12**, 303-305 (1972)

46. Kucerovsky, Z. , Brannen, E. , Rumboldt, D. G. , Sarjeant, W. J. , *App. Opt.* **12**, 226-231 (1973)

47. Penner, S. S. , *Quantitative Molecular Spectroscopy and Gas Emissivities*, Addison Wesley (Reading), pp. 32 (1959)

48. Demtroder, W. , *Laser Spectroscopy - Basic Concepts and Instrumentation*, in *Springer Series in Chemical Physics*, Vol. 5, pub. Springer-Verlag (Berlin), pp. 99 (1981)

49. Foley, J. ,I. , Gersten, H. ,M. , *J. Opt. Soc. Am.* **58**, 933-937 (1968)

50. Brunet, H. , Laures, P. , *Phys. Lett.* **12**, 106-107 (1964)

51. Belov, N. A. , Koval, A. K. , Mironov, V. D. , Popov, A. I. , Protsenko, E. D. , *Opt. Spectrosc. (USSR)* **31**, 1236-1239 (1980)

52. Moore, C. E. , *Atomic Energy Levels*, NBS Circ. No. 467 (1949)

53. Javan, A. , Bennett, W. R. , Herriott, D. R., *Phys. Rev. Lett.* **6**, 106-110 (1961)

54. Willett, C. S. , *Neutral Gas Lasers*, in *CRC Handbook of Lasers*, ed. R. C. Weast, pub. CRC Press (Cleveland, Ohio), pp. 183-241 (1971)

55. Willett, C. S. , *Laser Lines in Atomic Species*, in *Progress in Quantum Electronics*, Vol. 1, ed. J. H. Sanders and K. W. H. Stevens, pub. Pergamon Press (Oxford), pp. 273-357 (1971)

56. Boyd, G. D. , Gordon, J. P. , *Bell Sys. Tech. J*, **40**, 489 (1961)

57. Fox, A. G. , Li, T. , *Bell Sys. Tech. J.* **40**, 489 (1961)

58. Rigrod, W. W. , Kogelnik, H. , Brangaccio, D. J., Herriot, D. R., *J. App. Phys.* **33**, 743-744 (1962)

59. White, A. D. , Gordon, E. I. , *App. Phys. Lett.* **3**, 197-201 (1963)

60. White, A. D. , Rigden, J. D. , *Proc. Inst. Radio Engrs.* **50**, 1697 (1962)

61. Bloom, A. L. , Bell, W. E. , Rempel, R. C. , *App. Opt.* **2**, 317-318 (1963)

62. Lis, L. , *Physics Lett.* **39A**, 119-120 (1972)

63. Svelto, O. , *Principles of Lasers*, 2nd. ed., pub. Plenum Press (New York and London) (1982)

64. Bloom, A. L. , *Gas Lasers*, pub. John Wiley and Sons Inc. (New York) (1968)

65. Siegman, A. E. , *An Introduction to Lasers and Masers*, pub. McGraw-Hill Book Co. (New York) (1971)

66. Siegman, A. E. , *An Introduction to Lasers and Masers*, pub. McGraw-Hill Book Co. (New York), pp. 374-377 (1971)

67. Herzberg, G. , *Molecular Spectra and Molecular Structure I, Diatomic Molecules*, pub. Van Nostrand (New York), pp. 26-28 (1945)

68. Lengyel, B. A. , *Introduction to Laser Physics*, pub. John Wiley and Sons Inc. (New York) (1966)

69. Herzberg, G. , *Atomic Spectra and Atomic Structure*, pub. Dover Publications (New York), pp. 153 (1944)

70. Racah, G. , *Phys. Rev.* **61**, 537 (1942)

71. Faust, W. L. , McFarlane, R. A. , Patel, C. K. N. , Garrett, C. G. B. , *App. Phys. Lett.* **1**, 85-88 (1962)

72. Patel, C. K. N. , Faust, W. L. , McFarlane, R. A. , Garrett, C. G. B. , *App. Phys. Lett.* **4**, 18-19 (1964)

73. Patel, C. K. N. , Faust, W. L. , McFarlane, R. A. , Garrett, C. G. B. , *Proc. IEEE* **52**, 713 (1964)

74. McFarlane, R. R. , Faust, W. L. , Patel, C. K. N. , Garrett, C. G. B. , *Proc. IEEE* **52**, 318 (1964)

75. Heard, H. G. , Peterson, J. , *Proc. IEEE* **52**, 1258 (1964)

76. Faust, W. L. , McFarlane, R. A. , Patel, C. K. N. , Garrett, C. G. B. , *Phys. Rev.* **133**, A1476-A1486 (1964)

77. Foster, G. F. , Statz, H. , *J. Appl. Phys.* **32**, 2054-2055 (1961)

78. Faust, W. L. , McFarlane, R. A. , *J. Appl. Phys.* **35**, 2010-2015 (1964)

79. Gordon, E. I. , White, A. D. , *App. Phys. Lett.* **3**, 199-201 (1963)

80. Labuda, E. F. , Gordon, E. I. , *J. Appl. Phys.* **35**, 1647-1648 (1964)

81. Moeller, G. K. , McCubbin Jr., T. K. , *Appl. Opt.* **4**, 1412-1415 (1965)

82. Bloom, A. L. , *Gas Lasers*, pub. John Wiley and Sons Inc. (New York) pp. 52-59 (1968)

83. Jenkins, F. A. , White, H. E. , *Fundamentals of Optics*, 3rd. Ed., pub. McGraw-Hill Book Co. (New York), pp. 350 (1957)

84. Jenkins, F. A. , White, H. E. , *Fundamentals of Optics*, 3rd. Ed., pub. McGraw-Hill Book Co. (New York), pp. 490-491 (1957)

85. Brannen, E. , Rumbold, D. G., *Appl. Opt.* **8**, 1506-1508 (1969)

86. Siegman, A. E. , *An Introduction to Lasers and Masers*, pub. McGraw-Hill Book Co. (New York), pp. 304-325 (1971)

87. Svelto, O. , *Principles of Lasers*, 2nd. ed., pub. Plenum Press (New York and London), pp. 208 (1982)

88. Siegman, A. E. , *An Introduction to Lasers and Masers*, pub. McGraw-Hill Book Co. (New York), pp. 225 (1971)

89. Svelto, O. , *Principles of Lasers*, 2nd. ed., pub. Plenum Press (New York and London), pp. 156 (1982)

90. Siegman, A. E. , *An Introduction to Lasers and Masers*, pub. McGraw-Hill Book Co. (New York), pp. 346-372 (1971)

91. Rigrod, W. W. , *J. Appl. Phys.* **34**, 2602-2609 (1963)

92. Faust, W. L., *Appl. Phys. Lett.* **1**, 85-88 (1962)

93. Siegman, A. E. , *An Introduction to Lasers and Masers*, pub. McGraw-Hill Book Co. (New York), pp. 359 (1971)

94. Peele, J. R., Whitney, W. T., *Rev. Sci. Instrum.* **40**, 1114 (1969)

95. Kucerovsky, Z., Private Communication

96. Laser Focus Buyers Guide, pub. PennWell Co. (MA), pp. 499-510 (1982)

97. Fletcher, R. , Powell, M. J. D., *Computer J.* **6**, 163-168 (1963)

98. Hamming, R. W., *Numerical Methods for Scientists and Engineers*, 2nd ed., pub. McGraw-Hill Book Co. (New York), pp. 671-672 (1973)

99. Schneider, C. W. , *A Long Path Resonance Absorption Spectrometer*, Masters Thesis, University of Western Ontario, London, Ontario, Chapter 4 (1981)

100. Schneider, C. W., Kucerovsky, Z., Brannen, E., *Rev. Sci. Instrum.* **53**, 1376-1380 (1982)

101. Schneider, C. W. , *A Long Path Resonance Absorption Spectrometer*, Masters Thesis, University of Western Ontario, London, Ontario, Chapter 7 (1981)

102. Coggeshall, N. D., Saier, E. L., *J. Chem. Phys.* **15**, 65-71 (1947)

END

14 04 87

FIN